



**HAL**  
open science

# AC losses in superconductors: a multi-scale approach for the design of high current cables

Guillaume Escamez

► **To cite this version:**

Guillaume Escamez. AC losses in superconductors: a multi-scale approach for the design of high current cables. Electric power. Université Grenoble Alpes, 2016. English. NNT : . tel-01456495

**HAL Id: tel-01456495**

**<https://theses.hal.science/tel-01456495>**

Submitted on 11 Mar 2017

**HAL** is a multi-disciplinary open access archive for the deposit and dissemination of scientific research documents, whether they are published or not. The documents may come from teaching and research institutions in France or abroad, or from public or private research centers.

L'archive ouverte pluridisciplinaire **HAL**, est destinée au dépôt et à la diffusion de documents scientifiques de niveau recherche, publiés ou non, émanant des établissements d'enseignement et de recherche français ou étrangers, des laboratoires publics ou privés.



Distributed under a Creative Commons Attribution 4.0 International License

## THÈSE

Pour obtenir le grade de

### **DOCTEUR DE LA COMMUNAUTÉ UNIVERSITÉ GRENOBLE ALPES**

Spécialité : **Génie Électrique**

Arrêté ministériel : 25 mai 2016

Présentée par

**Guillaume Escamez**

Thèse dirigée par **Prof. Pascal Tixador**  
et codirigée par **Dr. Gérard Meunier**

préparée au sein **Génie Électrique de Grenoble (G2Elab)**  
et de **École Doctorale Électrotechnique Électronique Automatique et  
Traitement du Signal**

## **AC losses in superconductors : a multi-scale approach for the design of high current cables**

Thèse soutenue publiquement le **21 Octobre 2016**,  
devant le jury composé de :

**M. Christophe Geuzaine**

Professeur à l'Université de Liège, Président

**M. Bruno Douine**

Professeur à l'Université de Lorraine, Rapporteur

**M. Marco Breschi**

Professeur associé à l'Université de Bologne, Rapporteur

**M. Philippe Masson**

Professeur associé à l'Université de Houston, Examineur

**M. Arnaud Badel**

Chargé de recherche au CNRS, Examineur

**M. Christian-Éric Bruzek**

Docteur à Nexans France, Examineur

**M. Pascal Tixador**

Professeur à Grenoble-INP, ENSE<sup>3</sup>, Directeur de thèse

**M. Gérard Meunier**

Directeur de recherche CNRS, Co-Directeur de thèse

**M. Brahim Ramdane**

Maître de conférence à Grenoble-INP, ENSE<sup>3</sup>, Invité





**INSTITUT POLYTECHNIQUE DE GRENOBLE**

*N° attribué par la bibliothèque*

--	--	--	--	--	--	--	--	--	--	--	--	--	--	--	--	--	--	--	--

**THÈSE** pour obtenir le grade de **DOCTEUR DE GrenobleINP**

**Spécialité : « Génie Électrique »**

préparée au laboratoire de Génie Électrique de Grenoble (G2Elab) dans le cadre de  
l'École Doctorale « Électrotechnique Électronique Automatique et Traitement  
du Signal »

préparée et soutenue publiquement par

Guillaume ESCAMEZ

le 21 Octobre 2016

*Titre :*

**AC losses in superconductors: a multi-scale  
approach for the design of high current cables**

---

*sous la direction du Pascal Tixador et Gérard Meunier*

---

**JURY**

Christophe Geuzaine  
Bruno Douine  
Marco Breschi  
Philippe Masson  
Arnaud Badel  
Christian-Eric Bruzek  
Pascal Tixador  
Gérard Meunier  
Brahim Ramdane

Président  
Rapporteur  
Rapporteur  
Examineur  
Examineur  
Examineur  
Directeur de thèse  
Co-directeur de thèse  
Membre invité



*Eigentlich weiß man nur, wenn man  
wenig weiß. Mit dem Wissen wächst  
der Zweifel  
Goethe*



Tout d'abord, je tiens à remercier Monsieur Christophe Geuzaine pour m'avoir fait l'honneur de présider mon jury de thèse. Je remercie aussi les autres membres du jury, collègues et amis. La taille réduite de la communauté *supra* fait que les relations sont rapidement bonnes et propices à l'épanouissement scientifique. Je pense notamment à Philippe qui, il y a trois ans, blaguait sur le fait qu'il serait dans mon jury de thèse.

Ensuite je remercierai mes encadrants de thèse. Pascal et Gérard dont les échanges ont été intéressants. Je tiens surtout à remercier Frédéric Sirois que j'ai toujours considéré comme un autre directeur de thèse et qui m'a formé beaucoup. Brahim et Arnaud ont aussi beaucoup participé à mon encadrement sans compter leurs heures.

J'ai eu la possibilité de travailler dans deux laboratoires auprès de stagiaires mais aussi de personnel qualifié. Je remercie chaudement Cécile, Capucine, Benjamin, Julien, Pierre. Pour les voyages que j'ai pu faire au GREEN pour des mesures, je remercie Kévin, Jean, Hocine et Isabelle.

Lors de mon voyage à Montréal où j'ai pu découvrir la ville là bas, je remercie Kévin, Lucile et Maxime.

Pour Nexans, ma bouée de sauvetage a été portée par Jean Michel et Xavier. Deux amis qui m'ont toujours beaucoup apporté. Mon encadrement à Nexans a toujours été excellent grâce à Arnaud et Christian-Éric. Enfin, merci à Cécile qui m'a beaucoup assisté.

Je tiens à remercier mes amis Geoffrey, Anthony, Guilherme, Johnny, Thomas, Florian, Cédric, Kévin, Valentin, Pierre pour m'avoir aidé même dans les moments difficiles



# TABLE OF CONTENTS

ACKNOWLEDGMENTS	v
GENERAL INTRODUCTION	1
I SUPERCONDUCTIVITY AND NUMERICAL MODELING	5
I.1 SUPERCONDUCTIVITY	6
I.1.a Generality	6
Irreversibility field $H^*$	8
I.1.b Vortex and Flux pinning	10
I.1.c Flux Flow	11
I.1.d Thermally Activated Flux Motion	12
I.1.e E-J constitutive law of superconductor	13
I.1.e-i Critical state model	14
I.1.e-ii Power law model	15
I.1.e-iii Percolation law	18
I.2 AC LOSSES	19
I.2.a Definitions	19
I.2.b Hysteresis and screening current losses	19
I.2.c Coupling and eddy-current losses	20
I.2.d Magnetic losses	21
I.3 STUDIED SUPERCONDUCTORS	22
I.3.a HTS tapes and round wires (RW)	22
HTS tapes	22
Round REBCO wires by Nexans	25
One alternative : Bi-2212 round wires	25
I.3.b $MgB_2$	26
I.4 SUPERCONDUCTING LARGE SCALE APPLICATIONS	28
I.4.a Superconducting power cables	29
I.4.a-i Already operational SC power cables	29
I.4.a-ii The future of SC cables	30
CORC cables	30
Cables made with round HTS wires	31
$MgB_2$ high current DC power cables working at 20 K	31
I.4.b Other applications : magnets and dipoles	32
I.5 CALCULATIONS OF AC HYSTERESIS LOSSES	33
I.5.a Analytical	33

I.5.a-i	Calculations on tapes . . . . .	33
	Self-field AC losses . . . . .	33
	External field AC losses . . . . .	34
	AC losses with transport current and external field . . . . .	34
I.5.a-ii	Calculations on cylinders . . . . .	35
	Self-field AC losses . . . . .	35
	External field AC losses perpendicular to the cylinder . . . . .	35
I.5.a-iii	Calculations on tubes . . . . .	35
I.5.b	FEM modeling . . . . .	36
	Magnetic formulations . . . . .	37
	Electric formulations . . . . .	37
I.5.b-i	H-formulation . . . . .	38
I.5.b-ii	T- $\Phi$ formulation and associated formulations . . . . .	39
I.5.b-iii	Formulation comparison . . . . .	40
I.5.c	Integral method . . . . .	41
I.6	CHALLENGES AND GRIDLOCKS OF THE SUPERCONDUCTING MODELING . . . . .	42
I.6.a	Multi-scale problems . . . . .	43
I.6.b	Solving non-linear problems . . . . .	44
I.6.b-i	Fixed point method . . . . .	44
I.6.b-ii	Newton-Raphson method . . . . .	45
	Example $f(x)$ . . . . .	45
	Generalization . . . . .	45
	Algorithm to help the convergence . . . . .	46
I.7	CONCLUSION . . . . .	47
II	AC LOSSES IN HTS TAPES AND ROUND WIRES . . . . .	49
II.1	APPROACH AND CHALLENGES FOR HTS MODELING . . . . .	50
II.2	TRANSIENT ELECTRO-MAGNETIC MODELING OF HTS TAPES . . . . .	50
II.2.a	AC losses in HTS tapes . . . . .	50
II.2.b	Studied superconductors . . . . .	50
II.2.b-i	Superpower tape . . . . .	50
II.2.b-ii	SuperOx conductor . . . . .	53
II.2.c	FEM modeling . . . . .	54
II.2.c-i	Distribution of current in the layers . . . . .	56
II.2.d	Comparison FEM - Integral method . . . . .	59
II.2.e	Experimental validations . . . . .	61
II.2.e-i	Measurement protocol . . . . .	61
II.2.e-ii	Single tape results . . . . .	64
II.2.f	Conclusion : from tapes to round wires . . . . .	66
II.3	AC LOSSES IN HTS ROUND WIRES . . . . .	67
II.3.a	Model description . . . . .	67
II.3.b	FEM modeling . . . . .	69
II.3.b-i	Meshing . . . . .	69
II.3.b-ii	Effect of metallic layers in loss calculations . . . . .	71
II.3.b-iii	AC self-field losses . . . . .	73

II.3.b-iv	External magnetic field AC losses . . . . .	74
II.3.b-v	Combined AC losses . . . . .	75
II.3.b-vi	Comparison of different E-J power laws . . . . .	76
II.3.b-vii	AC losses in RW with anisotropic properties of the critical current . . . . .	77
II.3.c	Integral method . . . . .	78
II.3.c-i	Self-field AC losses . . . . .	79
II.3.c-ii	External magnetic field losses . . . . .	80
II.3.c-iii	Combined AC losses . . . . .	80
II.3.d	Design perspectives for high current cables . . . . .	82
II.4	CONCLUSION . . . . .	84
 III MULTI-FILAMENTARY 3-D AC LOSSES MODELING		<b>87</b>
III.1	MODELING 3-D MULTI-FILAMENTARY GEOMETRIES . . . . .	88
III.1.a	On the necessity of numerical modeling for AC loss calculations . . . . .	88
III.1.b	Comparison of 2-D and 3-D models for multi-filamentary geometries . . . . .	89
III.1.c	Softwares used for the numerical benchmark . . . . .	91
III.1.d	Problem description . . . . .	92
III.2	THREE FILAMENT BENCHMARK MODEL . . . . .	93
III.2.a	Model description . . . . .	93
	Preisach model for hysteresis calculations - case <i>hys</i> . . . . .	94
III.2.b	Results . . . . .	95
III.2.b-i	AC hysteresis losses - first test case <i>air</i> . . . . .	95
III.2.b-ii	Change of geometry for the calculations of combined AC losses . . . . .	96
III.2.b-iii	AC hysteresis losses in the case <i>air</i> - Coupled losses . . . . .	98
III.2.b-iv	Addition of a resistive matrix : case <i>res</i> . . . . .	100
	Coupling-Decoupling . . . . .	100
	Combined AC losses . . . . .	101
	AC losses versus frequency . . . . .	102
III.2.b-v	Addition of a magnetic matrix case <i>mag</i> . . . . .	103
III.2.b-vi	Addition of a hysteresis model . . . . .	103
III.2.b-vii	Conclusion on the simulations . . . . .	104
III.2.c	Impact of the E-J relationship on AC losses calculations . . . . .	104
III.2.d	Optimization of the numerical solving process . . . . .	105
III.2.e	Conclusion of the three filament benchmark . . . . .	107
III.3	MgB <sub>2</sub> MULTI-FILAMENTARY WIRES . . . . .	108
III.3.a	Model description . . . . .	108
III.3.b	Experimental characterization . . . . .	109
III.3.b-i	MgB <sub>2</sub> wires . . . . .	109
	Critical current measurement setup . . . . .	109
	Results . . . . .	112
III.3.b-ii	Nickel matrix . . . . .	115
III.3.b-iii	Monel . . . . .	118
III.3.b-iv	Conclusion . . . . .	119

III.3.c	Preliminary numerical studies . . . . .	119
III.3.c-i	Description of the model . . . . .	119
	Superconductor ( $\text{MgB}_2$ ) . . . . .	121
	Nickel . . . . .	121
III.3.c-ii	Test cases on 6 filament wires . . . . .	121
III.3.c-iii	Test cases on 18 filament wires . . . . .	124
III.3.c-iv	Test cases on 36 filament wires . . . . .	125
III.3.d	AC losses for complete $\text{MgB}_2$ wires . . . . .	125
III.3.d-i	Adjustment of the geometry and physical properties . . . . .	125
III.3.d-ii	Results . . . . .	127
III.3.e	To go further . . . . .	128
III.4	CONCLUSION . . . . .	129
IV	TOWARDS THE CALCULATIONS OF AC LOSSES IN HIGH POWER CABLES	<b>131</b>
IV.1	CALCULATION OF AC LOSSES FOR HIGH POWER CABLES . . . . .	132
IV.1.a	Multi-scale approach . . . . .	132
IV.1.b	Examples . . . . .	133
	IV.1.b-i Round wire cable . . . . .	133
	IV.1.b-ii $\text{MgB}_2$ cable . . . . .	134
IV.2	NUMERICAL MODELING OF AC LOSSES WITH DC BACKGROUND . . . . .	135
IV.2.a	Limit of the power law model . . . . .	135
IV.2.b	An alternative given with the E-J percolation law . . . . .	138
IV.2.c	AC ripples superposed to DC current . . . . .	139
IV.2.d	Conclusion on the E-J power laws . . . . .	142
IV.3	AC LOSS CALCULATIONS FOR MULTI-SINOSOIDALS WAVEFORMS . . . . .	142
IV.3.a	Problem description . . . . .	142
IV.3.b	Simulation and experimental validations . . . . .	143
IV.3.c	Examples of applications . . . . .	147
IV.3.d	Conclusion . . . . .	148
IV.4	RECOMMENDATIONS FOR THE CALCULATIONS OF AC LOSSES IN DC CABLES	149
V	APPLICATION TO A 10 kA SUPERCONDUCTING DEMONSTRATOR CABLE	<b>151</b>
V.1	INTRODUCTION : THE <i>BEST-PATHS</i> PROJECT . . . . .	152
V.2	DEMO 5 : $\text{MgB}_2$ SUPERCONDUCTING LINK . . . . .	153
V.2.a	Demonstrator design and requirements . . . . .	153
V.2.b	Cable design . . . . .	154
V.2.c	Advantages of the superconducting cable for DC grids . . . . .	155
	V.2.c-i Life-Cycle Analysis (LCA) . . . . .	155
	V.2.c-ii Cable foot prints . . . . .	155
V.2.d	Our contribution . . . . .	156
V.3	AC LOSSES CALCULATIONS . . . . .	156
V.3.a	Cable magnetic design . . . . .	157
V.3.b	Ripple field analysis . . . . .	157
	V.3.b-i Results for AC ripples superposed to DC environment . . . . .	158
	V.3.b-ii $\text{MgB}_2$ architectures . . . . .	160

---

V.3.c	Current inversion . . . . .	161
V.4	QUENCH MODELING . . . . .	162
V.4.a	Numerical model . . . . .	162
V.4.a-i	MgB <sub>2</sub> conductor modeling . . . . .	163
	Electrical resistivity . . . . .	164
	Thermal conductivities . . . . .	164
	Heat capacity and density . . . . .	165
V.4.a-ii	Helium effect - external forced convection in tubes . . . . .	165
V.4.b	Simulations of faults . . . . .	166
	Effect of the GHe velocity against a fault current . . . . .	167
	Variations on fault values and durations. . . . .	167
V.5	CONCLUSION . . . . .	171
	FINAL CONCLUSION	<b>173</b>
	REFERENCES	<b>175</b>
	RÉSUMÉ EN FRANCAIS	<b>191</b>



---

## General Introduction

THE INCREASE of renewable energies over the globe far for the customer are one of the new challenge of the XXI<sup>st</sup> century. Producing and delivering high power trough long distance are today a challenge that can be overcome by using different scattering edge technologies and a drastic change of the network architecture. Whereas, the electrical network work on AC transmitter with varying frequencies worldwide (50 Hz in continental Europe, 60 Hz in USA), a new scheme of electrical grid using DC power is investigated. The use of long distance DC cables allows the production of electricity in fertile area and its transport on thousand of kilometers. While investigating on this new architecture, cables manufacturer are looking for alternatives to build small and compact high power cables.

In this framework, superconducting materials are a viable option and are highly promising for high power applications. The carrying current densities are 10 times higher than copper, allowing the creation of high current cables in narrow spaces. The only drawbacks of superconductors, despite their relative high costs, is the necessity of working at cryogenic temperature, i.e. below 92 K for REBCO tapes for example. The superconductivity is characterized by a absence of measurable resistivity in particular conditions of temperature  $T$ , field  $B$  and current  $I$ . The superconducting area which refers to the domain where the resistivity of the material is almost equals to zero is delimited by a critical temperature  $T_c$ , a critical field  $B_c$  and a critical current  $I_c$ .

An absence of resistive does not mean necessarily an absence of losses. Classical Joule losses induced by the current passing trough a resistive materials are not occurring inside superconducting materials. However AC losses are losses that take place inside superconductors when the one is subjected to a time-environment. The variation of transport current inside the tape or the application of a external magnetic field with time generates a change of induction which leads to the existence of an electrical field and losses. Theses losses are referred as AC losses.

Even in a DC application, superconductors may be subjected to time varying current due to the converters which induce harmonics/ripples in the output. A change of direction of current is also possible in some applications. Hence, it is necessary to know with a certain accuracy the AC losses generated inside a full power cable to scale up the cryogenic system. This thesis aims to calculate first by considering simple examples, AC losses inside large scale applications and mostly inside superconducting cables. Analytical calculations of AC losses are possible but for a more detail description of the AC losses, numerical mo-

deling are necessary. For example, integral methods of finite-element modeling are usable. This thesis discloses numerical modeling of superconductors with these particular methods. Some experiments have been carried out along to validate the model.

The first chapter of this thesis gives the context and the necessity of assessing the AC losses inside superconductors. The calculations can be done analytically or numerically. After a brief introduction on the superconductivity, the losses mechanisms are explained. Two different conductors were investigated and they exhibit different geometric structures and properties. Both of them are described with precision. These superconductors are well suited for the development of high power cables. This chapter ends by describing first, the numerical tools available for the calculations of AC losses, and then the challenges and gridlocks inherent to the superconducting modeling. The following two chapters are dedicated to the calculations on AC losses in REBCO conductors and  $\text{MgB}_2$  conductors.

In Chapter II, numerical models using FEM and integral methods are developed for the calculation of AC losses in REBCO conductors. Solving these numerical models is challenging as the REBCO conductors exhibit anisotropic properties. The mesh has to be adapted to the geometry. We carried out two different methods for AC loss calculations with comparison to experimental results. In addition to these developments, the numerical model is adapted to a new shape of REBCO conductor : a round wire. The simulations try to asses the AC losses in this wire for a possible use in high current compact power cables.

For REBCO conductors, numerical model can be 2-D but as soon as the conductor is composed of twisted filaments inside a conductive matrix, it is necessary to develop a 3-D model. 3-D simulations of superconductors are not largely made as they include large numbers of elements, connexity problems and the convergence of the model is closely linked to the superconducting properties. In Chapter III, 3-D models are developed. First, within a three filament wire which has been investigated inside an international benchmark. After that, the complexity of the model is gradually increased to finally end with a realistic model of a  $\text{MgB}_2$  wire with up to 36 filaments. A series of characterizations is also presented to come up with a model as close as possible from the real wire.

After focusing in the previous two chapters on single conductors, the calculation of the AC losses on a power cable is investigated in Chapter IV. Modeling a full superconducting cable in details is beyond the capacity of the computed resources. That is why we suggest a mutli-scale approach with a preliminary calculation of the external magnetic field of the complete cable. This simulation is relatively fast and give a value of field amplitude the conductors are subjected. On a second time, the calculation of the losses can be made. To have a more flexible tool, the model is adapted to DC applications. Some simulations have been carried out to investigate on simulation with AC ripples superposed to DC background (current and field).

Finally, Chapter V focuses on the calculation of AC losses on a practical example, the 10 kA  $\text{MgB}_2$  demonstrator of the european project *BEST-PATHS*. As this demonstrator is a key element to asses the liability of long high current superconducting cable for real grids,

it is necessary to study the losses of the demonstrator and this is made possible by the model previously developed. Moreover, the question of the protection of the demonstrator is approached.



## Chapter I

---

# Superconductivity and numerical modeling

---

### CONTENTS

---

I.1	SUPERCONDUCTIVITY . . . . .	6
I.1.a	Generality . . . . .	6
I.1.b	Vortex and Flux pinning . . . . .	10
I.1.c	Flux Flow . . . . .	11
I.1.d	Thermally Activated Flux Motion . . . . .	12
I.1.e	E-J constitutive law of superconductor . . . . .	13
I.2	AC LOSSES . . . . .	19
I.2.a	Definitions . . . . .	19
I.2.b	Hysteresis and screening current losses . . . . .	19
I.2.c	Coupling and eddy-current losses . . . . .	20
I.2.d	Magnetic losses . . . . .	21
I.3	STUDIED SUPERCONDUCTORS . . . . .	22
I.3.a	HTS tapes and round wires (RW) . . . . .	22
I.3.b	MgB <sub>2</sub> . . . . .	26
I.4	SUPERCONDUCTING LARGE SCALE APPLICATIONS . . . . .	28
I.4.a	Superconducting power cables . . . . .	29
I.4.b	Other applications : magnets and dipoles . . . . .	32
I.5	CALCULATIONS OF AC HYSTERESIS LOSSES . . . . .	33
I.5.a	Analytical . . . . .	33
I.5.b	FEM modeling . . . . .	36
I.5.c	Integral method . . . . .	41
I.6	CHALLENGES AND GRIDLOCKS OF THE SUPERCONDUCTING MODELING . . . . .	42
I.6.a	Multi-scale problems . . . . .	43
I.6.b	Solving non-linear problems . . . . .	44
I.7	CONCLUSION . . . . .	47

---

### Summary

*Superconductivity was first discovered by Kamerlingh Onnes in 1911. It is characterized by the property of presenting no resistivity below a certain temperature and a certain field. This feature is particularly interesting for the transport of high currents in large scale applications. After a brief introduction of superconductivity, the AC losses mechanisms which are induced, in superconducting materials when subjected to time-varying environment, are explained. These losses can be in different forms depending on superconducting materials : REBaCuO or MgB<sub>2</sub>. After a description of these materials, their use in large power applications are detailed. To size cryogenic systems required for these large scale applications, different approaches to calculate AC losses are possible and detailed. All these approaches have advantages but also drawbacks mostly related to superconducting modeling (aspect ratio, non-linearity,...)*

## I.1 Superconductivity

### I.1.a Generality

Superconductivity is referring to a particular state of matter appearing in a number of materials such as metals, alloys, ceramics or organic compounds. The most observable property of superconducting materials is the absence of resistivity (criterion set at  $10^{-12} \Omega.m$ ) under a certain temperature value referred to as the critical temperature  $T_c$ . This effect was discovered by Heike Kamerlingh Onnes in 1911 after he successfully liquified helium. On April 8<sup>th</sup> 1911, he and his team observed the resistance of mercury becoming non measurable (nearly zero) at 4.2 K [1]. The name "superconductivity" was then used to refer to this particular state of the matter. After this discovery, several pure metals have been shown to exhibit superconducting properties for example lead [2] ( $T_c=7$  K) in 1922 or aluminum in 1958 [3]. Fig. I.1 displays the plot of resistivity versus temperature in mercury as it was recorded during the experiment in October 1911.

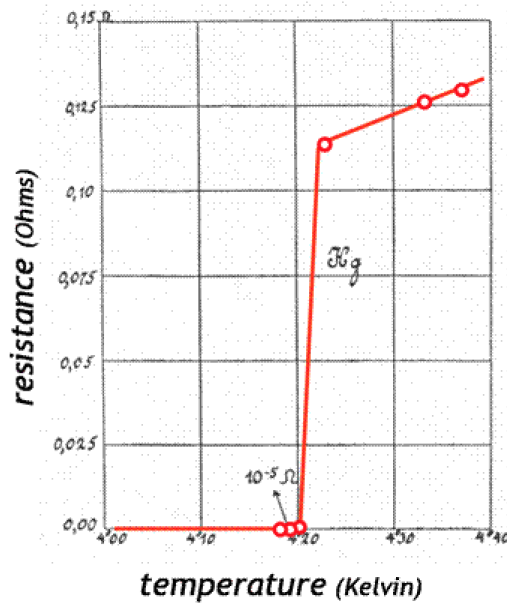


Fig. I.1 – Resistivity of mercury versus temperature measured by K.Onnes's team in Octobre 1911 [1].

Starting from 1962, Low Temperature Superconductors (LTS) such as NbTi et Nb<sub>3</sub>Sn are commercialized in large quantities. These superconductors with a  $T_c$  near 4.2 K have been used in large scale applications such as MRI, dipole magnets in CERN or superconducting motors. In the late 80's, superconducting properties have been discovered in ceramics (oxocuprates) for example in YBa<sub>2</sub>Cu<sub>3</sub>O<sub>7- $\delta$</sub>  or Bi<sub>2</sub>Sr<sub>2</sub>Ca<sub>n-1</sub>Cu<sub>n</sub>O<sub>2n+4+x</sub> (respectively 1986 and 1988). Because of their very high critical temperatures ( $T_c > 90$  K), these superconductors have be classified as High Temperature Superconductors (HTS). Finding superconductivity in ceramics (oxocuprates) was a major breakthrough, rewarded by a Nobel Prize in 1987. This feature allows the conductor to work with liquid nitrogen ( $T=77$  K

at ambient pressure), a cryogenic liquid far cheaper than liquid helium. In parallel to research focusing on enhancing oxocuprate properties, superconductivity was discovered in Magnesium Diboride  $MgB_2$  in 2001 [4] and in Iron-Based compounds (FeSC) [5, 6]. The increase of the critical temperature of superconductors is still the main of challenge of research to find ambient temperature superconductivity. The latest achievement is the discovery of superconductivity in sulfur hybrid  $H_2S$  at 203 K but under 150 GPa in 2015 [7]. Fig. I.2 displays the  $T_c$  achievements versus years for superconducting materials [8].

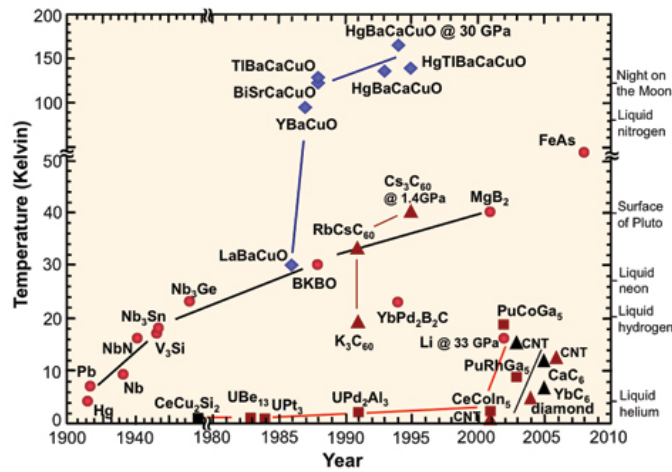


Fig. I.2 – Critical temperature of discovered superconductors over the years. The new discovery in 2015 of  $H_2S$  at 203 K and 150 GPa should be added.

Compared to perfect conductors, superconductors have the remarkable property of expelling all magnetic flux from their volumes in specific conditions. This phenomena is called Meissner-Effect [9]. The superconductors are classified in two types : Type-I superconductors which exhibit a perfect Meissner Effect and Type II superconductors where two states, perfect Meissner Effect and partial Meissner Effect exist. The two types of superconductors are shown in Fig. I.3.

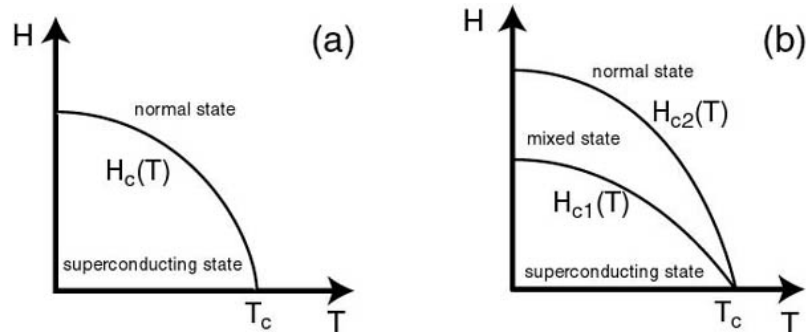


Fig. I.3 – Type I and II superconductors. One can notice the third state called mixed state in Type-II superconductors where the Meissner Effect is only partial.

Type II superconductors are mainly used because the values of critical field  $H_{c2}$ , which

delimits the mixed state from the normal state, are rather high compared to Type I superconductors (usually pure metals). From  $H_{c1}$  and  $H_{c2}$  values, it is also possible to define  $H_c$  (or  $B_c$ ) the thermodynamic critical field. The corresponding diagram of the magnetization  $M$  versus an external applied field is shown in Fig. I.4. In this diagram,  $B_{c1}$  refers to the field at which flux begins to penetrate and  $B_{c2}$  the field at which the material becomes normal.

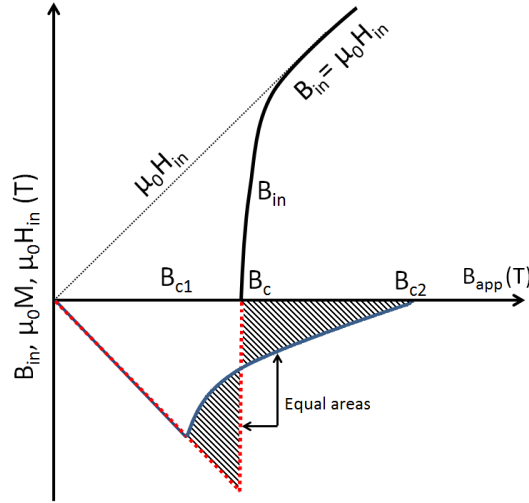


Fig. I.4 – Superconducting domain in terms of magnetic field for different superconductors versus temperature. The thermodynamic field is defined when the two areas are equal

The thermodynamic critical field  $B_c$  is defined [10] as :

$$\int_{B_{c1}}^{B_c} (B_{app} + \mu_0 M) dB_{app} = \mu_0 \int_{B_c}^{B_{c2}} (-M) dB_{app} \quad (I.1)$$

Adding to that, it is possible to see that the relationship  $B = \mu_0 H$  for values of field higher than  $H_{c1}$  is valid and will always be taken into account.

**Irreversibility field  $H^*$**  If a HTS sample is magnetized, it is possible to observe a third critical field called irreversibility field  $H^*$  significantly smaller than  $H_{c2}$ . The irreversibility field is a field at which the hysteresis curve does not follow its reversible trend [11]. This is because, at a certain temperature and beyond a certain field, the pinned vortices start moving and magnetization loops no longer behave in a reversible way [12, 13]. This value is referring as the irreversibility field  $H^*$ . Usually, the value of critical field of a type-II superconductor is taken equal to  $H^*$ . Fig. I.5 displays the critical field of different superconductors versus temperature.

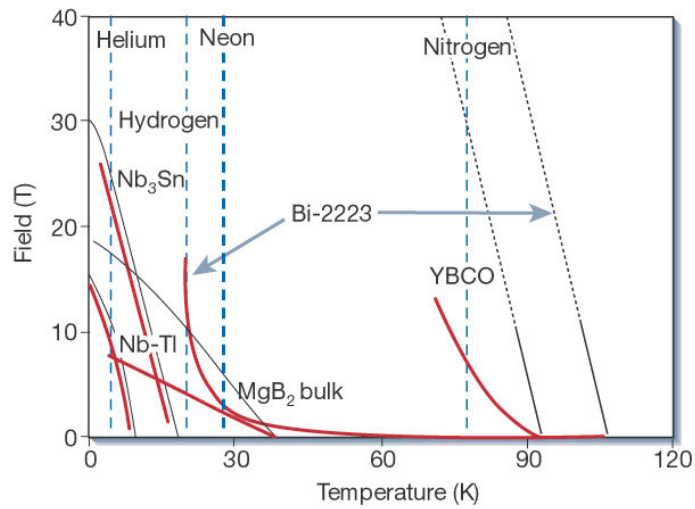


Fig. I.5 – Superconducting domain regarding field for different superconductors versus temperature [14].

With the critical temperature and the critical field, the superconducting state exists only with values of current density below a certain value called critical current density  $J_c$  linked to the critical current  $I_c$ . This  $I_c$  value is the current (critical current density  $J_c$  multiplied by the superconducting surface) given for a criterion of field observed on the superconducting material  $E_c$ . From the three introduced quantities, it is possible to delimit a superconducting domain with  $T_c$ ,  $H_c$  and  $J_c$ , for example in Fig I.6.

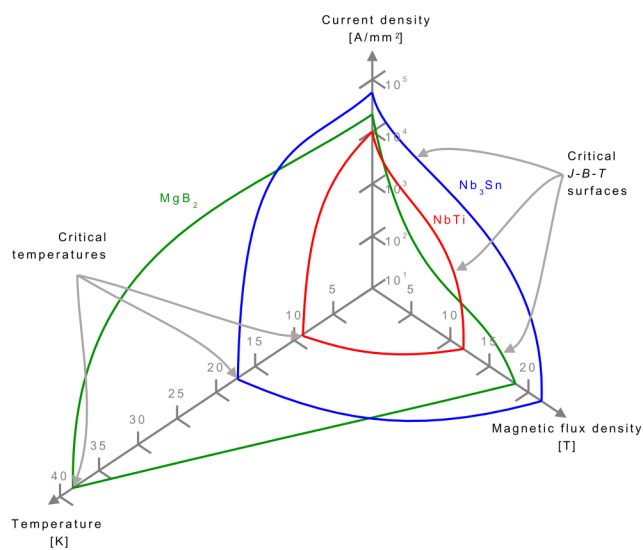


Fig. I.6 – Superconducting domain plotted in a temperature, field and current density graph for several superconductors [15].

### I.1.b Vortex and Flux pinning

Inside a superconductor, the magnetic flux density does not penetrate in an homogeneous way but locally in disconnected volumes called vortices. A vortex can be defined as a cylinder with a radius of  $\xi$  called the coherence length. Outside the vortex, the magnetic flux density decays with an exponential trend with distance. The characteristic length of decay is the London length  $\lambda_L$ . It is assumed that the magnetic flux density and the current from the vortex only exists in the cylinder delimited by the radius  $\lambda_L$  shown in Fig. I.7.

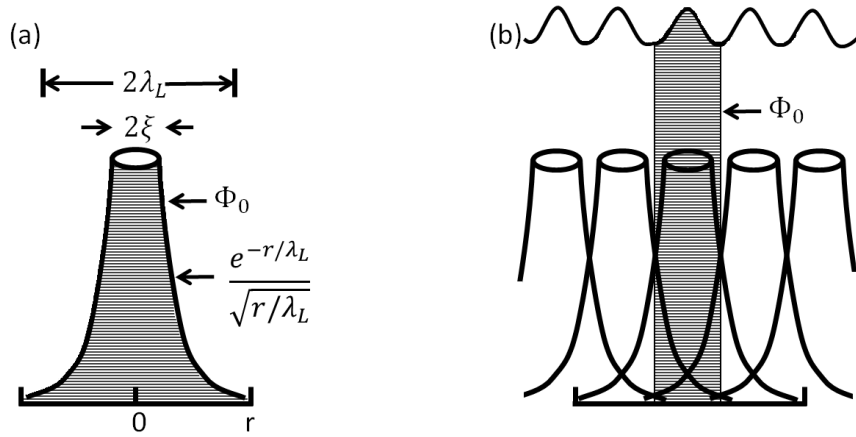


Fig. I.7 – In (a), distribution of the magnetic field around an individual vortex and (b) the field from a group of vortices. The region of  $\Phi_0$  is cross-hatched in both cases.

Each vortex carries a magnetic flux quantum  $\Phi_0$  that can be calculated. The magnetic flux  $\Phi$  is quantized in the superconductor according to the London theory [16]. It is possible to express the critical fields with  $\Phi_0$ . In a Type II superconductors,  $B_{c1}$ ,  $B_{c2}$  and  $B_c$  are given according to :

$$B_{c1} = \frac{\Phi_0 \ln \kappa}{4\pi\lambda^2} \quad (\text{I.2})$$

$$B_{c2} = \frac{\Phi_0}{2\pi\xi^2} \quad (\text{I.3})$$

$$B_c = \frac{\Phi_0}{2\sqrt{2}\pi\lambda\xi} \quad (\text{I.4})$$

where  $\kappa = \lambda/\xi$  is called the Ginzburg-Landau parameter [17]. It is also convenient to write these quantities in the form of a product as :

$$\sqrt{B_{c1}B_{c2}} = B_c(\ln \kappa)^{1/2} \quad (\text{I.5})$$

It is possible to observe the vortices with magnetic powder for example in Fig. I.8. Their number and also the distance between the vortices are directly proportional to the intensity of the applied field for fields much higher than  $H_{c1}$ .

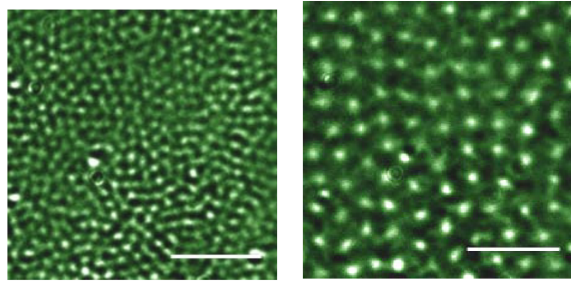


Fig. I.8 – Magneto-Optical images of vortices in a NbSe<sub>2</sub> superconducting crystal at 4.0 K in earth field (left) and in a 0.8 mT applied field (right). The scalebar is 10  $\mu\text{m}$  [18].

In the mixed state, when the superconductor is under a transverse field and a transport current, the vortices are subjected to Lorentz Forces  $\vec{F}$  according to :

$$\vec{F} = \vec{J} \times \vec{B} \quad (\text{I.6})$$

These forces will induce vortices displacement and then energy dissipation inside the material. To avoid this issue, structural defaults (pinning center) are made inside the material creating pinning forces to block the movements of the vortices. It is possible to represent the pinning forces as an average force density  $\vec{F}_P$  which is maximized when :

$$F_p = |\vec{J}_c \times \vec{B}| \quad (\text{I.7})$$

The efficiency is maximized when the size of the defect is equal to the coherence length  $\xi$ . Several ideas to induce pinning centers inside the superconductors are displayed in Fig.I.9

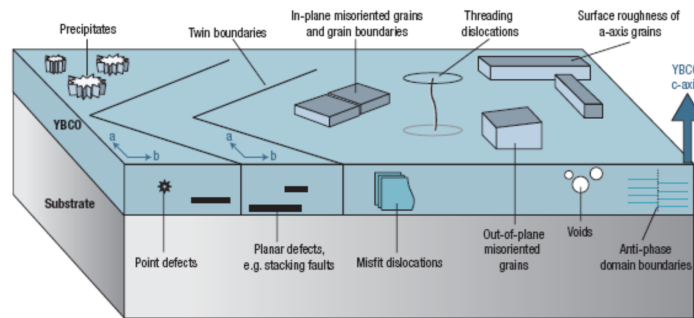


Fig. I.9 – Example of pinning centers inside a superconducting layer [19].

When the current density is equal to  $J_c$ , the Lorentz forces are predominant (Lorentz forces are proportional to the current density) over Pinning forces and the vortices are put in motion off the material creating what is called a *flux-flow* regime.

### I.1.c Flux Flow

The vortices start to flow in the material and are only slowed down by viscosity forces. As the vortices move freely inside the material, the *flux-flow* regime creates a voltage drop

along the superconductor. Inside a uniform vortex motion the dissipation per unit volume, is given by the product  $\vec{E}\vec{J}$  which is equal to the product of the Lorentz force and the flux flow velocity  $(\vec{J} \times \vec{B})\vec{v}$ . Hence, it leads to [20] :

$$\vec{E} = \vec{B} \times \vec{v} \quad (\text{I.8})$$

By introducing a independent velocity coefficient  $\eta$ , the energy dissipation is equal to :

$$\vec{J}\vec{E} = n_v \eta < v^2 > \quad (\text{I.9})$$

Where  $n_v$  is the vortex flux number defined as  $n_v=B/\Phi_0$ . Combining (I.8) and (I.9) :

$$\vec{E} = \rho_f \vec{J} = \frac{B^2}{n_v \eta} \vec{J} = \frac{\Phi_0 B}{\eta} \vec{J} \quad (\text{I.10})$$

In (I.10), it is possible to see that in the Flux-Flow regime, the electric field is linear with the critical current and is well defined.

#### I.1.d Thermally Activated Flux Motion

From last section, the current transition is defined linearly. However, in reality, the curve E versus J of a superconductor is curved. In addition, the current inside a bulk material decays, with a slowly logarithm time dependence. This phenomenon is called *flux-creep* and is linked to thermally activated rearrangement of flux lines to a more stable configuration. It has been suggested a creep model for flux lines in 1962 [21]. The jump rate R is assumed to have the shape of an exponential trend on the thermal energy according to :

$$R = \omega_0 e^{\frac{-U}{k_B T}} \quad (\text{I.11})$$

Where U is the barrier energy and  $\omega_0$  is the characteristic frequency for hopping attempts,  $k_B$  is the Boltzmann constant ( $k_B=1.38 \times 10^{-23} \text{ JK}^{-1}$ ) and T the temperature. The barrier energy U was suggested as :

$$U = U_0(1 \pm J/J_c) \quad (\text{I.12})$$

In (I.12), the sign depends on whether we consider a Lorentz force with or against the vortex displacement. In Fig. I.10, it is possible to see that the forces are more likely to be along the x axis. Hence, the motion in in the same direction as the force.

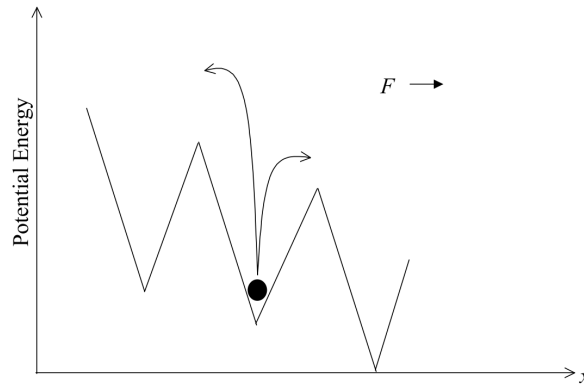


Fig. I.10 – Potential energy on a flux line subjected to a Lorentz force [22].

As consequence of this effect, the field trapped inside a Type II superconductor is decreasing with a logarithm trend [23]. As a consequence to it, the experimental measurement of  $E$  versus  $J$  can be a bit challenging coming from the fact that it is difficult to delimit the activation of flux motion. Hence, a criterion  $E_c$  defining  $J_c$  was assumed. In some HTS materials, the  $E$ - $J$  relationship has been observed as linear well below the critical current transition. This effect is called Thermally Activated Flux Flow [24].

### I.1.e E-J constitutive law of superconductor

Assuming that the superconductor is working below its critical temperature and field, going from superconducting state to normal state is only achievable if the transport current flowing inside the superconductor is higher than  $I_c$ . Between these two states, the transition is called dissipative state as shown in Fig. I.11. Being able to model with accuracy, the dissipative state when current is penetrating inside the superconductor is necessary for numerical modeling especially for electromagnetic calculations.

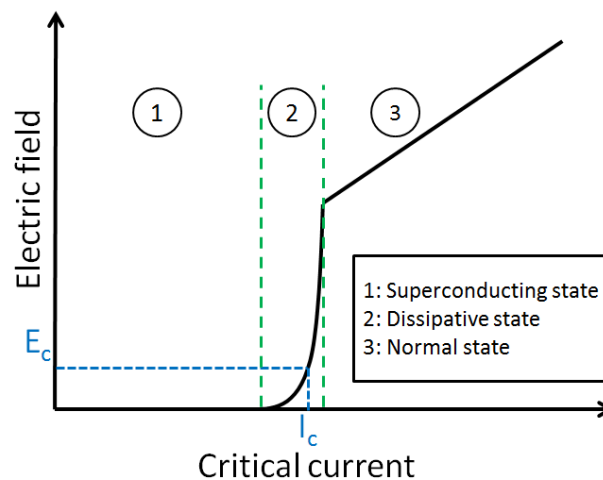


Fig. I.11 – Different states when current is flowing inside a superconductor below its critical temperature and field.

The E-J representation can be done by fitting experimental characterizations. In the superconducting state, the resistivity of the material is observed to be nearly zero for values of current density  $J$  under  $J_c$ . When the current density is higher than  $J_c$ , in the dissipative and normal states, the resistivity of the material starts to become non negligible. To model this behavior, a classic step function can be used with a threshold value of  $J_c$ , this suggested formulation is referring as the *critical state model* (CSM). Other types of fit which exhibit smoother transitions from superconducting state to normal state can be used for example the *power law model* or the *percolation law*.

### I.1.e-i Critical state model

The *critical state model* (CSM) or *Bean model* [25] was first suggested as a simple explanation of the hysteresis phenomena which was observed experimentally in superconductors when current or magnetic field is applied. The CSM offers a macroscopic relationship by linking the current density and the electric field in the superconductor as in (I.13), this refers to a instantaneous transition from superconducting state to a state where the conductor starts to dissipate. This transition is made when the current density is equal to  $J_c$  :

$$\forall |\vec{J}| < J_c, E = 0; \text{ for } |\vec{J}| \geq J_c, E \neq 0 \quad (\text{I.13})$$

In the critical state model, the current density inside the superconducting material can only be equal to discrete values  $\pm J_c$  or 0. Then, when current penetrates the superconducting material, the magnetic flux density reacts as :

$$\nabla \times \vec{H} = \pm \vec{J}_c \quad (\text{I.14})$$

In his work, Bean suggested that the critical current density is dependent on the magnetic field but the critical state model used a constant value of  $J_c$ . When a transport current is applied on the conductors (or a varying magnetic field is imposed), the current penetrates and so does the magnetic field. The area where the magnetic field (and the current) is absent is called virgin state. It means that the area has not been under any field or current from the start.

As an simple example to understand what is happening inside a superconductor when it is exposed to a current or field, let us consider the case of a superconducting slab exposed to a time varying magnetic field displayed in Fig. I.12. From (I) to (II), the magnetic field is increasing from zero to a certain value of amplitude  $H_a$ , the current and the magnetic field start to penetrate inside the superconductor. The total current is zero if we consider the complete surface because magnetization currents are looping inside the slab. This is shown in the figure as one of the two area carries  $+J_c$  (on the right) and the other one  $-J_c$  (on the left). If one is staying in (II), the current does not move inside the superconductor leaving a certain part of the area free of current. The magnetic field is decreasing from  $H_a$  (II) to  $-H_a$  (IV) down to 0 (III). As only discrete critical current density values coexist inside the superconducting material, the current start to penetrates inside the material but the looping is in this opposite direction. In (III) when the magnetic flux density is zero, there are still current densities inside the materials, this feature is referred to as *hysteresis* due to the particular capability of the superconductor to trap the current density at its

core. From (III) to (IV), the current densities looping in the opposite direction become predominant inside the material. From these simulations, it is possible to define  $H_p$  the penetration field as  $H_p = J_c a / 2$  with  $a$  the thickness of the slab.

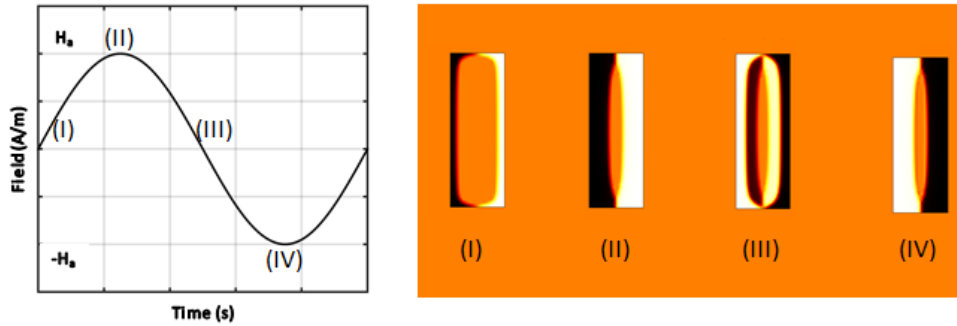


Fig. I.12 – Current density distributions when a superconductor is subjected to an time-varying external magnetic field.

This model is realistic in the case of LTS where sharp transitions are observed [26, 27]. However, HTS have smoother transitions and the CSM may not be used in all the cases of HTS applications. Different smoother relationships have been suggested by the community, for example, the two following.

#### I.1.e-ii Power law model

The transitions in HTS are observed to have a smoother shape. Hence, the E-J relationship exhibits a non-linear variation that can be approximated as a power law, suggested in [28, 29, 30]. This theory comes from the flux-creep model taking into account a logarithm dependence of the effective energy barrier explained in I.1.d. The critical current  $J_c$  is then defined as the value from which a certain electric field  $E_c$  is observed. In practice the criterion of  $E_c = 1 \mu\text{V}\cdot\text{cm}^{-1}$  is used. For a 1 cm sample, the voltage value is then 1  $\mu\text{V}$ . As a comparison,  $E_c$  of LTS is usually set at 100  $\text{nV}\cdot\text{cm}^{-1}$  [31].

This difference of  $E_c$  is explained as the HTS can work with liquid Nitrogen, a much cheaper cryogenic liquid. In liquid Nitrogen, having a criterion of 1  $\mu\text{V}$  in terms of dissipation is considered as acceptable regarding the low price of the liquid, where in liquid Helium it was not the case. For convenient use, the criterion for the  $\text{MgB}_2$ , even if it operates between 4.2 K and 20 K, has been chosen as 1  $\mu\text{V}$  but this criterion has to be further reconsidered. The power law fitted from measurements is written in (I.15). An example can be found in Fig. I.13. The value  $n$  indicates how sharp the transition is in the material (linked to the purity of the sample). For example LTS exhibit  $n$  values in the range of 80-100 [32] whereas HTS have  $n$  values between 30 and 50 [33].

$$\text{Power law : } \vec{E}(|\vec{J}|) = E_c \left( \frac{|\vec{J}|}{J_c(|\vec{B}|, T)} \right)^{n(|\vec{B}|, T)} \frac{\vec{J}}{|\vec{J}|} \quad (\text{I.15})$$

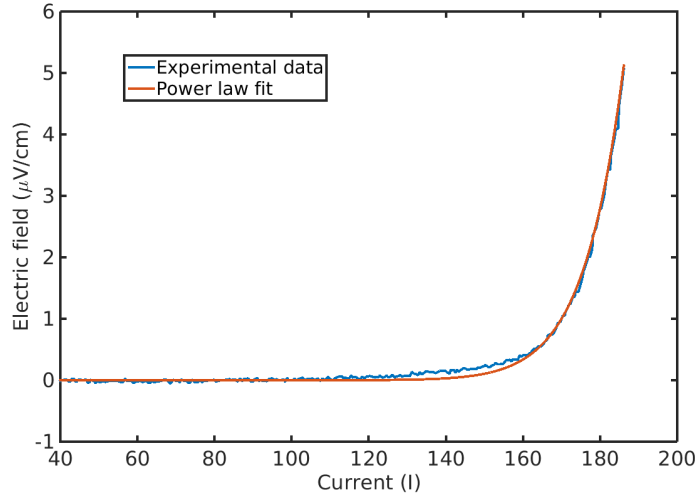
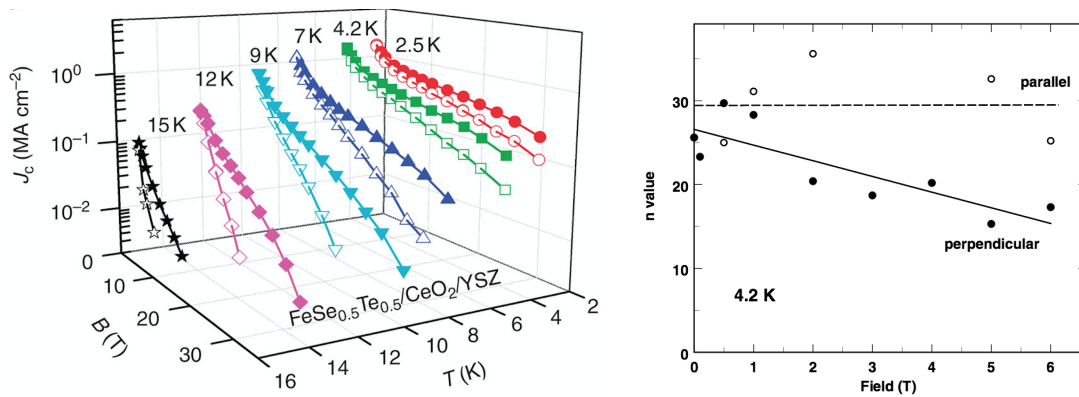


Fig. I.13 – Power law fit made on a I-V measurement on a MgB<sub>2</sub> sample at 20 K, 2.3 T. In this example the critical current and the  $n$  value were calculated respectively at 175 A and 30.

From (I.15), it is possible to add the dependencies of the critical current density and the  $n$  value with respect to magnetic field and temperature [34]. The critical current can be measured with different values of magnetic field [35] in laboratories equipped with commercial magnets that usually do not exceed 10 T. For more intense magnetic fields the measurements are made in High Field Laboratories such as NHMFL, TML or LNCMI where the values can be higher ( $> 30$  T) [36]. Fig I.14a and Fig. I.14b display some variations of  $J_c$  and  $n$  with temperature and field for FeSC in (a) and BSSCO in (b).



(a) Critical current versus external magnetic field [36]

(b) Dependence of  $n$  value with field and directions [35]

Fig. I.14 – Critical current measurement with field and temperatures.

As the CSM model is the limit case of the power law model (when  $n$  tends to  $\infty$ ), it is possible to see the macroscopic differences in terms of current density distributions in a superconducting material. Hence, the current distributions will be different when current penetrates inside the conductor generating a smooth decrease of current density inside the thickness when the power law model is used. Simulations have been made with different  $n$  values to see the sharpness of the transition inside the superconductor. By injecting a transport current the same superconducting slab with a 4 mm width and plotting the current density in the middle of the slab, it is possible to analyze the effect of the  $n$  value on the current distribution in Fig. I.15. In the simulation the critical current density was defined at  $1 \text{ kA/mm}^2$ . One can observe that when the  $n$  value is very low, the current densities penetrate with a smooth gradient inside the superconductor. With values above 20, the transition between virgin state area and region where the vortex are activated is clearly visible. Almost no macroscopic changes on the distribution profile are observed when the  $n$  value is above 30. This is good indication that analytical formulas based on the Bean model can be used as a good approximation in problems where the critical current dependency with magnetic field is not an issue.

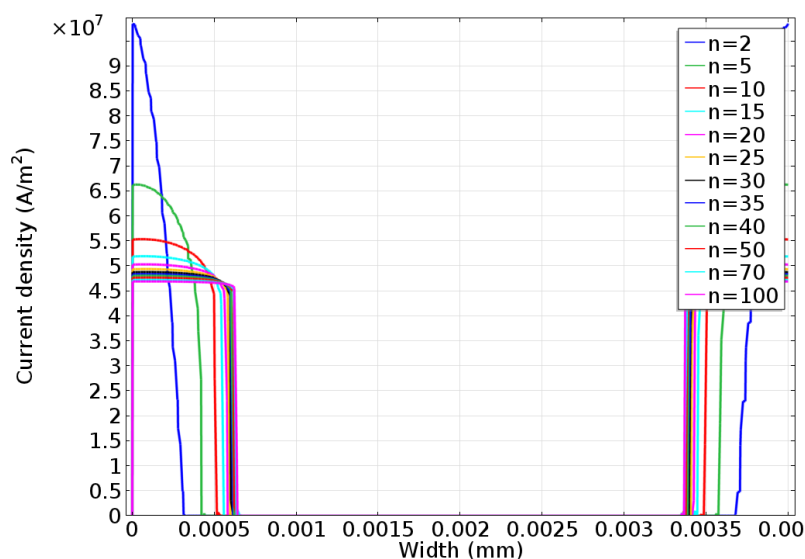


Fig. I.15 – Current density distribution inside the superconductor with different  $n$  values for the power law model  $I=0.4I_c$ .

The power law model is convenient to fit experimental data and has the advantage of providing continuous derivatives for the first and second order. This feature is interesting in terms of numerical modeling, for example when using Newton-Raphson method [37]. Despite this advantage, the power law exhibits a non-zero resistivity for all values of current density below  $J_c$  which is in contradiction with the observed phenomena of superconductivity (current density frozen in the superconductor and zero resistivity). In all major cases, where the AC phenomena are relatively fast, it is not a issue but it can be a problem when low time varying signals have to be taken into account (limit case for DC signals). A second fit has been suggested by the community, called *percolation law* and detailed in the next section.

### I.1.e-iii Percolation law

The second model based on the statistical physics is labeled as the percolation law [38]. The equation which sets the resistivity at zero for values below a threshold value of current density  $J_{c0}$  is detailed in (I.16). In this formula, the dependency of the electric field with the current density is still a power law but with a  $n_0$  value lower and preliminary observed as independent with temperature and field.

$$\text{Percolation : } \vec{E}_{PM}(\vec{J}) = \begin{cases} 0, & \text{if } |\vec{J}| \leq J_{c0}, \\ E_c \left( \frac{|\vec{J}|}{J_{c0}} - 1 \right)^{n_0} \left( \frac{J_c}{J_{c0}} - 1 \right)^{-n_0} \frac{\vec{J}}{|\vec{J}|}, & \text{if } |\vec{J}| > J_{c0}, \end{cases} \quad (\text{I.16})$$

The physical difference between (I.15) and (I.16) is that the percolation law exhibits a resistivity equal to zero when the current density  $J$  is below the threshold value of  $J_{c0}$ . In the interval  $J \in [0, J_{c0}]$ , no dissipation occurs in the material (no losses). This is in agreement with the experimental observations [39] that DC current fills only the external surface of the superconductor with a fixed value of current density, as it was suggested by the Bean model. This feature in Fig. I.16 can be perceived as a DC skin effect where, the current distribution remains fixed after some time without the current penetrating into the complete area of the superconductor. It corresponds to a maximum flux density gradient beyond which flux lines start to move inside the material [40].

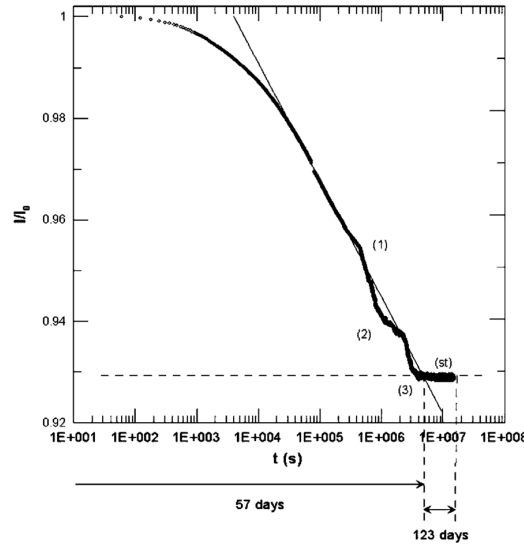


Fig. I.16 – Logarithmic plot of normalized current vs. time. ( $\diamond$ ) experimental data, (—) Anderson fitting and (- - -) stabilized base line [39].

In this case the value of  $J_{c0}$  corresponds to the limit value of the current density at an infinite time. The ratio in this case between  $J_c$  ( $E_c=1 \mu\text{V}\cdot\text{cm}^{-1}$ ) and  $J_{c0}$  is usually comprised according to our knowledge between 0.8 and 0.95. Regarding the  $n_0$  value, usually,

this value does not change so much with temperature and field and exhibits lower values compared to the power law, usually lower than 10.

After this introduction on the phenomenon of superconductivity and some knowledge on the theory, the next section is focusing on AC losses. This dissipation occurs when the superconductor (or a metal) is exposed to time varying environment and has to be investigated during the design of a large scale application.

## I.2 AC losses

### I.2.a Definitions

AC losses are referring to a specific type of losses, induced inside conductive materials, when they are subjected to an AC environment. This environment can be a current flowing into the material or an external field applied on the material. A time-varying environment leads to a temporal change of magnetic field locally, leading to the creation of an electric field  $\vec{E}$  according to Maxwell Faraday's equation :

$$\nabla \times \vec{E} = -\frac{\partial \vec{B}}{\partial t} \quad (\text{I.17})$$

The existence of an electric field  $\vec{E}$  in the material coupled with the presence of a current inside the material  $\vec{J}$  leads to instantaneous losses  $p_{AC}$  :

$$p_{AC} = \iiint_V \vec{J} \vec{E} dV \quad (\text{in } W) \quad (\text{I.18})$$

For a periodic signal with a frequency  $f$ , the AC losses  $P_{AC}$  can be calculated as :

$$P_{AC} = f \int_{1/f} p_{ac} dt \quad (\text{in } W) \quad (\text{I.19})$$

AC losses are referring to the general mechanism of a time varying environment applied to a conductive material. As this energy is dissipated inside the material, it is vital to know the value of dissipation but also its location to design and also optimize superconducting applications and the cryogenic system. Different names of AC losses occurring in diverse materials of superconductors have been given. Hysteresis losses that are generated by the penetration of the current densities (positive or negative) inside the superconducting material are detailed in I.2.b. Superconductors are usually manufactured with metallic elements, eddy current losses and coupling losses induced in these metals are created and described in I.2.c. In magnetic metals with hysteretic behavior, additional losses can be induced and are detailed in I.2.d

### I.2.b Hysteresis and screening current losses

When a superconductor is subjected to a time varying transport current or external magnetic field, magnetic flux and so currents will start penetrating inside it [41, 25, 42] as shown in Fig. I.17. When reversing the transport current or the external field, and applying

the same value of field or current but in the opposite direction, the same magnetic flux will penetrate inside the superconductor but with the reverse polarity as it was explained in I.1.e-i. Locally the vortices will be torn from their pinning center when the screening currents inside the superconductor change their polarities and this leads to energy dissipation.

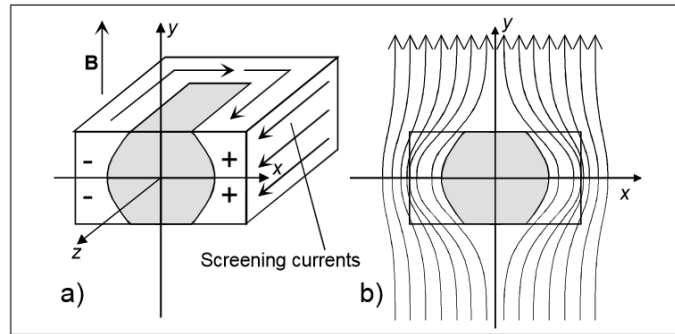


Fig. I.17 – Cross section of a superconductor when subjected to an time varying external field. In a) the screening currents are in white and the virgin area in grey [43].

The AC hysteresis losses are then induced during the change of polarity between  $+J_c$  to  $-J_c$  (or in reverse) in the vortices.

### I.2.c Coupling and eddy-current losses

Superconductor are often manufactured as superconducting filaments twisted inside a resistive matrix. This is the case for example in NbTi or MgB<sub>2</sub>. Coupling losses refer to losses induced by current flowing inside the metallic materials by looping from one filament to another. For example in a multi-filamentary superconductor, current may flow from one filament to another trough the metallic matrix as explained in Fig. I.18. These coupling currents can also be created from one tape to another in HTS devices.

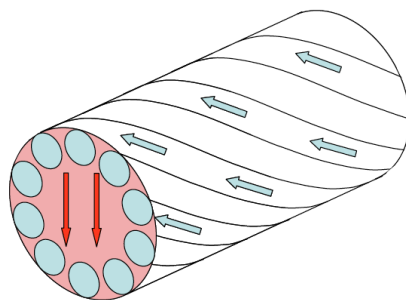


Fig. I.18 – Multi-filamentary conductor and coupling losses [44].

Analytical calculation of the coupling losses has been made [44] :

$$P_{CL} = \frac{AB_{max}^2}{2\mu_0} \left( \frac{\tau}{1-N} \right) \frac{\omega^2}{1+(\omega\tau)^2} \text{ in (W/m) where } \tau = (1-N) \frac{\mu_0}{\rho_t} \left( \frac{l_p}{2\pi} \right)^2 \quad (I.20)$$

In (I.20),  $A$  is referring to the cross-section area of the wire,  $\omega=2\pi f$  where  $f$  is the frequency of the signal,  $B_{max}$  is the peak value of the magnetic field,  $l_p$  is the filament twist pitch and  $\rho_t$  is the transverse resistivity of the normal matrix.  $N$  is the demagnetization factor which can be experimentally measured by magnetizing the sample below its critical temperature [45] or analytically calculated.

The coupling losses can be reduced by decreasing the constant  $\tau$ , this can be done by decreasing the twist pitch or by increasing the transverse resistivity. To increase the transverse resistivity, it is possible to add barriers on the outside of the filaments with cupronickel for example.

Eddy currents which are induced in metallic parts are largely covered in electromagnetism and used for example in inductive heating. The penetration depth (current going inside the material) is linked to the resistivity of the metal according to :

$$\delta = \sqrt{\frac{\rho_{metal}}{\mu_0 \mu_r \pi f}} \quad (I.21)$$

In our case, it is possible to calculate  $\delta$  by considering a resistivity of the matrix of  $\rho_{metal}=10^{-7} \Omega.m$  and  $\mu_r=1$ . At frequencies equals to 50 Hz and 1 kHz, the penetration depths are respectively 22 mm and 5 mm which is higher than the thickness of the metallic parts. Hence, eddy currents penetrate inside the metals and induce losses but they are generally negligible.

### I.2.d Magnetic losses

When the metal is subjected to a time-varying magnetic field, the magnetization of the material changes through microscopic changes in the metallic structure. The movement of the particles generates what is called hysteresis losses. It is possible to see the losses by plotting the magnetic flux density  $B$  versus the magnetic field  $H$ , which has the form of a closed loop (Fig. I.19). The hysteresis losses in one cycle are proportional to the area enclosed inside the hysteresis loop. As the losses are constant for one cycle, the losses are almost linear with frequency.

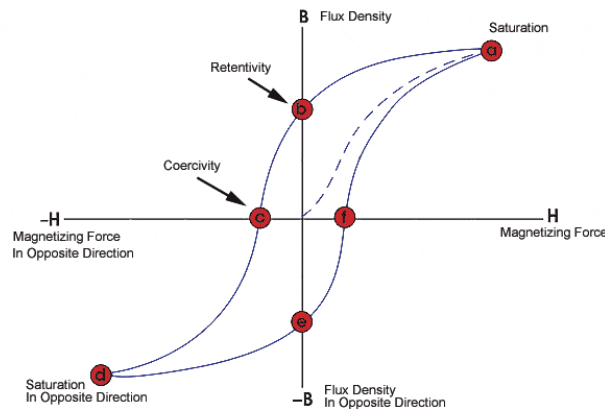


Fig. I.19 – Hysteresis of ferromagnetic materials. The initial magnetization is shown in the dotted line. The hysteresis losses are proportional to the area enclosed inside this curve [46].

In this section, an overview of the AC losses mechanisms has been made by presenting all the possible AC losses inside a superconductor and its surrounding matrix. The purpose of this thesis is the calculations of all the AC losses inside several superconductors for the design of cryogenic system and the implementation on the grid. In the following section, a presentation of the superconductors considered for the next generation of superconducting applications is made.

### I.3 Studied superconductors

Today, two types of superconductor are in the center of large scale developments : HTS and MgB<sub>2</sub>. With the increase of the worldwide production and its high critical current capacity at very high field, HTS conductors are well suited for large scale applications requiring the generation of magnetic field. They are always manufactured as tape which can be an issue in some applications. The cost is also one of the drawbacks for its use. Work have been made to build HTS wires made with tapes which can leads to more compact power applications such as cables.

For applications requiring high currents but where almost no magnetic field is generated (cables for examples), the use of MgB<sub>2</sub> can be a good alternative because the conductor is sold as a round wire with a lower price (2 € per meter for MgB<sub>2</sub> wires compared to 100 € per meter for HTS tapes). However, MgB<sub>2</sub> requires working in liquid or gaseous helium compared to HTS which can work in liquid nitrogen.

#### I.3.a HTS tapes and round wires (RW)

**HTS tapes** Two groups of oxocuprates are particularly interesting and produced in large quantities : BSSCO and REBCO. Today, these superconductors have been used for superconducting cables [47, 48, 49], transformers [50], fault current limiters [51] and motors [52].

BSSCO tapes are rather expensive due to the presence of a silver matrix surrounding the superconducting filaments. Their chemical compositions can be either Ba<sub>2</sub>Sr<sub>2</sub>Ca<sub>0.8</sub>Cu<sub>2</sub>O<sub>8+δ</sub> with a T<sub>c</sub>=85 K [53] or Ba<sub>2</sub>Sr<sub>2</sub>Ca<sub>2</sub>Cu<sub>3</sub>O<sub>10+δ</sub> with a T<sub>c</sub>=110 K [54].

On the other hand, a second group of HTS is showing great promises for large scale applications. However, these applications are still in developments. The initial chemical composition was YBa<sub>2</sub>Cu<sub>3</sub>O<sub>7-δ</sub> (or generally written YBCO) but the Yttrium element Y can be substitute with another rare earth element (except Ce,Pr and Tb) [55]. This group is called REBCO in reference to the plurality of possible compounds ('RE' stands for Rare Earth). The architecture of the elementary crystal of YBCO can be found in Fig. I.20.

The high critical current density of a single crystal was observed at values higher than 10 kA/mm<sup>2</sup> [57](@ T=4.2 K, B=0 T) and research is still ongoing to increase the J<sub>c</sub> [58]. The critical magnetic flux density is estimated to be over 110 T [59](@ T=4.2 K). The coherence length of the vortex are around 2-4 nm [60], it is then possible to create few micrometers thin superconducting layers. A MEB imaging of a superconducting layer placed inside substrate layer is shown in Fig. I.21.

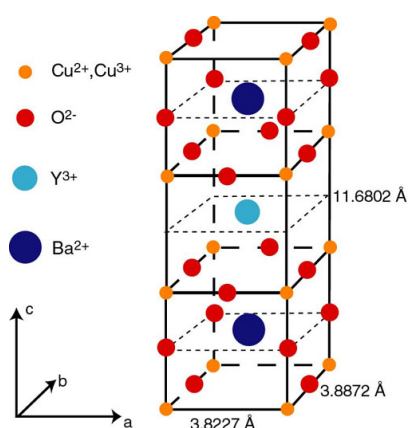


Fig. I.20 – YBCO crystal with lattice parameters  $a=3.8227 \text{ \AA}$ ,  $b= 3.8872 \text{ \AA}$ ,  $c=11.6802 \text{ \AA}$  [56].

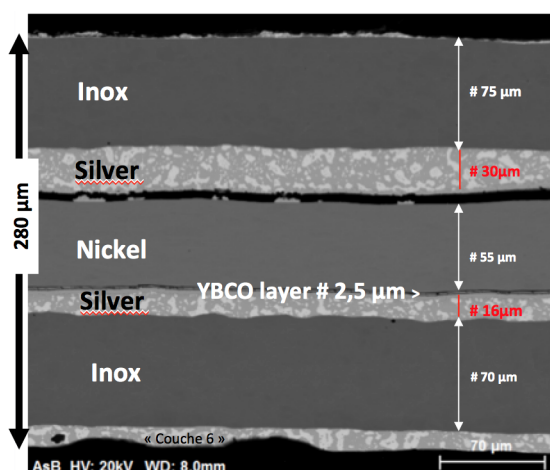


Fig. I.21 – YBCO layer in a double YBCO tape with Nickel and Inox as shunt layers.

To manufacture large length of REBCO tapes, different process can be made :

1. The RABiTS [61] process, (Rolling-Assisted Biaxially Textured Substrates), which consists of the deposition of the superconducting layer directly on buffer layer on the Hastelloy substrate. This technique is one the the most effective process to manufacture long single length.
2. The IBAD process [62], (Ion Beam-Assisted Deposition), consists in directly depositing the YSZ layer on the substrate layer (with or without a buffer layer). Then, by submitting the material to a Ion-Beam, the superconducting layer is made.
3. Others type of process, mostly chemical, can be done, for example MOCVD

A sketch of a typical produced tape can be found in Fig. I.22. Usually the superconducting layer is deposited on a substrate layer made of nickel or cupro-nickel, generally Hastelloy  $\text{\textcircled{R}}$ . On top the superconducting layer, silver is added to inject the current. For protection issues and also stability purposes, copper can be added on the top and under

the tape by electro-deposition. The tape is produced typically with a width between 2 mm and 12 mm and a total thickness between 100  $\mu\text{m}$  and 200  $\mu\text{m}$ .

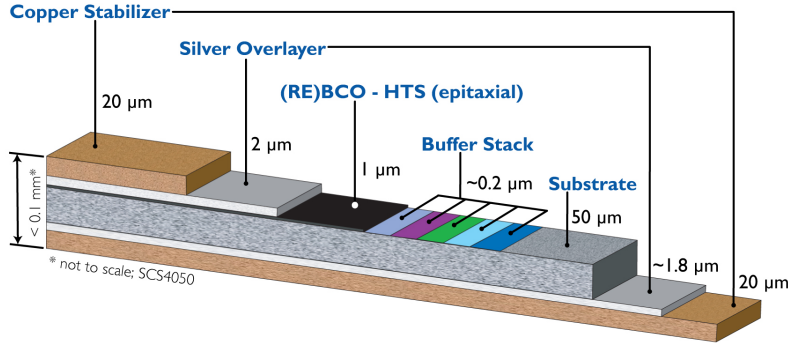


Fig. I.22 – Typical produced REBCO tape [63].

As the REBCO conductor is only manufactured in tapes, it exhibits anisotropic properties with field orientation. Fig. I.23 displays the evolution of current with the incident field angle ( $0^\circ$  is referring to the field being parallel to the flat surface). This dependence has been limited by stratifying the YBCO layer into an epitaxial structure.

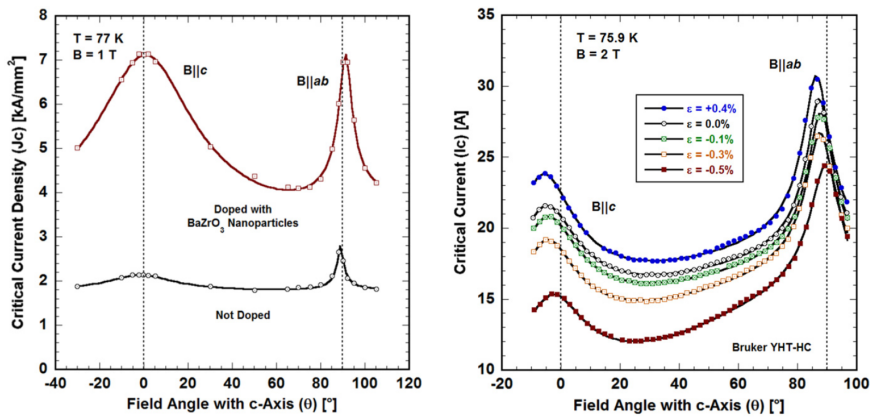


Fig. I.23 – Critical current density versus field orientation with different improvements made on the superconducting composition [64].

These tapes exhibit high critical currents which makes them a good candidate for large scale applications. However the anisotropic properties of the performance can be a problem if the magnetic field is not parallel to the tape. For power cables, the tapes have to be placed on a cylindrical former, creating a space in the middle than can be used for the cooling. Creating an HTS round wire (RW), is interesting because, the compactness of the cable can be improved and a circle geometry almost annihilates the anisotropic properties.

**Round REBCO wires by Nexans** Manufacturing and then producing long lengths of REBCO superconductors in a wire shape is then interesting and was investigated in the European Project EUROTAPES [65]. The two main objectives of this European project composed of 21 partners are :

1. The improvement of the conductor architecture for low cost applications with lengths superior to 500 m and a target cost at 100 €/m.
2. Use new technologies to enhance performances (larger thickness and  $I_c$ , enhanced pinning for high fields, reduced AC losses and increased mechanical strength).

To produce this round wire (RW), Nexans developed an industrial machine in Hannover. The main idea is to bend in several steps the tape on its width. To guarantee the performance, the superconducting layer was placed on the neutral plane of the completed tape by depositing layers of copper on each side of the tape [66]. The process of the RW former is displayed in Fig. I.24.

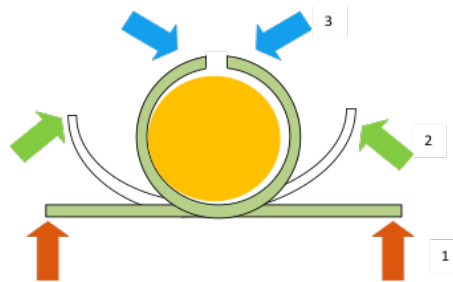


Fig. I.24 – Tube process [66].

After putting the conductor into a wire shape, a laser joint was made to close the wire. The goal of the process was the creation of a HTS wire with an inner radius of  $\Phi=0.9$  mm starting from a commercial tape from Superpower cut with a width of approximately 6 mm.

After several tests with different layer copper thicknesses, it has been observed a certain degradation of the superconducting layer from a displacement of several nanometers. As no extension has been asked in the project, it was decided to stop the production of further round wires. But as these round wires have been fabricated in laboratory [67], some adjustments may be done to reduce the displacement.

**One alternative : Bi-2212 round wires** To work under liquid nitrogen with round multi-filamentary superconducting wires, it is possible to use Bi-2212 round wires. In this configuration the filaments exhibit a radius of 0.7 mm to 1 mm. The heat treatment is made under 100 bar at 890 °C. Compared to REBCO tapes, the heat treatment is more challenging to do. It is possible to compare the price performance at 4.2 K versus field. This graph reveals the fact that the Bi-2212 round wire can be a good solution for cheap large scale devices. The tendency should be almost the same for operation in liquid nitrogen.

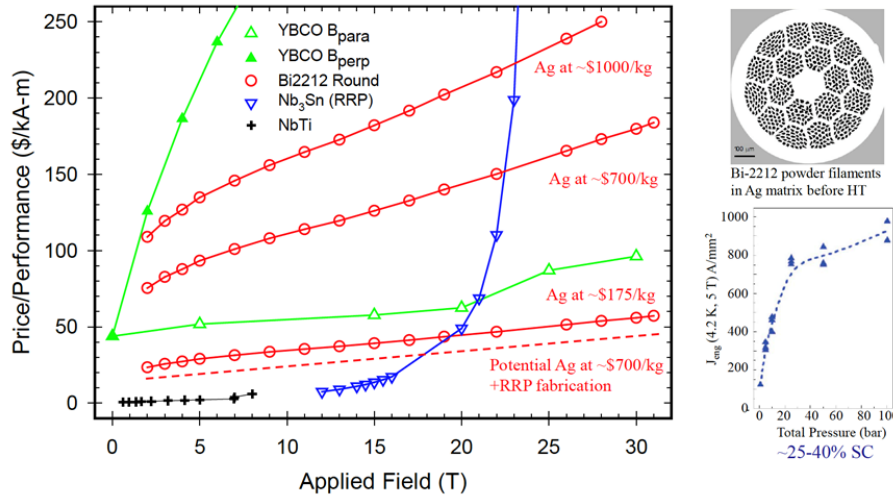


Fig. I.25 – Price of different superconductors with a focus on the Bi-2212 round wire. On the right hand side of the picture is shown the improvement of the critical current when the heat treatment is made under pressure [68, 69].

### I.3.b MgB<sub>2</sub>

MgB<sub>2</sub> compounds have been already commercialized for 50 years for industrial applications but the superconducting properties of this compound was only discovered in 2001. In the same year, the first MgB<sub>2</sub> superconducting tape was commercialized [70]. This superconductor has a critical temperature  $T_c$  observed at 39 K and a critical magnetic flux density  $\mu_0 H_c$  of 15 T [71]. This particular value of  $T_c$  is one of the disadvantage for the use of MgB<sub>2</sub> as it is not possible to cool it down with liquid nitrogen. Liquid or gaseous helium (or even liquid hydrogen) can be used. See Fig. I.26 for the structure of the elementary crystal of MgB<sub>2</sub>.

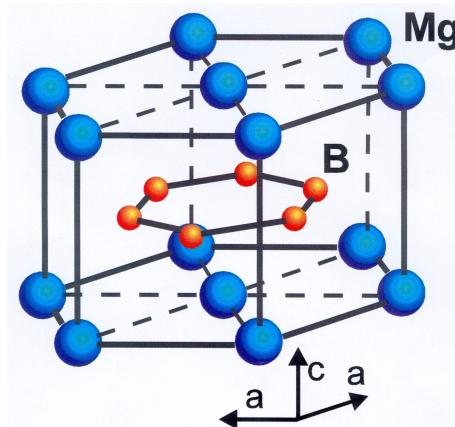


Fig. I.26 – Crystal structure with lattice parameters  $a=3.08 \text{ \AA}$  and  $c=3.52 \text{ \AA}$ , The bore is represented in orange and the magnesium in blue [72].

The drawback of working at lower temperature is counterbalanced by the relative ease of producing long length of MgB<sub>2</sub> conductor with different shapes and sizes at a reduced cost. Indeed, compared to REBCO tapes, the process is simpler and faster with the use of

a Power in Tube process (PIT). The structure is largely always the same,  $\text{MgB}_2$  conductors are composed of  $\text{MgB}_2$  filaments embedded into a metal matrix with several types of configuration.

The Powder in Tube (PIT) process is performed by injecting the Magnesium and Bore powders inside a metal tube (usually nickel), this process is named *in-situ*. Another alternative is injecting directly the  $\text{MgB}_2$  compound inside the metal tube and is called *ex-situ*. After this process, the wire is adjusted to specific dimensions and shapes : wires or tapes. A lot of configurations [73, 74] are possible according to Fig. I.27. Finally, a heat treatment is done to react the magnesium and the bore (in the *in-situ* process) or to regenerate the  $\text{MgB}_2$  (in the *ex-situ* process). Sometimes to improve the mechanical properties of the conductor, a layer of metal is added to the exterior of the wire for example with tungsten or cupro-nickel. Columbus Superconductor (SPA)<sup>®</sup> [75] is today the only company able to provide long lengths of  $\text{MgB}_2$  superconductor. The company is implemented in Italy in Genova.

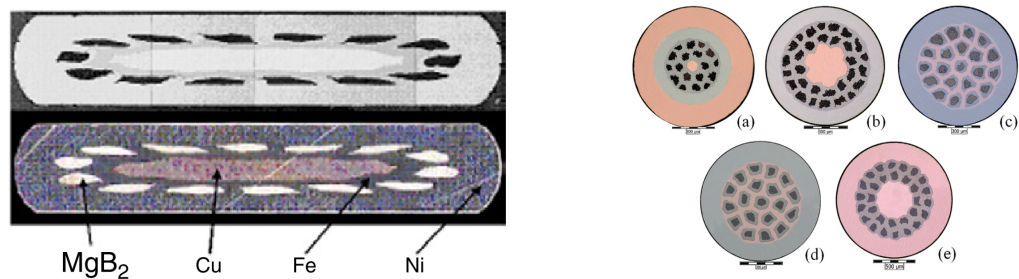


Fig. I.27 –  $\text{MgB}_2$  configurations of wires [76, 77].

In a multi-filamentary wire, anisotropic properties are not existing. Added to its round structure, this feature is the main advantage for the development of large scale applications especially for use in windings for SMES or magnets. The critical current density of  $\text{MgB}_2$  has been observed at value up to  $600 \text{ A/mm}^2$  for self field at 4.2 K. This high value is very promising for the development of high power applications. One of the drawbacks, is the critical field which renders the High field applications challenging (Insert coil for the generation of background field). Despite this feature, for low magnetic flux density values,  $\text{MgB}_2$  superconductors have been already tested successfully for applications [78, 79, 80, 81]. Several numerical investigations are done for example for the design of SMES [82] or wind turbine motor [83, 84, 85].

To conclude this section, Table. I.1 summarizes the main characteristics of REBCO tapes but also  $\text{MgB}_2$  wires.

After the presentation of these two superconductors, the following section presents some already functional superconducting links. At the end, the future of these links using the two introduced superconductors is detailed.

Superconductor	REBCO	MgB <sub>2</sub>
T <sub>c</sub> (K)	92	39
H <sub>c</sub> (T)	> 100 T	15 T
Forms	tapes	wires
Cost (/m)	100 €	2 €
Advantages	high H <sub>c</sub> and T <sub>c</sub>	wire forms
Drawbacks	tape forms	working at gaseous He

TABLE I.1 – Comparison between the REBCO tapes and MgB<sub>2</sub> wires.

## I.4 Superconducting large scale applications

In some cases, using superconductors is necessary because their high current carrying capacities have to be used [86, 87]. From Fig. I.28 it is possible to see the superconductor better suited for high field applications but also for high power applications such as motors [88, 84, 89]. HTS superconductors such as REBCO or BSSCO are the first choice for high field applications, while MgB<sub>2</sub> can be used for applications which does not produce large magnetic field such as cables.

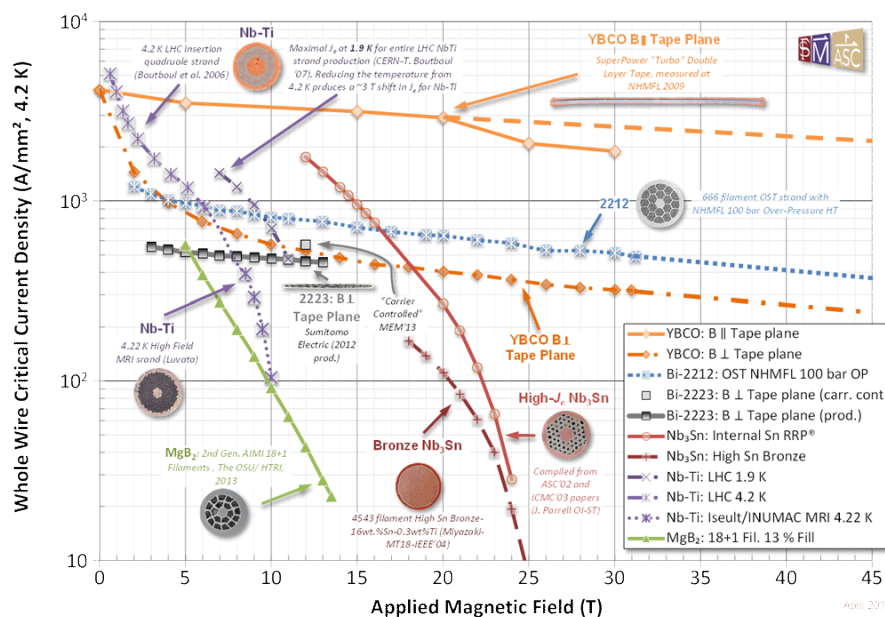


Fig. I.28 – Typical engineering current densities for practical superconductors at 4.2 K [90]

As liquid helium is expensive, it is paramount to avoid any kind of losses in the superconducting application. This is the reason why only DC applications have been made such as power cables. With HTS conductors, it is possible to work at liquid nitrogen which is a far cheaper liquid, hence, more AC losses can be generated inside the appliance that is why, for example, an AC cable has been fabricated and tested in Essen Germany.

### I.4.a Superconducting power cables

Superconducting power cables transmit ten to twenty times the electrical current of traditional copper or aluminum cables at the same voltage. Using superconductors allows for the reduction of the size of power cables that can work for all level of voltages and currents [91] as can be seen in Fig. I.29.

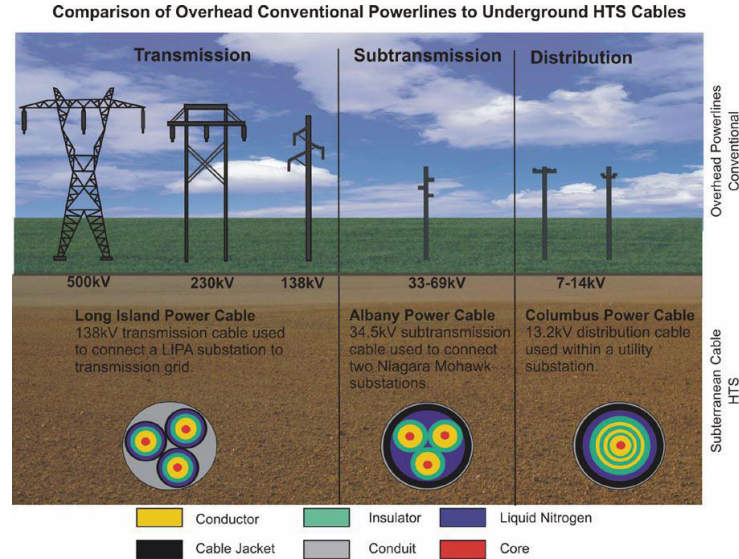


Fig. I.29 – Superconducting cable designs for various voltage levels [92].

With HTS superconductors, several projects have been completed with cables successfully in operation. Achieving more compact power cables with higher engineering currents is still important for cable manufacturers. That is why new generation of power cables are designed and tested.

#### I.4.a-i Already operational SC power cables

The LIPA (stands for Long Island Power Authority) superconducting cable has been installed and commissioned in 2008 [93]. The rated voltage and current of this power cable are respectively 138 kV and 2.4 kA (for a power of 600 MVA). This is a three-phase power cable where each cable is composed of three layers of BiSSCO tapes. The complete power cable is 600 m and cooled with liquid Nitrogen ( $T_{op}=73$  K). In total, more than 155 km of superconductor has been used. The short-circuit current has been sized at 51 kA for 200 ms. The cable, which was installed in Lake Ronkonkoma, (NY,USA), has been energized April 22, 2008 and is capable of delivering power to 300 000 homes and is an integral part of the LIPA grid. After an initial period to test the performance and the economic aftermath of this project, it was planned to retain this new superconducting link as a permanent part of the grid. LIPA and American Superconductor are now investigating the installation of other HTS cables in the LIPA grid.

In 2014, in Essen (Germany), a state of the art 10 kV superconducting cable was built to replace the conventional 110 kV lines between two substations in the city center [94]. This pilot project named AmpaCity has been made possible by grants from the German Federal Economics Ministry for the Environment and Energy (BMWI). The cable made with the

same architecture as the LIPA power cable is 1 km long with a junction. In this case, only a single cable is made with the repartition on the three phases on three concentric layers of BSSCO (see Fig. I.30).

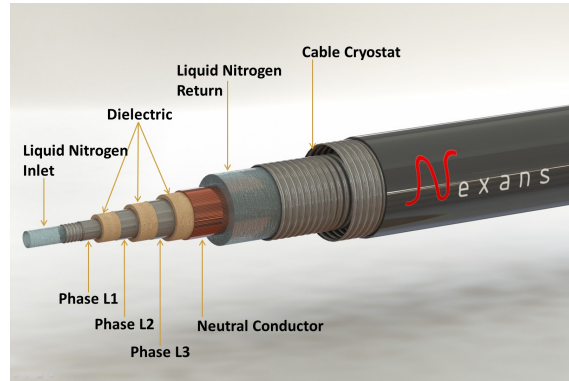


Fig. I.30 – AMPACITY power cable [95].

The three-phase power cable is designed for a power of 40 MW. Compared to a copper cable of the same size, the superconducting cable can transport five times more current. The AmpaCity cable provided about 20 million kilowatt-hours of energy, which powers more than 10 000 households for its first 180 days of operation. According to Frank Schmidt, head of Nexans Superconductor Division Germany, *the price of the superconductive cable was only twice as high as that of a similarly powerful copper cable. The whole system, Nexans said, can perform more efficiently than a conventional one, reducing operational cost by 10 M€ over a projected 40-year lifetime* [96].

#### I.4.a-ii The future of SC cables

The next generation of superconducting cables will be dedicated for very high current usage. In this section, we give three examples : CORC cables, round wire power cables, and the new generation of MgB<sub>2</sub> cables. Several others idea such as twisted stack cables can be found in [97].

**CORC cables** To design high current compact cables capable of carrying over 10 kA with REBCO tapes, one idea is the Conductor on Round Core (CORC<sup>TM</sup>) obtained by winding the HTS tapes in a helical path on a thin core [98, 99]. These cables are today the only REBCO based cables which provide no anisotropic properties and have high mechanical properties [100]. For example, CORC cables made with a former diameter of 6 mm are capable of reaching 7 kA at 4.2 K under a magnetic flux density of 17 T. This small diameter cable is flexible enough to be bent on a radius of 30 mm without significant degradation.

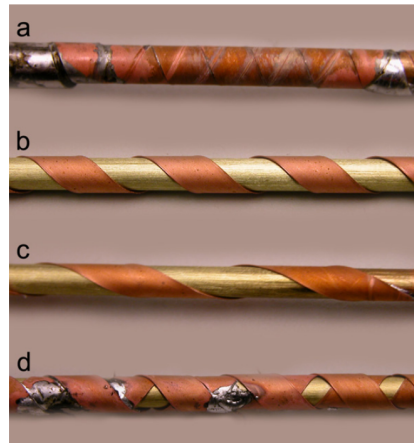


Fig. I.31 – CORC cable prototypes made by winding a single YBCO tape around a brass former, twist pitch : (a) 9 mm, (b) 20 mm, (c) 40 mm. In (d), two layers conductors are wounded with a 18 mm twist pitch [98].

**Cables made with round HTS wires** With the production of HTS wires in long length, the desire of creating more compact cables compared to previous HTS cables technologies can be achieved. Analytical works [67] have shown the advantage of these round wires for the creation of compact high current cable with an increase of the overall current density compared to HTS power cables in operation. From Fig. I.32, one can notice the enhancement of the engineering current density by four of the overall cable due to the compactness made by using round wires.

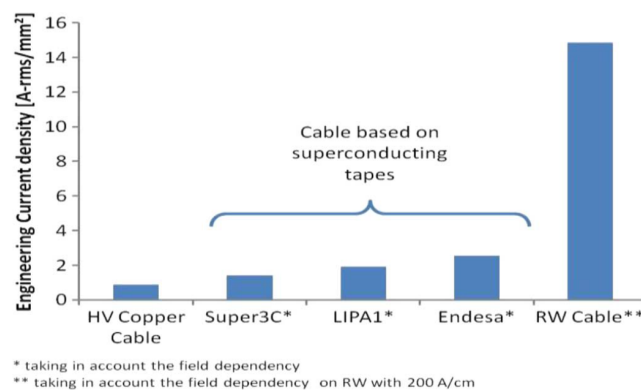


Fig. I.32 – Engineering current density of HTS cables with tapes and the foreseen with round wires [67].

**MgB<sub>2</sub> high current DC power cables working at 20 K** MgB<sub>2</sub> conductors with round wire form is a good candidate for high current cables as well. To counter-back the high cost of liquid or gaseous helium, only DC power cables are foreseen. In 2014, Ballarino *et al* [101] successfully beat the record of current going trough a superconducting cable with

30.4 kA at 4.2 K and 5 kA at 20 K, the upgrade of the LHC using 150 kA  $\text{MgB}_2$  cable is under investigation. A preliminary design of a  $\text{MgB}_2$  cable is shown in Fig. I.33.

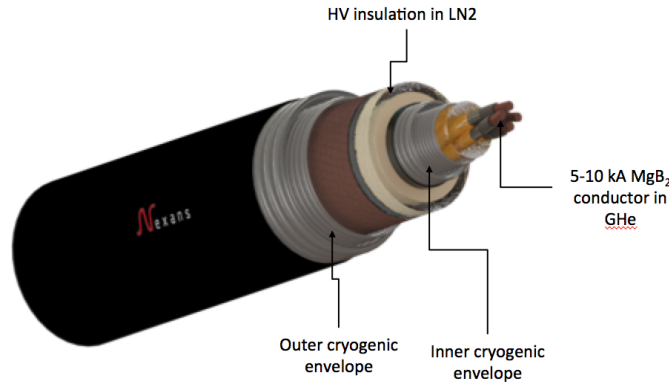


Fig. I.33 –  $\text{MgB}_2$  power cable design [102].

#### I.4.b Other applications : magnets and dipoles

Superconductors enable the construction of magnets that generate intense magnetic fields with a reduced electrical power input. This feature also allows steep magnetic field gradients to be generated at field so intense that the use of ferromagnetic materials for field shaping is limited in effectiveness. Since the current densities are high, SC magnets systems are quite compact and occupy only a small amount of laboratory space. Another feature is the stability of the magnet, in persistent mode. As the  $L/R$  time constant is extremely long (nearly zero resistance), magnets can operate for days or even years when short circuited on itself. Two in-lab projects are under investigation : the EUCARD and NOUGAT contracts for the design of HTS magnets (MRI, solenoids or dipoles).

1. **The EuCARD project** : The Large Hadron Collider (LHC) in CERN is the world's largest particle accelerator and instrument in the world. The LHC with a circumference of 27 km has the mission to investigate the fundamental laws of the universe. In the framework of EuCARD-2 project, the increase of the beam energy is foreseen with an upgrade on the produced magnetic field. The magnetic field generated is today 8.3 T and should be increase to 20 T with a contribution of 5 T HTS inserts. In EuCard-2, three HTS dipole magnets are studied with different architectures of HTS cables : ROEBEL or twisted stack cables.
2. **The NOUGAT ANR** : Several project of HTS magnets such as the one in Talahassee [103], Tohoku [104, 105] or KIT [106, 107] have been made and tested successfully. In France, the ANR Nougat supported by the French ministry have granted an ANR for the creation of an HTS insert expected to operated in 2018. The goal of the proposal is the development of an HTS insert capable of providing at least 10 T at 4.2 K in a background field of 20 T, to produce at least a 30 T [108]. The background field will be produced by a resistive magnet.

As it was previously explained, during the design of these large scale applications, it is necessary to calculate the amount of losses dissipated in the conductors but also in the

cryogenic envelope in the case of cables. Losses in the current leads or in the cryogenic envelope can be calculated with analytical formulas but the losses in the superconducting cable are more complicated especially AC losses. The next section will give few general knowledge on how it is possible to calculate these losses.

## I.5 Calculations of AC hysteresis losses

This section focuses mainly on hysteresis losses as coupling losses are not always generated inside a superconducting device. To calculate properly these losses it is then compulsory to use analytical or numerical tools. Analytical models are derived from constitutive equations with certain hypothesis and may be used in the case of simple problems. To go further, for more complex geometry or when it is necessary to take into account physical properties (dependency with temperature, field,...), numerical modeling can be performed such as Integral methods [109, 110], analytical (or semi-analytical) methods [111, 112], Finite-Element [113] or Finite-Volumes modeling [114, 115]. It is then possible to perform numerous studies with varying parameters and optimizes the design of large scale devices.

### I.5.a Analytical

Analytical calculations have been made to predict the current densities, magnetic field and electric field distributions over time when the superconductor is subjected to AC current or external field. AC hysteresis losses can then be deduced from these distributions. All the calculations<sup>1</sup> are based on the critical state model. Different geometries have also been studied such as tapes, cylinders or tubes.

#### I.5.a-i Calculations on tapes

**Self-field AC losses** Norris made the calculation of AC hysteresis losses for AC transport current with different geometry of conductors [116]. Analytical calculations for HTS tapes have been done when one is considering the tape either as an ellipse or as a very thin film. AC hysteresis losses for a periodic transport current with a peak value  $I$  and a frequency  $f$  can be either (I.22) or (I.23). In these formulas the parameter  $\beta$  is referring as the reduced current  $\beta=I/I_c$ .

$$P_{film,SF} = \frac{\mu_0 I_c^2 f}{\pi} \left[ (1 - \beta) \cdot \ln(1 - \beta) + (1 + \beta) \cdot \ln(1 + \beta) - \beta^2 \right] \quad (I.22)$$

$$P_{ellipse,SF} = \frac{\mu_0 I_c^2 f}{\pi} \left[ (1 - \beta) \cdot \ln(1 - \beta) + (2 + \beta) \cdot \beta \right] \quad (I.23)$$

In our calculations, it has been noticed a better correlation with (I.22) and was chosen when it was necessary.

---

1. All the formulas have the same formalism with SF meaning self field (AC transport current), EF external field, and BF both field (transport current and external field)

**External field AC losses** In 1996, Brandt *et al* [117] studied the resulting losses of the application of an external magnetic field on a tape. For a time-varying applied magnetic field with a peak value  $H_a$  and a frequency  $f$ , the AC losses generated by field perpendicular and parallel to the flat surface are listed in (I.24). The formalism for parallel and perpendicular field can be found in Fig. I.34.

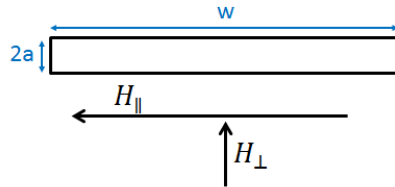


Fig. I.34 – Formalism for AC losses calculations on a tape subjected to an AC external magnetic field.

$$P_{tape,EF,\perp} = \mu_0 I_c^2 f \left[ \frac{2}{\pi} \cdot \ln(\cosh(H_a/H_{ctape,\perp})) - \frac{H_a}{H_{ctape,\perp}} \tanh(H_a/H_{ctape,\perp}) \right]$$

$$P_{tape,EF,\parallel} = \mu_0 I_c^2 f \cdot \frac{2d}{3w} \cdot \left( \frac{H_a}{H_{ctape,\parallel}} \right)^3 \quad \text{for} \quad \frac{H_a}{H_{ctape,\parallel}} \ll 1 \quad (\text{I.24})$$

$$P_{tape,EF,\parallel} = \mu_0 I_c^2 f \cdot \frac{d}{2w} \cdot \left( \frac{H_a}{H_{ctape,\parallel}} - \frac{1}{3} \right) \quad \text{for} \quad \frac{H_a}{H_{ctape,\parallel}} \gg 1$$

Where  $a$  is the half thickness,  $w$  the width of the tape, and  $H_{ctape}$  penetration field defined as  $H_{ctape,\perp} = wJ_c/2\pi$  and  $H_{ctape,\parallel} = aJ_c/\pi$ .

**AC losses with transport current and external field** The calculation of the losses when the superconducting strip is subjected to an alternating current  $I_w$  and transverse field  $H_{ext}$ , sinusoidal in time and in phase with each other. Let consider a magnetic field and a transport current as :

$$H_{ext} = H_a \sin(\omega t)$$

and

$$I_w = I_{wa} \sin(\omega t) \quad (\text{I.25})$$

We defined  $I_{wc}$  as the critical current per unit width  $I_{wc} = 2aJ_c$ .

The AC losses can then be calculated [41] as :

$$\begin{aligned}
P_{tape,BF} &= A \frac{2\pi f I_{wa}^3}{3 I_{wc}} \left( 1 + 3 \left( \frac{H_a}{2\pi I_{wa}} \right)^2 \right) \quad \text{for } H_a < 2\pi I_{wa} \\
P_{tape,BF} &= A \frac{f H_a^3}{12\pi^2 I_{wc}} \left( 1 + 3 \left( \frac{2\pi I_{wa}}{H_a} \right)^2 \right) \quad \text{for } 2\pi I_{wa} < H_a < 2\pi I_{wc}
\end{aligned} \tag{I.26}$$

For the case where  $H_a > 2\pi I_{wc}$ ,

$$\begin{aligned}
\frac{P_{tape,BF}}{A} &= f H_a I_{wc} \left( 1 + \frac{1}{3} \left( \frac{I_{wa}}{I_{wc}} \right)^2 \right) - \frac{4\pi}{3} f I_{wc}^2 \left( 1 - \left( \frac{I_{wa}}{I_{wc}} \right)^3 \right) \\
&+ 8\pi^2 \frac{f I_{wa}^2 (I_{wc} - I_{wa})^2}{I_{wc} H_a - 2\pi I_{wa}} - \frac{32\pi^3 f I_{wa}^2 (I_{wc} - I_{wa})^3}{3 I_{wc} (H_a - 2\pi I_{wa})^2}
\end{aligned} \tag{I.27}$$

### I.5.a-ii Calculations on cylinders

In this section, the AC losses in a cylinder with a radius  $R$  are detailed. Self field AC losses and transverse external field losses have been calculated in [41]. The penetration field is defined as  $H_p = J_c R$ .

#### Self-field AC losses

$$P_{cylinder,SF} = \frac{\mu_0 I_c^2 f}{\pi} \left( \beta - \frac{\beta^2}{2} + (1 - \beta) \cdot \ln(1 - \beta) \right) \tag{I.28}$$

**External field AC losses perpendicular to the cylinder** When the field  $H_a$  is less than the penetration field, the AC losses are calculated as (where  $J_c = I_c / (\pi R^2)$ ):

$$P_{cylinder,EF,nopenetration} = \frac{\mu_0 I_c^2 f}{\pi^2} \frac{128}{9} \left( \frac{H_a}{R J_c} \right)^3 \tag{I.29}$$

For  $H_a > H_p$ , the cylinder is fully penetrated and the AC losses are expressed as :

$$P_{cylinder,EF,fullpenetration} = \frac{16\mu_0 f I_c R}{3} H_a \tag{I.30}$$

### I.5.a-iii Calculations on tubes

For tubes with a layer thickness  $e$ , self field AC losses can be calculated according to (I.31) and external magnetic field AC losses according to (I.32) [118, 119]. The parameter  $\alpha_R$  defined as  $\alpha_R = 1 - (R_{in}/R_e)^2$  is introduced with  $R_{in}$  and  $R_e$  the inner and external radius of the tube ( $R_e - R_{in} = e$ ).

$$P_{tube,SF} = \frac{\mu_0 I_c^2 f}{\pi} \left( \frac{\beta}{\alpha_R} - \frac{\beta^2}{4} + \frac{1 - \alpha_R \beta}{\alpha_R^2} \cdot \ln(1 - \alpha_R \beta) \right) \tag{I.31}$$

$$\begin{aligned}
P_{tube,EF} &= \frac{\mu_0 I_c^2 f}{\pi} \cdot \left( \frac{2H_a}{H_{c_{tube}}} - 1 \right)^2 \quad \text{for} \quad \frac{H_a}{H_{c_{tube}}} \ll 1 \\
P_{tube,EF} &= \frac{4\mu_0 I_c^2 f}{\pi^2} \cdot \left( \frac{H_a}{H_{c_{tube}}} - 0.67 \right) \quad \text{for} \quad \frac{H_a}{H_{c_{tube}}} \gg 1
\end{aligned} \tag{I.32}$$

In (I.32), a threshold value of magnetic field defined as  $H_{c_{tube}} = J_c e$  can be introduced. This value, called penetration field, is the minimum field for which the current densities penetrate completely locally in the superconducting layer. When  $H_a < H_{c_{tube}}$ , no magnetic field is observed inside the tube. Above this value, the magnetic field penetrates and loops inside the tube. This leads to an increase of the current density in the superconducting area. The flux lines and also the current densities are displayed in Fig.I.35.

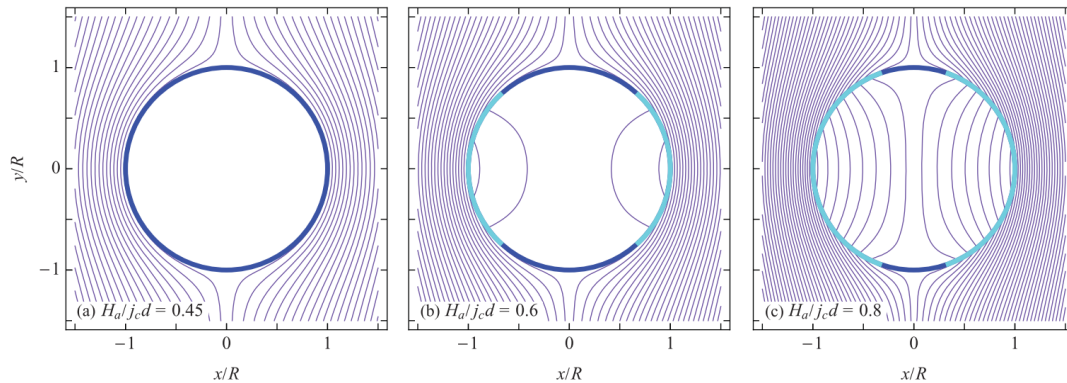


Fig. I.35 – Magnetic field flux lines and current density distributions for different values peak value of magnetic field ( $2d=e$ ) [119]. In light blue, the area where the layer is fully penetrated.

We have seen in this part the analytical calculations on various geometries. These formulas were developed under specific conditions (critical state model, constant  $J_c$ ) and the calculations are not applicable in all the cases, for example for a tube with transport current and external field. To go further, it is necessary to model numerically the superconductor and one way to do it, is to use finite element modeling.

### I.5.b FEM modeling

The finite element resolution methods is a technique used to solve partial differential equations. The studied domain  $\Omega$  is discretized into several sub-domains called elements. These elements can take several different forms such as, in 2-D, triangles or rectangles and in 3-D, tetrahedra, prisms or hexahedra. This thesis will not to give a complete description of FEM modeling, more informations can be found for example in [120, 121, 122].

The FEM method uses what is called a formulation to calculate a state variable in the whole domain, for example the magnetic field  $H$ . From the calculation of this variable, it is possible to assess the other physical quantities such as the current density  $J$  or the electric field  $E$ .

The number of degrees of freedom (DOFs) which is directly linked to the size of the mesh, determines the size of the problem to solve i.e. the size of the matrix to invert. For realistic problems, it is difficult to keep a reasonable number of elements (and then degrees of freedom) when one is considering large number of conductors, tapes without any homogenization techniques. The form and the size of the elements have an intrinsic impact on the convergence of the problem but also on the quality of the solution. For the modeling and the solving of problems with sharp non linear E-J relationships as it is in superconductors, the computation time can span from some minutes to several weeks. This time can be extended as the complexity of the physical properties increase (presence of magnetic material, dependence of critical current with magnetic field, ...)

To solve the numerical problem, it is possible to use as unknown the magnetic field  $H$  or any other state variable (magnetic vector potential  $A$ , electric field  $E$ , current density  $J$ ). By using Maxwell equations, two different classes of formulations can be used. The magnetic formulations ( $H$  or  $T$ - $\Phi$ ) and the electrical formulations ( $A$ - $V$ ) as presented below.

**Magnetic formulations** This series of equations uses the magnetic field  $H$  or its derivatives to solve the problem. Furthermore, these formulations have the electric field (or the resistivity) in function of the current density. One example is the H-formulation detailed as :

$$\nabla \times \vec{E}(\vec{J}) = \nabla \times (\rho(\vec{J}) \nabla \times \vec{H}) = -\mu \frac{\partial \vec{H}}{\partial t} \quad (\text{I.33})$$

**Electric formulations** These formulations in opposite to the magnetic formulations use the current density function of the electric field. The most well known formulation is the A-V formulation consisting in solving the set of equations :

$$\begin{aligned} \nabla \times \frac{1}{\mu} \nabla \times \vec{A} + \frac{\partial}{\partial t} (\vec{A} + \nabla V) &= \vec{J}_s \\ \nabla \cdot \left( \frac{\partial \vec{A}}{\partial t} + \nabla V \right) &= 0 \end{aligned} \quad (\text{I.34})$$

Where  $J_s$  is the source current constraint,  $A$  the magnetic vector potential and  $V$  the electric scalar potential.

To understand which formulations are most suitable for our use, it is possible to plot the residue of the problem. As the E-J relationship is a power law, the residue will be in the same form and shown Fig. I.36.

From this figure, it is clearly visible that a formulation using the electric field function of the current density leads to a better convergence of the problem [124]. Indeed the H and T- $\Phi$  formulations use the resistivity function of the current density (see (I.33) whereas

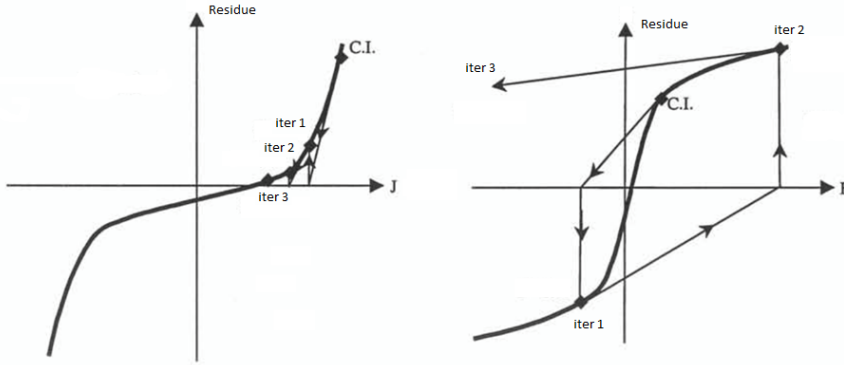


Fig. I.36 – Convergence for the  $E(J)$  and  $J(E)$  when considering a power law (still valid for a percolation law). This plot shows the convergence of the non-linear solver as the point where the residue is zero is the solution [123]

A-V formulation has the resistivity function of the electric field (see (I.34)). The two formulations suited for HTS modeling are the H-formulation and the T- $\Phi$  formulation. These two formulations are developed below.

### I.5.b-i H-formulation

In literature, the large majority of superconducting model are solved using the H-formulation [125, 126]. Starting from Maxwell-Faraday equation :

$$\nabla \times \vec{E} = -\mu \frac{\partial \vec{H}}{\partial t} \quad (\text{I.35})$$

Introducing the Ampere law :

$$\vec{E} = \rho(|\vec{J}|) \cdot \vec{J} \quad (\text{I.36})$$

By combining (I.35) and (I.36), it gives :

$$\nabla \times \left( \rho(|\vec{J}|) \vec{J} \right) = -\mu \left( \frac{\partial \vec{H}}{\partial t} + \frac{\partial \vec{H}_0}{\partial t} \right) \quad (\text{I.37})$$

Where  $H_0$  is the source term for the external magnetic field. It is possible to express  $\vec{J}$  function of the magnetic field  $\vec{H}$  with Maxwell Ampere equation :

$$\nabla \times \vec{H} = \vec{J} \quad (\text{I.38})$$

Finally by substituting (I.38) into (I.37), the formulation is obtained :

$$\nabla \times \left( \rho(|\vec{J}|) \nabla \times \vec{H} \right) = -\mu \left( \frac{\partial \vec{H}}{\partial t} + \frac{\partial \vec{H}_0}{\partial t} \right) \quad (\text{I.39})$$

This constitutive equation is relatively easy to implement in home-made software or in COMSOL. An example of a 3-D model [127] of a ROEBEL cable is presented below, first the model in Fig. I.37a and the comparison with experiment in Fig. I.37b.

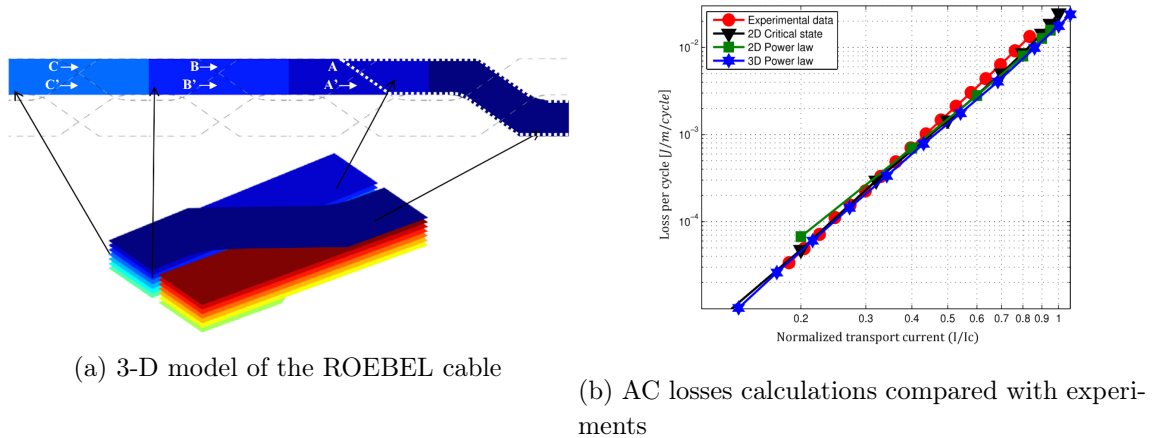


Fig. I.37 – ROEBEL cable and comparison with experiments [127].

The only drawbacks of this formulation is the resistivity which has to be set in each domain including the air. In practice, the resistivity for the air is defined several order of magnitudes higher than the resistivity of conductors in the model (between  $1 \text{ m}\Omega\cdot\text{m}$  and  $1 \Omega\cdot\text{m}$ ). This resistivity is not an issue in 2-D. But for 3-D modeling, the value of the air resistivity may induce non-physical currents in the air domain as it is shown in Fig. I.38 [128]. In this simulation, an external field was applied on 2 twisted filaments with a twist pitch of 5 mm (in Fig. I.38a). Periodic conditions were added to the normal surface to ensure a good decoupling of the filaments. The net current inside the filaments was observed at different height of the wire in Fig. I.38b. The H formulation is compared to another magnetic formulation which ensure a strong current conservation  $\text{T}-\Phi$  (called in the paper  $H-\phi-\Psi^2$ ) The  $\text{T}-\Phi$  was especially developed for this kind of simulations (see I.5.b-ii).

It can be observed that the net current in the filaments is not constant along the wire as it should be. This evolution of current inside the conductor length shows that the current conservation in each filaments is not valid and currents leak into the air domain. To avoid this feature, it is possible to used cohomology functions [129] or formulations that guarantee a strong current conservation such as the  $\text{T}-\Phi$  formulation.

### I.5.b-ii $\text{T}-\Phi$ formulation and associated formulations

The  $\text{T}-\Phi$  formulation has been developed, for example in the commercial software FLUX for solving 3-D problems [123]. This formulation was initially chosen because it ensure the strong current conservation in the conductors which is a key issue for solving electromagnetic systems. Two unknown are used depending on the physical properties of the domain, the current vector potential  $\vec{T}$  and the magnetic scalar potential  $\Phi$ . The two unknowns are defined according to :

$$\nabla \times \vec{T} = \vec{J} \text{ where } \vec{H} = \vec{T} - \nabla \Phi + \vec{T}_0 \quad (\text{I.40})$$

Where the current source term is  $\vec{T}_0$ . Two unknowns mean that two equations have to

---

2. In this formalism, the magnetic field  $\text{H}$  is expressed as  $\vec{H} = \nabla \phi + \vec{\Psi}$  with cohomology basis functions

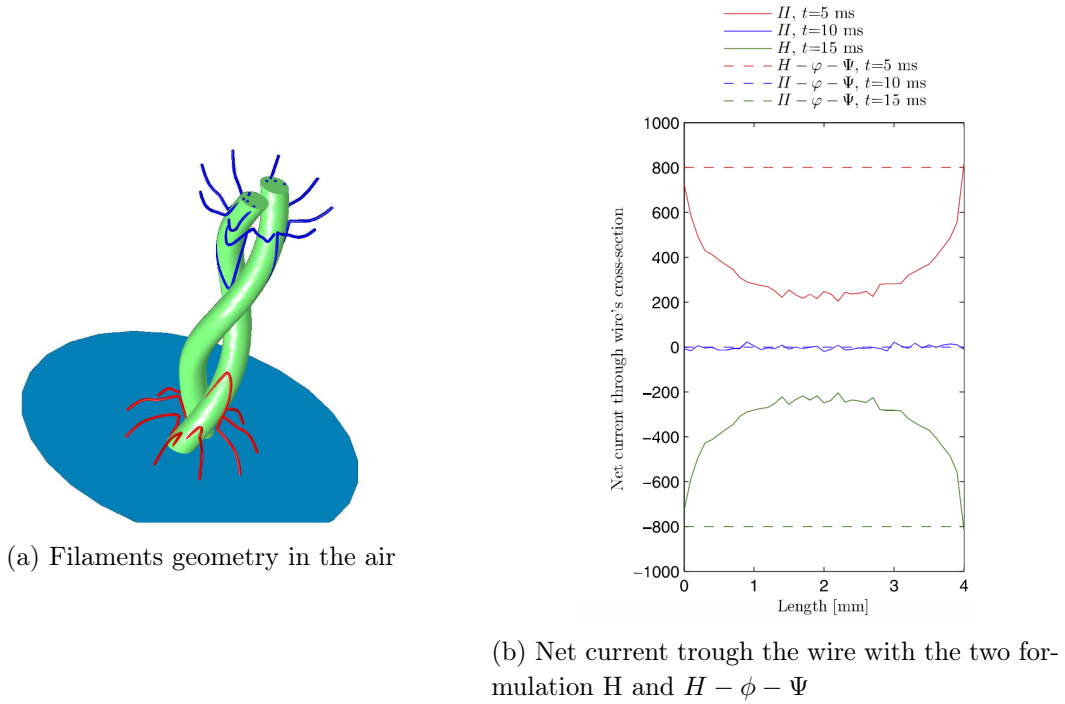


Fig. I.38 – Limit of the H formulation for 3-D models [128].

be solved :

$$\begin{aligned}\nabla \times \vec{E} &= -\frac{\partial \vec{B}}{\partial t} \\ \nabla \cdot \vec{B} &= 0\end{aligned}\tag{I.41}$$

By substituting  $\vec{B} = \mu \vec{H}$ , we obtained the set of equation to solve in (I.42)<sup>3</sup> :

$$\begin{aligned}\nabla \times \rho \nabla \times (\vec{T} + \vec{T}_0) + \frac{\partial}{\partial t} \left( \mu (\vec{T} + \vec{T}_0 - \nabla \Phi) \right) &= 0 \\ \nabla \cdot \left( \mu (\vec{T} + \vec{T}_0 - \nabla \Phi) \right) &= 0\end{aligned}\tag{I.42}$$

### I.5.b-iii Formulation comparison

It is possible to give an overall comparison of the two formulations. The H-formulation is relatively easy to implement and capable of handling high non linear E-J relationship. The implementation of a relative magnetic permeability dependent on the magnetic field is also straightforward. The leakage current in the air can be an issue in the case of filaments, it is then necessary to set a high value of resistivity for the air domain. This can lead

3.  $\vec{E}$  is function of  $\nabla \times \vec{T}$  but the unicity of  $\vec{T}$  and  $\Phi$  are not ensured unless a gauge condition is used, in our case  $\nabla \cdot \vec{J} = 0$

to convergence issues and an increase of the computation time. On the other hand T- $\Phi$  formulation, is more complicated to implement in multiple connected domains [130] but ensures current conservation. This formulation is available in some software and should be used when available.

Finite element modeling is a largely used method to solve problems including superconductors. However, as some of the studied conductors are very thin (tapes), it is interesting to consider what are called integral method which will not discretize the complete thickness of the tapes.

### I.5.c Integral method

HTS conductors are produced in tapes with a width between 2 mm and 12 mm. The superconducting layer where the current flows is several micrometers thick between layers of metals. The space ratio between the thickness and the width is approximately 2 000 rendering the simulations complex if one is considering the current inside the thickness. It is possible to calculate the current density distributions in this thin film by meshing with adapted elements but the calculations can be long especially when the number of conductors is high. With these particular geometries, an alternative can be used by considering only a line for the superconducting layer (no thickness) and solving it using integral methods. The use of integral equations, which consider the tape as a 1-D element, avoid to mesh the tape in details and save some computation time. The main hypothesis is considering a uniform current density inside the thickness of the conductor which is valid in several cases such as self-field AC losses. This approach has been suggested by Brambilla *et al* [131]. The fundamental expression is :

$$\vec{E} = \rho(\vec{J})\vec{J} = -\frac{\partial\vec{A}}{\partial t} - \nabla V \quad (\text{I.43})$$

Where  $\rho$  is the resistivity of the superconducting material and  $\vec{A}$  the magnetic vector potential. The unknown is the current density  $\vec{J}$ . The term  $\nabla V$  is the current constraint applied on the conductor. The vector potential can be expressed using the Green function as :

$$\vec{A} = \frac{1}{4\pi} \int_{\Omega} \vec{J}G(r)d\Omega + \vec{A}_0 \quad (\text{I.44})$$

Where G is the green function and  $\vec{A}_0$  the source field for the external magnetic field. By substituting (I.44), into (I.43), we obtain the formulation for the integral method :

$$\bar{\rho}\vec{J} + \frac{\partial}{\partial t} \left( \frac{1}{4\pi} \int_{\Omega} \vec{J}G(r)d\Omega + \vec{A}_0 \right) = -\nabla V \quad (\text{I.45})$$

This technique has been compared with FEM modeling and an example is shown in Fig. I.39.

As it can be seen from Fig. I.39, there is good agreement for the current density distribution between the 1-D (integral method) and the 2-D (FEM) models in the case of an applied field perpendicular to the flat surface. The computation times have been divided by

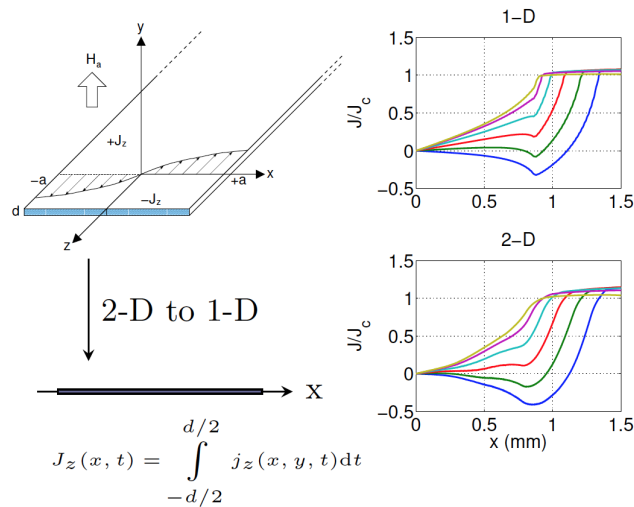


Fig. I.39 – Comparison between 1-D and 2-D simulations for an HTS tape under an applied field [132].

a factor 100. This method has been extended to coil with a large number of tapes [131] or HTS cables [133]. It has also been possible to calculate the complete AC losses in a power cable in 3-D with twisted tapes [134]. From these simulations, it is possible to calculate with accuracy the ideal twist pitch for multi-layered cables to minimize AC losses. This method is fully applicable in 3-D. Integral methods are one the main subject of research and novel technics may be considered in the future [135]. In the thesis, we will compare these methods to find the most suitable in each case. Some comparisons will be made when the modeling of thin tapes for example will be made with integral methods.

After this short presentation on the calculation of the AC losses, analytically or numerically, this chapter ends with some information on the challenges of the superconducting modeling. The sharp E-J power law and the non conventional geometries of some conductors render the solving of the problem sometimes difficult. We give some knowledge of techniques made to speed up calculations and improve convergence.

## I.6 Challenges and gridlocks of the superconducting modeling

The modeling of superconductors can be complicated due two particular features. First the geometry of the HTS tapes which are few micrometers thick inside a large scale applications with a high number of turns. Added to that, the peculiarity of the non-linear relationship has to be solved with great care. To improve the convergence of the model, it is possible to add algorithms to the non-linear solver.

### I.6.a Multi-scale problems

The E-J relationship makes the superconductor difficult to model especially when one is considering complicated geometries with various properties (critical current and  $n$  value dependent of field and orientation). Furthermore, in realistic devices [136, 89, 137], the number of turns of superconducting elements can be rapidly high. In these simulations no stationary study can be made. Because of the non-linear behavior of the E-J relationship, it is necessary to model the history of the model, for example, ramping the current from zero to a certain value. As the current densities are developed inside very thin layers and time dependent studies are compulsory it is necessary to adjust one of the two issues. One way to reduce the computation time is to optimize the model and associated mesh.

For example in a 2-D problem, modeling the evolution of current inside a thin tape several micrometers thick with a width three orders of magnitude higher is complicated if one is using triangle in 2-D. It would need approximately 200 000 elements to ensure a mesh acceptable inside the layer for a 4 mm-2  $\mu\text{m}$  HTS tape. It is possible in some case to expanded the thickness by ten or one hundred folds with keeping the same critical current (and recalculating the current density). In these cases, the aspect ratio is divided and allows the mesh with triangles. It could be used to do quick calculations on a single tape or to investigate current density distributions more rapidly. Unfortunately, when it is necessary to model windings made with a large number of tapes, this technique can not be used. It is then possible to mesh the tapes using rectangular elements for example mapped mesh [138]. The use of rectangles is then interesting to reduce the number of mesh elements in and between the coated conductors. A coarser mesh can be used between the superconducting layers or where the calculation is less important (air far from the conductor for example). A reduction of a least two orders of magnitude for the number of elements has been observed leading to faster computations [139, 140].

In some cases, it is possible to consider the homogenization of a winding, instead of considering all the conductors which compose the coil, a bulk model with the adapted superconducting properties is made. Some constraints are added for the imposition of current. This kind of homogenization are only valid if the critical current is considered constant with field. If the current is magnetic field dependent, the current distribution will be affected and not homogenous on the complete cross section of the coil. An example of this kind of modeling can be found in Fig. I.40.

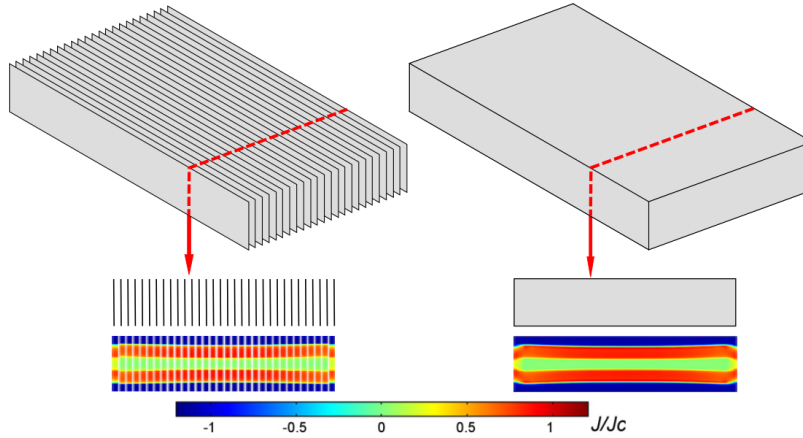


Fig. I.40 – Comparison of a complete model considering the actual layout of a stack of superconducting tapes (left) and its corresponding homogenized model (right). It is possible to see the good agreement of the current density distributions on both models [141].

### I.6.b Solving non-linear problems

The ability of solving superconducting problem is directly linked to the complexity of the non-linear equation to solve. For example, two non-linearities can lie inside the model : the inherent E-J relationship of the superconducting material and the presence of ferromagnetic materials which could have a non linear relative magnetic permeability function of the magnetic field (or even an hysteretic behavior). The relative magnetic permeability of the superconducting material is always neglected as the relationship  $\mathbf{B}=\mu_0\mathbf{H}$  is true after few millitesla. When the software is implemented with an H-formulation, the two non-linearities are well noticeable and shown in red on (I.46).

$$\begin{aligned} \nabla\times(\rho(|\vec{J}|)\nabla\times\vec{H}) &= -\mu_0\frac{\partial\vec{H}}{\partial t} \text{ inside superconductor} \\ \nabla\times(\rho\nabla\times\vec{H}) &= -\frac{\partial\mu(\vec{H})\vec{H}}{\partial t} \text{ inside magnetic materials} \end{aligned} \tag{I.46}$$

To solve the non linear system, several methods have been implemented in FEM software. The two main non-linear solvers are the Fixed point and Newton-Raphson methods.

#### I.6.b-i Fixed point method

To solve the equation  $f(X)=0$ , we rewrite the equation as  $F(X)-X=0$ . Finding the solution is then equivalent of locating the fixed point of the function F. To achieve the resolution, a sequence  $X_n$ ,  $n \in \mathbb{N}$  defined as [142] :

$$X_{n+1} = F(X_n) \tag{I.47}$$

is created to approach the solution  $f(X)=0$ , assuming that a solution exists. If the function  $F$  is monotone and contracting, there is a unique point which satisfies the equation  $F(X)=X$ . The convergence of this process is linear and may be slow. If the function  $F$  is Lipschitzian<sup>4</sup> uniformly monotone<sup>5</sup>, it is possible to create a function  $F_1$  as :

$$F_1(X) = X - \alpha(F(X) - X) \quad (\text{I.48})$$

where  $\alpha$  is a real number. The function  $X=F(X)$  admits one solution if the function  $F_1$  is contracting, which is the case if the parameter  $\alpha$  belongs to a certain interval  $[0, 2\lambda/\Lambda]$ . According to the Picard-Banach Theorem, this solution is the fixed point of the function  $F_1$  and it can be calculated by building the sequence  $X_{n+1}=F_1(X_n)$ .

The fixed point method is an algorithm, which usually converges but sometimes with a large number of iterations. To improve the convergence of non-linear systems and reduce the number of iterations, the Newton-Raphson method is largely used.

### I.6.b-ii Newton-Raphson method

In order to solve the non linear problem, the newton method determines the minimum of a function  $f(X)$  on each point  $X_k$  of the domain, the function in our case is the magnetic field if the model is solved using the H formulation. On each time step, the method use a Taylor series expansion of the first order to find iteratively the zero of  $f(X)$  on each point.

**Example  $f(x)$**  For example, if we consider a function  $f$  of one variable. Assuming that the function  $f$  is having a root  $X^*$ . Let  $X_0$  be the initial condition, we extrapolate the tangential slope starting from the point  $X_0$  to  $x$  axis.

$$f'(X_0) = \left( \frac{\partial f}{\partial X} \right)_{X_0} = \frac{f(X_1) - f(X_0)}{X_1 - X_0} \quad (\text{I.49})$$

To calculate  $X_1$ , in order to have  $f(X_1)=0$ , we set :

$$X_1 = X_0 - \frac{f(X_0)}{f'(X_0)} \quad (\text{I.50})$$

By iterating this solving, it is possible to create a sequence  $X_n, n \in \mathbb{N}$  to find  $X^*$

$$X_{n+1} = X_n - \frac{f(X_n)}{f'(X_n)} \quad (\text{I.51})$$

**Generalization** This part is the generalization of the latter. Let us consider a system  $F(X)=0$  with  $F$  the matrix defines as the  $N$  equations of the system with the vector  $X=(x_1, x_2, \dots, x_N)$  as :

4. A function is Lipschitzian on  $\Omega$  if there is a finite real  $\Lambda$  such as :  $\forall (x_1, x_2) \in \Omega, |f(x_1) - f(x_2)| \leq \Lambda |x_1 - x_2|$

5. A function is uniformly monotone on  $\Omega$  if there is a finite real  $\lambda$  such as ( $\langle x, y \rangle$  is the usual scalar product) :  $\forall (x_1, x_2) \in \Omega, \langle f(x_1) - f(x_2), x_1 - x_2 \rangle \geq \lambda \langle x_1 - x_2, x_1 - x_2 \rangle$

$$\forall i \in \llbracket 1, N \rrbracket, F_i(x_1, x_2, \dots, x_N) = 0 \quad (\text{I.52})$$

In the neighborhood of  $x$ , each function  $F_i$  can be expand as :

$$\forall i \in \llbracket 1, N \rrbracket, F_i(x + \Delta x) = F_i(x) + \sum_{k=1}^N \frac{\partial F_i}{\partial x_k} \Delta x_k + O(\Delta X^2) \quad (\text{I.53})$$

We introduce the Jacobian matrix  $J$  as :

$$\forall (i, k) \in \llbracket 1, N \rrbracket^2, J_{i,k} = \frac{\partial F_i}{\partial x_k} \quad (\text{I.54})$$

The equation simplifies into :

$$F(X + \Delta X) \approx F(X) + J\Delta X \quad (\text{I.55})$$

To simplify this equation and cancel the first term, the vector  $\Delta X$  is chosen as :

$$J\Delta X = -F(X) \quad (\text{I.56})$$

It is then possible to build the sequence  $X_{k \in \mathbb{N}}^{(k)}$  with  $X(0) = (x_1^{(0)}, x_2^{(0)}, \dots, x_N^{(0)})$  the initial condition of the system.

$$X^{k+1} = X^k + \Delta X(k) \quad (\text{I.57})$$

As the residual decreases throughout the iterations, the approximation  $X^{(k)}$  gets smaller from the solution. The solution is assumed when the quantity is inferior to a  $\epsilon$  as :

$$\frac{\|\Delta X^{(k)}\|}{\|X^{(k+1)}\|} \leq \epsilon \quad (\text{I.58})$$

As the solving is not relatively easy<sup>6</sup>, one solution is to relax the system to improve the convergence by adding a constant  $\alpha$  in (I.51) :

$$X^{(k+1)} = X^{(k)} - \alpha \Delta X^{(k)} \text{ with } \alpha \in [0, 1] \quad (\text{I.59})$$

In the configuration of the solver, it is possible to fix a value for  $\alpha$  (default value 1) prior to the solving of the problem. As the modeling community has worked since a long time on improving the solving of non linear problems, some algorithms are used to find an optimal relaxation factor to decrease the iteration number. In our cases, two different algorithms have been used which are implemented inside one of the software used : the Fujiwara method which minimizes the norm of  $F(X^{(k)} + \alpha \Delta X^{(k)})$  and the Optimal method.

**Algorithm to help the convergence** This sections discloses two ways to help the convergence, First the Fujiwara method and then the optimal method.

---

6. Newtown method can converges quickly if the problem has monotonic conditions which is almost never the case.

**Fujiwara method** One way to calculate the ideal optimal relaxation coefficient  $\alpha_o^{(k)}$  is to minimize the quantity  $(\|\Delta X\|_2)^2$ <sup>7</sup>. To do so, the idea is to calculate the derivative as follow where  $T$  is the transposed matrix :

$$\begin{aligned} \frac{(\|\Delta X^{(k+1)}\|_2)^2}{\partial \alpha^{(k)}} &= \frac{(\|\Delta X^{(k+1)}\|_2)^2}{\partial X^{(k+1)}} \frac{\partial X^{(k+1)}}{\partial \alpha^{(k)}} \\ &= 2\Delta X^{(k+1)T} \frac{\Delta X^{(k+1)}}{\partial X^{(k+1)}} \delta X^{(k)} \\ &= 2 \sum_{i=1}^N \Delta X_i^{(k+1)} \left( \sum_{j=1}^N \frac{\partial \Delta X_j^{(k+1)}}{\partial X_j^{(k+1)}} \delta X_j^{(k)} \right) = 0 \end{aligned} \quad (\text{I.60})$$

If the function  $\mathcal{F}(\alpha^{(k)}) = (\|\Delta X(\alpha^{(k)})\|_2)^2$  is quadratic, then its derivative is linear then it is relatively easy, when one is knowing two points of the derivative, to find the solution to the equation  $\partial \mathcal{F} / \partial \alpha^{(k)} = 0$ . If the function  $\mathcal{F}$  is not quadratic, it is possible to linearize the function  $\partial \mathcal{F} / \partial \alpha^{(k)}$  to find the minimum.

**Optimal method** Another way to find the optimal relaxation coefficient is to minimize the energy functional  $\chi^{(k)} = F(X^{(k)} + \alpha^{(k)} \Delta X^{(k)})$ . The optimal relaxation coefficient at the time step k,  $\alpha_o^{(k)}$  can be obtained by calculating a approximate value  $\alpha_a^{(k)}$  :

$$\frac{\partial \chi^{(k+1)}}{\partial \alpha^{(k)}} = \frac{\partial \chi^{(k+1)}}{\partial X^{(k+1)}} \frac{\partial X^{(k+1)}}{\partial \alpha^{(k)}} \quad (\text{I.61})$$

Supposing that  $\chi^{(k+1)}$  is quadratic so  $\partial \chi^{(k+1)} / \partial \alpha^{(k)} = 0$  is linear, it is possible to approximate this derivative leading to the equation to solve :

$$\frac{\partial \chi^{(k+1)}}{\partial \alpha^{(k)}} = \sum_{j=1}^N \Delta X_j^{(k+1)} \delta X_j^{(k)} = 0 \quad (\text{I.62})$$

where N is referred to as the number of unknowns in the system.

## I.7 Conclusion

The introduction chapter details some information on the theory of superconductivity. The mechanisms of AC losses occurring in the superconducting materials but also in the surrounding metals if there is any, have been presented in details.

The two superconductors considered for the design of new large scale developments have been introduced and their applications presented. To size the cryogenic system for these applications, it is necessary to calculate with accuracy the losses, including the AC losses if the superconductors are feed with AC signals or harmonics superimposed to DC backgrounds.

If one wants to calculate rapidly the AC losses of a superconducting material, one way is to use analytical formulas as it has been shown in this chapter. However, analytical calculations are only applicable to some geometries and sometimes with hypothesis which

---

7.  $\| \cdot \|_2$  is referred to the square norma.

are not valid in reality. Furthermore, some calculations simply do not exist. To cope with this issue, the use of superconductor modeling is necessary. One way to achieve these calculations, is to use Finite Element modeling, using magnetic formulations (formulations well suited to the superconductor E-J relationship). These simulations can be complicated and time-consuming. However, it is possible to develop and use some tools to speed up the calculations or to improve the convergence.

## Chapter II

---

# AC losses in HTS tapes and round wires

---

### CONTENTS

---

II.1	APPROACH AND CHALLENGES FOR HTS MODELING . . . . .	51
II.2	TRANSIENT ELECTRO-MAGNETIC MODELING OF HTS TAPES . . . . .	51
II.2.a	AC losses in HTS tapes . . . . .	51
II.2.b	Studied superconductors . . . . .	51
II.2.c	FEM modeling . . . . .	55
II.2.d	Comparison FEM - Integral method . . . . .	60
II.2.e	Experimental validations . . . . .	62
II.2.f	Conclusion : from tapes to round wires . . . . .	67
II.3	AC LOSSES IN HTS ROUND WIRES . . . . .	68
II.3.a	Model description . . . . .	68
II.3.b	FEM modeling . . . . .	69
II.3.c	Integral method . . . . .	79
II.3.d	Design perspectives for high current cables . . . . .	83
II.4	CONCLUSION . . . . .	85

---

### Summary

*High temperature superconductors show great promise for applications requiring high power ratings in compact spaces. To design the cryogenic system, an analysis of the AC losses has to be performed. Several methods exist to calculate the power dissipated when the application is operating with a time-varying current or under an AC external magnetic field such as analytical calculations, FEM or integral methods. Throughout two different geometries, this chapter details numerical modeling and experimental validations made to identify suitable codes and methods for AC losses calculations in various cases. We focus this part on the modeling to 2-D numerical problems with HTS tapes and round wires. These conductors are interesting in the case of cable carrying between 1 kA and 5 kA in a reduced space and working with liquid nitrogen. Given the architecture of HTS, the use of a 2-D FEM model is sufficient as long as the coupling losses are neglected and the model is not too big. Another approach can be to use integral methods which, under specific hypothesis, allow for the decrease of the number of elements and reduce the associated computation time. AC losses on HTS tapes have been calculated and compared to experiments with the two different approaches. On a second time, the possibility of using round wires for high current cables was investigated.*

## II.1 Approach and challenges for HTS modeling

To calculate numerically the AC losses of (HTS) tapes or round wires, it is vital to assess the most efficient way among diverse solutions. We focused our work on selecting and comparing three of them : analytical calculations, FEM and integral method [143]. Analytical work has been done with various geometries but does not take into account the real E-J relationship of the conductor nor the dependency of critical current on magnetic field. In some cases such as applications working at high fields, these properties can have a relative impact. Finite-Element modeling can be performed on small windings and the limit of solving lies in the computing power. Integral methods are far more elegant and can solve more complex models because no discretization of the superconducting layers is necessary. However this method can only be used in some cases and has to be validated. In a second part, the HTS round wires developed in the EUROTAPES project were modeled and the AC losses calculated.

## II.2 Transient electro-magnetic modeling of HTS tapes

### II.2.a AC losses in HTS tapes

This section reports the calculations made on HTS tapes. After a presentation of the two conductors used in the numerical modeling examples, simulations with Finite-Element method and integral method are developed and compared to experiments. Moreover, the simulation results are compared to analytical calculations when it was possible. Two superconductors have been studied in order to be numerically tested. Their performance at various temperatures but also the fit parameters for the E-J formulations can be found below. For applications at 77 K, a conductor from the company SuperPower [144] has been used. This tape was purchased without any copper layers. For applications at 4.2 K, another conductor from the company SuperOx [145] was characterized.

### II.2.b Studied superconductors

#### II.2.b-i Superpower tape

The Superpower tape is a typical tape produced by the Japanese company [144]. The superconducting layer is made with  $\text{YBa}_2\text{Cu}_3\text{O}_{7-\delta}$  with a average thickness of  $2 \mu\text{m}$ . The substrate layer made with Hastelloy is  $50 \mu\text{m}$  thick. On top of the superconducting layer, a  $2 \mu\text{m}$  silver layer is deposited. The very thin buffer layer (several nm), placed between the Hastelloy and the superconducting layers, has been neglected for the calculations. The rated critical current is defined at 130 A (@ 77 K, self-field). Regarding the resistivity of the metallic layers, as the purity of these compounds is not known with certainty, literature values were taken. The resistivity of Hastelloy was set as  $\rho_{\text{Hastelloy}}=1.26 \mu\Omega.\text{m}$  [146] and the resistivity of silver defined as  $\rho_{\text{silver}}=0.1 \text{ n}\Omega.\text{m}$  [147]. To validate the rated critical current of the tape, a characterization measurement was made at 77 K in a open bath of liquid nitrogen, we generated pulses of current with a time of 10 ms. This value of pulse time was the lower limit it was possible to achieve based on the voltage of the power supply and the inductance of the circuit. The sample is about 10 cm long which defines the voltage

threshold at  $10 \mu\text{V}$ . The rated current was found at 128 A. Non destructive techniques to characterize the superconducting such as induction [148, 33], susceptibility measurement [149] or a classic ramp of current exist, but was not used in our characterization.

The fit parameters for the power law model have been deduced as  $I_c=130$  A and  $n=30$ . For the percolation model, the value of  $J_{c0}$  is equal to  $1.60.10^{10}$  A/m<sup>2</sup> with  $n_0=2$ . These values are summarized with the geometric parameters in Table. II.1.

Quantities	Values
Hastelloy layer ( $\mu\text{m}$ )	50
Superconducting layer ( $\mu\text{m}$ )	2
Silver layer ( $\mu\text{m}$ )	2
Buffer layer (nm)	30
Critical current (A)	130
$J_c$ (A/m <sup>2</sup> )	$1.63.10^{10}$
$n$ (power law)	30
$J_{c0}$ (A/m <sup>2</sup> )	$1.60.10^{10}$
$n_0$ (percolation law)	2

TABLE II.1 – Geometric and physical parameters for the Superpower tape based on experimental characterization.

For the performance of the tape with respect to field amplitude and orientation, it was decided to take literature trends. Measuring the critical current of a superpower tape with field at 77 K is not commonly done in our laboratory and is not so interesting as HTS working under high field ( $>1$  T) are foreseen to operate at lower temperatures (to enhance the performances). Based on a critical current of 130 A (@ 77 K, self-field), the decrease of the critical current with external magnetic field was defined according to the results in [150], as displayed in Fig. II.1. For the anisotropic behavior, the trend of the critical current versus the incident field angle was modeled with [151] and plotted in Fig. II.2.

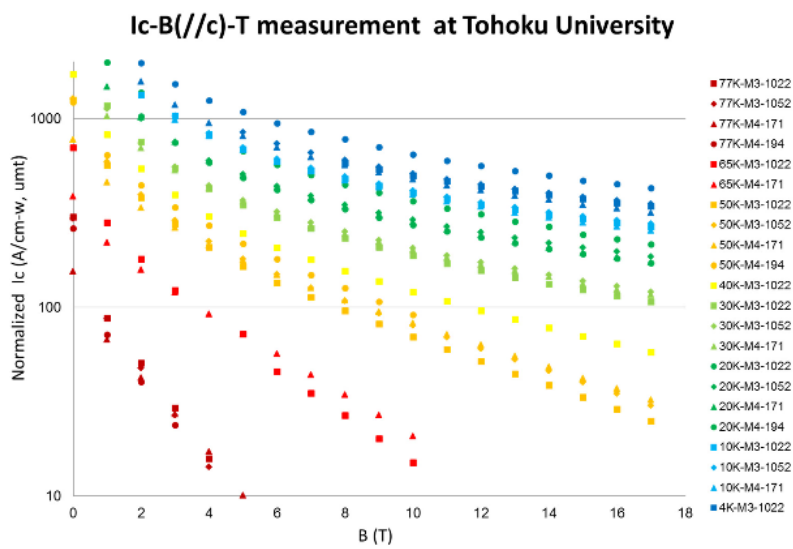


Fig. II.1 – Critical current of a SuperPower tape with various temperature and field [150].

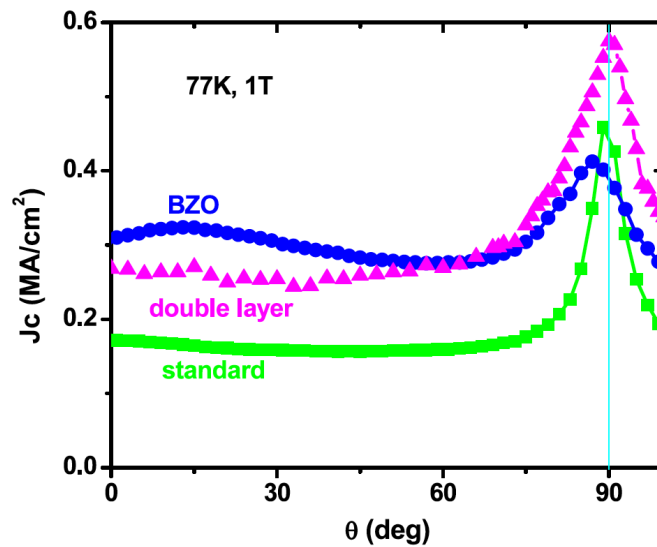


Fig. II.2 – Performance of a SuperPower tape at 77 K with various incident field angle [151].

### II.2.b-ii SuperOx conductor

The company SuperOx is able to produce HTS tapes in long length for a reduced cost with any configuration of shunt thicknesses [145]. The studied 4-mm tape is manufactured with a 2  $\mu\text{m}$  REBCO layer. An EDX (Energy-dispersive X-ray spectroscopy) study was performed on the superconducting layer and the results can be found in Fig. II.3. In this measurement, the Gadolinium (Gd) peak is predominant over other rare earth elements, meaning that the superconducting layer is made with GdBaCuO. The tape is formed with a 50  $\mu\text{m}$  Hastelloy substrate layer [152] and a layer of silver 2  $\mu\text{m}$  thick on top of the superconducting layer. For protection purposes, copper layers are deposited around the tape with a thickness of 30  $\mu\text{m}$  resulting to an overall thickness of 114  $\mu\text{m}$ .

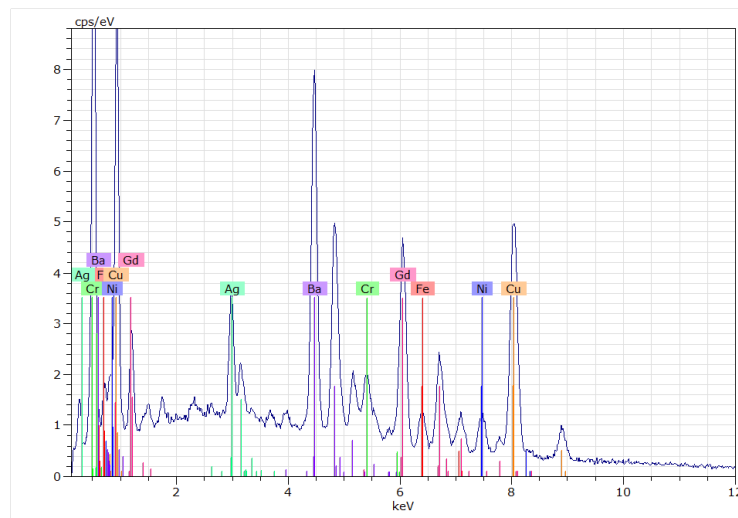


Fig. II.3 – SuperOx EDX of the superconducting layer. In this case, the REBCO layer is made with Gadolinium (Gd).

As this manufacturer has been selected for the design of high field applications working at 4.2 K, the knowledge of the performances of the tape under field with different field angles is available. In the framework of a joint ANR project, we performed these measurements in LNCMI Grenoble with a probe specially designed for the characterization of superconducting tapes with various magnetic field orientations [153]. Fig. II.4 displays the critical current of the tape versus the magnetic flux density at 4.2 K.

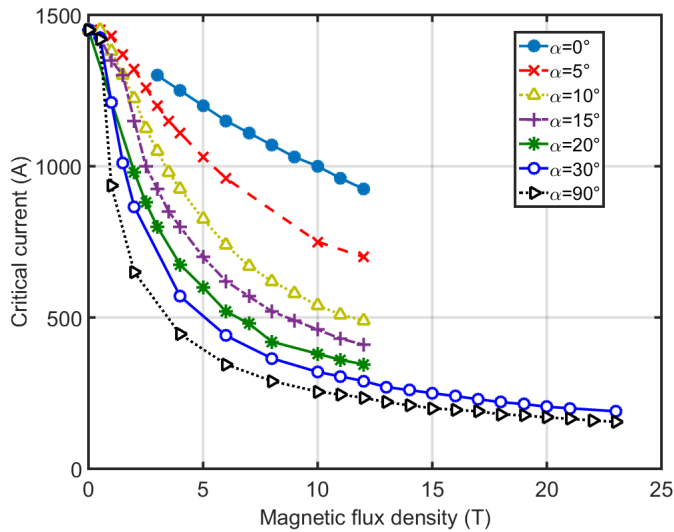


Fig. II.4 – Critical current versus magnetic flux density for the SuperOx tape at 4.2 K.

After the presentation of two of the superconductor having been characterized, the numerical model developed in COMSOL 4.3b is detailed below.

### II.2.c FEM modeling

For 2-D superconducting simulations, COMSOL has been chosen as it has been largely used in the superconducting modeling community in the past. More details on the implementation can be found in the literature for example in [154]. The H formulation is simplified into 2-D (cartesians coordinates) with  $\vec{H} = H_x \vec{u}_x + H_y \vec{u}_y$  and a current density along the z axis  $\vec{J} = J_z \vec{u}_z$ . To impose the transport current  $I(t)$  inside the tape, an integral constrain is set according to (II.1), where S is the surface of the conductor.

$$I(t) = \iint_S J_z dS \quad (\text{II.1})$$

For self-field AC losses, Dirichlet conditions are applied to the boundaries of the air domain (field equals to zero). The resistivity of the air was defined as  $\rho_{air} = 10^{-3} \Omega \cdot m$ . In the case of 2-D models, the risk of current leakage in the air domain is very unlikely to happen as the current constrain is set on the conducting domain and the current is only along one axis. However, a difference of a least 5 orders of magnitude between the resistivity of the air and the superconducting domain (or metallic domains) is implemented. When an external field is applied, the Dirichlet conditions are adapted to impose the field on the boundaries.

To solve these problems, COMSOL is using a time dependent solver with adaptive time stepping. The absolute tolerance of the solver is comprised between  $10^{-6}$  and  $10^{-8}$  to ensure fast calculations with reduced issues of convergence [155]. The solver is PARDISO using a Newton-Raphson technique for the non-linear problem. As the H-formulation is

not directly included in the software, the adaptive time step scheme is taking reduced time steps (between  $10^{-5}$  s and  $10^{-9}$  s) to ensure the convergence and minimize the error. Hence the computation times can be between some minutes to several hours for simulations of 50 Hz problems. This can lead to impossibility to solve complicated simulations with a large number of conductors. As these calculations are based on a non-linear problem with a zero initial condition, it is necessary to let the simulation run to remove the transient phase and reach the steady state. As this takes one quarter of a cycle, the simulations are carried out on one period and the AC losses are calculated with the second half period of the signal (or can be calculated between the first quarter and the third quarter). It is also possible to calculate the AC losses from the first quarter of the cycle to the third.

Regarding the mesh, as the layers are several micrometer thick for a width of 4 mm, the aspect ratio of the tape is about 1000. COMSOL offers the possibility of using various elements to mesh the domains; triangles or rectangles are the most suitable for these 2-D simulations. Concerning triangles elements; as a discretization in the superconducting layer is necessary, because the current density can be distributed non uniformly in the thickness, at least three or four triangles have to be placed along the superconducting thickness. This can be rapidly time consuming with the increase of the number of triangles [139]. For example, with a  $2\ \mu\text{m}$  superconducting tape with a maximum triangle size of  $0.7\ \mu\text{m}$ , the mesh will total  $\approx 47\ 000$  elements as it is shown in Fig. II.5 (a). Rectangle elements offer a good alternative with these geometries [156]. For example, if the thickness has to be discretized by 5, the number of elements can be easily reduced down to a few thousands of elements. This will divide the total of DOF's by more than 10. Fig. II.5 (b) displays the mapped mesh for the same tape.

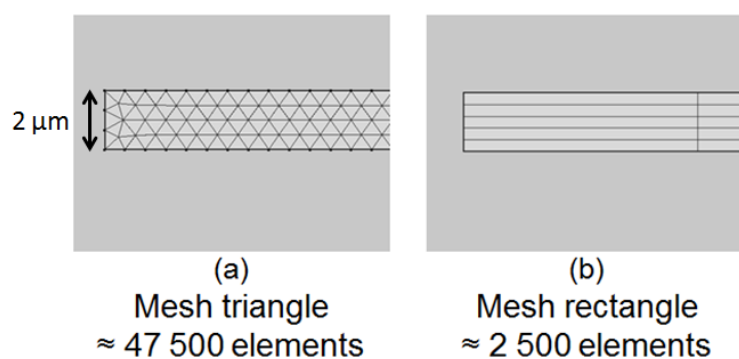


Fig. II.5 – Mesh of the HTS tape. the use of rectangle elements, in (b), is compared to triangles elements, in (a).

Outside the tape, the air domain is meshed with triangles, which ensures a good overall solution with a reduced number of elements. The total mesh for an HTS tape surrounded by air is plotted in Fig. II.6. In total, the mesh is reduced to 19 278 elements (compared to more than 50 000 elements for triangles) in the case of one superconducting tape surrounded by air.

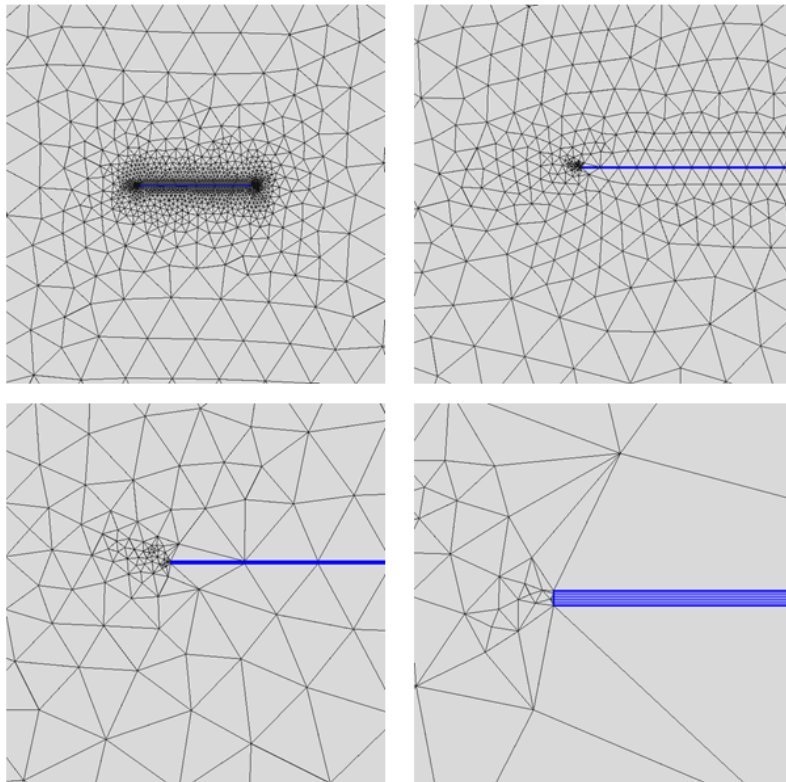


Fig. II.6 – Mesh of the HTS tape with a zoom on the superconducting layer discretized with rectangles.

### II.2.c-i Distribution of current in the layers

In principle, the simulations can be carried out on the complete tape with all the layers (except the buffer layer as explained before in II.2.b-i). For example, in the Superpower tape, it means taking into account the Hastelloy and the silver layers. It may be interesting to remove these layers in the AC losses calculations to reduce the number of elements. As the resistivity of the superconducting layer is several orders of magnitudes lower than the two others layers, this assumption can be reasonable and was tested numerically.

Simulations of self-field losses have been carried out by imposing the current on the whole surface of the tape and looking at the current ratio in each layer. Fig. II.7 displays these ratios (current in each layers divided by the total current) with various current amplitudes. These simulations have been made without taking into account the heat equation. The simulations are made at 77 K with  $I_c=130$  A and the power law model.

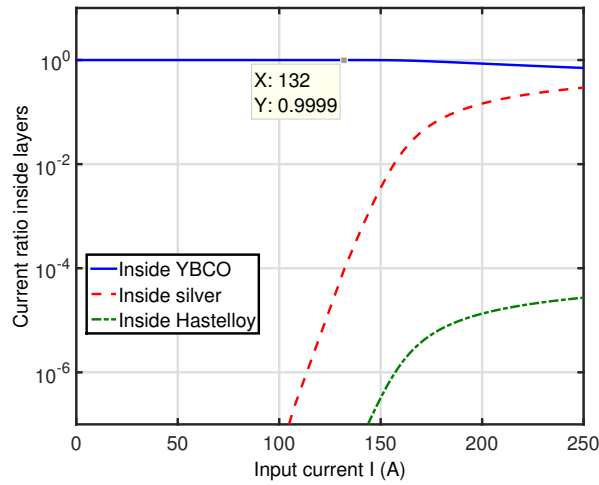


Fig. II.7 – Current ratio in each layer versus input current for the Superpower tape (without heat equation) with a current ramp of 10 A/s ( $I_c=130$  A).

If the ramp is higher, the current will screen inside the silver layer and the current ratio in each layer will change. Fig. II.8 shows this phenomenon with various values of current ramp. In this figure, only the ratio inside the superconducting and the silver layers are represented. As it can be seen from Fig. II.7, almost no current is flowing into the Hastelloy layer.

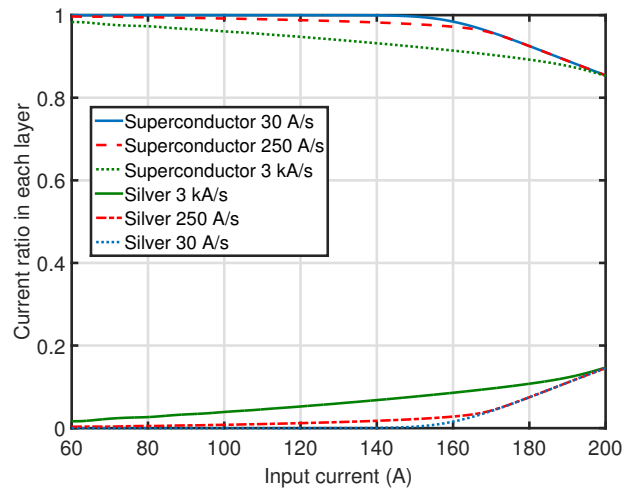


Fig. II.8 – Current ratio in the superconducting and silver layers versus input current for the Superpower tape (without heat equation) with various current ramps ( $I_c=130$  A).

As it was previously noticed, the current penetrates mainly inside the superconducting layer (more than 99 % for values below the critical current). As soon as the current is above  $I_c$ , the resistivity of the superconducting layer is becoming higher than the silver layer and current starts to flow inside the two layers. This result is the one expected according to the hypothesis made on the model (no heat equation solved). In this context, the resistance

of the superconducting layer and the silver layer are almost equal for an input current of  $I \approx 500$  A. Above this value, the current inside the silver layer shall become predominant over the amount of current inside the YBCO layer. In reality, the current flowing inside the shunt layers will increase the temperature and decrease the critical current of the tape. This phenomenon will speed up the increase of the resistivity of the superconducting material.

A multi-physics model has been implemented by adding the heat equation to the numerical model. We considered the problem as adiabatic as the current speed rates are high. Regarding the values of thermal capacities, conductivities and densities, the material database from COMSOL was used. The critical current of the superconducting layer was assumed at 130 A at 77 K and 0 A at 88 K with a linear decrease. Fig. II.9 displays the current ratio of each layer versus the input current changing at a speed of 10 A/s. On the second y-axis, the temperature in the superconducting layer was added. Regarding the temperature plotted in Fig. II.9, the temperatures, for example the one at 150 A was taken when the current reaches the value of 150 A.

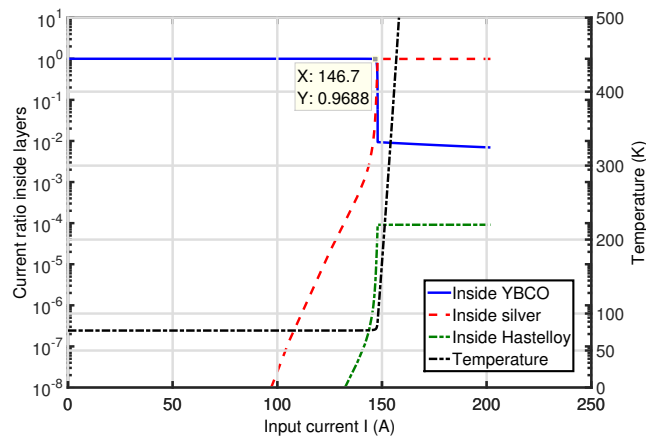


Fig. II.9 – Current ratio in each layer versus input current (with heat equation) with a rated speed of 10 A/s and associated temperature in the superconducting layer.

As soon as the input current is above  $I_c$ , a non-negligible amount of it starts to flow inside the shunt layers (mainly in the silver layer) and the superconductor is in the dissipative state. Hence, it dissipates Joule losses and the temperature inside the superconducting layer (and all other layers) increases. This phenomenon decreases the critical current of the superconducting material and the amount of current in the specific layer. In this case, the runaway effect is predominant as the ratio in the YBCO layer is almost zero with a total current of 148 A for a temperature of 400 K. The evolution of current in the YBCO layer can also be plotted with various speed rates as shown in Fig. II.10 as well as the temperature in the YBCO layer (right).

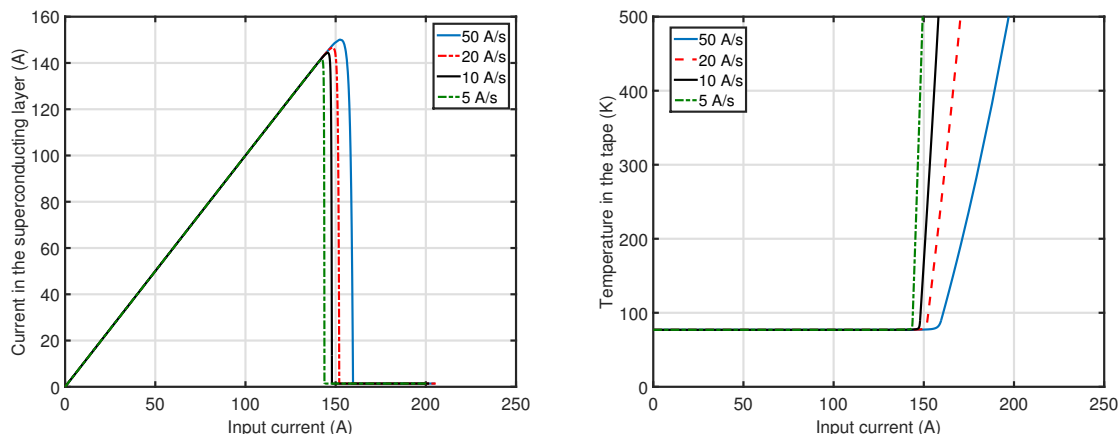


Fig. II.10 – Current in the YBCO for various speed (left) and YBCO temperature (right).

If the current increases faster, the temperature does not have sufficient time to homogenize in the tape (with adiabatic conditions). This means that more current can go inside the superconducting tape before the temperature reaches  $T_c$ . The results computed in COMSOL are in agreement with these explanations.

From all these calculations, if the current is below  $I_c$ , the current is largely going inside the superconducting layer. Hence, the model can be simplified by removing the shunt layers in the calculations. The problem is, in this case, simpler to solve with less elements. From now on, the shunt layers will always be neglected. If we only consider the superconducting layer, the integral method may be used under specific conditions detailed in the dedicated section. In the cases where, it is necessary to take into account the shunt layers, is it possible to do a complete FEM model or couple the integral method for the superconducting layer with a FEM method for the shunt layers but this novel technique [157] is outside the scope of this thesis.

#### II.2.d Comparison FEM - Integral method

The calculations using the integral method (see I.5.c) have also been carried out on COMSOL. The AC losses for a tape can be calculated using the integral methods if the current is homogeneous in the tape thickness. This can be considered even if the edges of the tapes induce a non-homogeneous current density distributions inside the tape. However, this effect has to be proven to be negligible for self-field AC losses but also for losses induced by external field transverse to the flat surface ( $H_{\perp}$  in Fig. I.34). Firstly, self-field AC losses can be computed with reduced current between 10 % and 90 % of the critical current  $I_c$  (with a sinusoidal current of 50 Hz), the results are displayed in Fig. II.11. Analytical calculations are also plotted for comparison purpose. The E-J power law was used in these calculations.

The results for the FEM and also the integral method are in good agreement with analytical calculations. This is expected as it was shown in (I.1.e-ii) that the Bean model follows closely the power law with a  $n$  value of 30 for the current distributions. In overall

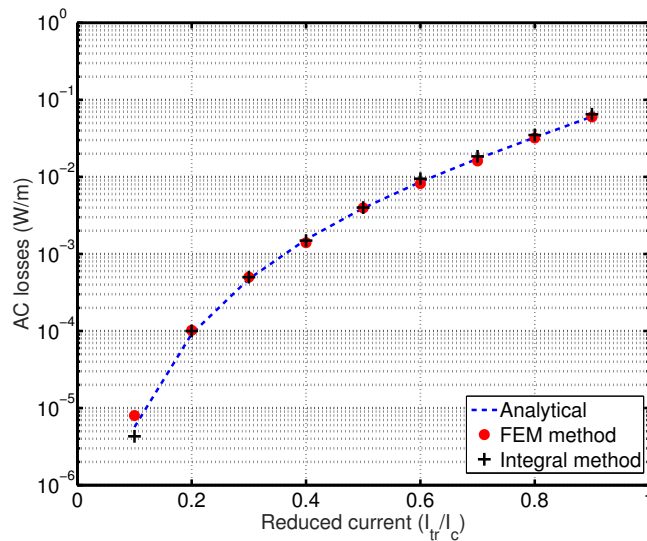


Fig. II.11 – Self-field AC losses for FEM and integral method on a single tape.

the difference between the two numerical methods is less than 3 % and less than 5 % for both models compared to analytical calculation. Fig. II.12 displays the AC losses induced by an AC external magnetic field perpendicular to the flat surface.

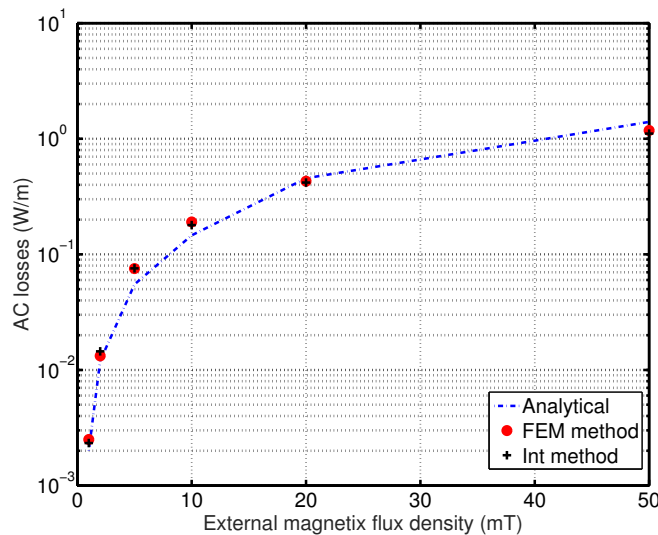


Fig. II.12 – External magnetic field AC losses versus magnetic flux density for the integral and FEM methods.

In these simulations, a reasonable agreement was found with differences in average less than 15 %, except for the lowest point of current where the coarse mesh might be an issue. From this figure, it is noticeable that the two AC losses method results versus external magnetic field are crossing at 20 mT with the analytical calculation. This is explained by the fact that above this value, the penetration field is reached and the behavior of the AC

losses is closely dependent of the form of the E-J relationship above  $J_c$ . Below 20 mT, the fact that the two E-J relationship are not zero below  $J_c$  explains also the higher AC losses results. Finally, the AC losses created by an external magnetic field (still transverse to the flat surface) and a transport current in phase are given in Fig. II.13.

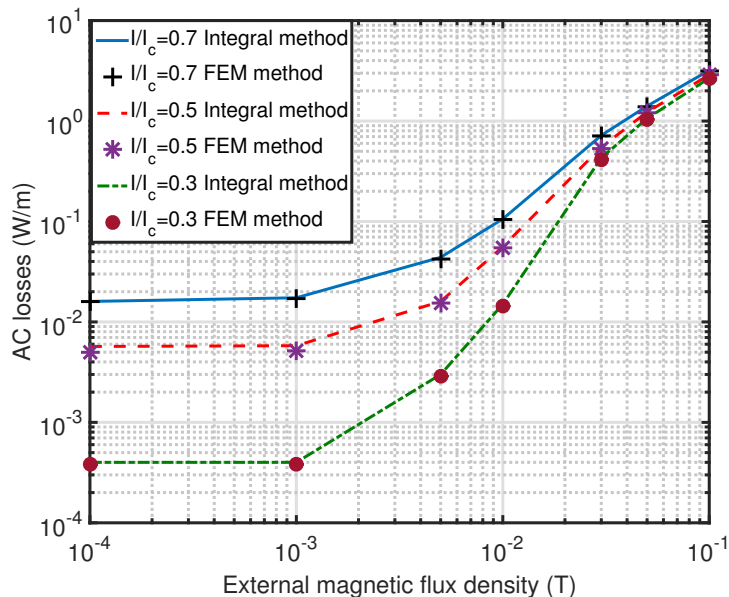


Fig. II.13 – Coupled AC losses for the FEM and integral method. A good agreement is noticeable between the two models.

The same conclusion as above can be drawn here, where an excellent agreement is found between the two methods (less than 10 % in overall). From all these calculations, the two models give close results compared to analytical calculations. In general the observed computation time is reduced by a factor four (4) for the integral method compared to the FEM modeling. Beside these results, a experimental validation has to be made to check the computed quantities with reality.

## II.2.e Experimental validations

With both methods, the implementation of the model is relatively fast and leads quickly to numerous calculations but it is necessary to validate the computed quantities. In this section, the methods are compared to experimental work. The workbench for AC losses measurements on one tape is presented followed by some results.

### II.2.e-i Measurement protocol

The measurement is made electrically by acquiring the voltage along the superconducting sample (Superpower sample). The electrical circuit is shown in Fig. II.14.

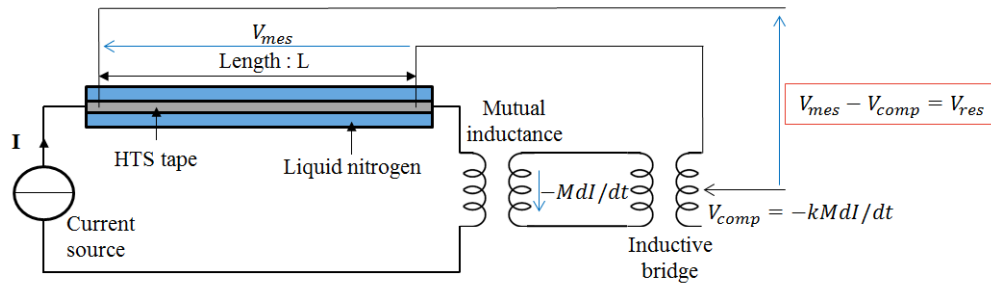


Fig. II.14 – Experimental workbench for the measurement of AC losses at 77 K on superconductors.

The typical length for the measurement is between 200 mm and 300 mm. To ensure a good contact resistance for the voltage tapes, different methods including silver paste, tin or press contacts have been used. No difference has been noticed between these three. The experiment is carried out in an open batch of liquid nitrogen as shown in Fig. II.15.



Fig. II.15 – Sample in the nitrogen bath.

To inject a transport current with different waveforms and amplitudes, a GBF driving 10 KEPCO® power linear amplifiers has been used. The rated current and voltage of each KEPCO are respectively 20 A and 20 V. These power amplifiers are capable of providing each 20 A (in total 200 A) from DC to AC signals up to 2 kHz. Above this value of frequency, the power amplifiers are not capable to inject their rated current due to the inductive voltage of the circuit. A view of the power supplies with the GBF can be found in Fig. II.16.

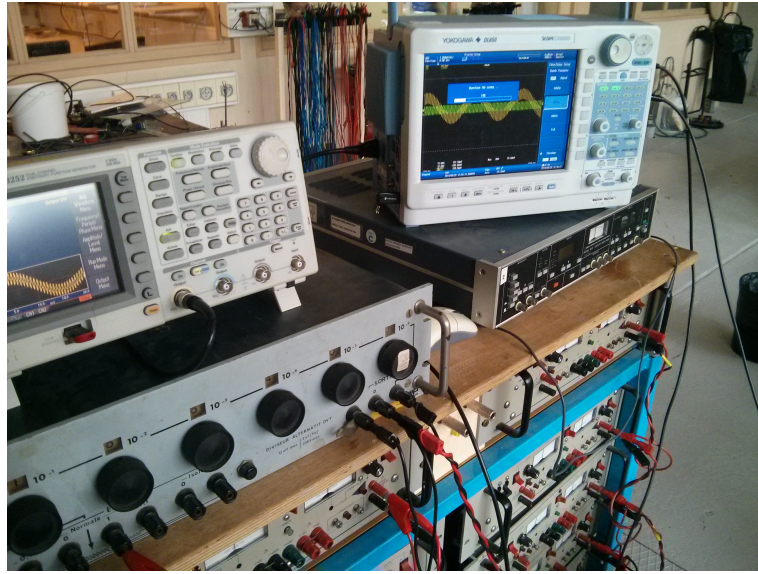


Fig. II.16 – GBF and KEPCO power supplies.

The voltage measurement on the HTS tape  $V_{mes}$  is the summation of the loss voltage  $V_{res}$  and the inductive voltage  $V_{ind}$  created by the inductance  $L$  of the power circuit.  $V_{mes}$  can be expressed as :

$$V_{mes} = V_{res} + V_{ind} = V_{res} + L \frac{dI}{dt} \quad (\text{II.2})$$

To suppress the inductive voltage, different methods can be used, for example using a lock-in amplifier to acquire the signal in phase with the current or a manual compensation of the inductive voltage. This one was chosen as a mutual inductance was designed in the Néel Institute few years ago. From the mutual inductance a signal proportional to the time derivative of the current  $MdI/dt$  is acquired and then subtracted to the measured voltage. To ensure a good compensation and have a more precise measurement of  $V_{res}$  (it is unlikely than  $M=L$  directly), an inductive bridge is used to add a gain  $k$  to the product  $MdI/dt$ . Hence, the voltage subtracted from  $V_{mes}$ , after a complete compensation, is  $V_{res}$  defined as :

$$V_{mes} = V_{res} + L \frac{dI}{dt} - kM \frac{dI}{dt} = V_{res} \quad (\text{II.3})$$

The value of  $k$  was adjusted with the inductive bridge to obtain a loss signal in phase with the current. This setting is done manually and may lead to some error on losses calculations. To overcome this issue, the result was checked by also doing some post processing on the experimental data.

In Fig. II.17 and Fig. II.18, the loss voltages are plotted with the current for a sinusoidal and triangle waveforms. The two signals have been obtained after the compensation of the inductive voltage with the mutual inductance and the bridge.

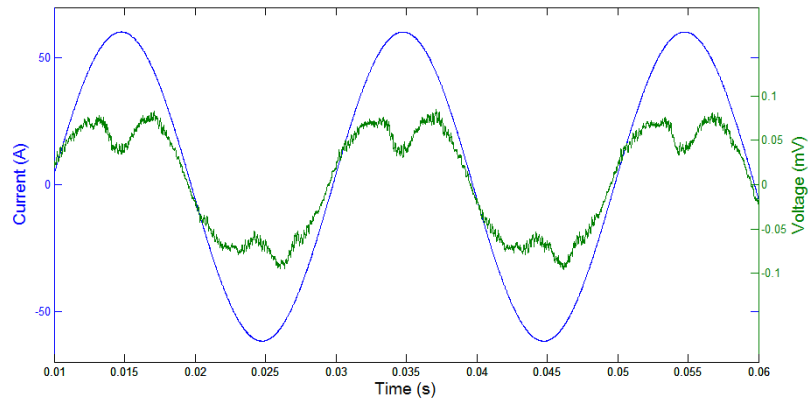


Fig. II.17 – Loss voltage and current for a sinusoidal waveform.

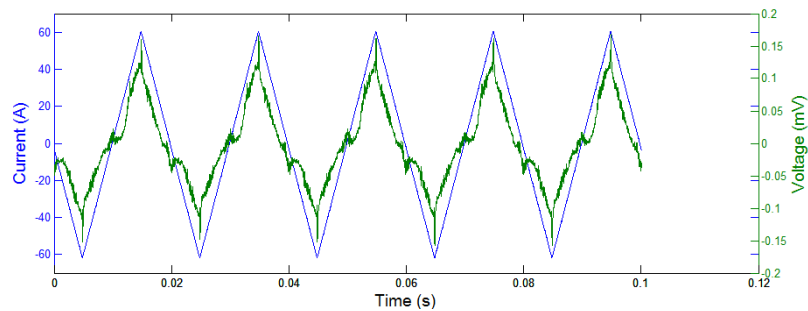


Fig. II.18 – Loss voltage and current for a triangle waveform.

### II.2.e-ii Single tape results

The Superpower tape was measured with different current amplitudes, waveforms and at diverse frequencies. The current injected inside the tape was comprised between 20 A and 100 A which corresponds to a reduced current between 15 % and 78 %. The self-field AC losses function of the peak current for a sinusoidal signal of 50 Hz are displayed in Fig. II.19. In these cases, only the FEM has been used as the section before showed the good agreement between integral method and FEM models for self-field AC losses.

In the FEM method, the power law and the percolation law have been used to check the accuracy of each E-J fits with the experiment. From Fig. II.19, the plotted AC losses are very close to each-others with a very good agreement between the experiment and the percolation law. The observed difference is less than 8 % while, with the power law formulation, the difference is less than 12 %. These calculations help validate first the FEM model but also the two E-J fits. As the integral and the FEM models give close results in self-field AC losses, these results can be extended and confirm the validity of the integral method. In these measurements, the percolation law seems to be closer to the power law and was kept for the following simulations. According to analytical calculations presented in I.5.a, the self-field hysteresis losses are proportional to the frequency as it can be observed in

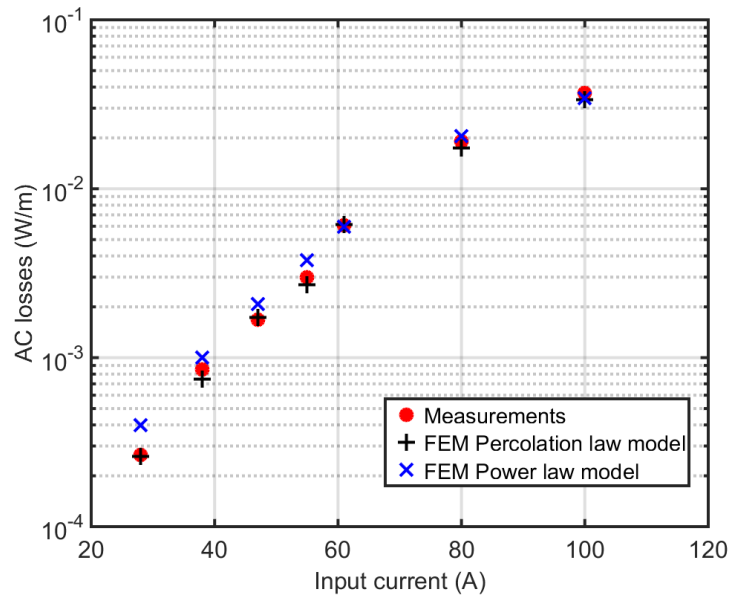


Fig. II.19 – Self-field AC losses versus input current for the SuperPower tape.

Fig. II.20 for a sinusoidal current with two different peak values.

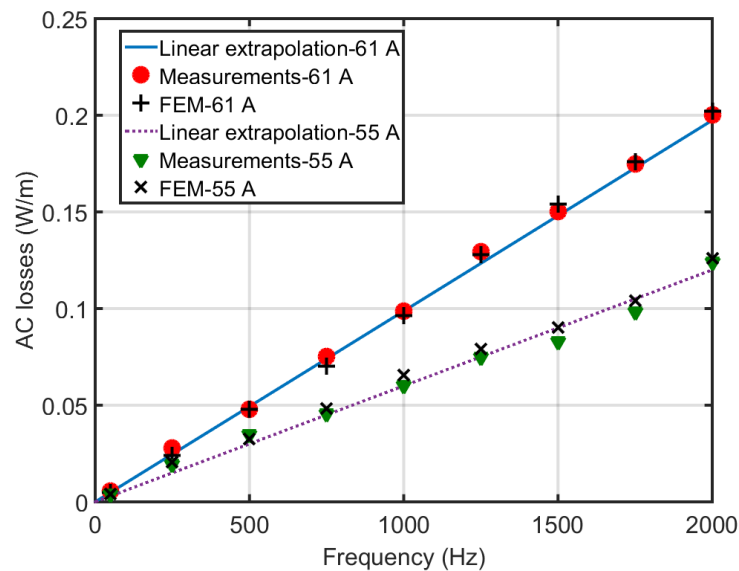


Fig. II.20 – Self-field AC losses versus frequency for a sinusoidal signal with a peak value of 61 A and 55 A. The results of the FEM model with the percolation law are also plotted.

Once again, the results of the numerical model and the measured quantities are very close from one to another (the difference is less than 6 %). The linear dependency of the AC losses with the frequency is validated. In analytical calculations following the Bean model, the current waveform does not influence the value of AC losses. This feature was numerically validated with simulations with the power law model with a  $n$  of 5 000. However, as

HTS tapes exhibit a smoother transition behavior, some differences can be observed with different waveforms. In Fig. II.21, the AC losses for a sinusoidal and a triangle currents with both a peak value of 61 A are plotted versus the frequency. Both measurements have been validated by COMSOL (error less in average than 5 %). The observed difference of AC losses per cycle (slope of the linear curve) is in the order of 20 % between sinusoidal and triangle waveforms.

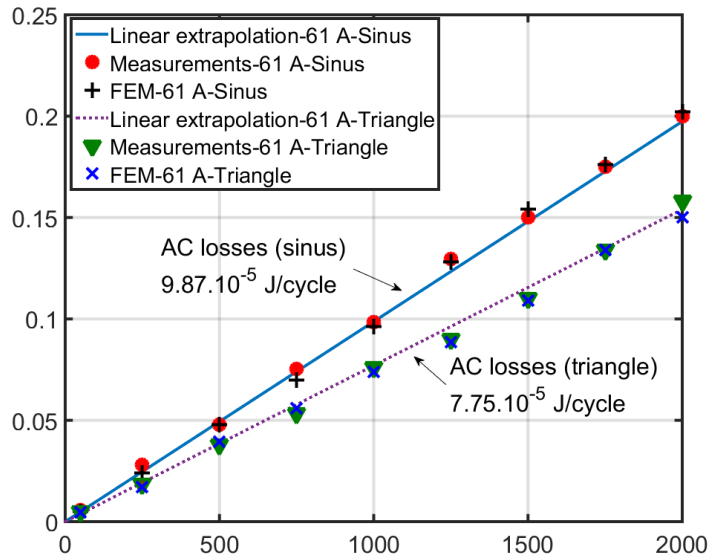


Fig. II.21 – Self field AC losses versus frequency for a sinusoidal and triangle signals with a peak value of 61 A.

In these measurements, good agreement has been observed between the FEM model and the experimental work. The error margins can be explained as some hypothesis have been made : fixed critical current over the length for the numerical model, noises of measurements or non-perfect compensation of the inductive voltage for the experimental part. The two different laws to represent the conductor characteristic have been tested and exhibit close results compared to measured quantities. However, a better correlation for the percolation law is noticeable. The measurements were also successfully validated with various current waveforms. It proves that the Bean model is not fully effective for HTS tape as the AC losses for different waveforms lead to diverse AC loss values.

In conclusion, this first series of tests reinforce the reliability of the model. Furthermore, the FEM method is validated by measurement and because the integral method and the FEM give results close to each-other, the two models are validated.

## II.2.f Conclusion : from tapes to round wires

In this section, numerical models with various methods have been developed for the calculations of AC losses in HTS tapes. Self-field AC losses have been measured and com-

pared with the results from the numerical calculations to validate the computed quantities. The models are in excellent agreement with the measurements. The next step would be to increase the size of the problem to achieve the modeling of a full size devices. Another perspective is to couple finite element modeling with integral methods to take into account the shunt layers. In addition to these developments, extended measurements should be done to validate more complicated cases such as fast ramps of current or faults inside superconducting devices.

However, in applications like compact power cables, tapes are not ideal. Round wires would be much easier to form into compact assembly (see I.4.a-ii). The numerical models, which were developed for tapes can be adapted to round wires. As these wires do not yet exist, no experimental work has been made and no validation of the calculations is possible. The numerical models were validated prior with HTS tapes and the fact that the results are close to experiments makes us confident about the computed quantities for round wires. Moreover, analytical calculations exist (see I.5.a-iii) and can be used to validate (as a first step) the calculations.

## II.3 AC losses in HTS round wires

Adapting the numerical models from HTS tapes to round wires is not difficult as they use both 2-D cartesian coordinates. Considering the round structure of the wire, the use of rectangle elements can bring error on the AC losses calculations and the sensitivity of the mesh has to be studied. After a description of the numerical models for the studied round wire, the same methodology as the one made for the HTS tapes is used along this section to validate the mesh and the removal of the shunt layers. The self-field and external field losses are then computed, followed by combined AC losses.

### II.3.a Model description

The geometry and physical properties were based on the preliminary work made in the EUROTAPES project [65]. The geometry was extracted from the sketch presented in Fig. II.22.

The geometric parameters are summarized in Table. II.2.

Parameters	values
Inner radius ( $\mu\text{m}$ )	900
Superconducting layer ( $\mu\text{m}$ )	2
Nickel layer ( $\mu\text{m}$ )	50
Copper layer (total) ( $\mu\text{m}$ )	100

TABLE II.2 – Geometric parameters for the round wire.

The process starts from a HTS tape of 6.5 mm width in order to produce a wire with a 0.9 mm inner radius. The initial tape has a critical current between 150 A and 180 A since a decrease of 30 % is foreseen for industrial wires. Hence, the critical current of the

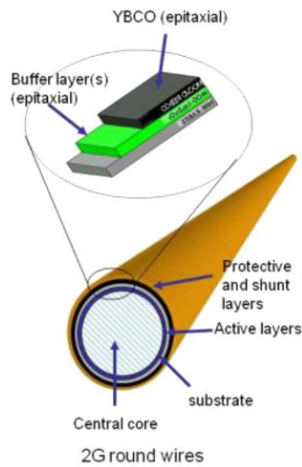


Fig. II.22 – HTS final wire design for the EUROTAPES project [65].

final wire was estimated at 130 A. Concerning the E-J relationship, the percolation law has been used at first for the AC losses calculation because it generates results closer to measurements on tapes. Some simulations with the two E-J laws have also been performed. The superconducting properties of the wire, as well as, the properties of the metallic layers were kept the same as the HTS tapes and summarized in Table II.3. A copper layer is added in the design and we took a value of RRR at 30 (choice arbitrary made to see the current distribution in the layers).

Quantities	values
Critical current (A)	130
$J_c$ ( $A/m^2$ )	$1.15 \cdot 10^{10}$
$J_{c0}$ ( $A/m^2$ )	$1.13 \cdot 10^{10}$
n value	30
$n_0$ value	10
$\rho_{Hastelloy}$	$1.26 \mu\Omega.m$
$\rho_{silver}$	$0.1 n\Omega.m$
$\rho_{copper}$ [158]	$0.85 n\Omega.m$

TABLE II.3 – Round wire superconducting and metallic properties.

Even if this wire is considered for large scale applications cooled down with liquid Nitrogen, the electrical resistivities of the shunt layers were set to the same values as before. These results on the current ratio in the layers should not change drastically with an increase of the operating temperature from liquid Helium to liquid Nitrogen as the resistivities of the layers increase with an elevation of the temperature.

## II.3.b FEM modeling

### II.3.b-i Meshing

As it was explained for the HTS tapes, using triangles to mesh the superconducting and shunts layers would lead to a non-manageable number of elements rendering the simulations impossible to solve in reasonable times. However, even if the radius of curvature  $R=1/(0.9 \text{ mm}) \approx 1000$  is not infinite, the use of rectangles may lead to the creation of distorted elements in the mesh leading to issues of convergence and miscalculation of the losses. It is necessary to know how fine the mesh should be to calculate properly but also rapidly the AC losses for a round wire. These result can afterwards be extended to multiple wires. The number of elements on the inner layer of superconducting thickness is denoted  $N_{perimeter}$  and the number of elements inside the thickness is  $N_{thickness}$ . These two values are represented in Fig. II.23.

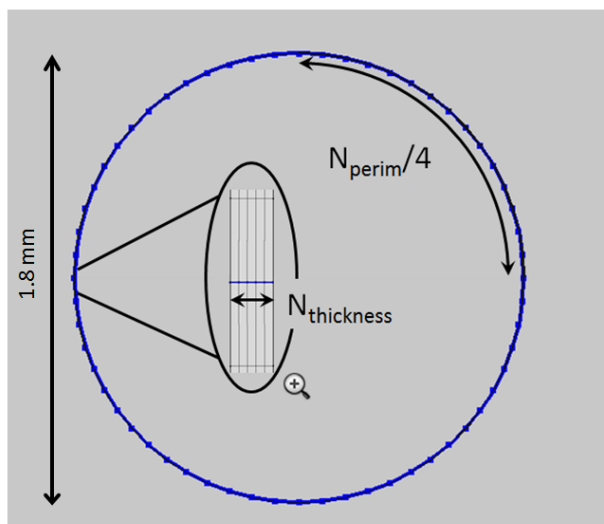


Fig. II.23 – Definitions of the mesh parameters based on the geometry.

Some pictures of the mesh are given in Fig. II.24, the air outside but also in the core of the round wire is meshed with triangles. In the figure, only one layer is represented but the mesh can be extended to all the other layers. All the layers including copper, silver and Hastelloy have been meshed with rectangles.

Some parametric studies have been carried out with several values of  $N_{perimeter}$  and  $N_{thickness}$ . A sinusoidal current with a frequency of 50 Hz was applied to the conductor with a peak value of 91 A (70 % of the critical current). AC self field hysteresis losses are displayed in Fig. II.25a compared with the analytical calculation in (I.31). In Fig. II.25b, the computation times associated to these calculations are shown. Self-field losses calculations have been chosen because the current densities are located inside the superconducting thickness going from the outer to the inner layer. In this case no homogenization of the thickness is possible.

From these simulations, one point can be noted : the AC losses do not vary much with

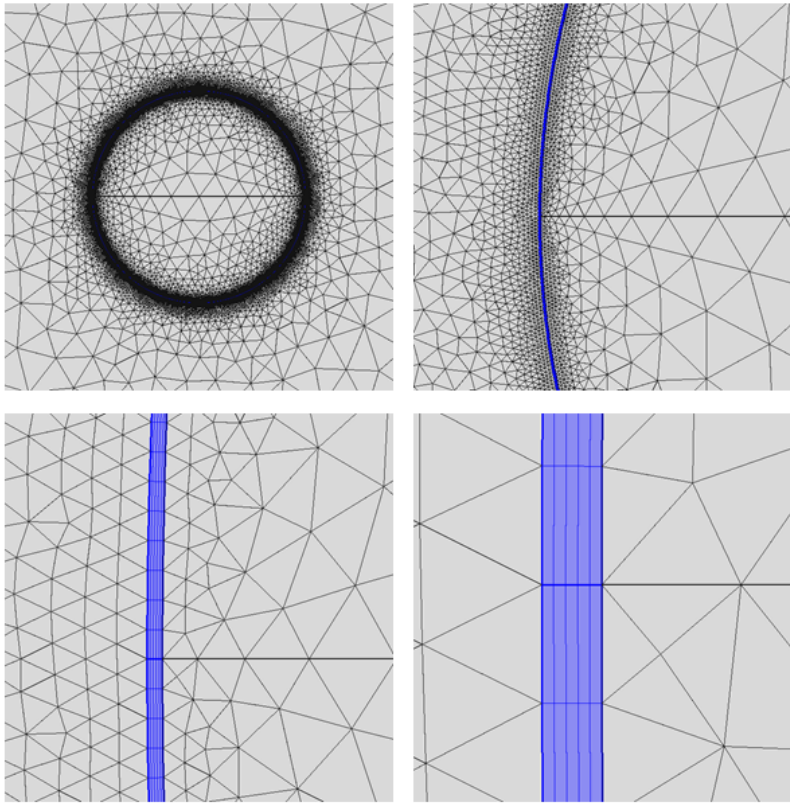


Fig. II.24 – Meshing of the round wire.

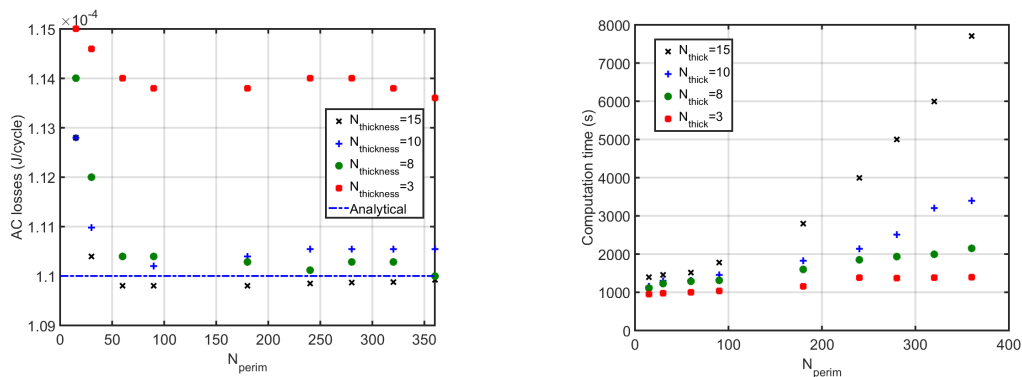
(a) AC losses calculations with respect to  $N_{perim}$  and  $N_{thickness}$ . (b) Computation time associated to the calculations.

Fig. II.25 – AC self field losses for the HTS with parametric studies on the mesh.

a variation of  $N_{thickness}$  but also with a change of  $N_{perimeter}$  (above 50). This property is not easily deducible because the current densities develop inside the thickness of the superconductor. On the other hand, an increase of the number of elements in the perimeter leads to a large increase of the computation time as the number of DOF is increasing rendering the problem heavier to solve. With a number of  $N_{perimeter}$  comprised between 0 and 200, the change of  $N_{thickness}$  does not have so much influence on the computation. At high values of  $N_{perimeter}$ , the change is noticeable. In conclusion, as it was expected, the

number of elements in the thickness in the most important as the current penetrates in a non-uniform way in the conductor thickness. For external field AC losses, as the current is uniform in the thickness; the results should not change with variation of  $N_{thickness}$  and the same trend of the losses with the change of  $N_{perimeter}$  should be found.

### II.3.b-ii Effect of metallic layers in loss calculations

As it was made on the HTS tape, simulations have been performed with all the layers (except the buffer layer) to calculate the current ratio in each layer when a transport current is applied. Fig. II.26 shows the current ratios (current in the layers divided by the total current) with various transport current values. In the figure *copper 1* is corresponding to the inner part of the RW and *copper 2* the outer copper layer of the RW. The current was purposely set to values above the critical current to see the distribution of current in the wire. At first no thermal equation has been solved.

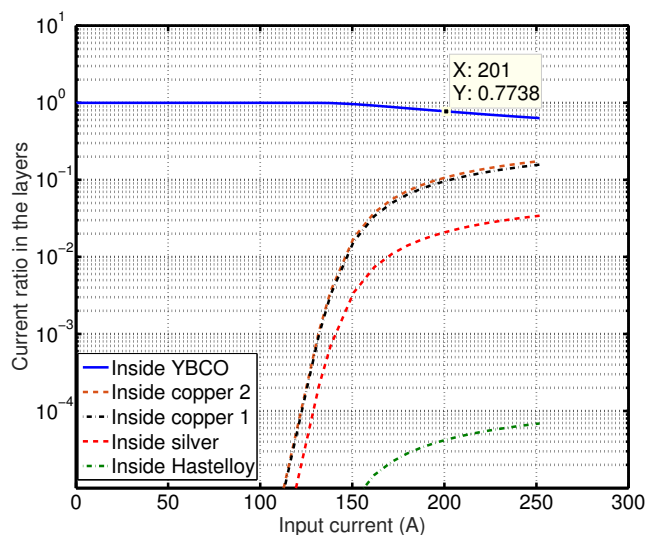


Fig. II.26 – Current ratio in each layer versus input current for the round wire (no heat equation) with a ramp current of 10 A/s ( $I_c=130$  A).

As it was expected and according to previous results, the current goes almost exclusively inside the superconducting layer for currents below the critical current. When this value is reached and as no thermal equation is solved, the current goes inside the layers with the lowest resistance, in this case, the copper but also the silver layers. Current is going more inside the *copper 2* layer than the *copper 1* as the section of *copper 2* is bigger than that of *copper 1*. In the model, the contact between the layers are supposed to be perfect (no contact resistance), which is not the case in reality. However, these results should not change drastically if these resistances are taken into account. The simulations was performed by solving the thermal equation similarly to the work done for the HTS tape in II.2.c-i. Fig. II.27 displays the current ratio in all the layers with the solving of the thermal equation and the decrease of the current density with temperature (same trend as the HTS tape).

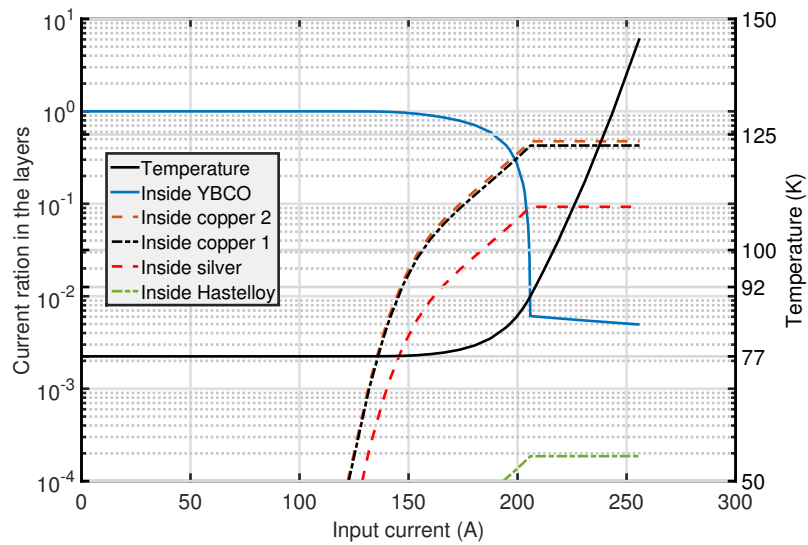
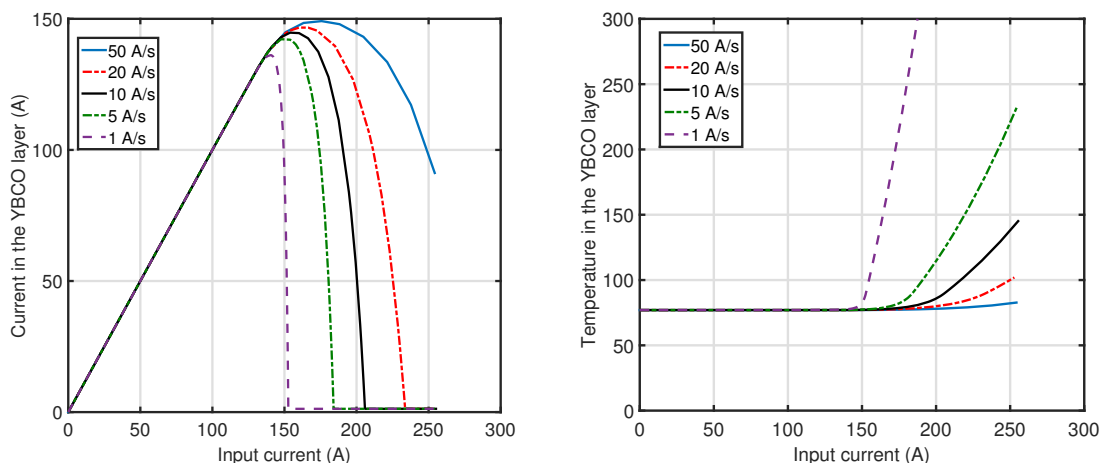


Fig. II.27 – Current ratio in each layer versus input current for the round wire (with heat equation).

The same conclusion can be drawn as it was for the tape. Below the critical current, the input current goes almost exclusively in the superconducting domain. With values of currents above  $I_c$ , the current is going into the shunt layers which increases the overall temperature of the wire. This increase of temperature decreases the critical current. The addition of copper layers helps with the thermalization of the tape and reduces the temperature in the tube when high currents are flowing into the wire. Fig. II.28a and Fig. II.28b display the current in the YBCO layer and the associated temperature with various speed rates of input current.



(a) Current in the YBCO layer for various speed. (b) Associated temperature in the YBCO layer.

Fig. II.28 – Current ratio and associated temperature for various current speeds.

The faster the current ramp the lower the hot spot temperature and more current can circulate in the YBCO layer in the dissipative state. From these simulations and similarly as before, the superconducting layer is kept and all the others layers are removed from the numerical model which leads to a simpler model in terms of number of elements.

### II.3.b-iii AC self-field losses

Self-field AC losses were calculated by considering a sinusoidal transport current with a peak value between 10 % and 90 % of the critical current (between 13 A and 117 A) and a frequency of 50 Hz. The analytical calculations in Eq. (I.28) are confronted to the numerical results in Fig. II.29. Additionally from these quantities, the AC losses of a HTS tape (see equation (I.22)) with the same critical current have been plotted [159].

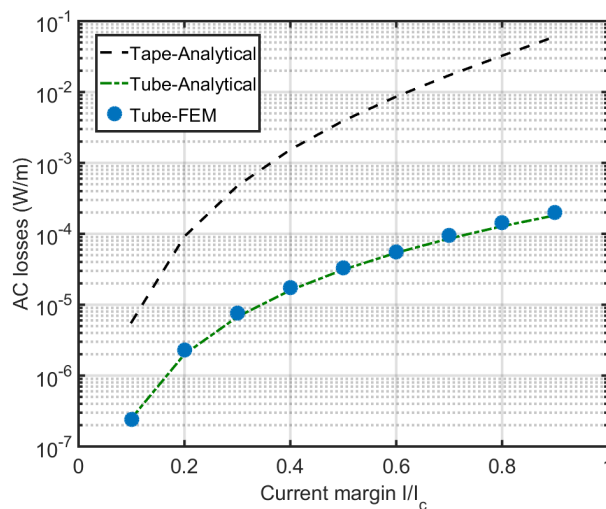


Fig. II.29 – Self-field losses in the RW and in a tape with the same properties.

From this figure, two major results can be deduced. First the analytical and numerical calculations are very close to each other. This conclusion is similar to what has been observed with the calculations made on a HTS tape (the difference is less than 8 %). Secondly, as it was predicted by literature, the round wire dissipates less losses compared to the tape.

### II.3.b-iv External magnetic field AC losses

In a power cable, HTS wires would be subjected to an external field generated by the surrounding neighbors. With high current cables in compact spaces, the value of magnetic flux density induced on the wires can be a few hundreds of millitesla. The numerical calculations have been done first with external magnetic field (no transport current). Results of AC losses calculations with a constant current density are represented in Fig. II.30 with analytical calculation for the round wire (Eq. (I.29) and Eq. (I.30)). In comparison, the analytical computation of AC losses created by an external field applied on a HTS tape are also plotted (width of the tape equals to the perimeter of the round wire) with parallel field and perpendicular field (see Eq. (I.24)).

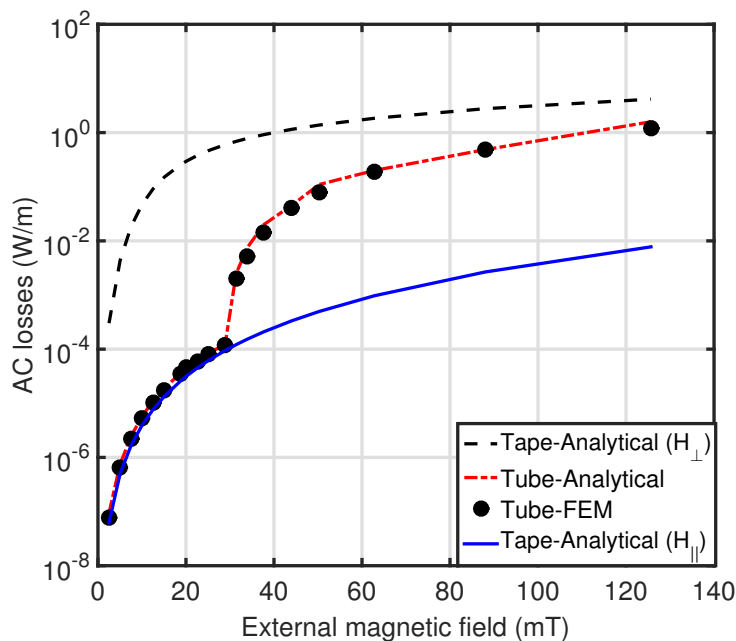


Fig. II.30 – External magnetic field losses dissipated in the RW and in a equivalent HTS tape with the same  $I_c$  (and  $J_c$ ).  $\perp$  is referenced as field perpendicular to the flat surface of the tape,  $\parallel$  is the field parallel to the flat surface.

One can notice the sudden raise of the losses when the external magnetic field reaches the threshold value of 30 mT. This value of field can also be calculated (only with no transport current superposed to the field) analytically :  $B_{p-analytical} = \mu_0 J_c e = 37$  mT. This is due to the full penetration of the current inside the superconducting layer. For amplitudes lower than 30 mT, the round wire screens the magnetic field and the losses appear to be equivalent to HTS tape under the action of a parallel magnetic field. When the value of 30

mT is reached and overcome, the magnetic field penetrates inside the tube which leads to an increase of the losses by a factor of almost 100. The current density distributions and the magnetic flux lines are shown in the case of no penetration in Fig. II.31a and in the case of penetration in Fig. II.31b. The superconducting layer has been purposely enlarged in this figure to see the phenomenon.

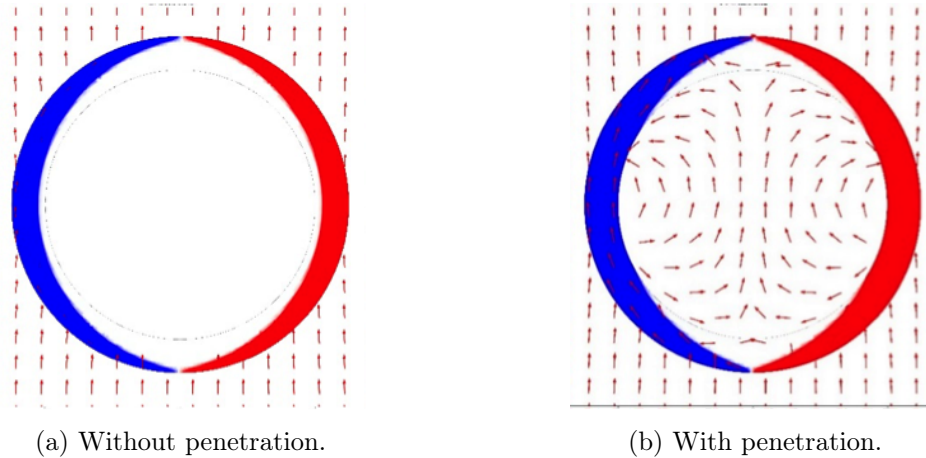


Fig. II.31 – Current density distributions and flux lines for the case without (a) and with (b) penetration. In red is plotted  $+J_c$  and in blue  $-J_c$ .

### II.3.b-v Combined AC losses

This part has been largely motivated by the fact that no analytical calculations are available for the round wire exposed to a transport current and external field. Calculations of a round wire exposed to a transport current and external magnetic field are computed in Fig.II.32. In the figure, the AC losses are plotted versus the amplitude of external magnetic field with different  $I/I_c$  ratio. The external field and transport current waveforms are in phase.

Two regimes are noticeable according to what was shown before : the first regime at low fields where the transport current is the main mechanism of dissipation. After the round wire is locally fully penetrated, the AC losses are mainly created by the AC external field. It is worth noticing that the AC losses increase, with the rise of the transport current at a given external field amplitude because the penetration field is reduced with the addition of transport current. For a viable use of the HTS tube, it seems compulsory to avoid any penetration by reducing the amplitude of the external magnetic field seen by the tubes. The limit domain is identified in Fig. II.33.

According to Fig. II.33, the penetration field of the round wire is comprised between 28 mT to 5 mT from  $I/I_c=0$  to  $I/I_c=0.8$  respectively. The AC losses in a power application where conductors are generating an external field on their neighbors, the AC losses will be mainly created by the external field (but also the transport current).

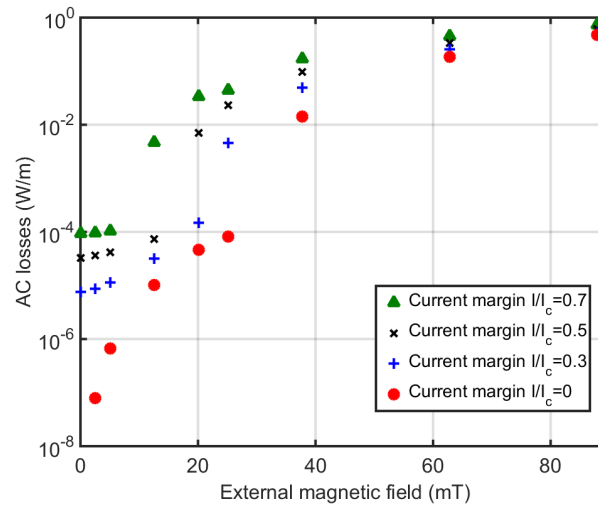


Fig. II.32 – AC losses induced by a transport current and an external magnetic field in phase.

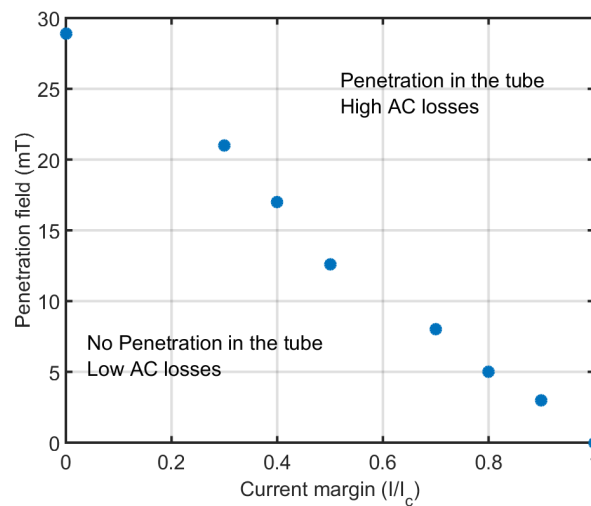


Fig. II.33 – Penetration magnetic flux density for a round wire with a constant  $J_c$ .

### II.3.b-vi Comparison of different E-J power laws

Simulations of the two power laws have been performed on various number of cases for the AC losses in the round wire in self-field and external magnetic field. Even if the percolation law exhibits results closer to experiments, it is interesting to compute and confront the results of the E-J power law with the percolation law. At first the self-field AC losses are calculated with the two power laws with input data from Table. II.1 and displayed in Fig. II.34a. External AC losses are displayed in Fig. II.34b.

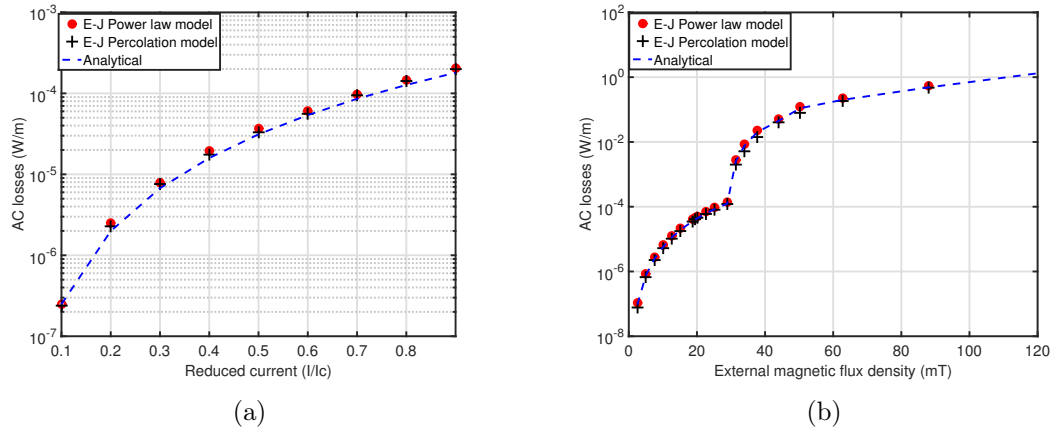


Fig. II.34 – Comparison between the two power laws for self field (a) and external magnetic field (no transport current) (b) AC losses.

The difference between the two E-J formulation is once again in the order of 5 % overall. The power law results are 13 % different from analytical calculations in average. It is also noticeable that the percolation law is closer to the analytical calculations, which is explained as the percolation E-J law is closer to the power law than the Bean model. However, the two models are very close to the analytical calculations which gives us confidence in the computed quantities.

### II.3.b-vii AC losses in RW with anisotropic properties of the critical current

The inherent anisotropic properties of HTS have to be taken into account, for realistic AC losses calculations. As it was detailed in the section presenting the conductor (see Fig. II.1 and Fig. II.2 ), the implementation of the critical current regarding the incident field angle and field values has been done and confronted to the AC losses with a constant critical current density. Self-field AC losses and external field AC losses are displayed in Fig. II.35a and Fig. II.35b for the E-J percolation law and in Fig. II.36a and Fig. II.36b for the E-J power law.

From these simulations, the self-field AC losses are only impacted with a very little difference (about 3 %) whereas the AC losses due to an external magnetic field increase by 15 %, if we take into account the critical current as a function of the field. These results are coherent as the self field AC losses should not be impacted as much as the external field AC losses (very little field is created in self-field scenarios). Overall, the complexity of the model taking into account the dependency of the critical current leads to an increase of the computation time by 30 %. These calculations show that the anisotropic behavior can be neglected as only small variations of losses are noticed compared to the increase of computation times. As these round wires will be used for applications such as power cables, the magnetic field produced by the wires is less than 1 T, in this range the error is less than 5 %. Hence, the critical current as function of the magnetic field can be assumed as a constant critical current for AC loss calculations.

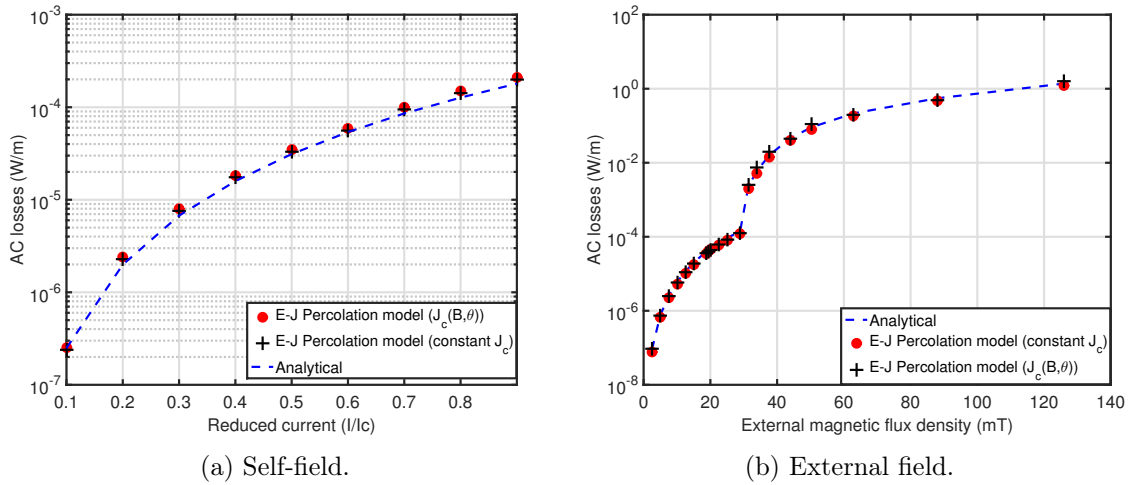


Fig. II.35 – Comparison between a constant critical current density and a field dependent anisotropic critical current density with the E-J percolation law.

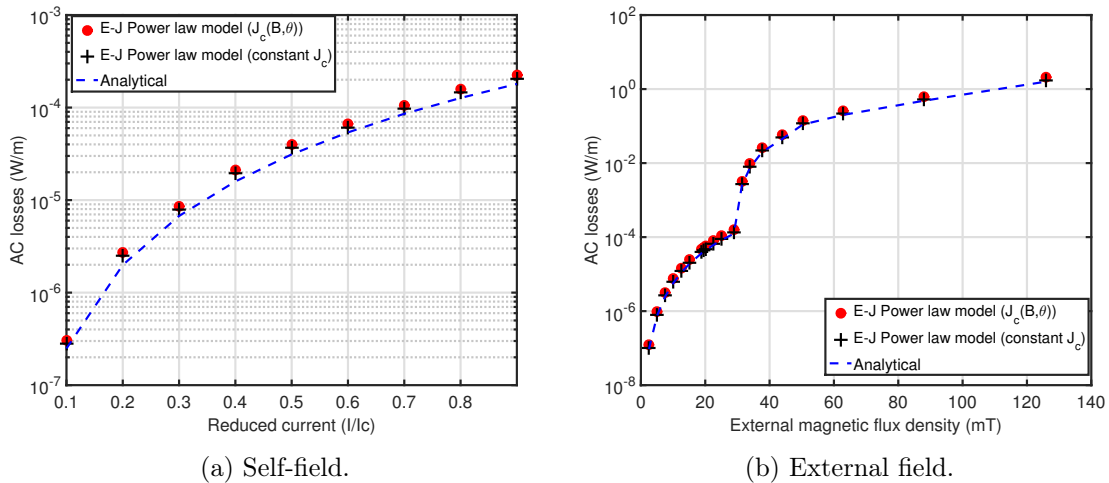


Fig. II.36 – Comparison between a constant critical current density and a field dependent anisotropic critical current density with the E-J power law.

### II.3.c Integral method

The integral method was also adapted for the round wire model and tested. In self-field simulations, the current will penetrate inside the thickness of the superconducting layer which violates the use of the integral method representing the tape as one line. However, when the wire is exposed to an external field, the current density is homogenous inside the thickness as soon as there is total penetration of current density in the layer. From previous calculations in Fig. II.33, we established the low penetration field of these wires. The integral method was adapted to round wires by developing in 2-D the constitutive equation Eq. (I.43) and confronted to the calculations obtained by the FEM model.

### II.3.c-i Self-field AC losses

In self-field AC losses, it is not possible to use the integral method with only one line representing the superconductor. To validate these losses, it is possible to use a summation of several lines as it is in a FEM mesh. A picture of the test model for self field AC losses is represented in Fig. II.37 confronted to the FEM mesh. In the integral methods, the air is not meshed, which decreases the size of the model.

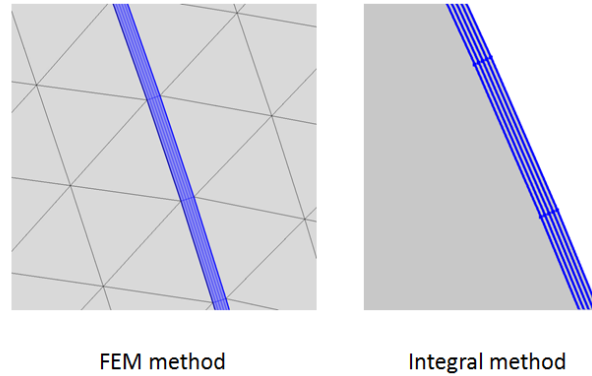


Fig. II.37 – Comparison of the mesh for self field AC losses. In (a) the mesh of the integral method, in (b) the mesh for the FEM model.

The self-field AC losses for sinusoidal current in 50 Hz are displayed in Fig. II.38. These results are compared to analytical and FEM calculations.

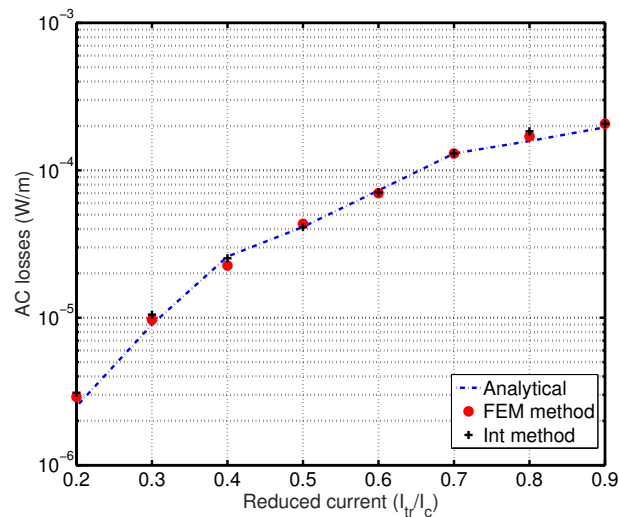


Fig. II.38 – Self-field AC losses for the integral method. The results from FEM and analytical calculations are also plotted.

The losses of the integral method are in a good agreement with a difference less than 5 % if we consider 5 layers. These simulations validate the integral method in the case of transport current in the round wire with this architecture. This result is the one expected

according to Fig. II.25a, where it was possible to see that, with a discretization of 5 in the layer thickness, the AC losses were close to the analytical calculations. It is noticeable that the computation time for the integral method is divided by a factor 2 compared to the FEM method. This is mainly because the air is not meshed.

### II.3.c-ii External magnetic field losses

When the round wire is subjected to an external magnetic field, above the penetration field, the current density will be uniform in the superconducting thickness. In the scenario where only an external magnetic field is applied, the simulations may be done with only one layer for the integral method. It means that, below the penetration field, the computed AC losses will be wrong but as soon the penetration field is reached the computed AC losses should be in agreement with the FEM method.

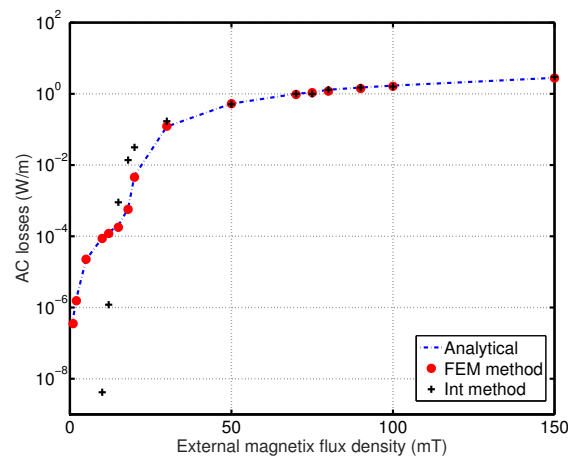


Fig. II.39 – AC losses generated by an external magnetic field for the FEM and the integral method.

The same conclusion can be extended to these calculations. The results found from the integral method are close to the FEM losses as soon as the current density is uniform in the thickness (above the penetration field). To compute AC losses below the penetration field, it is possible to use the same technique as the one used for self field losses.

### II.3.c-iii Combined AC losses

Finally, the simulations are made in the case of combined AC losses. Fig. II.40 displays the AC losses of the FEM model and the Integral method *with one layer*.

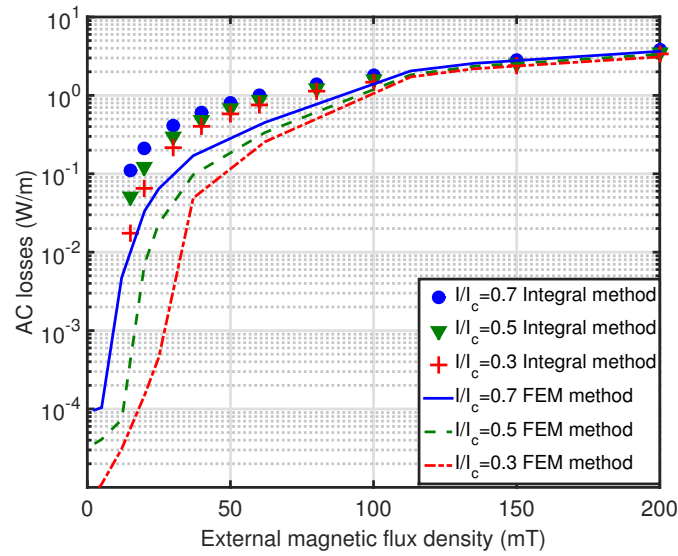


Fig. II.40 – Coupled AC losses versus external magnetic field amplitude. The comparison is made between the FEM and the integral method.

These results show a high difference between the integral method and the FEM model. These results are in agreement with previous calculations (for example Fig. II.25a) which have shown the importance of discretizing the superconducting layer to calculate the current distributions when a current is applied to the round wire. Fig. II.41 shows the calculations of the coupled AC losses with various number of layer for the integral method. In this case, the results are compared to the FEM model (with 5 element in the thickness).

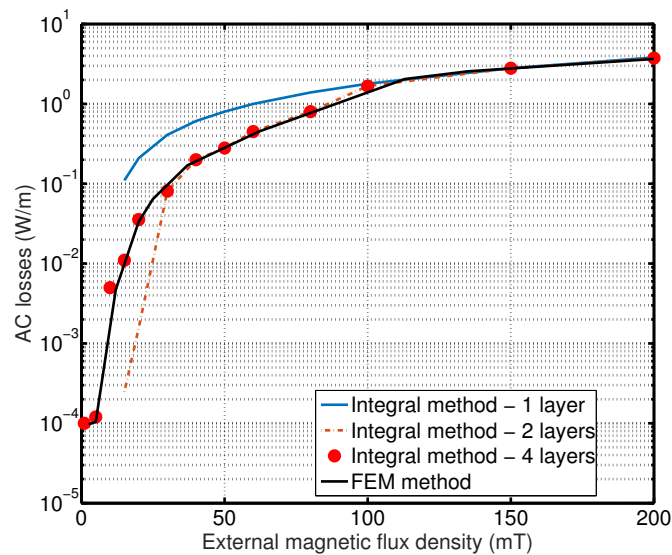


Fig. II.41 – Coupled AC losses function on the number of discretization layer for the integral method ( $I/I_c=0.7$ ).

From these results, to obtain the AC losses with a fair accuracy (difference of less than 5 %) the number of layers of the integral method has to be at least 4. This result is in

agreement with what was shown with FEM calculations regarding the number of element in the superconducting thickness. Even if the use of the integral method helps to decrease the number of unknowns in the system, the calculation times in these cases are not really different (division by 2) from the FEM method. This is explained by the fact that the integral method calculates the interaction between each point to all of the other points of the mesh and this can be an issue for more complicated simulations. This creates full matrices which are very heavy to invert.

The integral method is possible to use for HTS tape in a various number of applications, but is not suitable in the case of combined AC losses in round wires. The AC losses created by the transport current and the external magnetic field can only be calculated with accuracy with the use of the FEM model. In the next section, only the FEM model was used for the design of high current cables. To use the integral method, it would need to use the same artifact made with self field AC losses but with increasing the number of elements. This may be interesting as the computation are reduced by 2 but we loose the elegance of the integral method.

### II.3.d Design perspectives for high current cables

Compact cables in the range of 1 kA to 3 kA using round wires are foreseen. Above these currents, the magnetic field created by the wire will be too high to be competitive. One very simple example can be performed for a cable with a reduced number of round wires. Three architectures have been simulated and shown in Fig. II.42. *Geo.1* is a typical cable made with six wires similar to copper cables. This architecture is very simple, but the wires are very close from one to another which induces high external magnetic field values. To lower the field values, some changes to the geometry can be made for example *Geo.2* or *Geo.3*. The cables are supposed to be twisted along the length which leads to the same current going to every wire in each layer. The 2-D approach, which neglect the coupling losses, may give an under-estimated result which has to be studied further. In this section, we only analyze the hysteresis losses behavior on these three architectures.

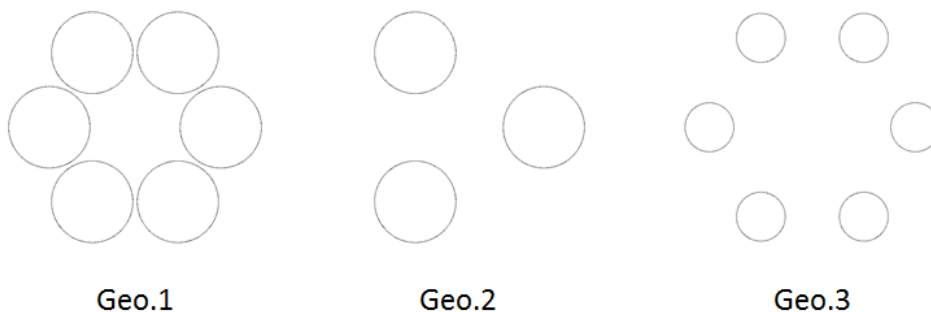


Fig. II.42 – Various architectures for wire cables.

In terms of numerical considerations, the computation time was in the order of several hours. In this case, the critical current was kept constant as taking into account the critical current dependency with external field was leading to a small increase of the AC losses (between 5 % and 8 %). The simulations have been made with various input currents

between 13 A to 117 A per tube corresponding to a reduced current  $I/I_c$  of 0.1 and 0.9. Fig. II.43 shows the AC losses in the three geometries. In all these cases the calculations have been conducted with an AC signal with a frequency of 50 Hz.

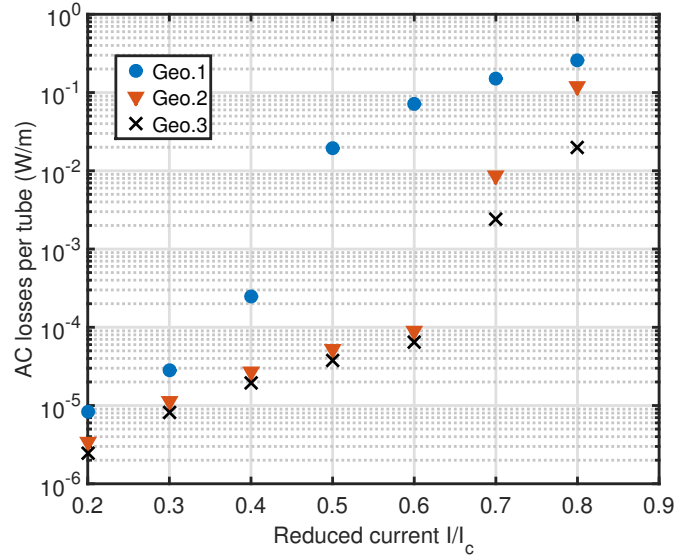


Fig. II.43 – AC losses (in W/m) for the three architectures of cables presented above. The critical current is set at 130 A.

In *Geo.1*, the field created by the wire is rapidly ( $I/I_c > 0.3$ ) above the penetration field which leads to an increase of the AC losses in each round wire. The two other geometries, where the distance between wires is increased, have the benefit of generating less magnetic field. This comes with an increase of the cable cross section. In this case, if the power cable is working with a reduced current of 0.7, the change of geometry from *Geo.1* to *Geo.2* allows a decrease of the AC losses by almost two orders of magnitude. This is interesting as it adds only a second layer of wires. In this example, the cross section is increased by 77 %.

For a more realistic example on a power cable with 18 wires carrying a total current of 1.6 kA. Each wire is carrying 91 A corresponding to a reduced current of  $I/I_c = 0.7$ . At this reduced current, the penetration field is 5 mT. Fig. II.44 shows two different architectures for this cable. *Geo.I* which is the simplest cable made with two concentric layers of round wires but the high value of external field is well above the penetration field and *Geo.II* where the wires have been spread out to have magnetic field less than the penetration field on each wire.

In this example, the AC losses have been calculated at 17.4 W/m for *Geo.I* and  $9.1 \cdot 10^{-2}$  W/m for *Geo.II* with a cross-section increased by a factor five. In DC power applications, as the DC field will induce non homogeneous critical current densities distributions in the round wires, it is likely that the AC losses created by the AC ripple will be very high. The same kind of architecture can be created as *Geo.II* to use these wires efficiently.

As title of comparison, if the 1.6 kA cable was made with 18 HTS tapes uniformly

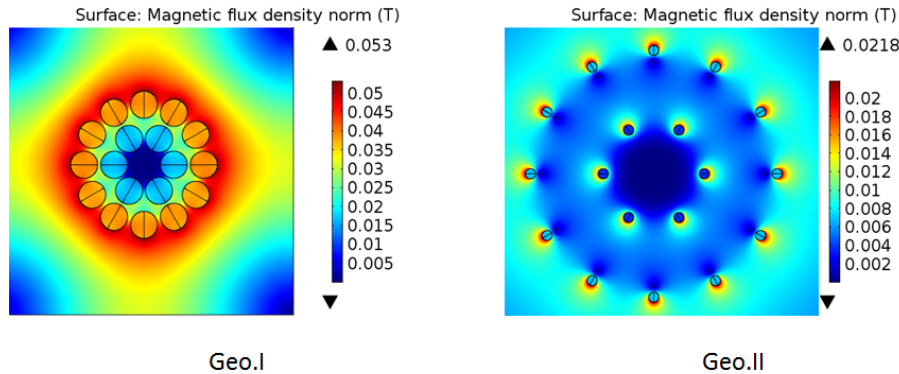


Fig. II.44 – Space necessary to reduce the external field created by each wire below the penetration field for an operating current of 70 % of  $I_c$ .

spread on a circle, the cross section of the cable will be  $408 \text{ mm}^2$  (diameter=22 mm). For the same power cable with 18 wires, the cross section of the cable will be  $314 \text{ mm}^2$  (diameter=20.4 mm).

## II.4 Conclusion

In this chapter, AC losses calculations have been performed for tapes and round wires. The REBCO wires have been investigated with respect to the possibility of achieving applications which require high currents in very compact spaces. Two numerical models have been developed to calculate AC losses on various cases and geometries. These two models have been compared with experimental work with a excellent correlation. The development of these methods has been done in parallel as they both have advantages and drawbacks but they complement one another. From these calculations, it is possible to select a method regarding the type of geometry we are dealing with and the hypothesis that we are willing to take.

The FEM method is highly powerful and is capable to solve with high efficiency complicated problem with a large number of elements. The implementation of the superconducting solving with the H formulation is fast in COMSOL and may lead to quick calculation on very simple geometries. Unfortunately this method is only limited by the complexity of the model. The number of HTS tapes in a large scale application can be more than a thousand and in these cases the meshing of the complete system including the air is not reasonable. One solution can be to use integral methods which have the advantage of not meshing the air or inside the conductor thickness. This method is only valid if the hypothesis of homogenous current is respected.

For round wires, the two methods can be used (not in all cases), but the FEM model is more adapted. This is firstly explained by the computation time which is acceptable for a reduced number of conductors (less than 30). In addition, the current distributions in the case of coupled current and external field is not fully homogenous and leads to the invalidity of the integral method. However, the calculations of AC losses have been made

on these round wires. The results show the importance of reducing the external magnetic field on the wires as the AC losses are highly dependent on it. The promise of creating very high compact cables is dependent on this feature as the penetration field is comprised between 5 mT and 30 mT which require the wires to be distant one from each other.



## Chapter III

---

# Multi-filamentary 3-D AC losses modeling

---

### CONTENTS

---

III.1 MODELING 3-D MULTI-FILAMENTARY GEOMETRIES . . . . .	88
III.1.a On the necessity of numerical modeling for AC loss calculations . . . . .	88
III.1.b Comparison of 2-D and 3-D models for multi-filamentary geometries . . . . .	89
III.1.c Softwares used for the numerical benchmark . . . . .	90
III.1.d Problem description . . . . .	91
III.2 THREE FILAMENT BENCHMARK MODEL . . . . .	92
III.2.a Model description . . . . .	93
III.2.b Results . . . . .	95
III.2.c Impact of the E-J relationship on AC losses calculations . . . . .	104
III.2.d Optimization of the numerical solving process . . . . .	105
III.2.e Conclusion of the three filament benchmark . . . . .	107
III.3 $MgB_2$ MULTI-FILAMENTARY WIRES . . . . .	107
III.3.a Model description . . . . .	108
III.3.b Experimental characterization . . . . .	109
III.3.c Preliminary numerical studies . . . . .	119
III.3.d AC losses for complete $MgB_2$ wires . . . . .	125
III.3.e To go further . . . . .	129
III.4 CONCLUSION . . . . .	129

---

### Summary

*AC losses calculations on 2-D problems are relatively easy to implement and fast to solve. Their predictions are validated by experiments with good agreements. However, in some cases, to calculate with accuracy the AC losses in a multi-filamentary conductor, the use of a fully 3-D model is necessary. This is due to the coupling phenomenon of the twisted filaments inside a resistive matrix. This phenomenon is occurring when the conductor is exposed to transverse external magnetic field. Besides the problem of formulations which can induce non-physical quantities in the solution, the increase of the number of elements makes the problems heavier to solve and time consuming. To simulate a  $MgB_2$  wire, a full 3-D model including the electrical properties of the metallic matrix has been solved. To test the software and the reliability of our models, a benchmark has been made to assess and investigate the problems appearing in 3-D calculations and check the computed quantities.*

## III.1 Modeling 3-D multi-filamentary geometries

### III.1.a On the necessity of numerical modeling for AC loss calculations

Multi-filamentary superconductors have been manufactured since the very beginning of superconducting industrial production. They are composed of filaments spread on a various number of layers embedded inside a resistive matrix. To have a full transposition of the filaments and ensure that the same current is flowing inside each filament, they have to be arranged as a Litz wire, where all the filaments take the same path. As the matrix is resistive, current may be created inside it when the wire is exposed to an external magnetic field. This is the main reason why, MgB<sub>2</sub> simulations have to be made with a 3-D model.

In terms of convergence, the addition of a conductive matrix will not affect the solving process as the H-formulation already solve the magnetic field inside the air with a very high resistivity. As it is in 2-D models, only the non-linearity coming from the constitutive E-J characterization of the superconductor is affecting the convergence of the system. When it is necessary to consider the relative permeability of the matrix, another non-linearity on  $\mu_R(\vec{H})$  is added which will affect the non-linear solving process and convergence. In these cases, two non-linearities have to be considered and even if they are affected to two different domains, the solving is impacted by the presence of these two dependencies. In certain cases, the matrix can also possess a hysteric behavior which add another complexity for the convergence of the problem.

Analytical calculations exist for all the losses that will occur in the complete wire subjected to an external field and transport current. The hypothesis of the analytical calculations are :

1. The Bean model is used for analytical calculations of hysteresis losses.
2. The current density is supposed to be constant with field (or temperature).
3. All the AC losses are evaluated independently (coupling, eddy current, hysteresis,...) and simply summed.
4. The effect of the relative magnetic permeability of the matrix is not taken into account in the calculations.

Analytical calculations of AC losses inside these wires are always done by assuming a simple summation of the losses. It is interesting to know how far these calculations are from the numerical modeling when the model takes into account all the electrical properties of the realistic wire. Added to these comparisons, experimental work can be made to validate the computed quantities. In our case, the difficulty of theses measurements lies into the generation of AC signals in a metallic cryostat with liquid Helium because it will create eddy current inside the metal. To avoid this issue, a fiber glass cryostat can be designed.

### III.1.b Comparison of 2-D and 3-D models for multi-filamentary geometries

Solving 3-D numerical models involves handling a large number of elements which is always time consuming. In some cases, 2-D models can be considered, it is necessary to check which model (2-D or 3-D) is the most suitable, i.e. if the coupling losses can be neglected or not. Our approach has been to launch a series of simple test on a 3-D superconducting geometry shown in Fig. III.1, composed of six filaments embedded inside a conductive matrix. The simulations have been carried out in 2-D in COMSOL and in 3-D in Daryl-Maxwell (see III.1.c for more details).

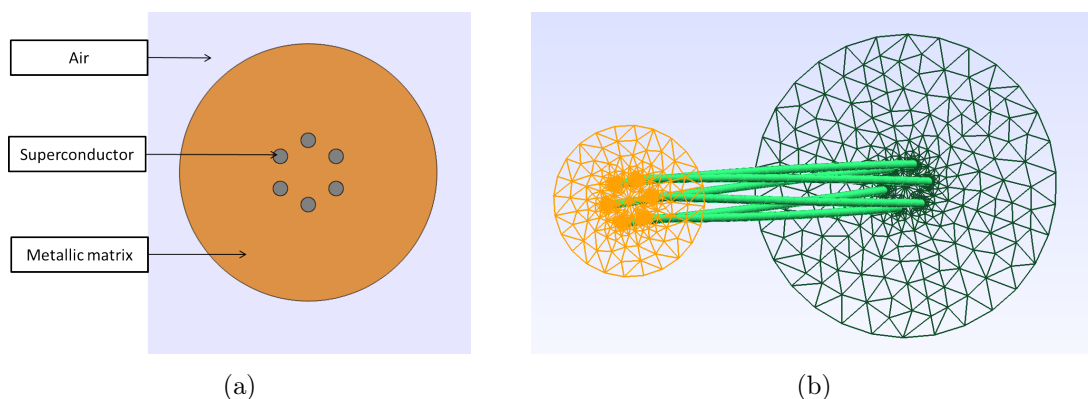


Fig. III.1 – 2-D with manual decoupling of the filaments in (a) and complete 3-D model in (b) for the AC losses calculations. The limit for the metallic matrix is shown in orange.

Simulations were done both for the 3-D model and the 2-D model which is the cross-section of the former shown in Fig. III.1a. We considered first only the superconducting filaments and then a resistive matrix (in orange) was added with a resistivity of  $\rho=10^{-8} \Omega.m$ .

To manually force the decoupling of the filaments in the 2-D model, one way is to add constraints according to (III.1) to ensures an equality of current in each filament :

$$\iint_{S_1} J_z dS_1 = \iint_{S_2} J_z dS_2 = \dots = \iint_{S_6} J_z dS_6 \quad (III.1)$$

Where  $J_z$  and  $S_i$  are respectively the current density and the surface of the filament where  $i$  and  $j$  denote the filament numbers. The transport current was sinusoidal with a peak value of 500 A (with a frequency of 50 Hz). For the superconducting material, the critical current was 700 A and the power law model was used with  $n=30$ . An AC external magnetic field in phase with the current was imposed on the boundaries of the air domain. AC losses calculations for the case where there is no matrix and where there is a conductive matrix are reported in Fig. III.2.

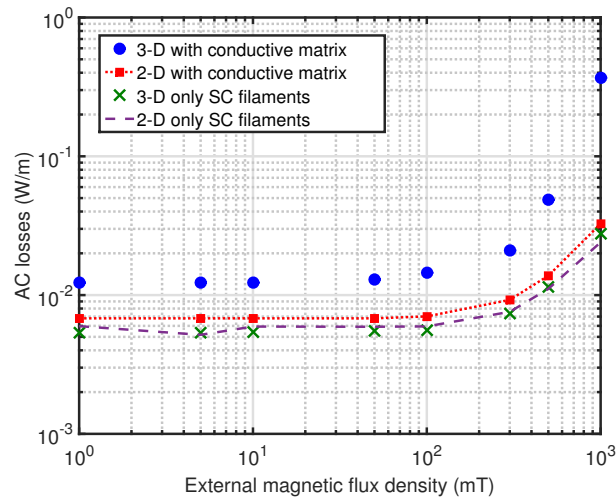


Fig. III.2 – AC losses in the case of a 3-D and 2-D models when considering or not a metallic matrix surrounding the superconducting filaments.

From these simulations, several conclusions can be made. First if only the superconducting filaments are taken into account, the 2-D and 3-D models are in agreement. For the 2-D model, with the metallic matrix, the AC losses are higher meaning that additional losses are created inside the matrix (mainly eddy current losses). Finally between the 3-D model with or without the metallic matrix, a certain difference of AC losses can be seen. In the 3-D model with the conductive matrix, the AC losses created inside the matrix are the summation of eddy current and coupling losses but also another type of losses which is relatively constant with the field. To be practical we will refer as coupling losses, all the losses inside the matrix except eddy current losses.

From these simulations it is possible to see that, when an external field is considered, coupling losses are occurring inside the conductor and can not be neglected. These simulations show the importance of taking 3-D into account with multi-filamentary geometries. In order to model a real MgB<sub>2</sub> wire, our approach has been to develop a simple 3-D numerical model to study the convergence of these multi-filamentary models and investigate the AC loss mechanisms.

As a first step towards the establishment of a realistic numerical model, some simulations have been made on a very simple geometry consisting of only three filaments. Because no validation is possible on a simple geometry as the one considered, benchmarking with various software was performed (see section below for the list of the software used). The complexity of the model was gradually increased as explained in III.2. Finally, after reaching the conclusion that these problems can be solved, the model was adapted to geometries similar to MgB<sub>2</sub> wires (in III.3).

### III.1.c Softwares used for the numerical benchmark

The benchmark was made with four pieces of software and two other Universities. We mainly developed the models on the first three software, while the software from Tampere University has been used to validate our computed quantities :

1. **Flux** : Flux is a commercial software developed by the company CEDRAT [160] jointly with G2ELab from Grenoble. This FEM software is specialized for the simulations of rotating machines, transformers and induction heating devices include a superconductivity module for AC losses [124] and quench calculations [161]. Its formulation (T- $\Phi$ ) added to multiple tools to optimize the solving process are two interesting features.
2. **Daryl-Maxwell** : Daryl-Maxwell is a university made software from Polytechnique Montréal designed to solve large electromagnetic problems dedicated to superconducting and ferromagnetic materials. The software is open source and available on GitHub<sup>1</sup>. The electromagnetic software is used with a H-formulation. Several features are implemented especially for ferromagnetic materials (including hysteresis), superconducting modules.
3. **COMSOL** : This software has already been presented in II.2.c. The H-formulation in 2-D can easily be extended to 3-D simulations.
4. **LoSt** : A dimension-independent FEM based modeling tool for simulating AC losses in superconductors developed in Tampere University [162], implemented as a compact part of GMSH<sup>2</sup> using its Riemannian manifold interface. Currently, the H-formulation and the H- $\phi$ - $\psi$  [129] formulation are implemented in the software.

Table III.1 gives the different features of the four pieces of software used for the benchmark. It summarizes the formulations, the time scheme but also if the relaxation coefficient of Newton-Raphson non-linear solver is optimized or not. SC and MPI are referring to single core and parallel solving.

	<b>Flux</b>	<b>DarylMaxwell</b>	<b>LoSt</b>	<b>COMSOL</b>
Formulation	T- $\Phi$	H	H- $\Phi$ - $\Psi$	H
Time step	fixed	fixed or adaptative	fixed or adaptative	adaptative
SC/MPI	MPI	SC	SC	MPI
Relaxation coefficient	algorithm	algorithm	fixed	fixed

TABLE III.1 – Comparison between the four softwares used along the benchmark. The H- $\Phi$ - $\Psi$  and the T- $\Phi$  formulations are equivalent.

1. For further information, contact Pr.Sirois at f.sirois@polymtl.ca

2. GMSH is an open-source finite element method mesh generator with pre- and post-processor facilities.  
<http://geuz.org/gmsh/>

### III.1.d Problem description

All the models in this chapter follow a same approach, some information and acronyms are given in this section. The filaments are embedded in a conductive matrix which will be referred as matrix or *mat*. In certain cases, another conductive layer has been added around the matrix made with monel. The air domain which can have a rectangular or a cylindrical form is referenced as *air*. The resistivity of the air (when the H formulation is used) in all the simulations has been set at  $\rho_{air}=10^{-3}$   $\Omega.m$ , which is at least several orders of magnitude higher than the superconducting material or the resistive matrix. This ensures no current in the air and also a good overall convergence of the model.

Unless it is specifically written, the transport current and the magnetic field are applied to the external boundaries of the air domain (using Ampere's law to impose the current). The external magnetic flux density is written  $B_{ext}$ . Regarding the normal faces of the model, periodic conditions are used in all the simulations. These conditions are possible as soon as the mesh on both normal faces are conforming and that the length through the extrusion is enough to guarantee a recurring pattern. The AC losses will be calculated inside the conductive domains, superconductors and the matrix when it is conductive by the volume integration of the quantity  $\vec{J}\vec{E}$ . Since these calculations are based on a time transient nonlinear simulation with zero initial conditions, it is important to simulate for enough time to let the initial transient die out and reach a steady state, which takes only one quarter of a cycle, therefore the simulations are done on 75 % of a cycle or a full cycle.

Concerning the electrical and magnetic properties taken for the matrix, the different cases are listed below and summarized in Table III.2 :

1. *case air* : the matrix is considered as air, only superconducting domains are considered conductive. The resistivity of the matrix for the case of the H-formulation is set at the same value as the surrounding air.
2. *case res* : In this case, the resistivity of the matrix is set at a typical metallic value. The resistivity is still very low compared to the resistivity of the air. Hence, the AC losses will also be calculated inside the matrix (coupling and eddy-current losses).
3. *case mag* : Added to the resistivity of the metal matrix, a relative magnetic permeability depend of the magnetic field is set in the domain.
4. *case hys* : In this case, the matrix possess an magnetic hysteresis behavior.

Case reference	$\rho$ ( $\Omega.m$ )	$\mu_R(\vec{H})$
<i>air</i>	$10^{-3}$	1
<i>res</i>	$\rho_{mat}$	1
<i>mag</i>	$\rho_{mat}$	$\mu_{Rmat}(\vec{H})$
<i>hys</i>	$\rho_{mat}$	hysteresis

TABLE III.2 – Case summary, the value  $\rho_{mat}$  and the dependency of the relative permeability  $\mu_{Rmat}$  are given in each section when the model is detailed.

## III.2 Three filament benchmark model

The three-filament model is a good first try to handle 3-D simulations which involve usually a large number of elements (and DOFs). The model was kept as simple as possible to ensure fast calculations but with a mesh detailed enough inside the filaments for accurate AC losses evaluations. This model has been used in a large number of simulations with various properties for the matrix and the two superconducting E-J relationships.

### III.2.a Model description

The model and mesh can be found in Fig. III.3. The geometry is composed of three filaments with a diameter of  $\Phi_{3fil}=1$  mm and a total cross section of  $A_{3fil}=2.35$  mm<sup>2</sup>. The filaments are twisted on a whole pitch of  $l_{p,3fil}=20$  mm, which are embedded in a cylindrical matrix (in turquoise) with an external radius of 2.5 mm. On top of that, a rectangular box of air is added to impose boundary conditions for the external field. The mesh was created using the software COMSOL with tetrahedron. To use periodic conditions, the mesh was copied<sup>3</sup> from one normal face (in orange) of the conductor to the other.

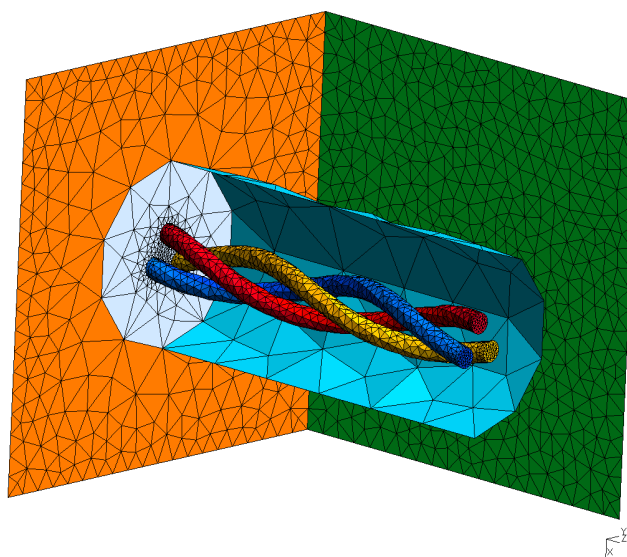


Fig. III.3 – Three filament geometry and mesh.

The mesh is composed of 52 200 elements and 65 205 edges. Table III.3 summarizes the input parameters of the physical properties.

In the *mag* case of non-linear magnetic permeability of the matrix, it has been modeled according to :

$$B(H) = \mu_0(H + \sigma(\beta - 1) \times \tanh(H/\sigma)), \quad (\text{III.2})$$

where  $\sigma$  and  $\beta$  are respectively equal to  $4.2 \cdot 10^3$  A/m and 50. The parameter  $\beta$  is the initial permeability slope at zero field. The values stem from experimental characterization of a matrix presented in [163].

<sup>3</sup>. This feature is compulsory because periodic conditions are handled in the studied FEM software with a substitution method

Physical quantities	Values
$I_c$ (A)	700
$J_c$ (A/mm <sup>2</sup> )	284
n	30
$J_{c0}$ (A/mm <sup>2</sup> )	205
$n_0$	10
$\rho_{mat}$ (n $\Omega$ .m)	1.0

TABLE III.3 – Three filament input parameters.

**Preisach model for hysteresis calculations - case *hys*** In some cases, the metallic matrix can have an hysteretic behavior. To compute the hysteretic behavior of the matrix, a Preisach approach has been used. The reader can find more informations on the following readings [164, 165, 166]. This feature which was developed by M.Tousignant from Polytechnique Montréal in Daryl-Maxwell has been tested by us on the model. In terms of complexity, this case is probably the most complicated one as the non linear solver has to handle the hysteresis of the matrix coupled with the non linearity of the superconducting filaments. The outer hysteresis domain is delimited by the equations :

$$\begin{aligned} M_+(H) &= M_{s1} * \tanh(c_1 * H + r_1) + M_{s2} * \tanh(c_2 * h + r_2) \\ M_-(H) &= M_{s1} * \tanh(c_1 * H - r_1) + M_{s2} * \tanh(c_2 * h - r_2) \end{aligned} \quad (\text{III.3})$$

The parameters chosen for the simulations are listed in Table. III.4.

Parameters	value
$M_{s1}$ (T)	0.31
$M_{s2}$ (T)	0.31
$c_1$ (m/A)	$1.26.10^{-5}$
$c_2$ (m/A)	$1.26.10^{-5}$
$r_1$	1
$r_2$	1

TABLE III.4 – Parameters for the hysteresis domain.

The magnetization function of the field H is shown in Fig. III.4.

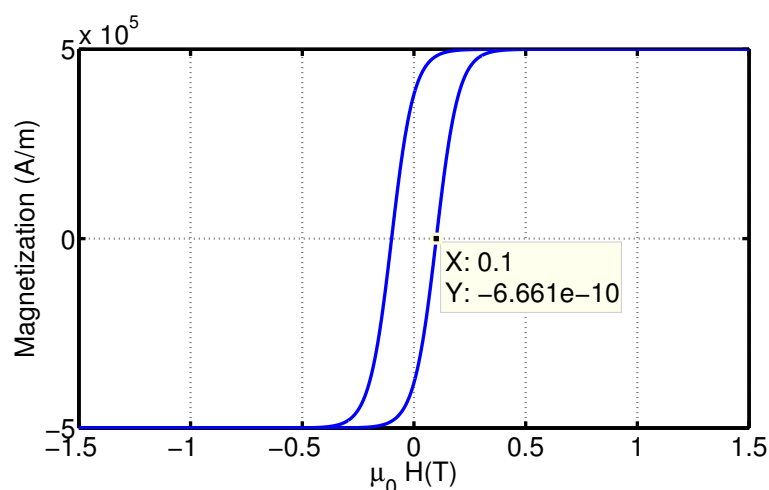


Fig. III.4 – Preisach magnetization curve for the numerical model. The outer limit of the domain delimits the hysteresis loop.

### III.2.b Results

#### III.2.b-i AC hysteresis losses - first test case air

Simulations have been carried on the four software (presented in III.1.c) with a transport current  $I$  between 10 % and 90 % of the critical current and an external magnetic fields of 50 mT and 200 mT. The signals are sinusoidal at 50 Hz. The AC self field hysteresis losses are plotted in Fig. III.5 versus the input current  $I$ .

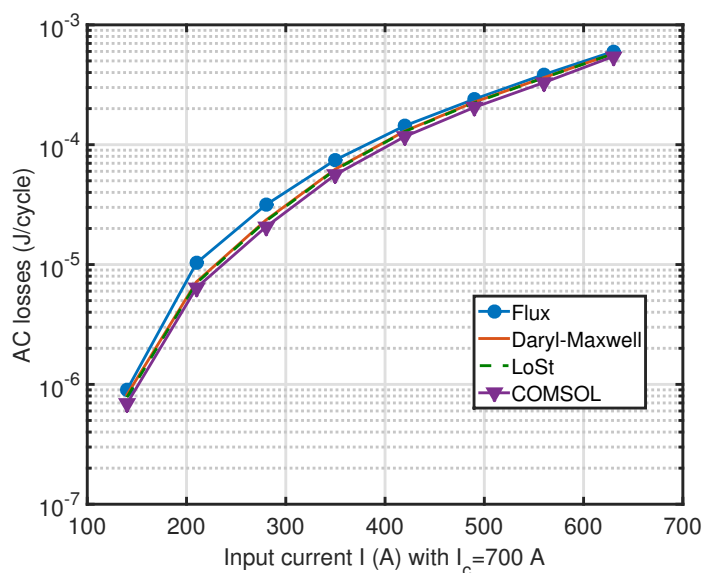


Fig. III.5 – Self-field AC losses for the four different software.

AC losses generated by two different fields are referenced in Table III.5. As the penetration field for the filaments is equal to  $B_p = \mu_0 J_c r = 180$  mT, a value below (50 mT) and

above (200 mT) were chosen.

External magnetic flux density value	Flux	Daryl	LoSt	COMSOL
50 mT	$7.69 \cdot 10^{-5}$	$6.81 \cdot 10^{-5}$	$7.25 \cdot 10^{-5}$	$6.62 \cdot 10^{-5}$
200 mT	$1.7 \cdot 10^{-3}$	$1.8 \cdot 10^{-3}$	$1.8 \cdot 10^{-3}$	$1.7 \cdot 10^{-3}$

TABLE III.5 – AC losses (J/cycle) for external magnetic flux densities of 50 mT and 200 mT with  $I=0$ .

From these simulations, a good agreement can be noticed between all the software regarding the computed quantities especially between the software LoSt and Daryl-Maxwell where the error in self-field AC losses is less than 1 %. COMSOL and Daryl-Maxwell calculations are in agreement within a range of 5 %. For FLUX, the difference increases largely at low currents. The coarse mesh is a possible explanation as the current is very low inside the filaments and the error can be induced as the current distributions are developing very locally in the filaments. It is also worth noticing that the formulation does not impact much the computed quantities as the software Daryl-Maxwell is implemented with a H formulation and LoSt a derivative of the T- $\Phi$  formulation. Fig. III.6 displays the current density distributions for self field AC losses and external magnetic field AC losses.

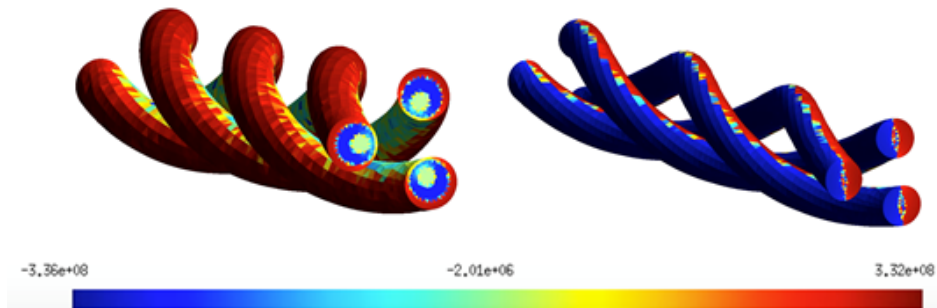


Fig. III.6 – Current density distributions for self-field AC losses (left) and external magnetic field (right) at 5 ms.

### III.2.b-ii Change of geometry for the calculations of combined AC losses

To impose both a transport current and an external field to the model, it is necessary to make some changes on the geometry. With the imposition of current as an integral constrain over the surface, the resultant self field will be circling around the filaments. This will be in contradiction with an imposed field (external field) along the y-axis on the boundaries. This can lead to divergence of the solver because of a wrong imposition of constrains on the problem. To overcome this issue, one way is to set the Dirichlet conditions on the outer boundary as a summation of a self-field generated by current flowing into the filaments and an external field. Fig. III.7 displays the two approaches to impose a transport current

inside the superconducting filaments : with a net surface or by setting a field.

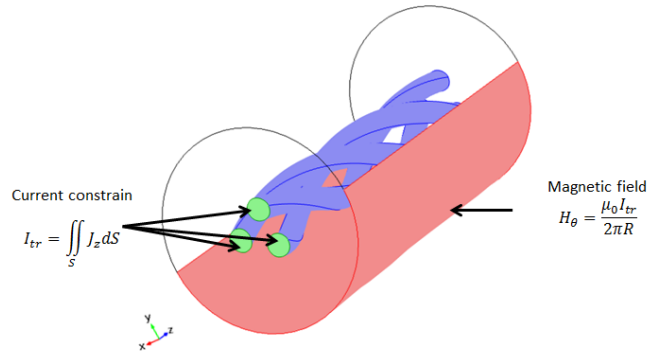


Fig. III.7 – New geometry for the air domain to generate transport current and external field.

Far from the filaments, the self-field is mainly created as if it was one big filament carrying the total current as :

$$H_\theta = \frac{\mu_0 I_{tr}}{2\pi R} \quad (\text{III.4})$$

By putting this equation into cartesian coordinates,  $H_x$  and  $H_y$  are defined as (III.5) :

$$H_x = \frac{\mu_0 I_{tr} y}{2\pi(x^2 + y^2)} \quad \text{and} \quad H_y = -\frac{\mu_0 I_{tr} x}{2\pi(x^2 + y^2)} \quad (\text{III.5})$$

Starting from the same geometry as before, the air domain geometry was changed from a rectangular box to a cylindrical one. The mesh resulting from the new geometry is shown in Fig. III.8. To ensure the validity of the previous results, the mesh inside the filaments and in the matrix was kept the same.

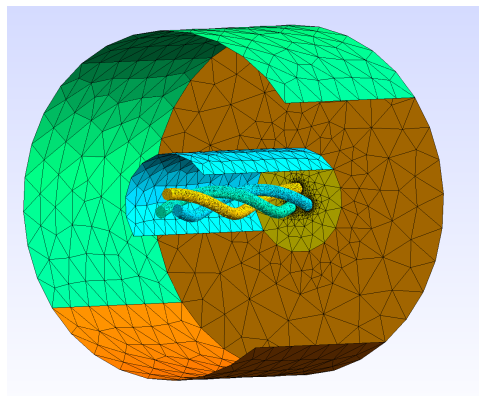


Fig. III.8 – New geometry for the air domain to generate both transport current and external field.

Imposing the current as a self-field has to be validate with simulations as the boundaries of the air domain are close to the filaments. Using (III.4) shall correctly be used as infinite boundary condition. Fig. III.9 displays the self-field AC losses calculations with both methods. In the figure, *Field imposition* is referring to the imposition of current using

a Dirichlet magnetic field (see (III.5)), and *Surface imposition* is referring at the imposition of current using integration over the normal surface of the filaments (see(II.1)).

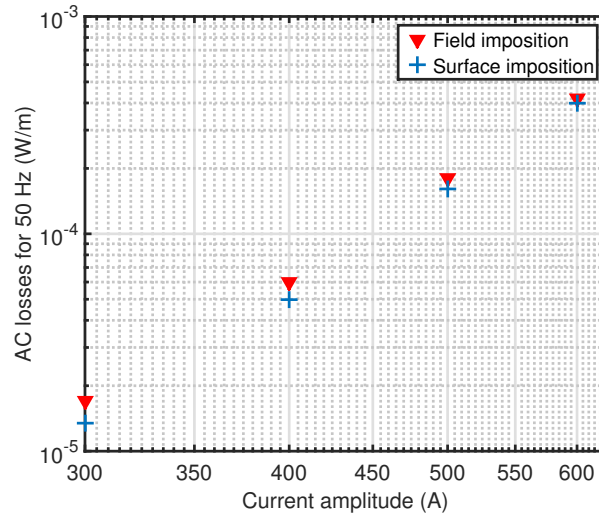


Fig. III.9 – Self-field AC losses for the two impositions of transport current ( $I_c=700$  A). No external field is added in these simulations.

The method to impose the transport current as a field is the most elegant way to ensure the good imposition of field if an external field is added on the boundaries and is validate with these calculations. Between the two impositions, the error on AC losses calculations is less then 5 % for current higher than 400 A ( $I/I_c > 0.5$ ). Some differences can be noticed as the imposition of current by the field is made close from the filaments (no infinite domain is used), to ensure a better correlation, simulations should be done with a larger air region.

According to these calculations, it is possible to impose the current as a form of field and superpose it to a external magnetic field. Next section discloses the calculations of AC hysteresis losses on this new geometry with transport current and external field.

### III.2.b-iii AC hysteresis losses in the case *air* - Coupled losses

As first, the case air was investigated by considering only the superconducting filaments. COMSOL has been used to validate the computed quantities (error about 5 % in general). Fig. III.10 displays the AC losses with transport current  $I$  and external magnetic field  $B_{ext}$  in phase. Analytical calculations exist for self-field or external field losses with external field values below and above the penetration field. The trends of the analytical calculations are also reported in the figure.

From this figure, several validations with analytical calculations can be made. As it was expected by (I.29), the AC losses generated only by an external field are proportional to  $B^3$  below the penetration field. For values of field higher than the penetration field, the slope is equal to 1 as it was predicted by (I.30). For low values of external magnetic field, the AC losses are mainly generated by the transport current. When the filaments start to be fully penetrated, the AC losses are driven by the external field with a slope close to 3

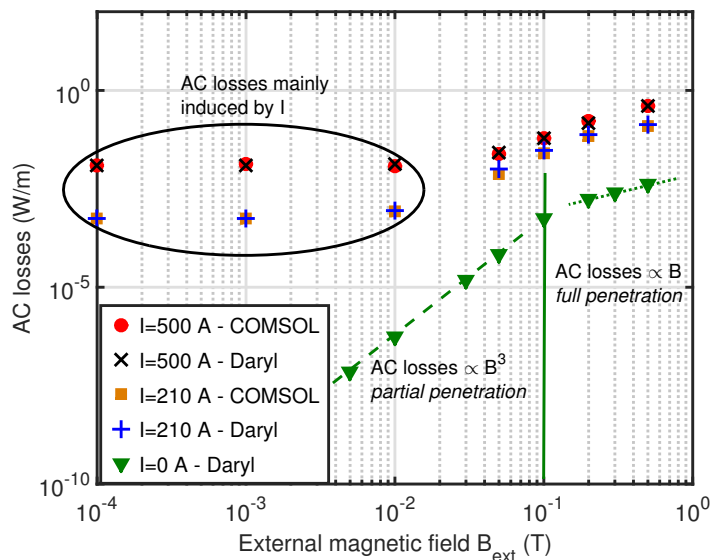


Fig. III.10 – AC losses in the case *air* for different transport current amplitudes and external magnetic field values.

(2.7 in average).

Hysteresis AC losses are constant in each cycle, hence the AC losses in Watt are proportional to the frequency (see section I.5.a-ii). The AC losses for each case : only current or field and a combination of the two, are plotted on Fig. III.11.

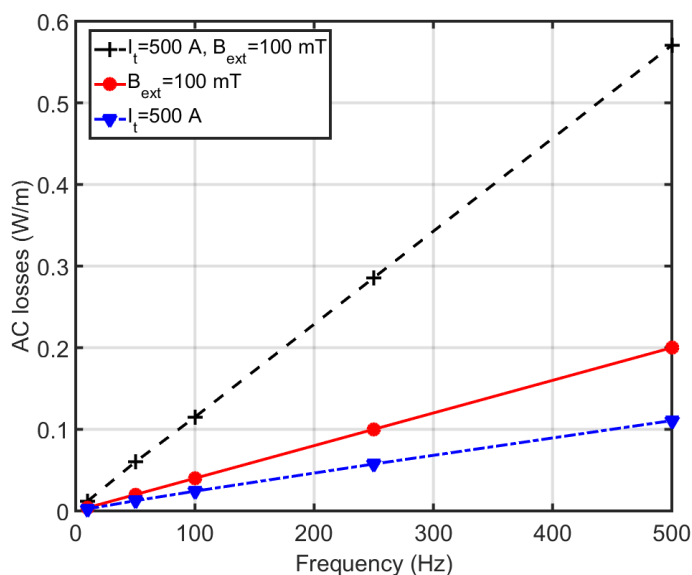


Fig. III.11 – AC losses in the case *air* for various cases versus frequency. The AC losses are proportional (hysteresis losses) to the frequency as predicted by literature.

As it was predicted by analytical calculations in (I.29) or (I.28), hysteresis losses are proportional to the frequency.

### III.2.b-iv Addition of a resistive matrix : case *res*

The resistivity of the surrounding matrix was set according to the case *res*. All the calculations have been made with the H formulation but as the resistivity of the matrix is several orders of magnitude lower than the resistivity of air, the presence of non-physical currents is reduced. In these cases, the AC losses are generated inside the superconducting filaments but also in the matrix. The complete AC losses calculated by the FEM software take into account the eddy-current and coupling losses inside the matrix and the hysteresis losses in the filaments. According to (I.20), if the coupling losses are predominant over hysteresis losses, the trend of the complete AC losses is with the square of the field but also of the frequency.

**Coupling-Decoupling** From the equation (I.20), the time constant  $\tau$  can be calculated with  $N=0.6$  :

$$\tau = (1 - N) \frac{\mu_0}{\rho_{matrix}} \left( \frac{l_p}{2\pi} \right)^2 = 5.09 \text{ ms (193 Hz)} \quad (\text{III.6})$$

It is possible, by changing the frequency of the external magnetic field, to force the coupling or the decoupling of the filaments. The simulations have been made with various frequencies by looking at the hysteresis losses inside the filaments with three different values of external field. The AC hysteresis losses (calculated by volume integration of  $\vec{E}\vec{J}$  only inside the filaments) are displayed in Fig. III.12. Analytical calculations only exist for the case where the filaments are fully decoupled and an approximation of the hysteresis losses when the filaments are fully coupled (by considering a big filament).

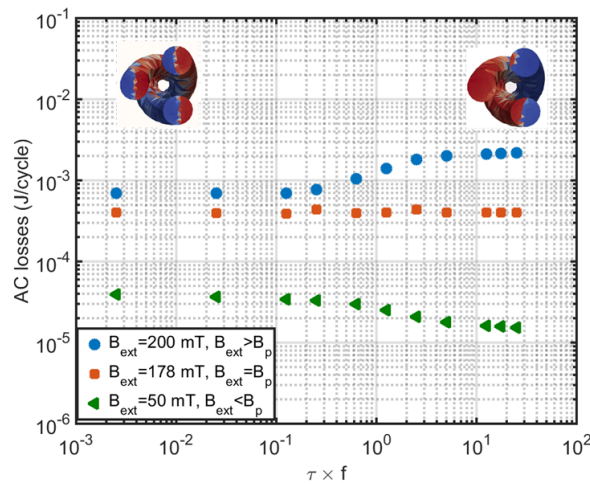


Fig. III.12 – AC losses hysteresis vs  $f \cdot \tau$  at three different magnetic flux density values and the current density distributions in the case of a low and at high frequency.

From these calculations and the current distributions presented on the graph, it is possible to see the coupling and the decoupling effects on the filaments. For values of magnetic field higher than the penetration field, the AC losses increase with the coupling phenomenon which was expected. For values of field less than the penetration field and

because the *surface* for the coupling case is taken as a big wire circling all the filaments, the AC losses decrease. Added to these calculations, the losses inside the matrix have been plotted with the hysteresis losses in Fig. III.13.

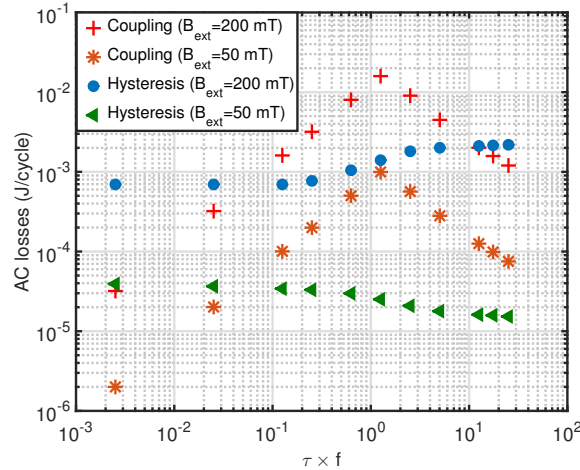


Fig. III.13 – AC losses in the filaments and in the matrix versus  $f \cdot \tau$  (hysteresis and coupling).

In these cases, the coupling losses are rapidly higher than the hysteresis losses. At high frequencies, the coupling losses become lower than the losses inside the superconducting filaments (screening effects).

**Combined AC losses** Fig. III.14 displays the complete AC losses with various transport current and external field at 50 Hz (in phase). Once again the agreement between COMSOL and Daryl-Maxwell is very good with a difference of 3 % in average. In the case of only external magnetic field, the slope of the curve is around two (2) which is explained as the coupling losses are the main mechanism of losses inside the model. When an external field and transport current are applied, the AC losses are almost constant at low values of fields, which means that the AC losses are mainly induced by the transport current (hysteresis losses). In addition to that, with high values of field the coupling losses start to become predominant inside the model.

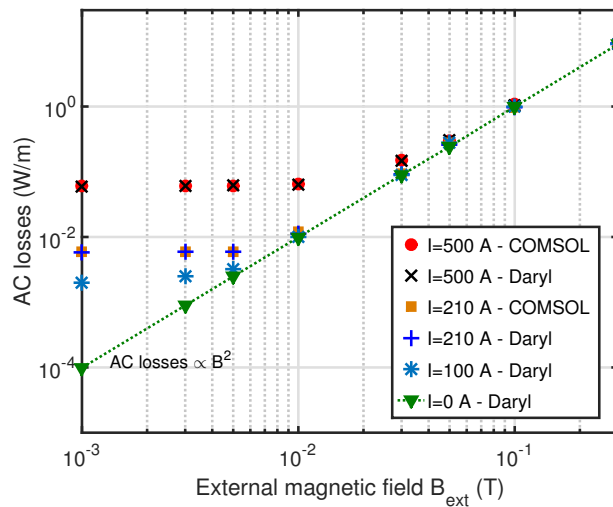


Fig. III.14 – AC losses in the case *res* for various transport current amplitudes and external magnetic fields at 50 Hz in phase.

**AC losses versus frequency** Another way to see the difference between the case *air* and the case *res* in terms of losses is to do calculations with various frequencies as hysteresis losses are linear with the frequency and coupling losses are in the square of the frequency (until saturation). Three situations have been tested. One with only transport current, one with only external field and one with the combination of the two. When the wire is only under the action of the transport current, the losses will be mainly hysteresis losses and should be linear with the frequency. With the addition of an external field, coupling losses occur in the material which may change the slope of the curve. A log-log graph of the AC losses versus the frequency is displayed in Fig. III.15.

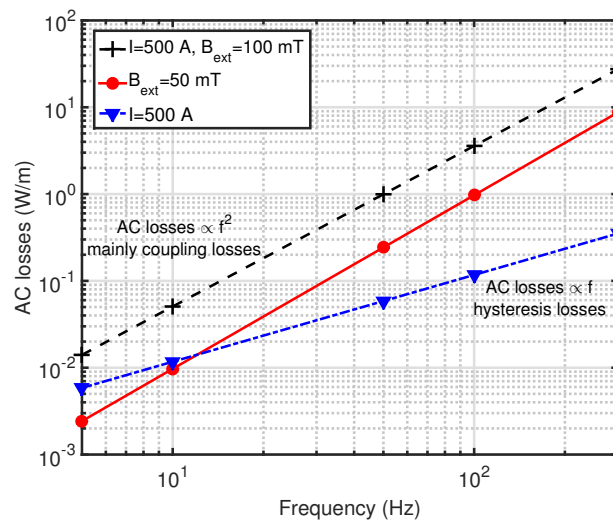


Fig. III.15 – AC losses versus frequency in the case *res* for various cases.

From this figure, the assumptions made before can be validated. With only an external

field, the AC losses are almost as the square of the field meaning that the coupling losses are predominant. In the situation where the wire is under the action of the transport current and external field, the AC losses are a summation of hysteresis and coupling losses which explains a lower slope.

### III.2.b-v Addition of a magnetic matrix case *mag*

A relative magnetic permeability has been added to the property of the matrix (case *mag*) by taking into account the relationship (III.2). The AC losses are displayed in Fig. III.16 with various transport currents and external field values.

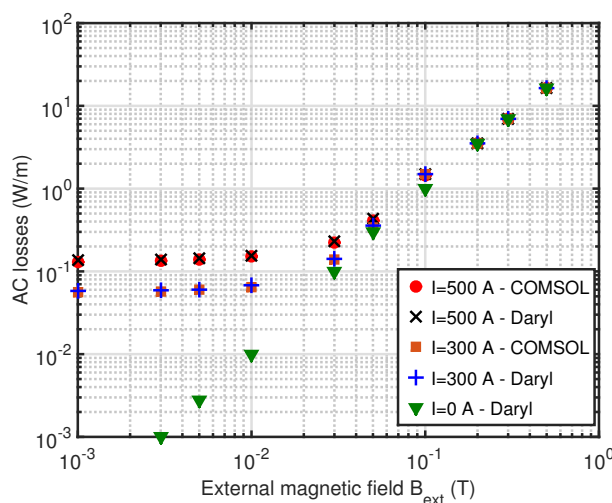


Fig. III.16 – AC loss versus field and current in the *mag* case.

These trends of the AC losses curves are in agreement with the calculations reported before. These calculations have been made with two different software to check the computed quantities. They are in agreement (see the implementation of  $\mu_R(H)$  in COMSOL in [154]) with a difference of less than 5 % which is comforting. Compared to the case *res*, the difference of AC losses calculation is in average in the order of 30 %. The addition of the relative permeability has led to an increase of the computation time of about 20 %.

### III.2.b-vi Addition of a hysteresis model

Finally, the case *hys* has been simulated with only external magnetic field. AC losses and ferromagnetic losses are displayed in Fig. III.17. The ferromagnetic losses have been calculated by the volume integration of the quantity  $\vec{B}\vec{H}$  in the matrix. Only Daryl-Maxwell has been used for these calculations as the Preisach model is not implemented in COMSOL.

These results are also difficult to interpret as two highly non-linear mechanism are involved in this model. The difficulty of convergence was a real issue in this case and if there is any simulations to do further with these kinds of model, adaptations of the non-linear solver have to be done.

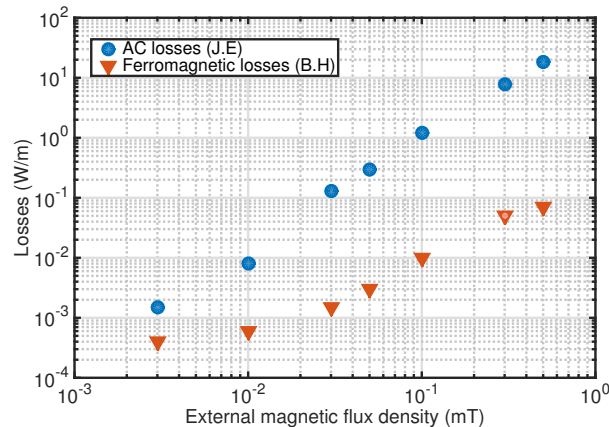


Fig. III.17 – AC losses versus field and current in the *hys* case.

### III.2.b-vii Conclusion on the simulations

About the used software, all these calculations (except for the case *hys*) have been performed with Daryl-Maxwell and COMSOL. The first software is more flexible and the fixed time step scheme allows for fast calculations. COMSOL with the adaptive time stepping take in general 5 to 6 times the computation time of Daryl and may not be used for more complex models but give results very close. Added to that, it is not possible to optimize its solving process. For these reasons, the use of this software was stopped and validation quantities are reported with FLUX and LoST.

In all the simulations, the power law was used as it is the most classical representation of the E-J curve for the superconductor. The benchmark was also conducted with this power law. However, for calculations of AC ripples superposed to DC currents, the percolation model shall be more suitable (see IV.2.b). In the next section, we compare the AC losses with the two different power laws and two different software.

### III.2.c Impact of the E-J relationship on AC losses calculations

To solve AC losses calculations created by AC ripples in DC background, one way is to use the percolation law as it was explained before. Self-field AC hysteresis instantaneous losses calculations between FLUX and Daryl with the two power laws are plotted for an AC current of 500 A (50 Hz) in Fig. III.18 (case *air*).

The two laws gives the same instantaneous losses for AC signals (results already seen for the HTS tapes). The two E-J models are very close from each other around the critical current which explain the good agreement between the calculations on each software. The differences between the two FEM software can be explained by the different formulations as all the solving parameters have been the same to ensure a good comparison. The problem was solved on a 20 ms time frame, with 400 time steps, no adaptation of the relaxation coefficient and PARDISO as the solver. The current was imposed as an integral of current over the surface for Daryl-Maxwell and a circuit coupling for FLUX. We can note that between 8 ms and 12 ms a difference in trend for the increase of the losses which could be explained by how the software handles the current imposition. For the all current

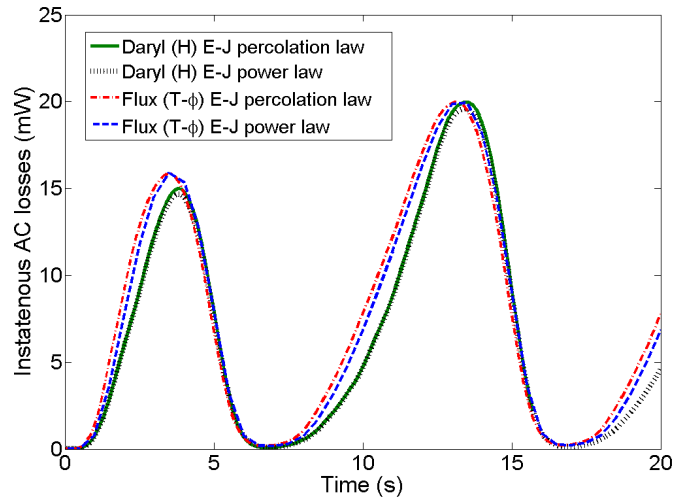


Fig. III.18 – Instantaneous AC losses for the three filaments - transport current 500 A.

amplitudes, the AC losses are reported in Fig. III.19

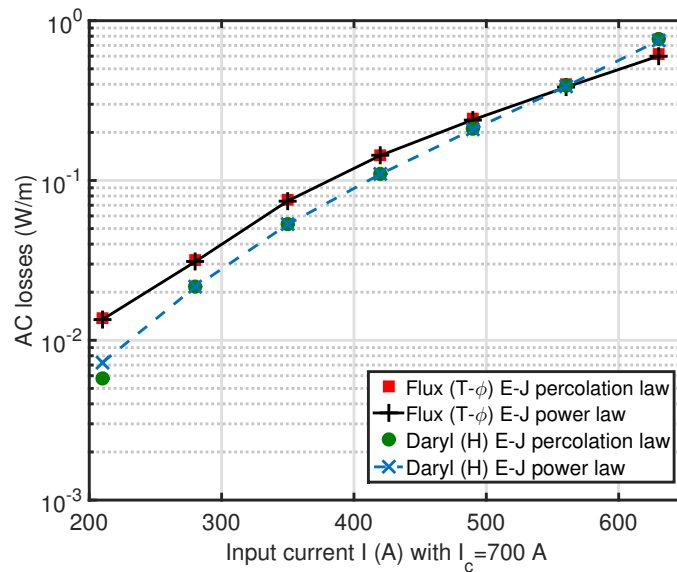


Fig. III.19 – AC self field losses for the two software but also the two E-J fits.

### III.2.d Optimization of the numerical solving process

The software FLUX has, inside its solving process, the two algorithms in I.6.b-ii dedicated especially for non-linear problems. Hence, it was tested on the model. The imposition of a 100 mT external field was analyzed with no transport current. First, it is interesting to note the number of steps required to run the simulation on one period. For the software Daryl-Maxwell, the number of steps per period was set at 400 ( $\Delta t = 5 \cdot 10^{-5}$  s). With this value, the calculations were lasting about 50 minutes to complete the whole cycle. Decreasing the number of time steps leads to divergence of the non linear solver. In FLUX, even

without relaxation factor algorithm, it was possible to converge the complete problem with 40 to 100 time steps per period. This may be explained by the use of a  $T-\Phi$  formulation compared to an H-formulation, because it leads to a better matrix conditioning of the system. This results is an important factor as the community is largely using the H formulation for its convenient implementation into FEM software. However, the  $T-\Phi$  is more adapted to solve superconducting problems.

The impact of using a variation of the Newton-Raphson method, with one of the two algorithms mentioned above, has been investigated. The two E-J relationship has been implemented with varying numbers of time steps with different algorithms for the relaxation factor. The average number of iterations for all these simulations are reported in Fig. III.20.

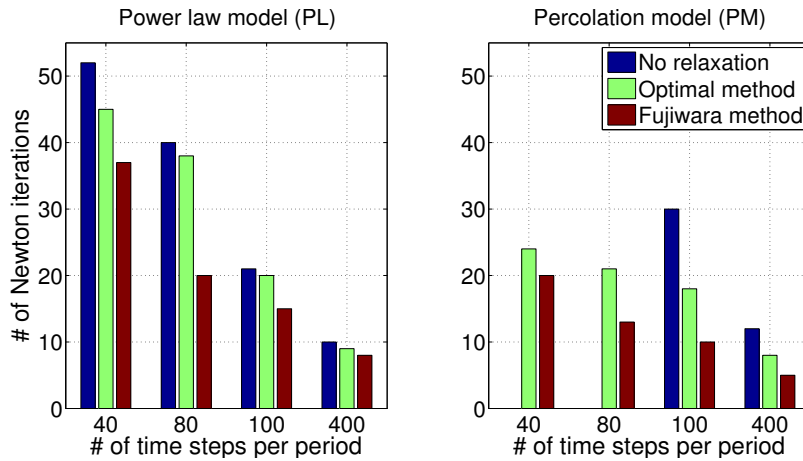


Fig. III.20 – Average number of iterations for the power law model (left) and percolation model (right).

From these simulations, it is noticeable that the use of an algorithm for the relaxation factor helps to converge with less iterations. The percolation model, which appears to be less stable in the solving, does not converge without any adaptation of the relaxation factor for numbers of time step below 100. With the percolation model, the problem appears not to converge for 40 and 80 time steps per period without any adaptation of the relaxation factor. Less iterations should lead, if the algorithms are time-equivalent to compute to faster calculations. Fig. III.21 displays the computation time versus the number of time steps per period with the different algorithms.

According to these results, the Fujiwara method is more time consuming despite the fact that the method requires the smallest number of iterations. This is explained by the time taken to calculate the proper relaxation factor compared to the optimal method. Another important aspect is that the use of a  $T-\Phi$  formulation seems to lower the number of time steps per period. It was possible to go as low as 40 times steps per period (which an error on the AC losses of 2%), with relaxation and 100 without any relaxation.

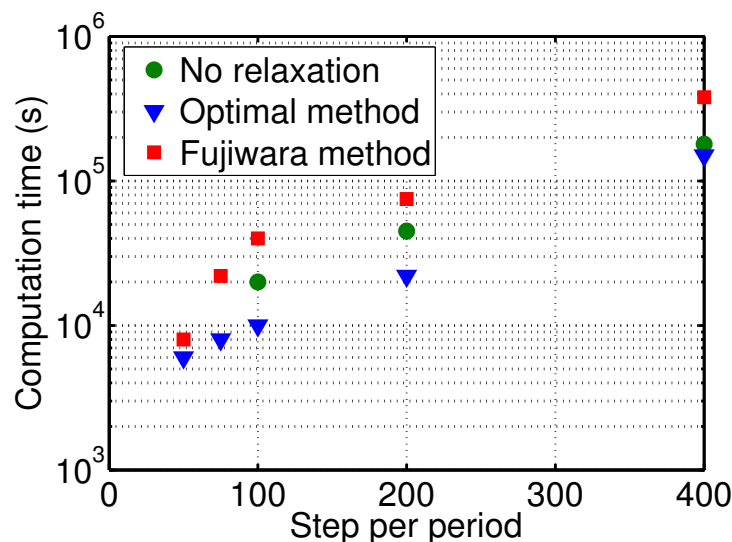


Fig. III.21 – Computation time for the three methods in the software FLUX vs the number of time steps per period.

### III.2.e Conclusion of the three filament benchmark

Along this section, a numerical model has been developed and tested with various electrical properties. Starting from a 3 filaments geometry, the AC losses have been calculated without and with the presence of a resistive and magnetic matrix. Analytical calculations and comparisons between software validated the computed quantities in each case. The complexity of the model was increased by taking into account several properties for the metallic matrix to give us the confidence that we are able to handle this kind of complicated calculations in a reasonable time (less than 16 hours maximum). All these calculations lead to the conclusion that it is possible to create and calculate 3-D simulations with various properties of the constituents and that the size of the problem and therefore the computation are the only limitations. In the end, some hints on how to speed up the calculations have been found and can be used to access more rapidly the convergence. From the results, the optimal method seems the most promising method to speed up the calculations and reduce the number of iterations.

Regarding the numerical software used in the simulations. We have been experimenting some difficulty to impose a transport current and an external field inside the software FLUX. This problem has been a limitation for the development of complicated model in the software. However, the software has the advantages of providing efficient tools for non-linear solving and shall be promising if the problem reported before is fixed. Regarding COMSOL, the adaptive time scheme is rapidly a problem as it takes long computation times to solve even this simple problem. During these simulations, the limit was almost reached in terms of computation times and it has been decided to stop the developments of 3-D numerical model in this software. Daryl-Maxwell which was open-source and very flexible was kept as the main software for our numerical models. The simple core was, however, one of the main limitations for the solving of a large number of problems.

After numerical developments on this tree filament geometry, more realistic models have been made and tested.

### III.3 MgB<sub>2</sub> multi-filamentary wires

At first, a full description of the MgB<sub>2</sub> wires is made. The physical properties of the wire have been measured in order to be implemented in the model and come up with the most realistic model possible.

#### III.3.a Model description

The studied MgB<sub>2</sub> wires are all manufactured by the company Columbus. They are build with 36 filaments spread on three concentric layers. The metallic matrix which is surrounding the conductor is made with nickel. Usually a layer of monel is added around the wire to reinforce it. All these wires can have different diameters such as 1.13 mm, 1.33 mm or 1.52 mm. In these cases, the increase of the wire diameter is proportional to the side size of the filaments, which kept the value of  $J_c$  constant with all the wire diameters. In addition to these wires, a special 1.1 mm wire has been manufactured for critical current measurement (Sample RRT). We focused our investigations of the MgB<sub>2</sub> wires made with nickel with a diameter of 1.13 mm and 1.33 mm (see Table. III.6).

MgB <sub>2</sub>	Sample A	Sample B	Sample RRT
$\Phi$ diameter	1.13 mm	1.33 mm	1.1 mm
Nb filament	36	36	36

TABLE III.6 – MgB<sub>2</sub> samples.

The Sample B is displayed in Fig. III.22a. A close up of one of the diffusion layer [167] is shown in Fig. III.22b.

An EDS study made in Nexans Lens by D. Leroux, of the same wire is displayed in Fig. III.23. The composition of magnesium (Mg), nickel (Ni) and copper (Cu) are shown added with the complete EDX. The outer layer is an alloy composed of about 40 % of copper and 60 % of nickel. From this figure, it is possible to see very thin light green lines embracing the filaments which is corresponding to the diffusion layer and composed of almost of just magnesium.

To establish a realistic model, it is necessary to characterize all the constitutive elements of the wires. This means measuring the critical current of each wire with enough precision to be confident during the sizing of the application, and also characterizing the resistivity and the relative magnetic permeability of the metals in the wire. To measure the critical current of the wires, two different setups have been used : one at LNCMI Grenoble and one in GREEN Nancy. The resistivities of the constitutive metals have been measured at LNCMI Grenoble as the facility offers a proper way to measure, with temperature, metallic samples resistivities. For the relative magnetic permeability of the metals, the

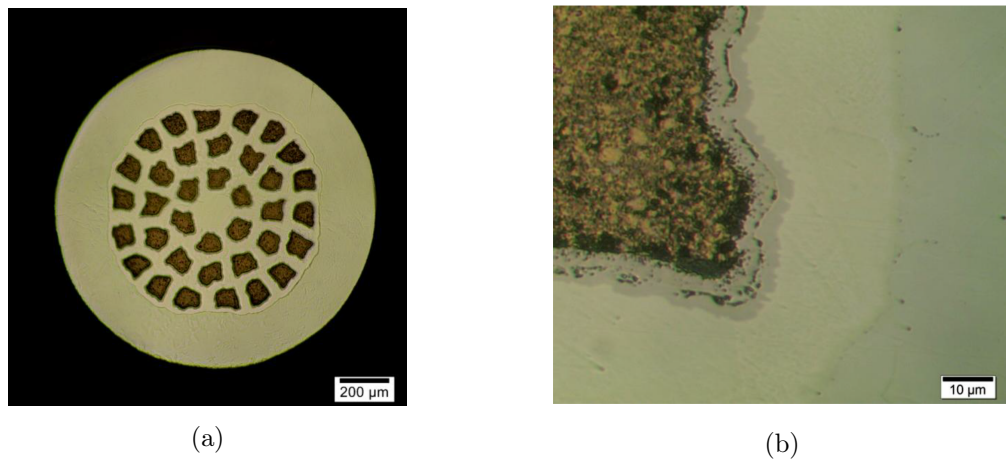


Fig. III.22 – Cross section in (a) and a close focus on one  $MgB_2$  filament (b) of the Sample B.

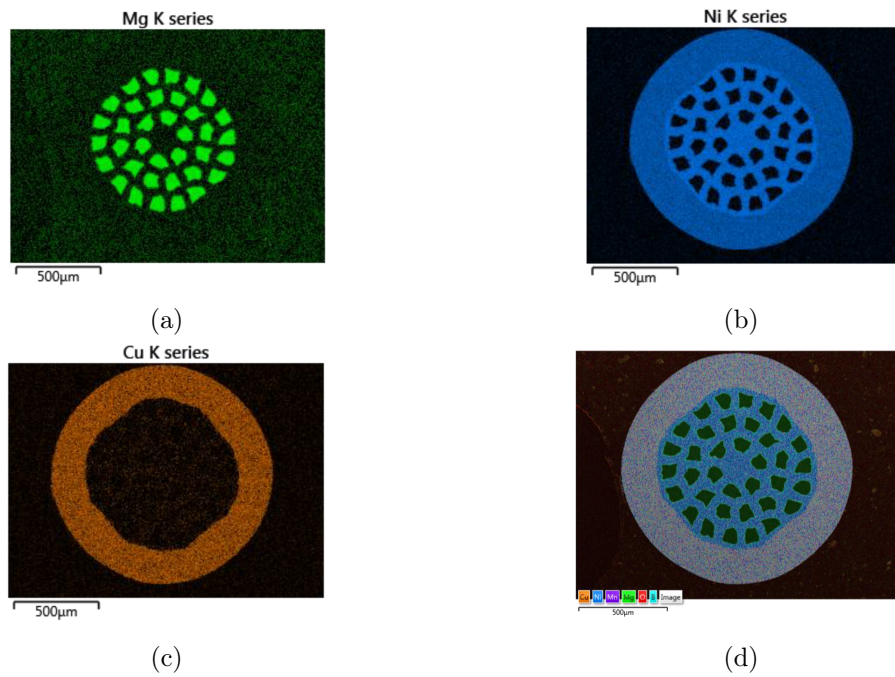


Fig. III.23 – EDX showing the composition of the  $MgB_2$  wire (Sample B).

Magnetometric department of the Néel Institute has devices capable of measuring the relative permeability of short samples.

### III.3.b Experimental characterization

#### III.3.b-i $MgB_2$ wires

**Critical current measurement setup** Two campaigns of measurement have been developed and carried out for measuring the critical current of these wires. One which took place in LNCMI Grenoble and one in GREEN of Nancy. The two facilities have different advantages and drawbacks. In LNCMI Grenoble, the flexibility of temperature and field

are interesting for measuring the critical current over the whole range of operation but the sample holder is not long enough in some cases to reach the transfer length. If the current is not injected on a distance higher than the transfer length, the current will not circulate inside the superconducting filaments. Current flowing inside the nickel or monel will heat the wire and also create a voltage on the sample. In the experimental workbench in GREEN, the temperature and field are not easily adjustable on the whole range of operation but the sample holder is longer and allows for the characterization of multiple samples.

**LNCMI facility** In LNCMI Grenoble, the critical current measurement was made with a magnetic flux density  $|\vec{B}|$  transverse to the wire in a cryostat filled with liquid Helium at 4.2 K. The length of the sample was 220 mm. Measurement were made at a variable temperature between 4.2 K and 20 K. The magnet was 400 mm in diameter with a magnetic flux density up to 10 T as shown in Fig. III.24.



Fig. III.24 – MgB<sub>2</sub> critical current measurement setup.

The measurement was performed using the 3 kA probe designed for the EUCARD project [168] and shown in Fig. III.25, powered by a 5 V-3 kA current source. The low inductance of the probe allows current slopes up to 500 A/s.

For this experiment a new sample holder was designed for the probe dedicated for a straight wire. It is composed of pieces of copper cut in the middle with a v ring along it where the sample is placed and soldered. The sample is cut in the middle to force the current inside the superconducting wire. The wire was soldered with Indium on a distance of 100 mm on each side as shown in Fig. III.26. Voltage taps were soldered with tin on the sample with a measurement length of 12 mm. Temperature measurements were performed with a CERNOX mounted on the sample holder next to the sample. The temperature regulation was performed with two CERNOX and two resistors (50  $\Omega$ ) located on the current leads. Thermal equilibrium at each temperature of measurement was established between the CERNOX mounted on the sample and CERNOX located near the heaters.

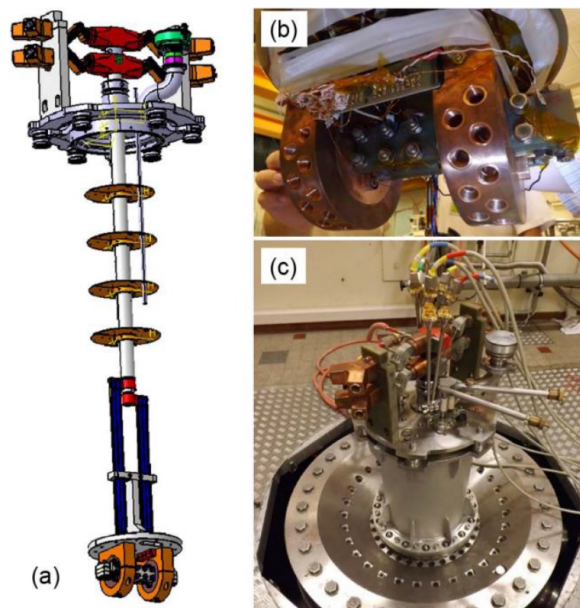


Fig. III.25 – LNCMI probe [168].

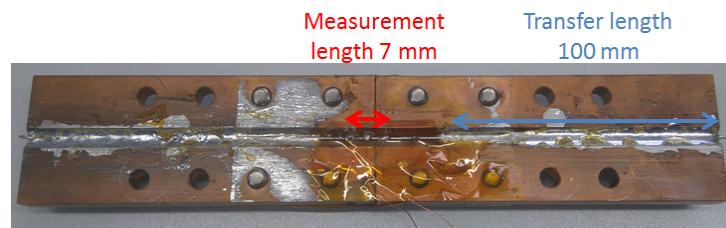


Fig. III.26 –  $MgB_2$  sample mounted on the sample holder. The voltage taps are 20 mm away from the soldering parts.

**GREEN workbench** To complete the measurements done at LNCMI, a series of measurement has also been performed at GREEN in Nancy. This laboratory which is specialized in electrical engineering focusing on superconducting motors and next generation of fuel cells has the capability of measuring superconducting materials at cryogenic temperatures. To measure critical current of  $MgB_2$  wires in the same environment as the superconducting cable, a workbench was specifically designed. The critical current had to be measured in temperature between 15 K and 25 K with a external magnetic flux density between 1 T and 1.5 T. This experiment has been implemented jointly by the people at GREEN and the Grenoble team. A picture of the device is shown in Fig. III.27.



Fig. III.27 – MgB<sub>2</sub> measurement workbench with the magnet in A, the thermal parts in C and the cryocooler head in D.

To impose a static external flux density on the wire, two 30 cm long permanent magnets have been designed with a maximum value of 1 T. The wire is then mounted on a copper plate which is cooled down by a cryocooler and placed between the two magnets. To change the value of external field, the space between the north and the south poles of the magnets can be adjusted. The magnets are cooled down at 40 K with the help of a second cryocooler. As the magnetic field is generated in a static way, it is difficult to do a lot of measurements quickly (need to fix a value of field by adjusting the magnets then cool it down and warm it back up), but this measurement workbench is interesting to validate some points of the critical current versus temperature and field. It is also possible to investigate the impact of the bending radius of the MgB<sub>2</sub> wire.

During this thesis, the experimental setup has been completely developed and measurements shall be performed in the upcoming years.

## Results

**Sample RRT** The RRT sample is produced with 36 filaments and an external diameter of 1.1 mm. An external layer of copper which eases the soldering process is deposited outside the monel. A smaller wire is also interesting as the critical current is expected to be lower so as the transfer lengths. Fig. III.28 displays a cross-section of the wire. In this wire, a barrier of Niobium has been added to avoid the pollution of the MgB<sub>2</sub> compound during the process. The soldering has been made with tin inside an oven regulated at 230 °C, the obtained soldering lengths are in the order of 100 mm.

The measurements have been made at 4.2 K with the 3 kA current source as the team

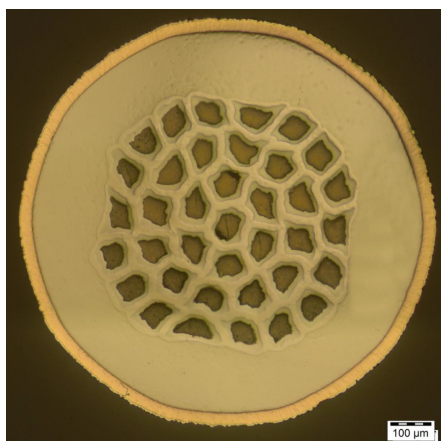


Fig. III.28 – Cross-section of the Sample RRT. The external layer of copper is clearly visible.

had no idea about the expected critical current (first team to do the RRT). The current ramp was set at 50 A/s which was a good compromise between the heat generation and the detection system. The critical current of the sample with various magnetic flux density from 0 to 6 T are shown in Fig. III.29 (LNCMI measurement). The voltage criterion is  $E_c=1 \mu\text{V}/\text{cm}$ . As the measurement has only been made in liquid Helium at 4.2 K, it would have been interesting to use the voltage of the LTS ( $E_c=1 \text{ nV}\cdot\text{cm}^{-1}$ ) but to ensure a good overall result on all the team, a higher criterion has been defined.

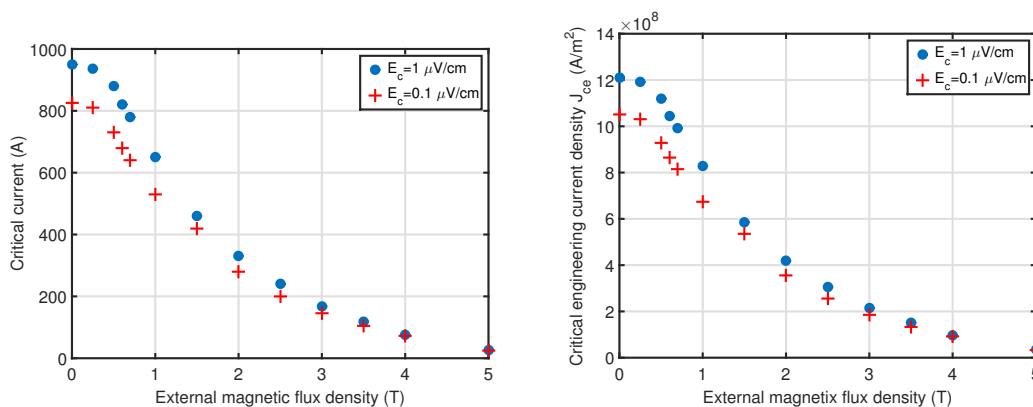


Fig. III.29 – Critical current and engineering critical current density versus magnetic flux density for the sample RRT ( $E_c=1 \mu\text{V}/\text{cm}$ ). The measurement has been made at 4.2 K with measurement length of 8 mm

These results have to be compared to others laboratories results to show the reliability of the experiment ( $< 5\%$  difference).

**Sample A** Fig. III.30 displays the critical current of the sample A with magnetic flux density up to 5 T and with a temperature range between 4.2 K and 20 K. One can notice that the sample loses its superconducting properties at values of magnetic flux density above 4-5 T. This is explained by the use of carbon doping inside the superconducting

material which has an effect on the reversibility magnetic field (source Columbus internal).

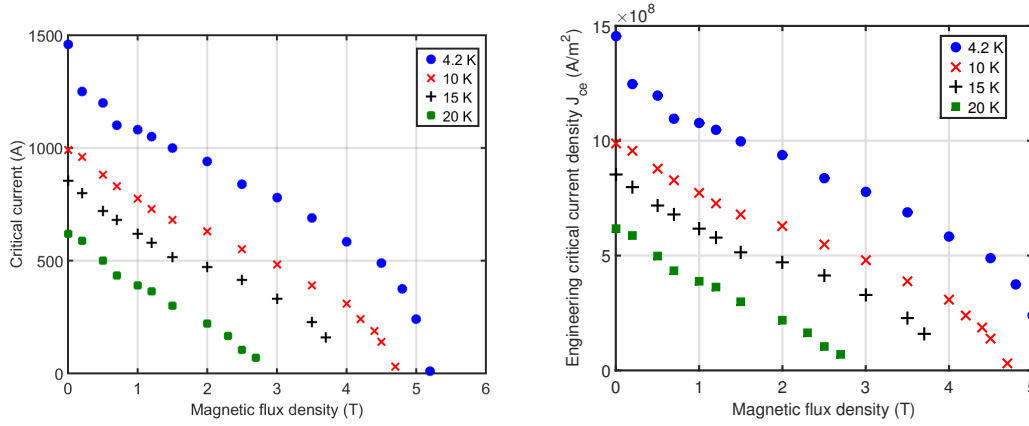


Fig. III.30 – Critical current and engineering critical current density of the Sample A MgB<sub>2</sub> wire versus the magnetic flux density at different temperature ( $E_c=1 \mu\text{V}/\text{cm}$ ).

Regarding the  $n$  values of the power law found in the measurements, the results are plotted in Fig. III.31. At self-field, the  $n$  values are relatively close to LTS superconductors such as NbTi (at 4.2 K) denoting a very brutal transition [169]. When the external field increases, the  $n$  value is decreasing with a homogeneous trend, until the critical current becomes low (300 A-400 A). As it was observed in HTS, the  $n$  value decreases with the increase of the operating temperature. At 20 K, the  $n$  values are in the range of HTS superconductors which reveals a smoother transition.

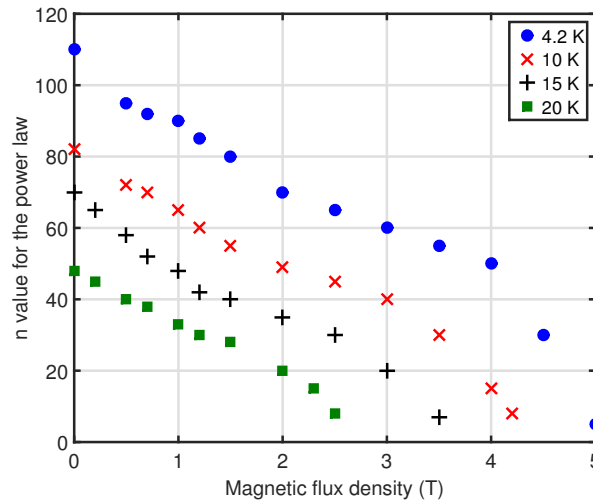


Fig. III.31 –  $n$  values for the power law of Sample A at different temperatures and various fields. The values have been calculated with electric field comprise between 0 and approximately  $4 \mu\text{V}/\text{cm}$ .

However, as it was seen in previous chapters, the percolation model seems more suited for AC losses calculations. It is possible to fit the E-J curves found in experiments with the percolation model. From the measurement, the value of  $J_{c0}$  can be found to be equals

to  $J_{c0}=0.9J_c$ . The E-J curves fitted are plotted in Fig. III.32.

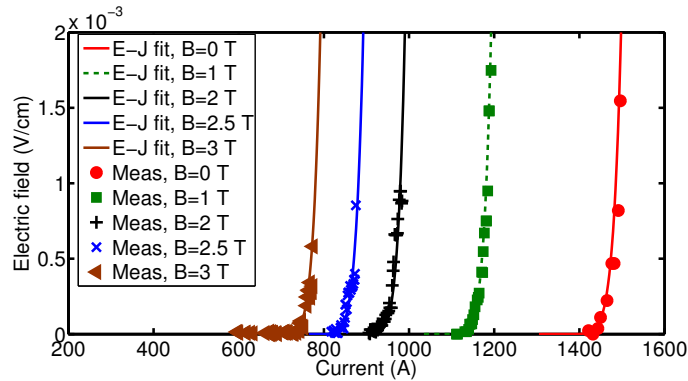


Fig. III.32 – E-J curves fitted with the percolation model.

The  $n_0$  values are displayed in Fig. III.33. The  $n_0$  values are nearly constant (compared to the  $n$  values), as it was expected by the theory, with temperature and field.

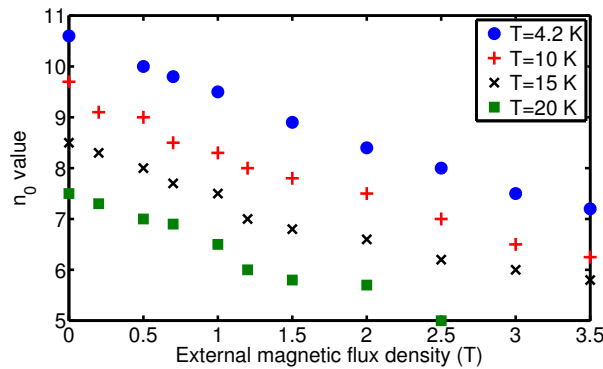


Fig. III.33 –  $n_0$  values of Sample A at different temperatures and various fields.

**Sample B** Unfortunately due to the transfer length, it has not been possible to measure the critical current in LNCMI. Measurements should be carried out in GREEN in the next upcoming year.

### III.3.b-ii Nickel matrix

As the metal surrounding the MgB<sub>2</sub> influences the AC losses (see I.2.c or [170]), it is necessary to characterize the constitutive elements of the matrix. In the case of the nickel matrix, the electrical resistivity with temperature but also its relative permeability with field have to be measured. The sample has been under the same heat treatments and mechanical deformations as the industrial wire. The heat treatments are higher than the Curie temperature of pure nickel which is around  $T_{currie}=650$  K [171].

To measure the electrical resistivity of the sample, a V-I measurement was made inside a cryostat filled with liquid Helium at 4.2 K and we let the temperature increase naturally

up to ambient. The 150 mm long sample was placed horizontally to ensure a good uniform temperature. The long time (approximately 3 days) to warm up the sample assure a good overall temperature uniformity on the complete sample. The temperature on each sample was monitored with a CERNOX mounted in the middle of the sample. The resistivity of the Nickel versus temperature can be found in Fig. III.34.

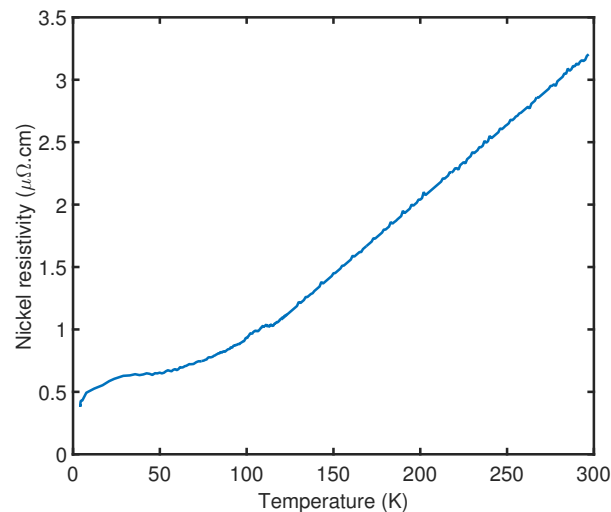


Fig. III.34 – Resistivity of the nickel sample between 4.2 K and 300 K. The injected current was set at 10 mA.

To measure the relative permeability of the two metals, a magnetometric measurement has been made. The samples have been cut to 4 mm length using electro-erosion method which was estimated as the softest type of cutting for the wires. The sample is shown in Figure III.35.

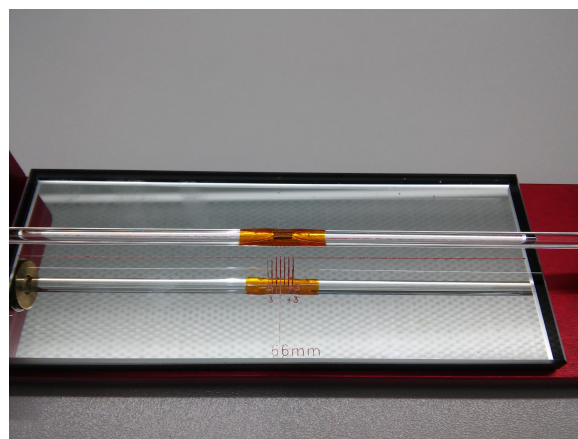


Fig. III.35 – Nickel sample for the VSM.

A Squid VSM-QD was used. The magnetometer is capable of reaching  $\pm 7$  T with temperature between 1.8 K and 400 K. The nickel sample has been measured at different temperatures between 4.2 K and 300 K. Fig. III.36 displays the magnetization versus the applied field parallel to the sample at these various temperatures.

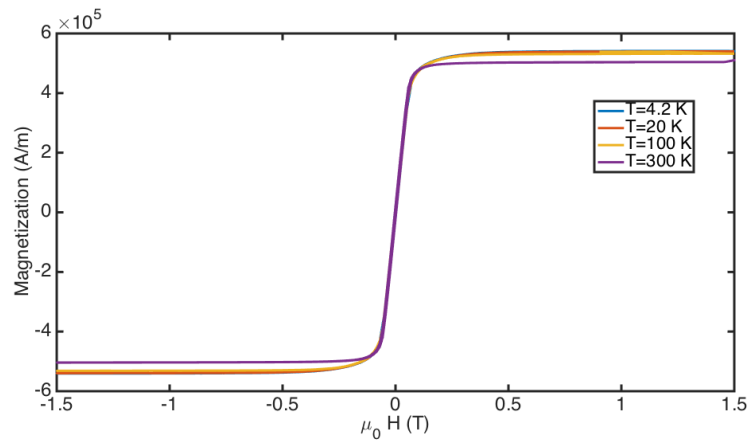


Fig. III.36 – Magnetization versus  $\mu_0 H$  of the nickel matrix with different temperatures.

No hysteresis has been measured in the sample whatever the temperature (below 300 K), while, in pure Nickel, hysteric behavior has been observed [172]. In our cases, the resolution of the sensor which is about 30 Oe (3 mT) can be a limitation. To validate these results, a measurement of relative permeability of the  $MgB_2$  wire in the normal state (100 K) was made. No hysteresis was also observed. From this measurement, it is possible to neglect the hysteric behavior. To measure the relative permeability with a field transverse to the sample, another magnetometer was used.

Fig. III.37 shows the relative permeability of nickel at 4.2 K with field longitudinal and transverse to the sample.

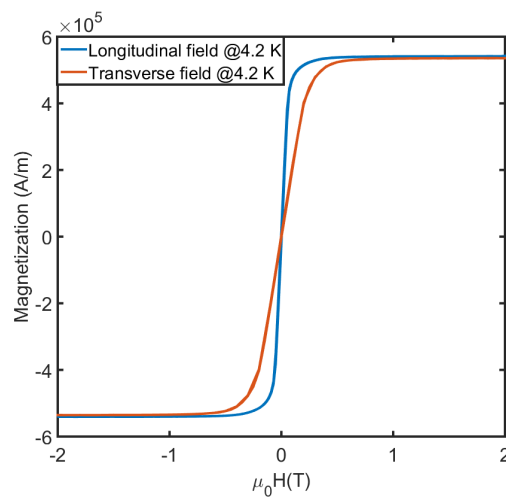


Fig. III.37 – Magnetization of the nickel at 4.2 K with transverse and longitudinal field to the sample.

The same conclusion can be drawn for the hysteresis behavior. The change of relative magnetic permeability can come from the shape of the sample but also from the cut. Heat treatments or high stress may also affect the hysteresis behavior and sometime annihilate it [173, 174]. However, the most reasonable explanation for a non-observable hysteresis may

be linked to the purity of the nickel sample which can have some others compounds in it. In our model we chose the longitudinal relative permeability as it is closer to usual nickel measurements.

### III.3.b-iii Monel

The monel layer is also supposed to exhibit a higher resistivity compared to the nickel to reduce eddy-current losses. The resistivity of the monel sample has also been measured and plotted in Fig.III.38.

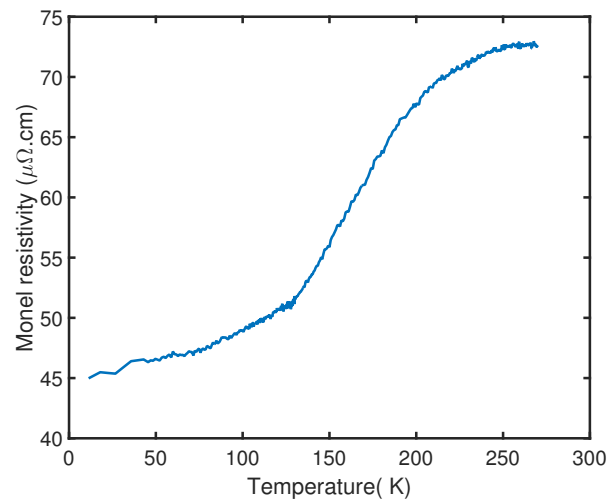


Fig. III.38 – Resistivity of the monel sample between 4.2 K and 300 K. The injected current was set at 10 mA.

As it was made on the nickel sample, the relative permeability of the monel sample was measured with a field longitudinal to the sample. Fig.III.39 displays the B-H curve at different temperatures.

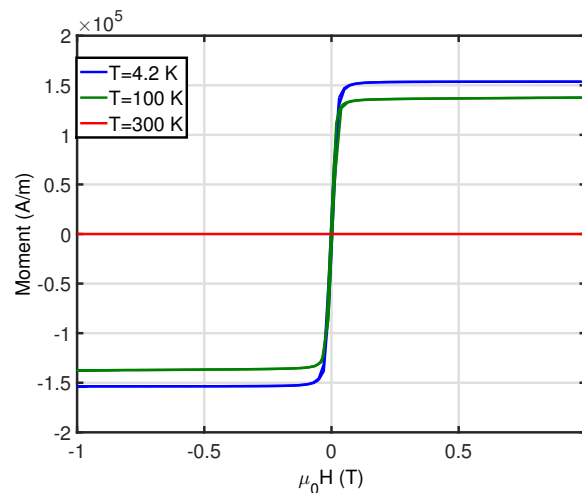


Fig. III.39 – Magnetization of the monel sample at different temperatures

At 300 K, the sample does not exhibit any magnetic behavior. Below 100 K, magnetization of the sample is saturated for values around  $1.5 \cdot 10^5$  A/m for magnetic flux density above 30 mT.

### III.3.b-iv Conclusion

In this section, the wire has been electrically characterized. After critical current measurements of these wires, the company Columbus provided us some nickel and monel samples. These samples have been made with the same heat treatment and mechanical process as the produced wires. The resistivity and the relative magnetic permeability of these samples which have been measured can be used for future calculations on real  $MgB_2$  wires. In order to build the complete model, some numerical calculations were made with almost the same geometry as the  $MgB_2$  wires and by taking into account the properties of the nickel matrix.

### III.3.c Preliminary numerical studies

Along the development of a realist numerical model on the complete  $MgB_2$  wire, including the properties of all materials. Several test cases have been conducted. By considering a  $MgB_2$  wire, different models have been created and tested. The objectives were, first to handle more and more complicated models with an increase number of elements. The second objective was to investigate on a possibility of predicting AC losses with various numbers of filaments and layers based on results made with 1, 2 or 3 layers of filaments. This is interesting as the architecture of the wire is likely to evolve.

#### III.3.c-i Description of the model

The calculations have been made on a 1.33 mm wire from Columbus with the nickel matrix (no monel so far). Fig. III.40 is a reminder of the cross-section geometry. The filaments which are sort of square have been changed to a circle with the same area to ensure a simpler and more regular mesh inside the filaments. In Fig. III.40 (right), is the cross section made on the software COMSOL with a color representation on the different layers of the wire.

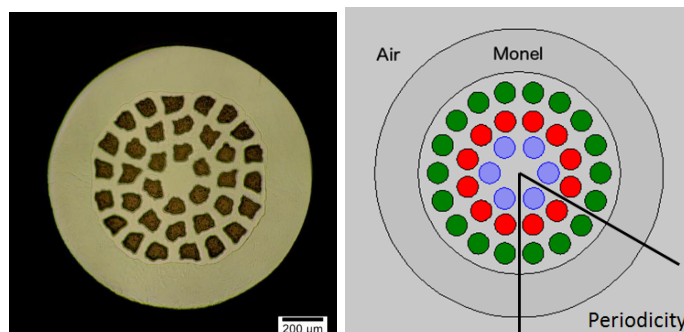


Fig. III.40 – 2-D cross section of a single  $MgB_2$  wire. On left the SEM image and on the right the numerical representation.

As the wire is not perfect, the diameter of the wire but also the size of the filaments evolve along the wire. To ensure a good precision on the values, several cuts and pic-

tures have been made on the wire and the parameters have been averaged. The geometric parameters of the wire are summarized in Table III.7.

TABLE III.7 – Geometric parameters for the 36-filament MgB<sub>2</sub> wire.

Parameters	Values ( $\mu\text{m}$ )
Filament radius	25
First layer radius	131
Second layer radius	251
Third layer radius	380
Outside nickel radius	430
Outside monel radius	650
Twist pitch (mm)	120

This geometry is twisted with a twist pitch of 120 mm (typical value for the produced wires). As the cross section of the wire has a 60° pattern (see Fig. III.40), it is possible to reduce the length of the wire to one sixth ( $60/360=1/6$ ) of the twist pitch to end with two same faces. Then periodic boundary conditions are forced to the model. A swept mesh was made starting from a normal face of the MgB<sub>2</sub> wire and extruded along a patch of one sixth of the twist pitch. This reduces the problem size substantially (84% smaller, i.e. one sixth of full wire model). After the creation of the prismatic mesh, the prisms have been cut in tetrahedra according to the technique in [175]. The electrical resistivity of monel is about two orders of magnitude higher than nickel (11.4 nΩ.m vs. 0.48 nΩ.m for nickel). We therefore decided to neglect this layer in these preliminary studies. Fig. III.41 displays the geometry with all the superconducting layers embedded in the nickel matrix delimited in green and the associated mesh.

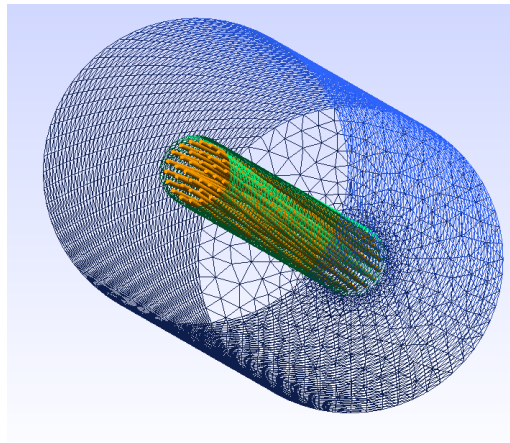


Fig. III.41 – MgB<sub>2</sub> preliminary model (with no monel) - geometry and mesh.

Starting from this 36-filament model shown in Fig. III.41, two simpler geometries were generated, firstly by considering only the 6 filaments in the inner layer, then by taking the 18 filaments of the two inner layers. For all geometries the outer radius of the nickel domain was kept constant. In order to ensure a fair comparison of AC loss computations, we used

the same finite element mesh for each simulation case that has been run. Daryl-Maxwell has been the primary software used in the calculations and some comparisons are made with FLUX and LoSt. Table. III.8 details the number of elements and degrees of freedom (DOFs) for the studied geometries, as well as typical computation times observed with Daryl-Maxwell finite element code, with 400 steps for 20 ms of simulated time.

TABLE III.8 – Key numbers for the studied geometries for Daryl-Maxwell code.

Geometries	6 filaments	18 filaments	36 filaments
Number of elements	93 960	347040	659 250
DOF (H-formulation)	110 540	405 980	770 725
Computation time	6 Hours	3 Days	12 Days

For all the cases in these preliminary studies, the properties of the model are listed below.

**Superconductor (MgB<sub>2</sub>)** The non-linear resistivity of the superconducting material was modeled with the power law model, i.e.

$$\text{Power law : } \rho(|\vec{J}|) = \frac{E_c}{J_c} \left( \frac{|\vec{J}|}{J_c} \right)^{n-1} \frac{\vec{J}}{|\vec{J}|}, \quad (\text{III.7})$$

The  $n$  value was set to 30 which is a good compromise between real measurements on MgB<sub>2</sub> wires [176] and the difficulty of convergence for the non-linear solver. After our experimental validations, it appears that this value is rather (see Fig. III.31) low compared to the real  $n$  values but it should not change the AC losses too much (see Fig. I.15). To compare the different geometries, the critical current was kept constant to  $I_c = 700$  A in all simulations, and the critical current density was determined by considering the total cross-section  $A$  of the filaments, i.e.  $J_c = I_c/A$ .

**Nickel** The electrical resistivity of the nickel was set as  $\rho_{nickel} = 0.48$  n $\Omega$ .m at 4.2 K (in agreement with [177] and measurements).

A smooth relationship can be deduced from the measurement of magnetic relative permeability in longitudinal field. This value was kept in all the directions.

$$B(H) = \mu_0(H + M(H)) = \mu_0(H + \sigma(\beta - 1) \tanh(H/\sigma)) \quad (\text{III.8})$$

Where  $\sigma_{nickel} = 7.5 \cdot 10^4$  A/m and  $\beta_{nickel} = 8.23$  have been found from the fit of the experimental data.

### III.3.c-ii Test cases on 6 filament wires

As first, the calculations of AC losses on a geometry made with only six filaments of the inner layer have been done. The simulations for cases defined in section III.1.d were performed on the 6-filament wire (3-D model simulated with DarylMaxwell). Fig. III.42 shows the AC losses in the case *air* for various transport currents and external field amplitudes [178].

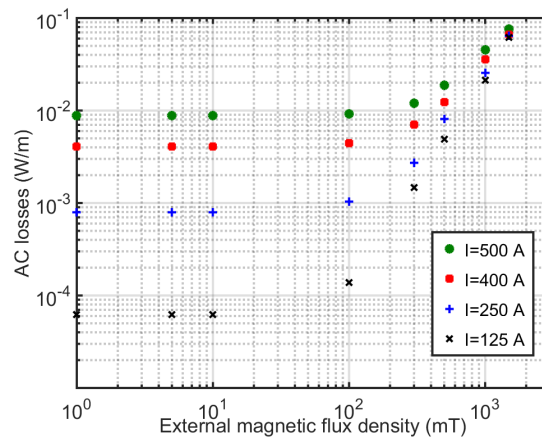


Fig. III.42 – Computed AC losses for the 6-filament wire and for the case *air* ( $I_c=700$  A).

Two different behaviors are observed for the AC losses. The first one is at low magnetic flux densities, where the AC losses are mainly self-field losses and are virtually independent of the applied field. The second behavior occurs at higher applied field (above  $\approx 500$  mT), where losses become larger than self-field losses. In this case, the AC losses are mainly generated by the action of the external magnetic field.

Fig. III.43 shows the results of the case *res*. Here, the software LoSt was used to validate the computed quantities as its formulation ensures no current in the air. The same trends as in case *air* are noticeable, although the slopes of the AC losses curves at high field are larger (i.e. we had  $\approx 1.4$  above, and now we have  $\approx 2.2$ ). This makes sense according to the theory: in a pure superconducting wire, the slope of the AC loss vs. applied field curve should tend towards 1 for fields higher than the penetration field, whereas in presence of a conducting matrix, it should tend towards 2 [179]. This is coherent with the fact that coupling losses prevail over hysteresis losses at higher field values and suitable frequency.

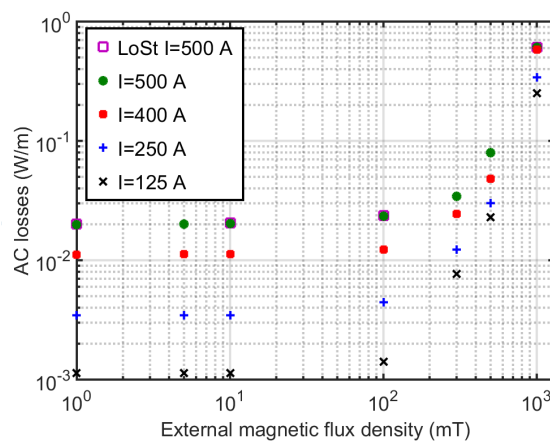


Fig. III.43 – Computed AC losses for the 6-filament wire and for the case *res*.

Finally, if we take into account the magnetic behavior of nickel by modeling its  $B-H$  curve, as suggested in case *mag*, we obtain the results shown in Fig. III.44. For low values of external field, we observe that AC losses decrease as the applied field increases.

This is explained by the reduction of the relative permeability of nickel as it saturates with increasing field (either self or external). Indeed, a high value of relative permeability concentrates the magnetic field around the filaments. When the external magnetic field is around  $\approx 100$  mT, this behavior stops. At even higher applied field (above  $\approx 400$  mT), we observe more or less the same trend as with case *res*, i.e. losses are mainly due to the coupling losses inside the nickel matrix (nickel completely saturated).

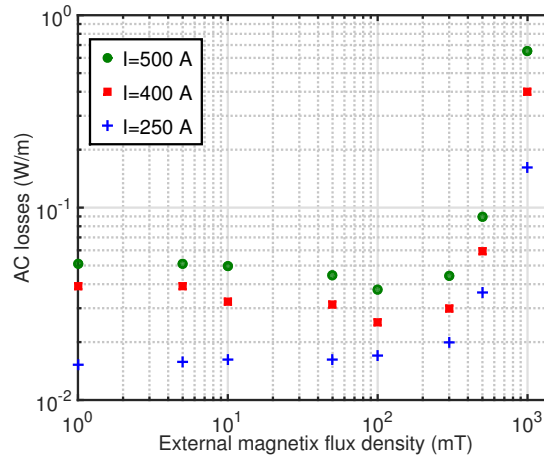


Fig. III.44 – Computed AC losses for the 6-filament wire and for the case *mag*.

From these simulations, the weight of each loss mechanism can be assessed, as shown in Fig. III.45 for an applied field varying from 1 mT to 300 mT and  $I=500$  A. The hysteresis losses have been calculated inside the superconducting filaments. Regarding losses in the nickel matrix, the losses coming from the eddy current were calculated with the use of a 2-D model taking into account the filament and the matrix as in III.1.b (no possible coupling losses in a 2-D model). In the 3-D model, the losses in the matrix include both eddy current and coupling losses. To quantify the two loss mechanisms, we subtracted the 2-D eddy current losses from the total 3-D losses in nickel to get a value for the coupling losses. In addition to that, the increase of the losses when one is taking into account the magnetic properties of the matrix was added. These increase have been observed to be mainly (90 % of it) located in the matrix.

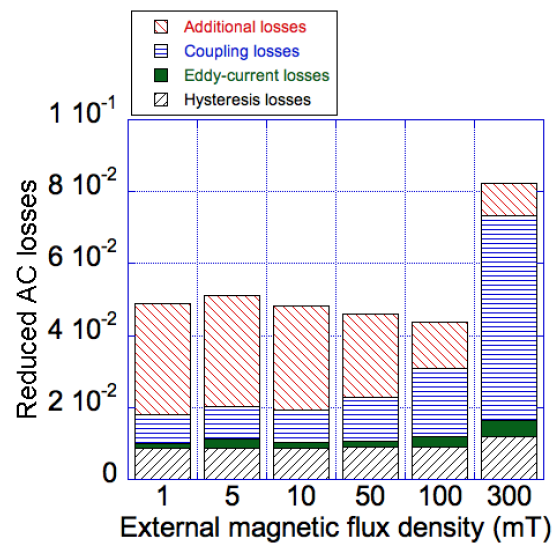


Fig. III.45 – Weight of each loss mechanism for the 6-filament wire. *Additional losses* refers to the additional losses resulting from taking into account the  $B(H)$  curve for the nickel matrix.

### III.3.c-iii Test cases on 18 filament wires

Our second test case is the 18-filament superconducting wire, which is just an intermediate step to test the limits of the software packages to solve problems with large numbers of DOFs. It is also interesting to see how AC losses evolve as we increase the number of filaments in the wire. Fig. III.46 shows the AC losses for case *air*, at various transport current and applied field values. Comments and trends observed in section above also apply directly to this figure, and are not repeated here. The AC losses for the 6 filament in the same case is also plotted as a comparison.

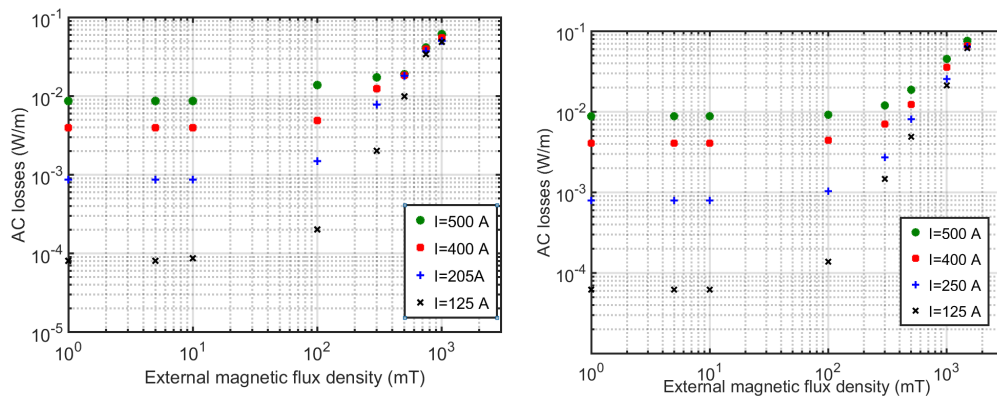


Fig. III.46 – Computed AC losses for the 18 filament wire on the left and the 6 filament on the right for case *air*.

The AC losses can be compared as the critical current was kept constant between the two geometries. At low field, we observed that the AC losses do not change between the two geometries. For high values of field, where the AC losses are mainly generated by it,

the AC losses are increasing for the 18 filament wire.

### III.3.c-iv Test cases on 36 filament wires

Only a limited number of simulations have been performed with the 36-filament wire model, due to the high number of DOFs, which leads to very long computation times. We considered only an air matrix for the moment, but there is no problem to take into account the resistive and magnetic behaviors of the nickel matrix, provided that we are willing to accept the associated increase in computation time ( $\approx 50\%$  longer than with the 18-filament model). Several tests have been made with a transport current of 350 A and different applied field values. The results are summarized in Table III.9. The results obtained with the different software packages are in good agreement for all the simulated cases. The difference is observed in the range of  $\approx 8\%$ . It is worth noticing that the choice of a formulation induces no significant change in the AC losses calculation. This shows that it is possible to compute the losses for a full 36-filament MgB<sub>2</sub> wire.

TABLE III.9 – AC losses (W/m) computed for the 36 filament MgB<sub>2</sub> wire and case *air*.

Current	External field	DarylMaxwell	LoSt	Flux
350 A	no	$3.210^{-3}$	$3.18.10^{-3}$	$3.23.10^{-3}$
no	50 mT	$2.73.10^{-4}$		$2.86.10^{-4}$
no	100 mT	$1.18.10^{-3}$		$1.25.10^{-3}$
no	300 mT	$9.8.10^{-3}$	$9.45.10^{-3}$	$1.05.10^{-2}$

All these simulations have been made to test our capability of modeling the actual MgB<sub>2</sub> wire for the calculation of AC losses in power cables. The results show that it is possible to calculate the AC losses if the computation time is not an issue.

The calculation on the real MgB<sub>2</sub> wire are developed in the section below. Two main additions have been made in the model : the monel layer but also the dependency of critical current with magnetic field.

### III.3.d AC losses for complete MgB<sub>2</sub> wires

#### III.3.d-i Adjustment of the geometry and physical properties

In this section, we calculate the AC losses on the real 1.33 mm MgB<sub>2</sub> wire with 36 filaments. Starting from the model disclosed in the previous section, some adjustments have been made. First a change on the geometry with the addition of the monel layer. The electrical properties of the monel were added according to the experiments detailed above. Moreover, the trend of critical current with field was implemented.

**Geometry** : The monel layer was build in the geometry according to the dimensions in Table. III.7. The new model is shown in Fig. III.47 were the monel layer is in orange.

Adding this layer increased the number of elements of the mesh. The mesh is now composed of 682 560 elements with a total of 798 520 Degrees of Freedom (DOF's).

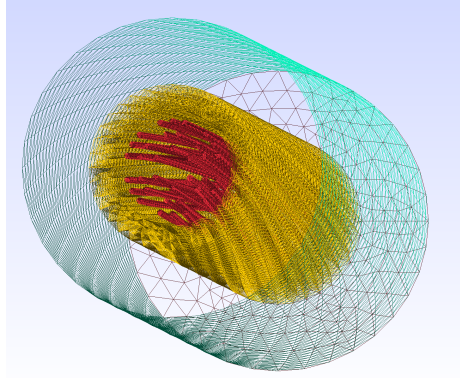


Fig. III.47 – Complete MgB<sub>2</sub> model - geometry and mesh. The 36 filaments are in red, while the monel layer is in orange. The air domain is delimited in light green.

**MgB<sub>2</sub>** : To model the non-linear resistivity of the superconducting material, the percolation law was used with the dependence of the critical current with magnetic flux density. This choice has been motivated by several aspects. First the AC losses calculations with the two different power laws are in good agreement. Added to this aspect, this model is dedicated for AC losses calculations in AC but also for practical use, meaning DC+AC calculations. From this view point, the percolation law is compulsory for accurate calculations (see IV.2).

$$\rho(\vec{J}, \vec{B}) = \frac{E_c}{|\vec{J}|} \left( \frac{|\vec{J}|}{J_{c0}} - 1 \right)^{n_0} \left( \frac{J_c}{J_{c0}} - 1 \right)^{-n_0} \text{ for } |\vec{J}| > J_{c0} \quad (\text{III.9})$$

For our simulations we choose the value of  $n_0=10$  which corresponds to a temperature of 4.2 K and a external field of 500 mT with  $J_{c0}=0.90.J_c$ . A polynomial fit for the critical current density versus magnetic flux density at 4.2 K was made according to data<sup>4</sup> measured in III.30 :

$$J_c(|\vec{B}|) = J_{c-sf} \cdot (1 + C_1 \cdot |\vec{B}| + C_2 \cdot |\vec{B}|^2 + C_3 \cdot |\vec{B}|^3) \quad (\text{III.10})$$

Where  $J_{c-sf} = 2.05 \cdot 10^{10}$  A/m<sup>2</sup>,  $C_1 = -0.542$  T<sup>-1</sup>,  $C_2 = 0.26$  T<sup>-2</sup>,  $C_3 = -0.0915$  T<sup>-3</sup>.

**Monel** : For the electrical properties of monel, the resistivity of the material was set at  $\rho_{monel} = 4.58 \cdot 10^{-7}$  Ω.m as it was measured at 4.2 K. For the relative magnetic permeability of the monel, a smooth relationship can be deduced from the measurement in longitudinal field.

$$B(H) = \mu_0(H + M(H)) = \mu_0(H + \sigma(\beta - 1) \tanh(H/\sigma)) \quad (\text{III.11})$$

The deduced fit from this measurement is listed the same as (III.11) with  $\sigma_{monel} = 2 \cdot 10^4$  A/m and  $\beta_{monel} = 8.64$ .

---

4. As it was not possible to measure the critical current with field for sample B, the critical current densities found for sample A were used.

### III.3.d-ii Results

The calculations have been made with two different transport currents (50-Hz sinusoidal) 500 A and 800 A which correspond to a reduced current ( $I/I_c(0\text{ T})$ ) of 0.34 and 0.55. The operating temperature was set at 4.2 K but as the resistivity of the nickel and monel does not change so drastically between 4.2 K and 20 K, only the change in critical current has to be considered from 4.2 K to 20 K. This is the reason why the AC losses in this section are reduced AC losses (division by the critical current at self field). The AC external magnetic field, in phase with the current was also added transverse to the wire. The analytical calculations are plotted by adding the coupling losses (equation (I.20)) and hysteresis losses (equation (I.28)). Two models have been tested. The real model with all the implementations above and referring as *full model*. This model takes about 18 days to compute in Daryl-Maxwell. To investigate the effect of the relative magnetic permeability of nickel and monel, a *reduced model* was also computed by taking into account everything except the relative magnetic permeability of the two metals. The reduced AC losses  $Q/(\mu_0 I_c(0\text{ T})^2)$  for a transport current of 500 A with external field is plotted below in Fig. III.48 and for a transport current of 800 A with external field in Fig. III.49.

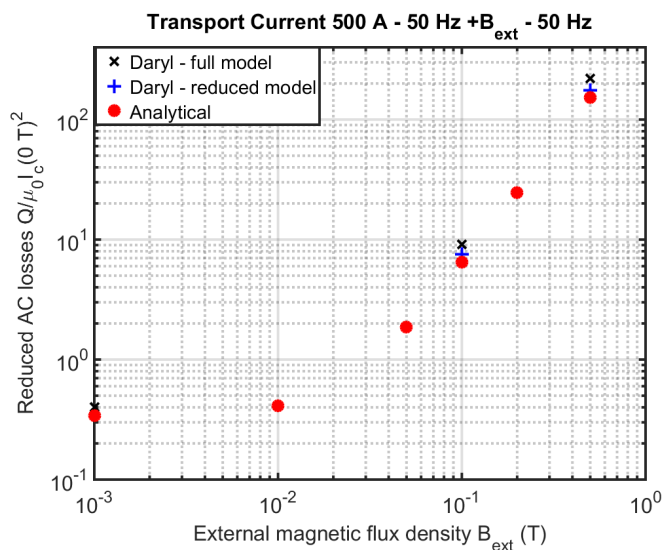
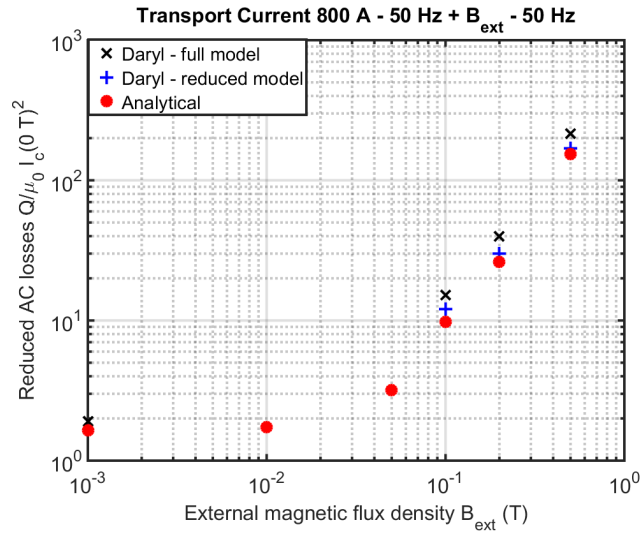


Fig. III.48 – AC losses for the MgB<sub>2</sub> wire with 500 A transport current

It is possible to see that the calculations from the *full model* but also the *reduced model* are higher than the analytical calculations. This is explained by the fact that several properties have been taken into account in the model compared to analytical calculations. As the log-log plot is good to see the trend of losses with regards to the field, but not the difference from one result to another. For comparison, table. III.10 gives all the computed quantities in reduced AC losses.

From this table it is possible to see that by summing the losses analytically, the difference between the result and the numerical model is 20 % to 30 %. For the reduced model, the main difference between analytical calculations and numerical results come from taking

Fig. III.49 – AC losses for the MgB<sub>2</sub> wire with 800 A transport current

$I_t$ (A)	$B_{ext}$ (mT)	Analytical	Full model	% variation	Reduced model	% variation
500	0	0.34	0.38	11	x	x
500	100	6.45	8.1	24	7.55	17
500	500	153	195	27	179	16.9
800	0	1.65	1.9	15	x	x
800	100	9.77	13.2	33	11.8	20
800	200	26.1	35.4	34	33.4	26.4
800	500	154	214.4	39	190.1	23

TABLE III.10 – Reduced AC losses  $Q/\mu_0 I_c^2(0\text{ T})$  from Fig. III.48 and Fig. III.48.

into account the monel layer but also the current density function of the field which are two causes of loss increase : current inside the monel and increase of the hysteresis losses due to a decrease of the critical current. From the reduced model to the full model, the difference is only done by taking into account the relative magnetic permeability which increases the value of the local field around the filaments. This effect tends to decrease the local critical current of the filaments which will increase the hysteresis losses.

Added to these explanations, it is possible to see, the total losses for a combined action of AC transport current and external field are very high and can not be used in a practical applications. This is explained by the wire is not being optimized to reduce AC losses (too much coupling losses).

### III.3.e To go further

The MgB<sub>2</sub> model was tested with success in various cases. The long computation time of the model (18 days max) is a limitation which makes the calculation not possible on the whole domain of operation. But as an increase of almost 30 % of the losses is observed

compared to analytical calculations, this approach can be necessary in some critical cases for the sizing of large scale applications. However, the AC losses are extremely high and these wires can not be used for AC large scale applications. Even in DC applications with AC ripples, the model should be performed to calculate with accuracy the AC losses as a difference of almost 30% is noticed between analytical calculations and numerical results (even 50 % in some cases). This is explained, by this wire not being designed to reduce coupling losses

As it was explained before, the diffusion barriers were neglected inside the numerical model because it would impact the mesh. Some codes allow the introduction of surface contact resistances, which may not perfectly take into account the diffusion layer geometry, but at least can model its resistance for further work. Another possibility is to model these barriers as shell elements coupled with the FEM. In our calculations, the diffusion barriers were neglected and the transverse resistivity was considered as the resistivity of the nickel sample. Some experimental work has been made to measure the resistivity of these barriers but the values are highly dependent of the quality of the MgB<sub>2</sub> compound but also the manufacturing process. However, these diffusion barriers have an effect of the coupling losses (coupling losses proportional to the conductivity of these barriers) and for reducing AC coupling losses, one way would be to add shields with high resistivity around the filaments combined with a reduced twist pitch.

### III.4 Conclusion

In this chapter, it has been reported 3-D numerical calculations on twisted multifilamentary geometries. Starting from a really simple model, numerous calculations have been carried out by taking into account several and complex electrical properties. As a first step, a three-filament wire has been designed and meshed specifically for an international benchmark involving the University of Tampere and Polytechnique Montréal. From these calculations, which gave very good agreements, the geometry was extended to more realistic cases by taking into account the electrical properties of the matrix surrounding the conductors. As this matrix may have an electrical resistivity but also a magnetic behavior (hysteresis or  $\mu_R(H)$ ), it was necessary to calculate the losses by considering these properties. From these tests, the good agreement between the software packages has been a way to be confident of the computed quantities. Finally, on this simple geometry, different E-J power laws and optimization techniques have been used to speed up the calculation which are mandatory for real models.

After the calculations on the-three filament wire, the model was adapted to real wires for AC losses calculations. Despite the long computation time (18 days), the calculations gave good estimates to see the differences between the computed quantities and analytical calculations. Some adjustments can be made in the used software to speed up the calculation (parallel solving) or improvement on the non-linear solver (relaxation coefficient algorithm).



## Chapter IV

---

# Towards the calculations of AC losses in high power cables

---

### CONTENTS

---

IV.1 CALCULATION OF AC LOSSES FOR HIGH POWER CABLES . . . . .	132
IV.1.a Multi-scale approach . . . . .	132
IV.1.b Examples . . . . .	133
IV.2 NUMERICAL MODELING OF AC LOSSES WITH DC BACKGROUND . . . . .	135
IV.2.a Limit of the power law model . . . . .	135
IV.2.b An alternative given with the E-J percolation law . . . . .	138
IV.2.c AC ripples superposed to DC current . . . . .	139
IV.2.d Conclusion on the E-J power laws . . . . .	142
IV.3 AC LOSS CALCULATIONS FOR MULTI-SINOSOIDALS WAVEFORMS . . . . .	142
IV.3.a Problem description . . . . .	142
IV.3.b Simulation and experimental validations . . . . .	143
IV.3.c Examples of applications . . . . .	147
IV.3.d Conclusion . . . . .	148
IV.4 RECOMMENDATIONS FOR THE CALCULATIONS OF AC LOSSES IN DC CABLES	149

---

### Summary

*In the two previous chapters, numerical models have been created to compute the AC losses in REBCO or MgB<sub>2</sub> conductors. In a REBCO application, 2-D models offer some possibilities to compute geometries with a large number of turns. However, if the idea is to be able to calculate the AC losses on a power cable to optimize the system, the principle of calculation has to be adapted. This approach is even more important for MgB<sub>2</sub> applications as the model is very heavy to solve for a single conductor. Instead of calculating the complete cable, one can do a multi-scale approach by first calculating the external magnetic field created on each wire and then the AC losses induced by the transport current and external field. As these conductors are well suited for DC applications, it is also necessary to investigate the numerical modeling of AC ripples coming from harmonics superposed to a DC background. These developments are divided into two components : first the calculation of an AC signal with DC background is studied and then a criterion on the calculation of multi-harmonics AC signals is presented.*

## IV.1 Calculation of AC losses for high power cables

### IV.1.a Multi-scale approach

As it has been explained previously, fast calculation of the AC losses created by a complete cable, is beyond today's computation capabilities if one is using a full description of a cable. The simulations would be time consuming and no optimization of the cable architecture could be done. To have a rough idea of the AC losses in a particular geometry of cables, one way is to do a multi-scale approach. In this method, a preliminary step is to calculate the AC losses on a single conductor with respect to transport current and external magnetic field values. After that, a calculation of the magnetic field distribution in the cable coupled with the knowledge of the AC losses can give rapidly an estimation of the AC losses for a particular geometry. Admitting that the preliminary step has been done, the calculation of losses is then very quick and optimization is possible. This method has been developed in a home-made code in MATLAB by C. Granger. The approach can be summarized into Fig. IV.1.

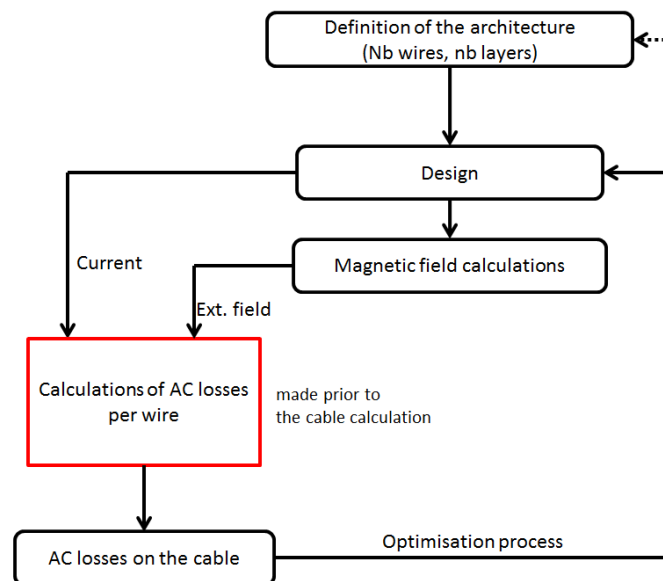


Fig. IV.1 – Principle for the AC loss calculation for a full superconducting cable.

In the AC loss calculations of a single wire, the external magnetic field is supposed to be in a straight direction, which is not the case in a power cable. However, as the magnetic field is a global quantity, the effect of a distortion of the field shall not be important. For example, in the case of  $\text{MgB}_2$  wires under the action of an external field, the coupling losses are the main mechanism of losses, hence, the most important parameter is, in this case, the peak value of the external field and not its direction. Nevertheless, it is mandatory to validate this approach on some examples to check the relevance of this method.

### IV.1.b Examples

Two examples of calculations in superconducting cables are presented, one with HTS round wires and one with MgB<sub>2</sub> conductors. These practical examples are not intended to be fabricated but are just used to show an example of result of the code for each conductor in AC applications. The AC losses for each conductor versus transport current and external field were given in II.3.b-v and in III.3.d-ii

#### IV.1.b-i Round wire cable

As it was seen in II.3, to reduce the AC losses in round wires, it is necessary to spread the conductors in order to lower the external magnetic field. One example is given with 18 wires carrying each 91 A ( $0.7.I_c$ ). The magnetic field distribution is plotted in Fig. IV.2. The calculations have been made in our code but the Fig. IV.2 is using the post-processing of COMSOL.

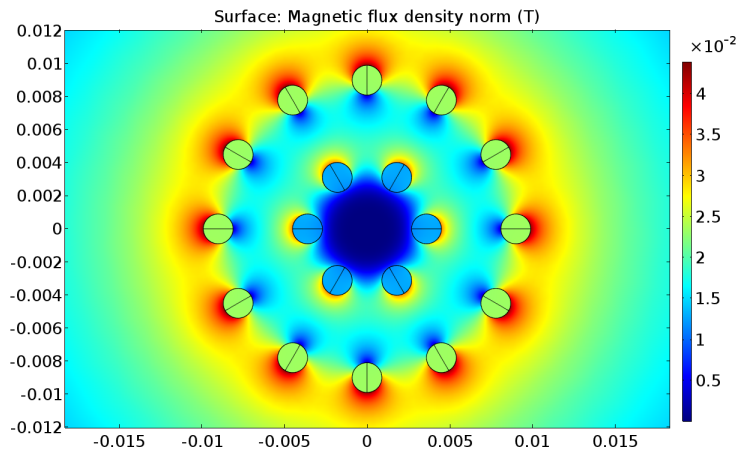


Fig. IV.2 – Magnetic field distribution (static) for a round wire cable example carrying 1.6 kA.

From this figure, it is possible to extract the average external field seen by each wire of the external and internal layers. By looking at the AC losses versus the transport current (91 A) and external field, the AC losses in the total cable can be calculated. All these data can be found in Table. IV.1

Layers	Current	External field	AC loss per wire (W/m)
External	91 A	24 mT	0.8
Internal	91 A	15 mT	$5 \cdot 10^{-3}$
		Total	$\approx 10$

TABLE IV.1 – AC losses calculation for the complete cable round wire in AC condition (50 Hz) with a rated current of 1.6 kA.

The AC losses calculated with this method are about 10 W/m (9.63 W/m) which is still very high compared to the cryogenic envelope (2-3 W/m). As this model is simple to compute, we performed the FEM analysis of this particular case, we found a value of

10.45 W/m. A difference of 8 % is observed and can be explained as in the model made to calculate the AC losses on one round wire in II.3.b-v is using a homogeneous external field, which is not the case in the cable. This validates the approach used in our calculations. It is then possible to change the configuration of the cable to decrease the losses.

#### IV.1.b-ii MgB<sub>2</sub> cable

Superconducting cables made with MgB<sub>2</sub> wires are highly promising if one wants to carry high currents in reduced spaces. The example is one cable capable of carrying 10 kA with 18 MgB<sub>2</sub> wires. Each wire is 1.33 mm in diameter and is fed with a current of 500 A and a frequency of 50 Hz. As it was shown before, these wires dissipate too much AC losses in the case of AC current or fields. It is just an example to give a idea on this type of calculations. The distribution of magnetic field of the MgB<sub>2</sub> cable is shown in Fig. IV.3.

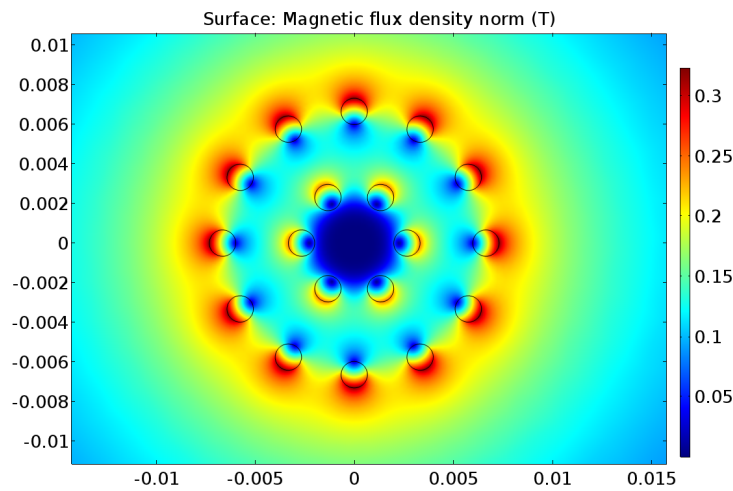


Fig. IV.3 – Magnetic field distribution (static) for a MgB<sub>2</sub> cable example.

The AC losses can be found in Table. IV.2 following the calculations made in III.3.d-ii.

Layers	Current	External field	AC losse per wire
External	500 A	189 mT	77 W/m
Internal	500 A	120 mT	30 W/m
		Total	1.1 kW/m

TABLE IV.2 – AC losses calculation for the complete MgB<sub>2</sub> cable in AC condition (50 Hz) with a rated current of 9 kA.

The AC losses are very high for this conductor to be considered for AC applications. For DC applications, the results on the AC losses calculations on a given cable are given in the next chapter. Unfortunately, as this model of cable would be very heavy to be solved in 3-D, no comparison can be made but the fact that the fist example gives a rough estimation of AC losses compared to the FEM full model is very promising.

We have developed one approach for the calculations of AC losses in large superconducting cables with multiple conductors. This code is validated on a simple example and gives quick results if we know in advance the AC losses of a single conductor when it is exposed to an external magnetic field and a transport current in phase. However, two examples have already shown some limitations for these superconductors for AC applications as they tend to generate too much AC losses. At 77 K, AC losses applications can be made as the cost of nitrogen is low. It is even possible to decrease the temperature of liquid nitrogen down to 66 K by decreasing the pressure of the bath. This doubles the performance of the conductor. It seems almost clear, that the effort for the production of large-scale applications with superconductors should be mainly focused for DC usage. It is now interesting to focus our calculations on signal with AC ripples superposed to DC background.

## IV.2 Numerical modeling of AC losses with DC background

As the source, which feeds the DC application (for example a cable) is not perfect, the current will contain harmonics (or ripples). It is then important to calculate the AC losses induced by these AC signals superposed to a DC current. In the Bean model, the AC self-field losses are not impacted by an addition of a DC current as long as the peak value of current is below  $I_c$ . This feature is found in experiments, for example in HTS tapes. However as we do not use the Bean model in our numerical calculations, it is important to study AC ripples superposed to a DC background with the two E-J power laws. In this section, we only focus on a AC ripple with a fundamental frequency of 50 Hz with an amplitude  $I_{AC}$  superposed to a DC current  $I_{DC}$ . The following section IV.3 reports the calculations we made on signals with multiple frequencies.

### IV.2.a Limit of the power law model

The power law model which is mainly used by the community for the calculations of AC losses do not represent the correct behavior of the conductor in DC conditions [180]. To understand the fundamental error we made by using the power law to simulate the actual behavior of the conductor, it is possible to do a simple example. We considered a cylinder with a radius of 1 mm and a critical current of 130 A. The critical current is considered to be constant with field, the voltage criterion is  $E_c=1 \mu\text{V}/\text{cm}$  and the  $n$  value is, at first, equals to 30. A DC transport current of 65 A is imposed to the cylinder after a ramp up time of 5 ms. The current is maintained constant over time and the evolution of the distribution of current is recorded. Fig. IV.4 displays the current density distributions in the cylinder at various times. In these figures, the scale is kept constant with a maximum value at  $J_c$ . At  $t=0$  s the current starts to be constant at 65 A.

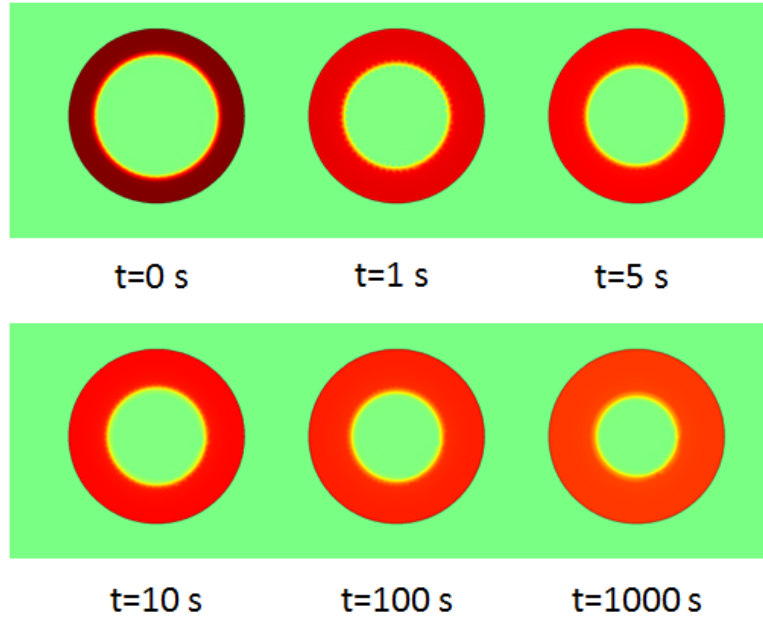


Fig. IV.4 – Current density distributions at different times when a DC transport current is imposed in the conductor with the E-J power law.

According to Fig. IV.4, the current penetrates into the superconducting cylinder even when the current is constant. It follows a decrease of the current density values inside the cylinder. At a time of  $5.10^5$  s, the cylinder is completely full with a current density value homogenous in the cylinder which corresponds to 65 A divided by the area of the cylinder. *As soon as the cylinder is completely full, it starts to dissipate with a very low value of resistivity.* Another way to understand this phenomenon is to look at the resistivity of the superconducting material which is modeled as :

$$\rho(J) = \frac{E_c}{J_c} \left( \frac{J}{J_c} \right)^{n-1} = \rho_0 \left( \frac{J}{J_c} \right)^{n-1} \quad (\text{IV.1})$$

In this equation, the resistivity is only zero when the current density is null. At 5 ms when the current reaches the value of 65 A, the resistivity of the material is not uniform. The area which carries the current density  $J_c$  (50 % of the cylinder area) exhibits a resistivity equals to  $\rho_0$  while the area in virgin state as a resistivity of zero. The phenomenon of current penetrating inside the cylinder tends to make the resistivity uniform in the cylinder. This is achieved when the cylinder is completely penetrated. When this moment is reached, the resistivity of the cylinder is equal to  $\rho = \rho_0 0.5^{n-1}$ . This result is in contradiction with the critical state model and the fact that only a portion of the conductor carries a fixed current density.

The velocity of current penetration inside the cylinder is directly linked to the shape of the power law i.e. the value of  $n$  as it can be seen in Fig. IV.5. After the current is set constant, the maximum current density in the cylinder is plotted over time with various  $n$  values. Having high  $n$  values is equivalent as solving a quasi-static problem close to the Bean model. This means that the current densities are frozen inside the material when the

current stays constant. It is likely, that if the  $n$  value is infinite, the evolution of current density inside the material will be stopped.

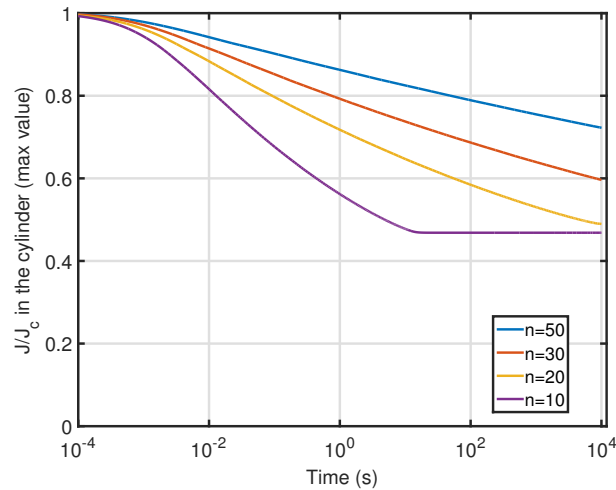


Fig. IV.5 – Evolution of the current density value versus time with the power law and various  $n$  values.

The penetration of current inside the cylinder, will induce losses based on the same principle as the AC losses. For example, if one is considering an AC signal superposed to a DC current, the instantaneous AC losses versus time is shown in Fig. IV.6. An AC signal with  $I_{AC}=40$  A is superposed to various DC current values. The AC ripples start at 20 ms. In the figure, only the portion after 35 ms, is interesting as the losses before this value of time are the consequences of the establishment of the local current densities due the non-linear phenomenon of the superconductor.

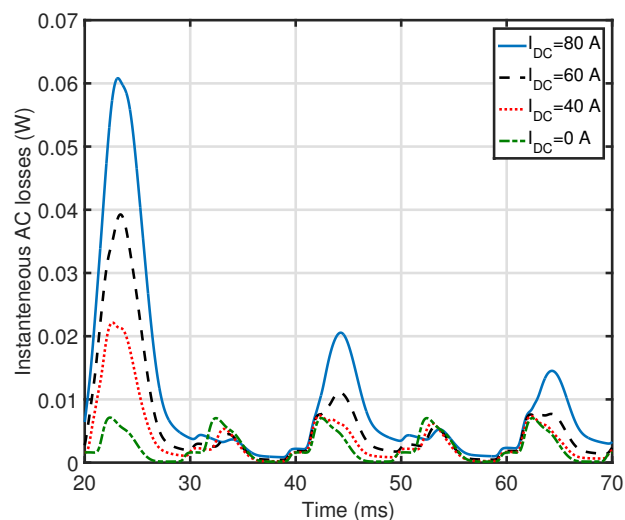


Fig. IV.6 – Instantaneous AC losses with various DC currents with the E-J power law.

In this figure, it is clearly visible that the instantaneous AC losses are increasing with the increase of  $I_{DC}$  which is linked to the penetration of current inside the material. It is also possible to see that the differences between the instantaneous losses is decreasing over time. The AC losses are constant as soon as the cylinder is completely penetrated. In other work, some results show that it is necessary to compute at least 50 periods to observe a identical value of AC loss with or without DC current [181], we used this reference of the infinite case.

#### IV.2.b An alternative given with the E-J percolation law

As it has been suggested in I.1.e-iii, the percolation law can be used as a reasonable alternative to model the actual behavior of the superconductor in DC conditions. The percolation law is given with the two quantities  $J_{c0}$  and  $n_0$  :

$$\rho(|J|) = \frac{E_0}{|J|} \left( \frac{|J|}{J_{c0}} - 1 \right)^{n_0} \text{ if } |J| > J_{c0}, \rho=0 \text{ else} \quad (\text{IV.2})$$

In the equation  $E_0 = E_c (J_c / J_{c0} - 1)^{-n_0}$  is a reduced voltage criterion. This percolation law does not only exhibit a better correlation with the experiment (see II.2.e-ii), it also has a resistivity equal to zero for a wide range of current density values between 0 and  $J_{c0}$ . Starting from the same model presented in the previous section, it is likely that when the current is penetrating inside the conductor, the value of current density will be mainly around  $J_c$ . After the DC condition is reached, the current will also start penetrating as it was observed with the power law. When the current density reaches the value of  $J_{c0}$  inside the conductor, the resistivity of the cylinder is everywhere equals to zero which means that the equilibrium point is reached. The same calculations for the maximum current density in the cylinder over time can be made and is plotted in Fig.IV.7.

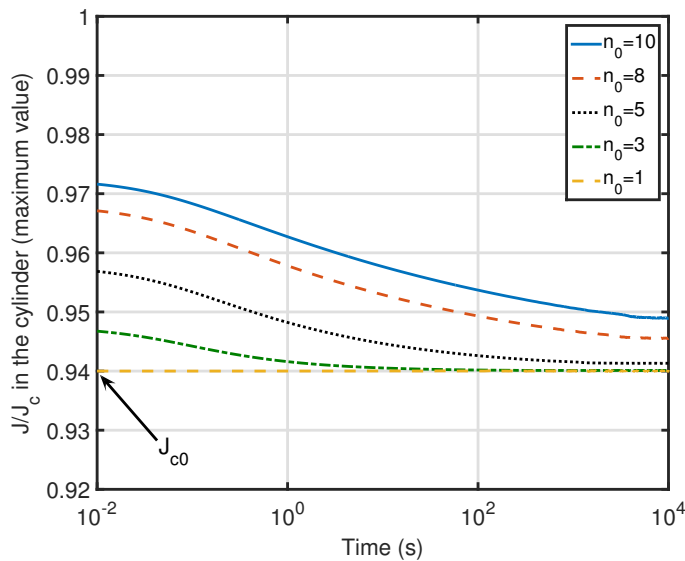


Fig. IV.7 – Evolution of the current density value versus time with the percolation law.

Consequently to a change of power law, the  $n_0$  value is lower and the equilibrium point is reached much faster. Also, when DC conditions are reached, the value of current density inside the cylinder is not equal to  $J_c$  but  $J_{c0}$ , which is very close to  $J_c$  ( $J_{c0}=0.9J_c$ ). In all these calculations, the equilibrium point is reached after few periods and no large change of current density is noted inside the conductor. In addition to these results, the low value of  $n_0$  leads to a more uniform current density when the current penetrates inside the cylinder.

### IV.2.c AC ripples superposed to DC current

In II.2.e-ii, it has been shown, that the two power law models are in good agreement in pure AC losses calculations and experiments. In the case of an AC ripple superposed to a DC background, it has been quickly shown, that the losses are highly depend upon the power law models. *Experimentally it was noticed, that for peak current values below the critical current, no increase of AC losses has been observed with the addition of a DC current.* Our numerical models which, are dedicated to DC applications with AC ripples created by harmonics can be tested with this kind of current waveform to assess the differences. In a 2-D numerical model, a AC ripple of 5 A (50 Hz) is superposed to a DC current. The AC losses are computed in the 1<sup>st</sup> periods of the signal after the steady state is reached and in the 4<sup>th</sup> and 50<sup>th</sup> periods as shown in Fig. IV.8. In addition in the figure, the instantaneous losses for the power law model ( $n=30$ ) are shown.

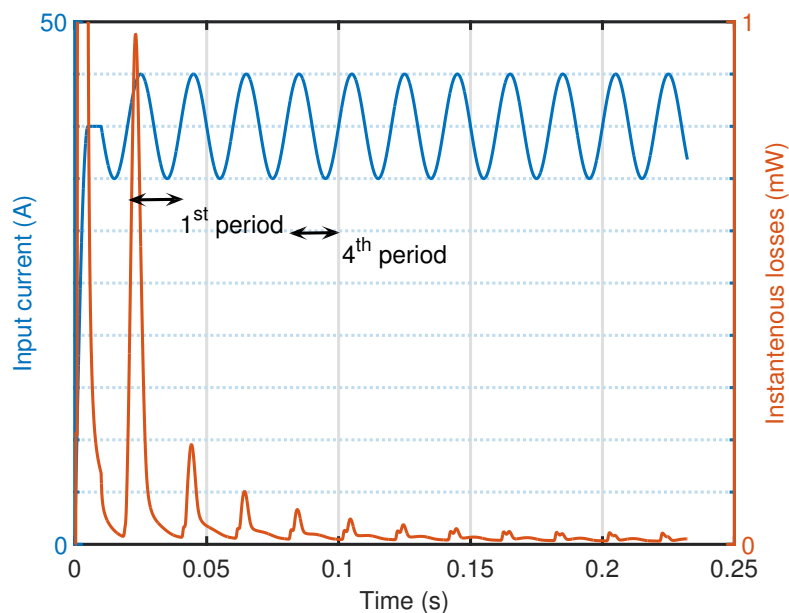


Fig. IV.8 – Waveform of AC ripples superposed to a DC current with the power law.

Various DC currents have been simulated including the case of pure AC signal with the power law model ( $n=30$ ). The AC signal is sinusoidal with a frequency of 50 Hz. The AC losses for the 1<sup>st</sup>, 4<sup>th</sup> and 50<sup>th</sup> periods are reported in Fig. IV.9. The calculation for the 50<sup>th</sup> has been considered as infinite [181].

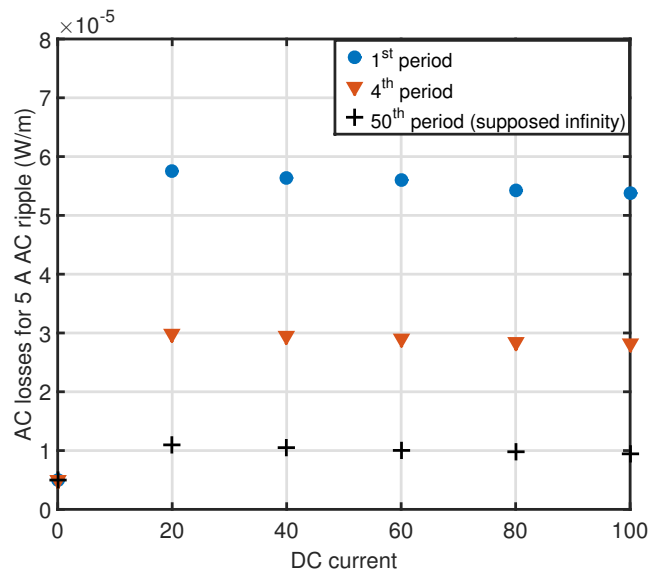


Fig. IV.9 – AC losses created by AC signals superposed to DC background current with the E-J power law.

As it was expected from IV.2.a, the losses are highly dependent on the addition of a DC current. The AC losses are expected to be around  $5 \cdot 10^{-6}$  W/m and the results found for the 1<sup>st</sup> and 4<sup>th</sup> periods are more than 10 times higher. Even for the 50<sup>th</sup> period the AC losses found with a DC current are almost twice the expected value. This is explained by the penetration of current not reaching inside the conductor. At the infinity time the AC losses will also be higher as the superconductor is fully penetrated by the DC current. Unfortunately it was not possible to calculate the AC losses for AC ripples superposed to DC current when the penetration is reached as it would be time consuming to simulate an AC signal up to  $5 \cdot 10^5$  s.

The same simulations have been made with the percolation law. The results are shown in Fig. IV.10.

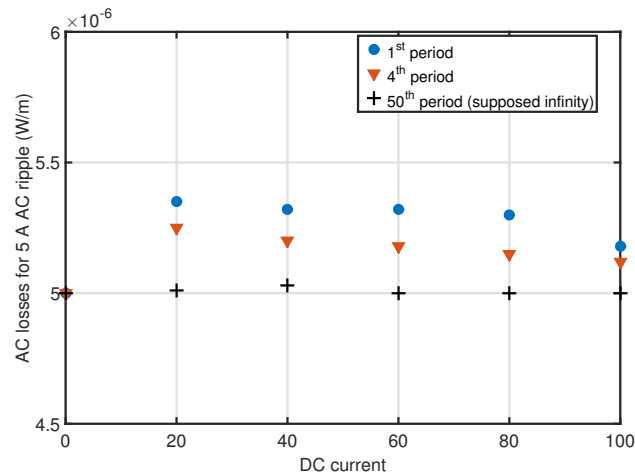


Fig. IV.10 – AC losses created by AC signals superposed to DC background current with the E-J percolation law.

The AC losses in the case of the percolation law are less dependent of the addition of a DC current. First we can notice that the values of AC losses at the first period are different by 8 % compared the value for pure AC. For the 4<sup>th</sup> period the difference is lower than 5 % and the AC losses found for a AC ripple superposed to a DC current for the 50<sup>th</sup> are the same as pure AC. In Fig. IV.11, the two results with the two different power laws are plotted.

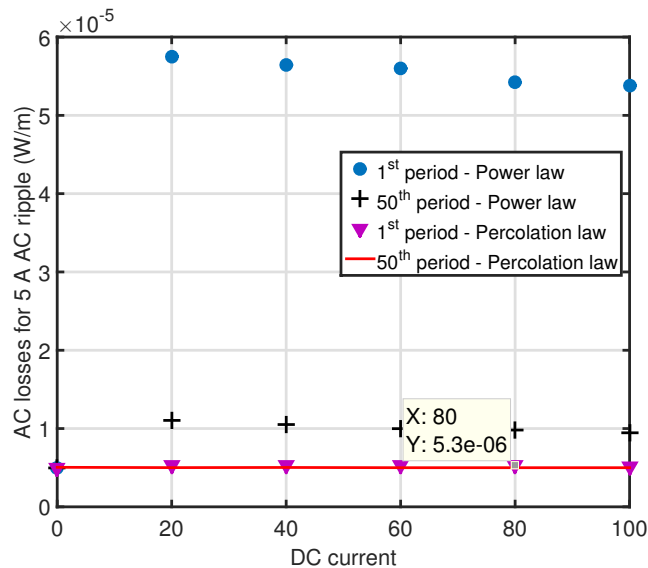


Fig. IV.11 – AC losses created by AC signals superposed to DC background current with the E-J percolation

From this figure, it is clearly visible that the percolation law is more suited for AC ripple superposed to a DC current as even the 1<sup>st</sup> period gives result with an acceptable difference.

#### **IV.2.d Conclusion on the E-J power laws**

In this section, we have been studying the influence of the two power laws with numerical calculation of AC ripples superposed to a DC background.

The power law model that is largely used by the community has shown its limit when a DC current is imposed to the numerical model. This is in accordance with already published work [180]. For pure AC signal, the problem is not visible which explains the reason why no work has been made on this fundamental problem (i.e. the current distribution evolution over time). Results in II.2.e-ii have shown that the power law model presents good correlations with experimental results. However, when one is considering AC ripples superposed to DC signals, the power law may induce large errors in the AC losses calculations due to the penetration of current inside the superconductor. This issue can be a problem leading to an over estimation of the losses besides the fact that at an infinite time the model is in contradiction with the superconducting state.

We focused on experimenting another E-J fit called percolation law. This percolation law has provided more realistic result with the AC losses calculations with or without DC background and we are confident about the fact that this power law is in agreement with the superconducting properties. Unfortunately, the fit of the experimental point of the E-J characterization is more complicated as it involves a couple of parameters. This reason coupled to the fact that the AC losses calculated with the power law are very close in pure AC, is one of the explanation on why this percolation law has to be more deeply investigated over the coming years.

However, it is difficult to give more credit to the percolation law compared to the power law model. These two models are a description of the macroscopic evolution of electric field with current and do not intend to describe the complete behavior of the conductor but give validated results for AC losses calculations. More developments are required to find more realistic models.

### **IV.3 AC loss calculations for multi-sinoidals waveforms**

#### **IV.3.a Problem description**

In last section, the AC losses created by ripples superposed to a DC signal have been calculated. To simplify the calculation, only AC signal at 50 Hz was considered. In reality, the harmonics created by the environment of the cable are likely to be spread on a large range of frequencies with various amplitudes. These AC ripples called harmonics in classical power systems can come from a non-perfect source of DC current for example. In general the considered harmonics are between 50 Hz and 2 kHz and their amplitudes are given by what is called a FFT of the harmonic spectrum.

As these harmonics are really dependent of the converters used in each part of the network and the upper limit of frequency is high, simulating the complete spectrum of harmonics for AC losses can be time consuming and not adapted for industrial calculations

(expected to be quick). If we consider harmonics coming from frequencies from 50 Hz to 2 kHz it is necessary to calculate the AC losses on a complete cycle of 50 Hz with a time step in agreement with Shannon theorem for the 2 kHz signal (maximum time step of  $2.5 \cdot 10^{-4}$  s).

In this thesis, we studied the effects of the AC losses with multi-frequency signals and suggest a criterion. Instead of taking into account all the harmonics of the signal, we calculate the AC losses at the fundamental frequency (50 Hz) with an amplitude equals to the summation of all the harmonics (shape signal). Taking into account only a signal at 50 Hz will improve the convergence of the system and speed up the calculations. This hypothesis comes with an intrinsic error as the signal is not the real one. In our calculations, our criterion has been to set a upper limit of 10 % difference between the AC losses of the real signal and the shape signal.

### IV.3.b Simulation and experimental validations

In this section, several tests with different waveforms have been made to test the criteria for AC losses calculations. Before considering harmonics on a real case, some calculations have been made with waveforms composed of two or three sinusoids. To begin with a simple case of study, only a summation of two sinusoidal waveforms was used. The constitutive equation of the final waveform is :

$$I(t, m, k, \alpha) = I_{ac}(\sin(2\pi \cdot 50 \cdot t) + m \sin(2\pi k \cdot t + \alpha)) \quad (IV.3)$$

The current is an addition of a sinusoidal current with an amplitude of  $I_{ac}$  and a frequency at 50 Hz and a second sinusoid with an amplitude of  $m \cdot I_{ac}$ , a given frequency  $k$  (between 50 Hz up to 2 kHz) and a phase shift  $\alpha$ . The AC losses will be compared to the shape current which is a sinusoidal waveform with a 50 Hz frequency and an amplitude  $I_{peak} = (1 + m) \cdot I_{ac}$ . One can notice, than this waveform is obtained when the frequency  $k$  is equal to 50 Hz and the phase shift  $\alpha$  is zero. A drawing of the two waveforms and the shape current in red is displayed in Fig. IV.12 with  $m=0.3$ .

From (IV.3), a sensitivity study can be achieved with four parameters. At first the parameter  $m$  was set at 0.1, which is an upper limit value for harmonics on an AC current. No phase shift was added in these simulations. Fig. IV.13 displays the AC losses with  $k$  between 50 Hz and 2 kHz with different  $I_{ac}$ . The circles represent the experimental results (noticed as  $E$ ) and the crosses the numerical model (noticed as  $C$ ). The experimental points have been made using the bench presented in II.2.e-i

The AC losses are nearly constant with the addition of the second sinus and the change of its frequency. Only low frequencies give different results in terms on AC losses. This can be explained by the peak value of the distorted current which can be lower when the frequency of the second sinus is close to 50 Hz whereas when  $k$  is above 500 Hz,  $I_{peak}$  is constant and equals to the value at 50 Hz. The experimental and numerical results agree with an error lower than 5 %. It can be noted that the AC losses does not depend so much on the addition of the second sinus which validates the criterion of using a shape current

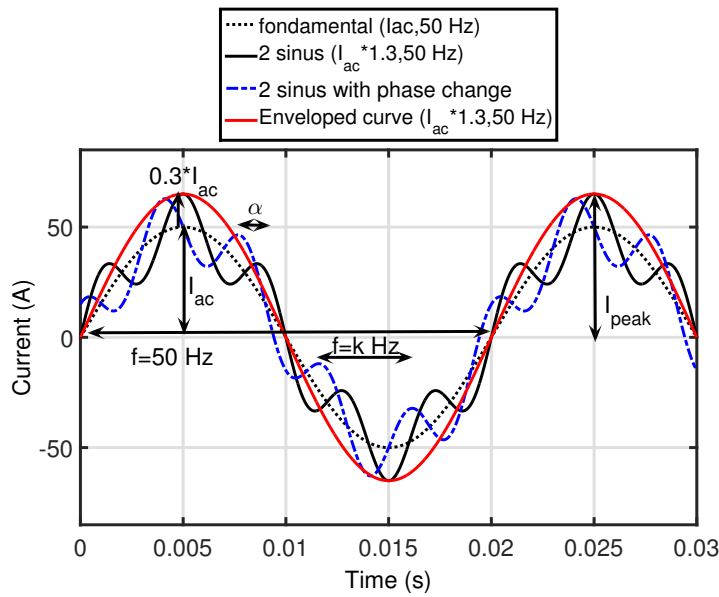


Fig. IV.12 – Waveforms for the 2 sinus calculations with  $m=0.3$ .

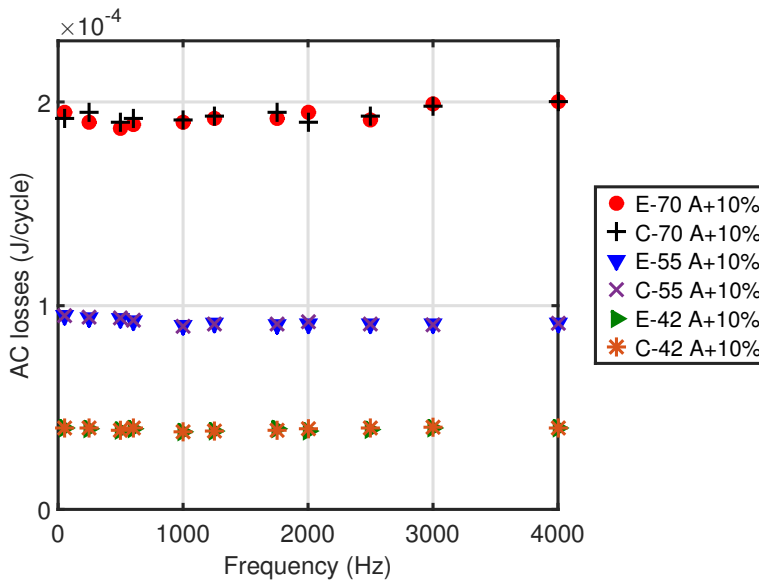


Fig. IV.13 – AC losses versus frequency for  $m=0.1$  and  $\alpha=0$ . The 'E' labels are the experimental results and 'C' the numerical results.

taking into account both amplitudes of the two sinusoids. The change in AC losses with the phase shift (with  $k=250$  Hz) is displayed below. Due to symmetric considerations, only the AC losses with a shift angle between  $0^\circ$  and  $180^\circ$  are plotted. This has been modeled to see the impact of the phase shift from one sinusoid to the other in Fig. IV.14.

Once again, the addition of the second sinusoid has no impact on the AC losses. This result is confirmed experimentally and numerically with an excellent correlation between them. From this set of results, it can be noted that the AC losses do not depend on the

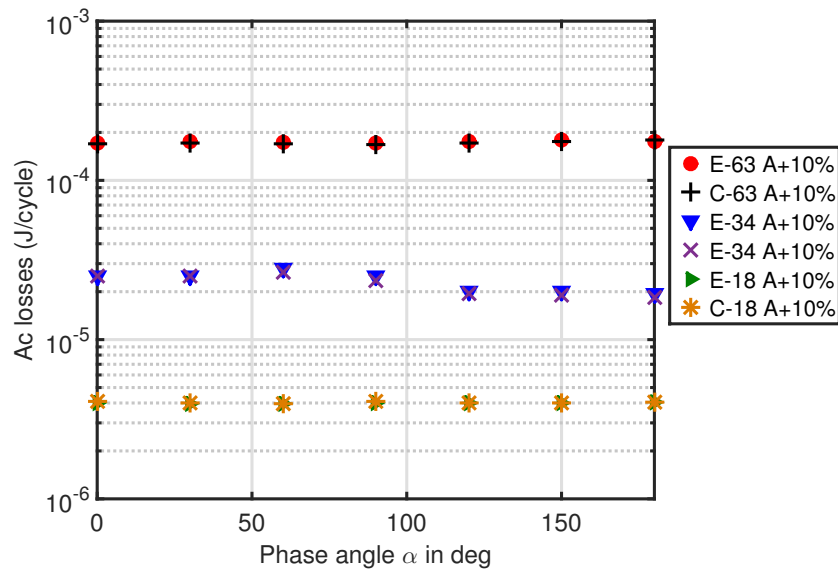


Fig. IV.14 – AC losses vs phase change (in degree) with  $m=0.1$ . The 'E' labels are the experimental results and 'C' the numerical results.

waveform of the real current but on a shape current which has an amplitude equal to the peak value of the real current. As a limit case, the  $m$  value was multiplied by a factor of 5 ( $m=0.5$ ), this can be the case with DC application where two harmonics of currents are generated by the current source. The results are plotted in Fig. IV.15.

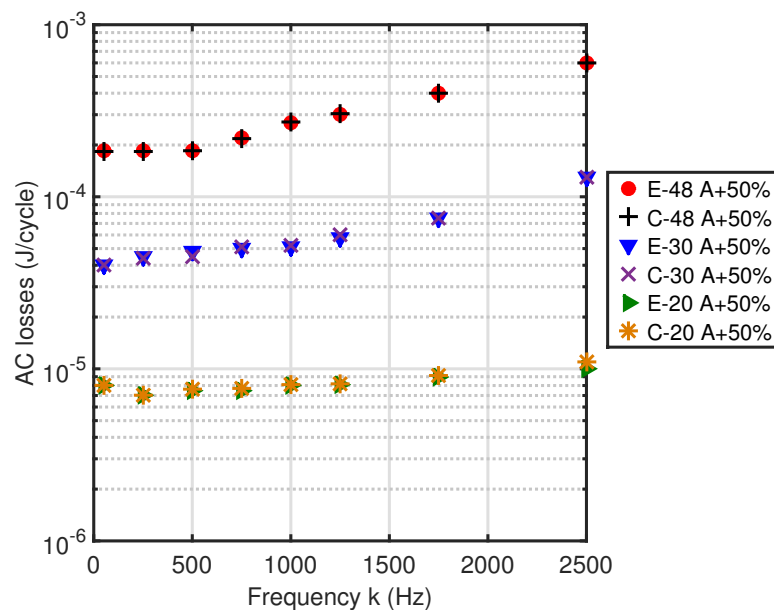


Fig. IV.15 – AC losses vs frequency with  $m=0.5$ . The 'E' labels are the experimental results and 'C' the numerical results.

The numerical model is once again in agreement with the experimental results, with a little deviation at 2.5 kHz. The AC losses are increasing with the frequency for a current amplitude equal to  $I_{ac}=48$  A and  $I_{ac}=30$ A. In these cases, a varying current with an amplitude of 24 A and 15 A respectively dissipates more AC losses at high frequency and influences the overall AC losses. With  $I_{ac}=20$  A, the slope of the AC losses with the frequency is almost flat but is likely to increase with large values of frequencies. From this set of measurements, the FEM model agrees with an excellent accuracy. The error in every case is less than 5 %, which is rather good considering that the criterion used aims to assess the AC losses with a 15 % margin. Only an m value equal to 0.5 with high frequency dissipates more AC losses than the AC losses of the envelop current.

After the exploration of a two-sinusoid waveform, the model was extended with a current made of a summation of three sinusoids. This distorted current was created with an arbitrary waveform GBF connected to a KEPCO linear amplifier. Firstly, the equation used was :

$$I(t, m) = I_{ac} [\sin(2\pi \cdot 50 \cdot t) + 0.5 \sin(2\pi 300 \cdot t) + 0.2 \sin(2\pi k \cdot t)] \quad (IV.4)$$

Fig. IV.16 shows the AC losses measured and calculated for the equation (IV.4). The envelop current with a frequency of 50 Hz and the amplitude of  $0.6I_{ac}$  is displayed in Figure 8 at the frequency of 50 Hz.

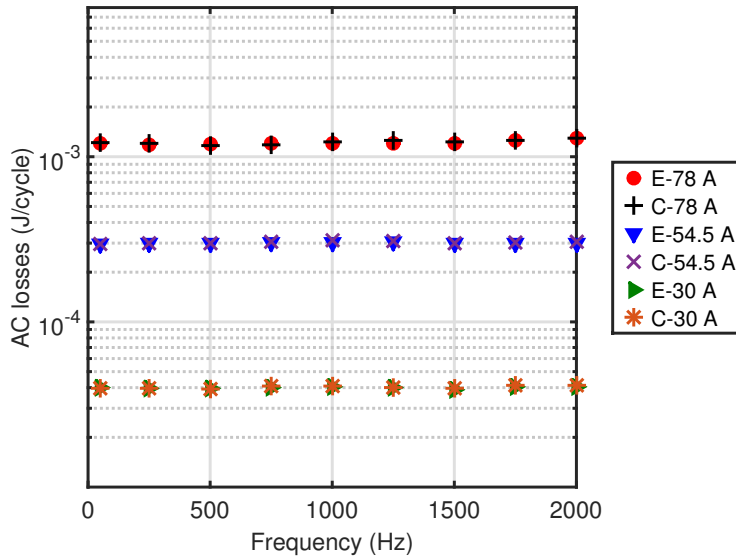


Fig. IV.16 – AC losses vs frequency with the waveform given in (IV.4).  $E$  is referring to experimental results and  $C$  COMSOL. The value after is  $I_{ac}$

Once again, the AC losses do not depend on the frequency of the third current. The measurements are in agreement with numerical modeling. From now on, only numerical modeling results are shown. The results below validate the numerical model compared with experiments and can be extended to a general study. A second waveform was used with more realistic harmonic amplitude decreases. The equation used is :

$$I(t, m) = I_{ac}[\sin(2\pi \cdot 50 \cdot t) + 0.15 \sin(2\pi 300 \cdot t) + 0.05 \sin(2\pi \cdot k \cdot t)] \quad (\text{IV.5})$$

The AC losses are displayed in Fig. IV.17.

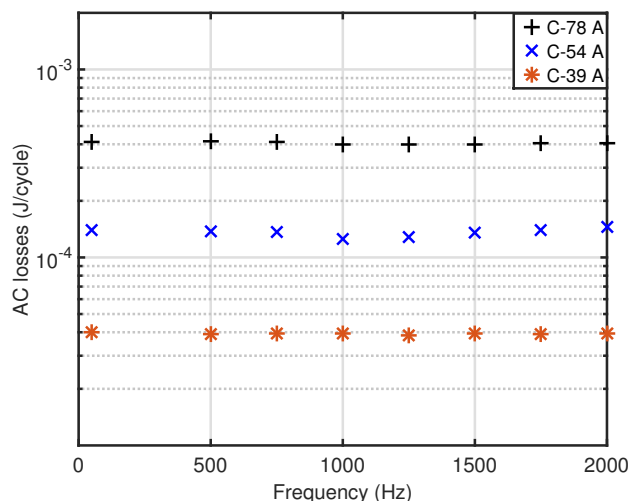


Fig. IV.17 – AC losses vs frequency with the waveform given in (IV.5).

### IV.3.c Examples of applications

With the decrease of natural resources used to obtain energy, renewable energies are growing strongly. These ones come from unlimited resources as for example the sun or the wind. Several worldwide projects aim to generate huge amount of energy for the network but the use of these renewable energies has an impact on the electrical system. For example, a solar power plant, due to the use of multiple stages of power electronics generates a large spectrum of harmonics on the output current. This part focuses on a solar plant system. The network architecture (FFT) was first computed with the software PSCAD®. The harmonic signature of the current was then used as an input to calculate the AC losses on a tape. The solar plant is composed of 88 PV panels in series with a 50 m cable. The network architecture can be found in Fig. IV.18 [182]. A PV panel electrical circuit is composed of a single diode in parallel with a resistor as commonly used in the literature. To avoid a large panel of harmonics, a second order low pass filter with a cut frequency at 1800 Hz was added.

From this architecture, it has been possible to compute the harmonic signature of the current. The fundamental frequency is 50 Hz. The FFT of the current in the output of the inverter *OutInv* and in the Input of the Transformer *InpTrans* are given in Fig. IV.19. After a frequency of 2050 Hz, the amplitude of the harmonics are considered zero.

The peak current of each distorted currents are 60 A and 82 A respectively. Table. IV.3 displays the AC losses calculated with these two waveforms and also the comparison with the shape currents.

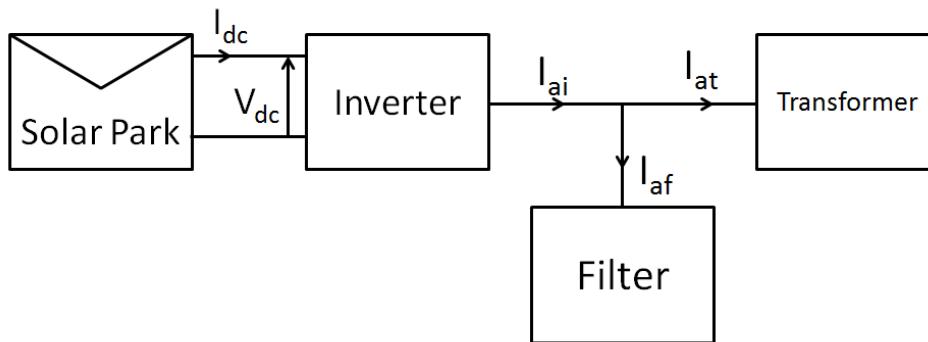


Fig. IV.18 – Filter schematic of the installation [182].

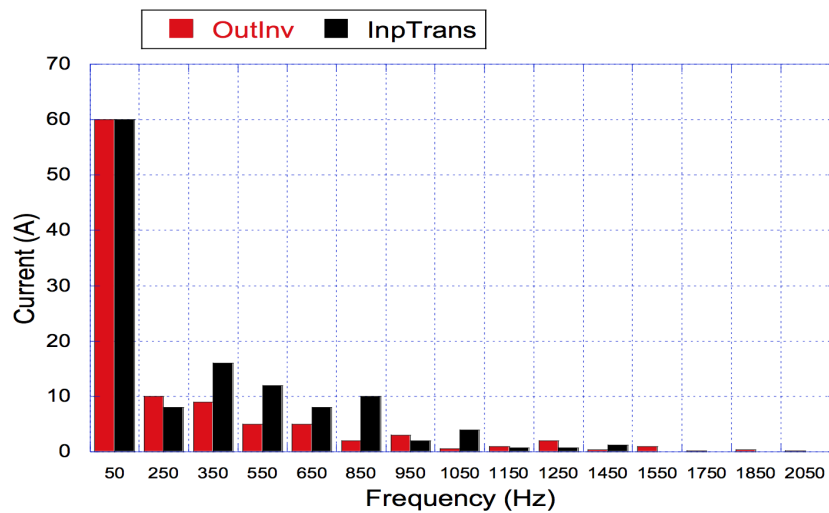


Fig. IV.19 – FFT of the two output currents.

Current shape	AC losses (mJ/cycle)	Error between shape current and real current
60 A-50 Hz	0.106	
<i>OutInv</i> (COMSOL)	0.113	6.61 %
<i>OutInv</i> (Experiment)	0.118	10.37 %
82 A-50 Hz	0.284	
<i>InpTrans</i> current (COMSOL)	0.306	7.74 %
<i>InpTrans</i> current (Experiment)	0.314	10.5 %

TABLE IV.3 – AC losses comparison between the experimental measurements and COMSOL on a practical example.

#### IV.3.d Conclusion

The AC losses generated by a summation of harmonics to simulate a distorted current were investigated in this section. Starting from a basic sinusoidal current, the input current was set as a summation of different sinusoidal currents at various frequencies. Experimental

work validates the modeling part with good agreement. From this work, the assumption made to approximate the current with a shape sinusoidal waveform with the fundamental frequency and the amplitude equal to the peak current is validated with a range of 15 % error. These results are in agreement with development made with odd-order harmonic currents. In a full power cable, the superconductors are under the action of current but also and an external magnetic field generated by the others superconductors. Further work will investigate the validation of this criterion with a combination of external magnetic field and input current.

## IV.4 Recommendations for the calculations of AC losses in DC cables

This chapter contains miscellaneous points on our approach for the calculation of AC losses in DC cables. Our multi-scale approach has been presented and is able to calculate rapidly the AC losses of diverse architectures of cables, knowing the AC losses with current and field on one conductor. The calculations of AC losses created by harmonics on DC cables are also challenging, as the numerical model using the E-J power law does not give the expected results. From these developments, two points about the calculations of cables can be :

1. The percolation model is closer to reality compared to the E-J power law. Beside the fact, that the fitting of experimental data of the dissipative state is more challenging, this percolation law gives results closer to experiments in all the scenarios and the convergence is generally improved.
2. Instead of considering the complete FFT spectrum of harmonics, taking into account a shape signal gives reasonable result. This shape signal is defined as a sinusoid with a frequency equals to the fundamental frequency of the harmonics and the amplitude equal to the summation of all harmonics. From the results, in this chapter, a difference of less than 10 % is observed overall.



## Chapter V

---

# Application to a 10 kA superconducting demonstrator cable

---

### CONTENTS

---

V.1	INTRODUCTION : THE <i>BEST-PATHS</i> PROJECT . . . . .	152
V.2	DEMO 5 : $MgB_2$ SUPERCONDUCTING LINK . . . . .	153
V.2.a	Demonstrator design and requirements . . . . .	153
V.2.b	Cable design . . . . .	153
V.2.c	Advantages of the superconducting cable for DC grids . . . . .	154
V.2.d	Our contribution . . . . .	155
V.3	AC LOSSES CALCULATIONS . . . . .	156
V.3.a	Cable magnetic design . . . . .	156
V.3.b	Ripple field analysis . . . . .	157
V.3.c	Current inversion . . . . .	161
V.4	QUENCH MODELING . . . . .	162
V.4.a	Numerical model . . . . .	162
V.4.b	Simulations of faults . . . . .	166
V.5	CONCLUSION . . . . .	170

---

### Summary

*The upgrade of the grids to transmit renewable energy requires the implementation of HVDC technologies. It offers a unique opportunity for superconducting applications to be investigated and tested. In this framework, very high current superconducting cables are interesting in many ways. In the European project BEST-PATHS : a 20 m HVDC demonstrator composed of  $MgB_2$  wires will be build and tested. This demonstrator will transmit a total current of 10 kA under 320 kV. Beside the power transmitted in steady state, several aspects have to be investigated including the losses in the system (AC losses calculations created by harmonics on the DC current) or the protection of the cable against faults. The numerical model developed in the previous chapter has been used to calculate the AC losses generated in the power cable during operation. In the requirements of the power link, the system should also sustain fast changes of current polarity. Additionally, a FEM model has been developed to calculate the temperature of the cable when a quench of the superconducting wires occur in the case of faults. This model, which couples circuit equations and the heat equation has been used to check the robustness of the cable designs in various cases.*

## V.1 Introduction : The *BEST-PATHS* project

By 2050, the majority of Europe's electricity will come from renewable sources [183], but the transmission of the power to citizens or consumers will require the modernization of nearly 300 000 km of transmission lines. To support this transition, the *BEST-PATHS*<sup>1</sup> project was started in 2015 for 4 years [184]. 39 partners from 11 European countries are gathered with a budget of 62.8 M€ including a european contribution of 35.5 M€. It aims at developing state of the art high-capacity transmission technologies and upgrading the multi-terminal links. These interconnections should be in DC as it is the most efficient way to transport high power over long distances [185, 186]. The scope of this project is to come up with a reasonable solution to meet energy goals in Europe after 2025.

The objectives of the project are divided into five items (called DEMO) listed below and summarized in Fig. V.1 :

1. DEMO 1 : HVDC offshore wind farms and interconnections
2. DEMO 2 : HVDC multi-vendor inter-operability
3. DEMO 3 : Upgrading multi-terminals HVDC links
4. DEMO 4 : Innovative AC corridors
5. DEMO 5 : DC superconducting cable

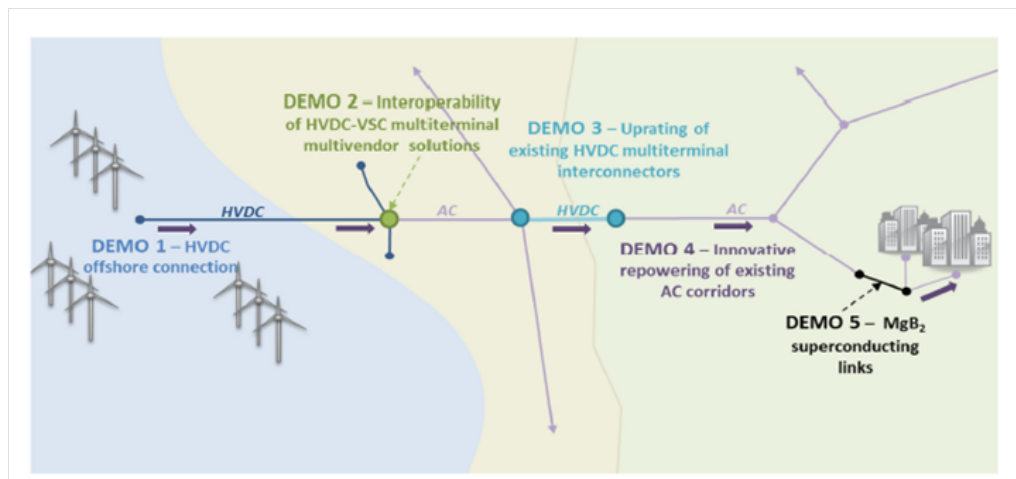


Fig. V.1 – *BEST-PATHS* project summarized in the five packages. From the offshore HDVC connections to general housing with superconducting links [184].

Our work is focused on the DEMO 5 package : a superconducting link. Specifications of this package are presented in the following section.

1. *BEST-PATHS* stands for 'BEyond State-of-the-art Technologies for rePowering Ac corridors and multi-Terminal HvdC Systems

## V.2 DEMO 5 : MgB<sub>2</sub> superconducting link

### V.2.a Demonstrator design and requirements

In the package (DEMO 5), a superconducting demonstrator made with MgB<sub>2</sub> wires will be fabricated and tested in a dedicated platform. This demonstrator will be assembled in Nexans and tested in 2017-2018. The cable system will operate at 10 kA under a voltage of 320 kV. This corresponds to a transmitted power of 3.2 GW. For comparison, the transmitted power of the cable is equal to the total solar power generated in France in 2011 [187]. Only 20 bipolar superconducting power links, will be sufficient to transmit the total wind power installed in Europe in 2013 [188]. The operating temperature of the cable is 20 K with gaseous Helium. The requirements of the demonstrator are summarized in Table. V.1.

Characteristics	Details
Structure	Monopole
Power	3.2 GW
Voltage	320 kV
Current	10 kA
Length	≈ 20-30 m
Operating temperature	20 K
Cooling	He gaz for MgB <sub>2</sub> conductor
	LN <sub>2</sub> for voltage insulation
Fault current	35 kA during 100 ms
Change of polarity	up to 10 GW/s

TABLE V.1 – DEMO-5 superconducting cable characteristics.

As soon as the demonstrator is successfully tested, the principle of such a link will be extended to longer lengths in a real network. This is why some of the aspects of the demonstrator, for example the fault characteristics have been considered. To follow the energy market price evolution, the possibility of fast change in direction of current is important. Hence, the cable should be able to withstand a change of power direction at a rate of 10 GW/s. It means that the current should go from +10 kA to -10 kA in 640 ms at 320 kV, corresponding to a ramp of 31.25 kA/s.

To couple cryogenic temperature and high voltage, a innovative design for the demonstrator has been developed. The Helium gas which flows inside the cryogenic envelope is circulating in a close loop. The electrical potential of the close loop is at the ground voltage. The cooling system will maintain the output temperature at 20 K before injecting it back into the cable. A scheme of the design is shown in Fig. V.2.

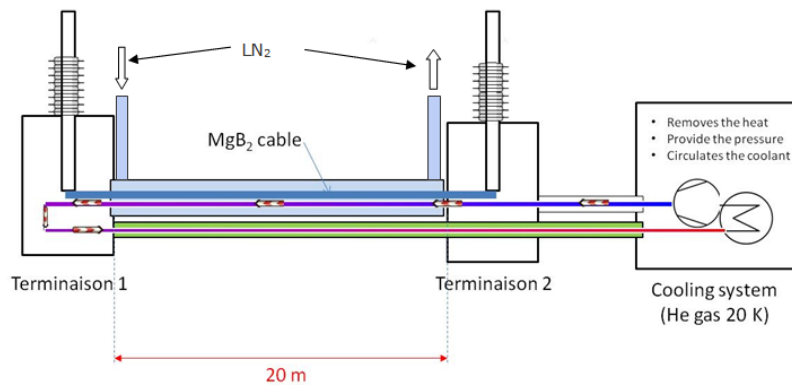


Fig. V.2 – DEMO 5 demonstrator working at 320 kV and 20 K. The helium close loop and the LN<sub>2</sub> path are shown.

### V.2.b Cable design

One of the suggested designs for the cable is composed of 18 MgB<sub>2</sub> wires developed by Columbus. The wires, which have a diameter of 1.33 mm, are assembled around a copper wire core. In normal operation, each wire will carry 555 A for a total current of 10 kA. A prototype of the cable design is shown in Fig.V.3. In comparison, a copper cable carrying 2 kA is placed next to a 24 wire MgB<sub>2</sub> cable.

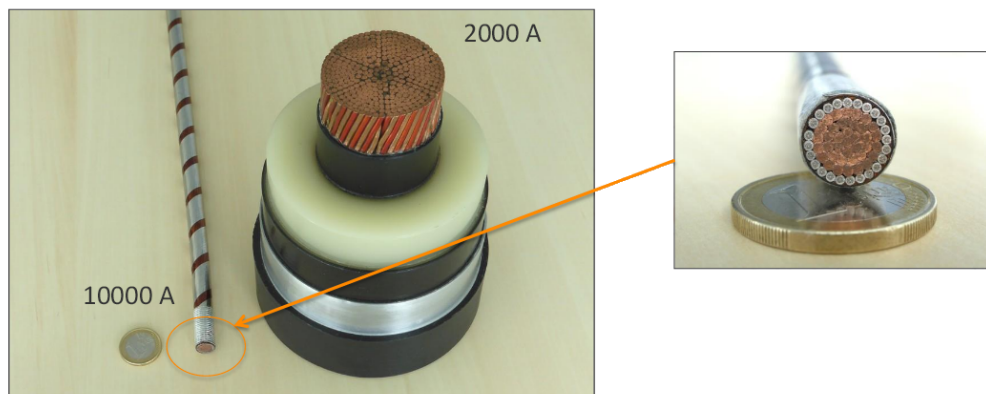


Fig. V.3 – An example of a cable design with 24 wires is shown in comparison with a 2 kA copper cable.

As it was expected, the high current capacity of the superconductor allows for the reduction of the size of the cable conductor by almost a factor 5. This design is one of the suggested designs for the cable but as the MgB<sub>2</sub> manufacturing process is under improvements, the cable design may be adjusted to benefit from the increase of performance and properties. In this work, we focused our calculations on this design with this specific wire.

## V.2.c Advantages of the superconducting cable for DC grids

### V.2.c-i Life-Cycle Analysis (LCA)

To start, a life cycle analysis (LCA) has been carried out by taking into account all the steps of the manufacturing of the cable but also its performance during operation. The complete life cycle analysis is shown in Fig. V.4 [189]. The LCA is based on the ISO 14040-44 standard series and derivatives [190, 191]. The MgB<sub>2</sub> system takes into account the performance of the two cooling systems, one for LN<sub>2</sub> and one for GHe. The unit considered for the LCA is *transmitting 3.2 GW over a distance of 1 km for 40 years at 100 % usage rate in accordance with the relevant standards*. The manufacturing processes of the wires (done by Columbus) and also the dielectrics and cryostats (done by Nexans) are not taken into account due to inconsistent or unavailable data. However, the addition of these contributions should not dramatically impact the final result. The LCA of the superconducting system is compared to a conventional system based on copper [192].

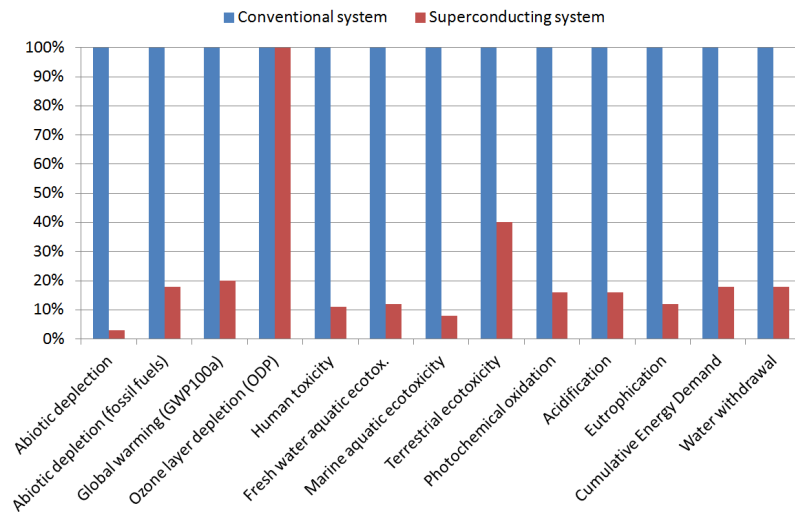


Fig. V.4 – Simplified LCA comparison between conventional system and superconducting system [189].

From Fig. V.4, one can notice that the superconducting system has a better energy cycle in all aspects of the standard compared to conventional system. This is very promising for superconducting cables as component of next generation grids. As MgB<sub>2</sub> wires are inexpensive (10 €/kA/m), the replacement of resistive copper cables by these MgB<sub>2</sub> links can be a good alternative for the environment but also for the cost of the system.

### V.2.c-ii Cable foot prints

Another aspect relates to compactness of the cable. To transmit 6.4 GW, a superconducting cable system has a reduced foot print of 0.8 m for two superconducting cables compared to conventional systems, which require a foot print of 7 m as shown in Fig. V.5. Consequently it will be easier to find spaces to install the superconducting cable than the

resistive ones, especially in urban areas.

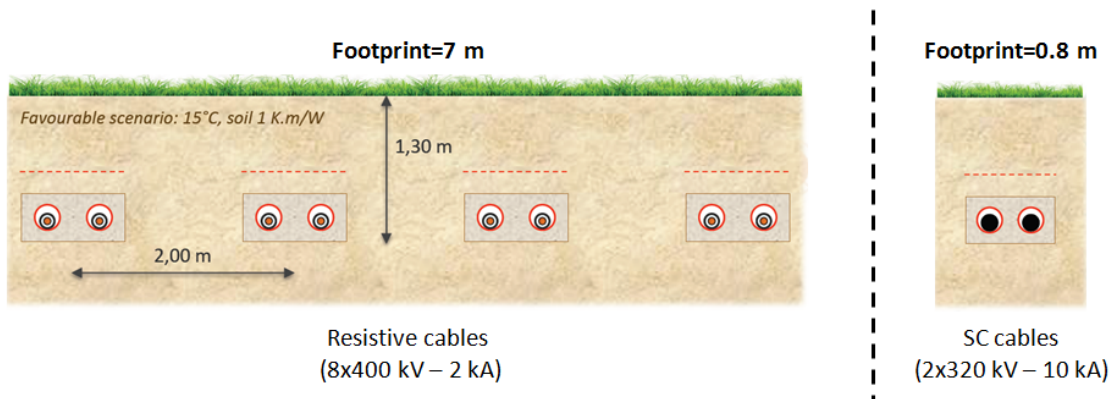


Fig. V.5 – Example of foot prints for a 6.4 GW DC power link with resistive cables (left) and superconducting cables (right).

#### V.2.d Our contribution

To scale the cryogenic system of this power cable, it is necessary to calculate all the losses including AC losses. The cable will work in DC, but harmonics are created by the power supplies. It was assumed that the AC ripples applied to the power cable will have amplitudes below 1 %. It means that, for a cable working at 10 kA, AC ripple amplitudes will not be over 100 A. To calculate the AC losses inside the cable, we developed a method based on the calculation on a single wire which is then extended to the whole cable as presented in III.3.d and IV.1.a. The AC losses in the single wire will be calculated with the FEM model and compared to analytical calculations. As the cable is a single phase, all the wires are under the same magnetic field and the total AC losses of the cable will be 18 times the AC losses of one strand.

In addition, the demonstrator should comply with the standards set by RTE. The power cable should be able to handle a change of polarity of the total current (from 10 kA to -10 kA) in 0.64 s. Therefore, it is interesting to calculate the total losses generated during this inversion of current.

The dynamics of the cable shall also be studied against a fault current over 35 kA for times of some hundreds of milliseconds. To see if any damage will occur during a fault : a quench model of the cable has been developed and tested with various fault current scenarios.

### V.3 AC losses calculations

In this section, the numerical model developed in Chapter III has been used for the calculation of AC losses coming from the AC ripples in the power cable and during the

inversion of current from 10 kA to -10 kA. At first, a stationary magnetic study of the demonstrator design was made to calculate the external field induced on each wire.

### V.3.a Cable magnetic design

The magnetic distribution was computed in COMSOL by taking into account the real geometry and the relative permeability of the metals (nickel and monel). However as the magnetic field is a global physical quantity, the local change of current distributions on the wires will not affect the value of the surrounding field. Fig. V.6 displays the magnetic flux density distribution of the complete power cable.

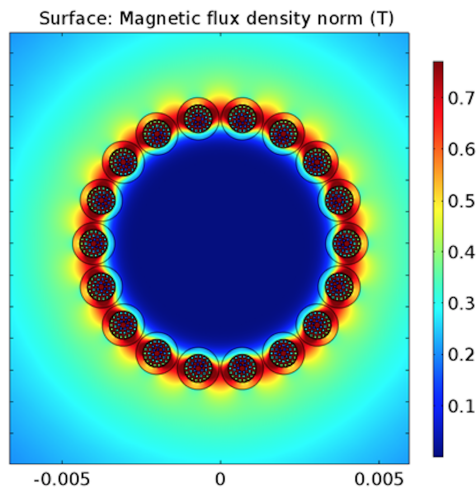


Fig. V.6 – Magneto-static analysis of the power cable by taking into account the wire architecture and the relative magnetic permeability of the material. The value of external field seen in average by the wire is 0.65 T.

From Fig. V.6, it is possible to extract the external flux density value seen by each wire at an operating current of 10 kA. The magnetic flux density is in average 0.65 T on each wire. As the external magnetic field seen by each wire is proportional to the current it is then possible to calculate the magnetic field ripple generated by the current ripple. The values are summarized in Table. V.2.

Variation	Total current	Current per wire	External field
AC ripple ( $\delta_{AC}=1\%$ )	100 A	5.5 A	6.5 mT
AC ripple ( $\delta_{AC}=2\%$ )	200 A	11 A	13 mT

TABLE V.2 – Associated current and external field values for DC and AC ripples for 1 % and 2 % for a 10 kA cable built with 18 MgB<sub>2</sub> wires.

### V.3.b Ripple field analysis

Simulations have been carried out with various percentage of AC ripples at a frequency of 50 Hz superposed to DC operating current and field. The waveform of current (and field) is plotted on Fig. V.7. We decided to use the approximation developed in IV.3 and

concentrate all the AC ripples amplitudes on one fundamental frequency of 50 Hz. The results coming from the calculations will have an error margin of less than 10 % which is acceptable considering that the AC losses coming from AC ripples are expected to be low ( $<0.01$  W/m) compared to the losses of the 20 K cryogenic envelop (around 0.07 W/m).

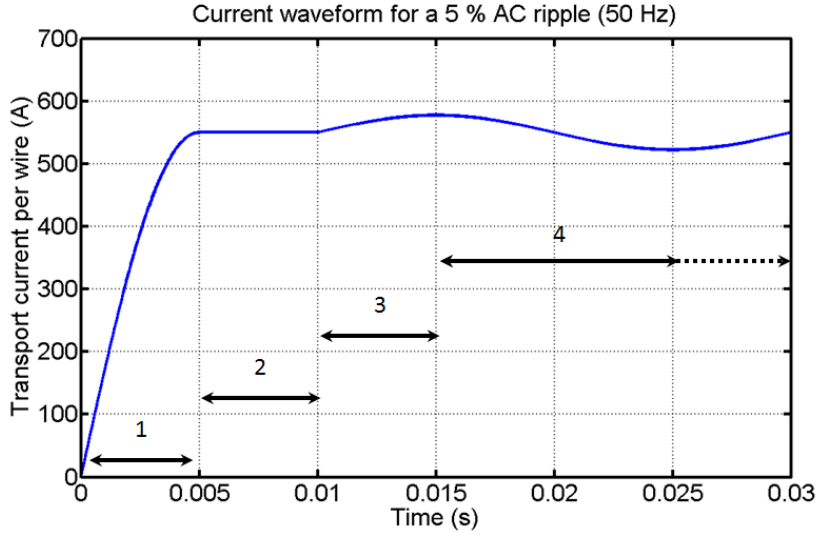


Fig. V.7 – Current waveform for AC + DC simulations. (1) is referring as the ramp up time to achieve DC state, (2) is the time taken to let any relaxation inside the material. (3) is the magnetization of the superconductor coming for AC ripples. (4) is the actual AC signal for losses calculation.

The current (and field) is increased from 0 to the operating current  $I_{DC}$  in 5 ms (1). The DC regime is then maintained for 5 ms to allow for any relaxation effect in the wire (2). With the percolation law, these effects will only take a few milliseconds. In (3) and (4) the AC harmonic is superposed to the DC condition according to the equation with  $\delta_{AC}$  defined in Table V.2 :

$$I(t) = I_{DC} \cdot (1 + \delta_{AC} \sin(2\pi f \cdot t)) \text{ for } t \geq 10 \text{ ms, } f=50 \text{ Hz} \quad (\text{V.1})$$

For the same reason as previously explained, the first quarter period of the signal (3) is not taken into account for the calculation as steady state is only reached after one quarter of the period. The AC losses calculations are then computed in the period (4). Compared to these calculations, the analytical calculations of the AC losses inside the conductor will be plotted by summing the hysteresis losses in the superconducting filaments, the eddy current losses and the coupling losses in the matrix with the assumptions in III.1.a. Each calculation with the model takes 25 days to compute so only few simulations have been performed with DC+AC ripples.

### V.3.b-i Results for AC ripples superposed to DC environnement

At first, the AC losses calculation for AC ripple amplitude of  $\delta_{AC}=1$  % has been made with a harmonic frequency of 50 Hz. Fig. V.8 displays the AC losses with various frequen-

cies. In addition to the numerical results, analytical calculations i.e. hysteresis eq. (I.28), coupling eq. (I.20) and overall losses (summation of the two) are also shown.

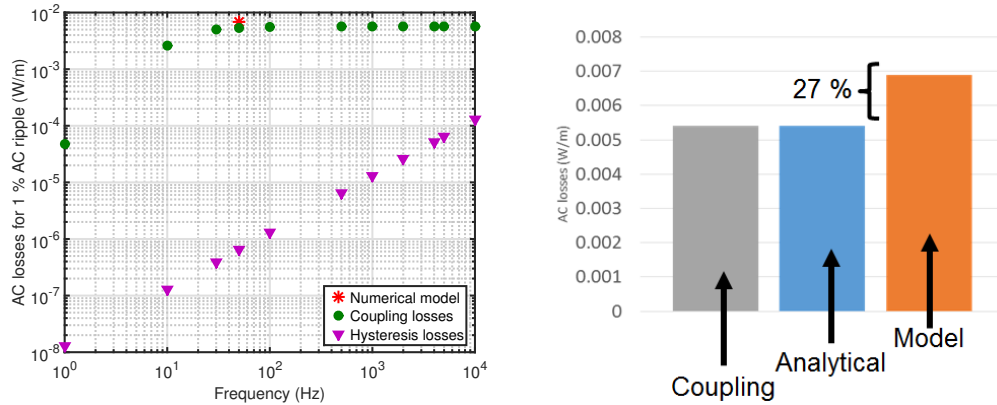


Fig. V.8 – AC losses calculations for 1 % AC ripple **for one wire** vs frequency (on right) with a 120 mm twist pitch. Analytical calculations are compared to the numerical model. On the left, the weight on the analytical calculation compared to the numerical model for the calculated point.

From these calculations, it is worth noticing that the coupling losses are predominant over hysteresis losses in the filament. The difference between the numerical model and the analytical calculation is in the order of 27 % which is similar to the difference found before (see III.3.d-ii). The difference is explained by the model taking into account the relative permeability of the metal matrix, the E-J power law and the dependency of  $J_c$  with field. In Fig. V.9, the complete AC losses are plotted versus the AC ripple amplitude  $\delta_{AC}$  between 1 % and 10 % with only few results on the numerical model.

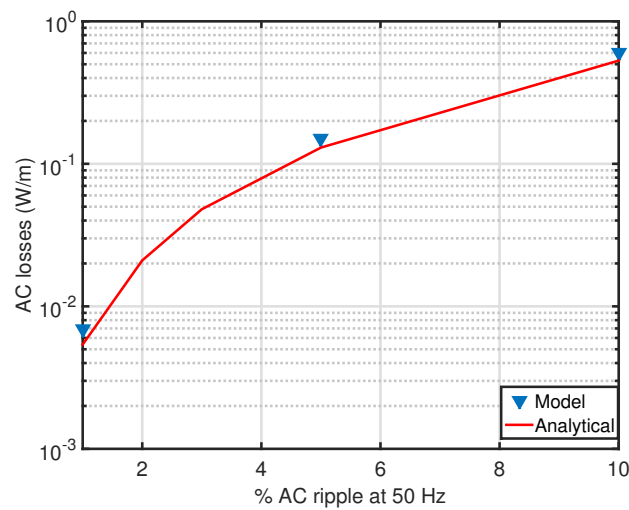


Fig. V.9 – AC losses vs the amplitude of AC ripple **for one wire**. Analytical calculations are compared to the results of the numerical model with a 120 mm twist pitch.

All the calculations are in agreement with the previous results. The difference between

the analytical calculations and the numerical model is still in the order of 20 %-25 %. In reality for HVDC systems, the summation of the amplitudes of harmonics  $\delta_{AC}$  is commonly largely below 1 % [193, 194, 195]. For the demonstrator, the AC ripple amplitudes were purposely enlarged to have an upper limit for the value of AC losses in the demonstrator. In our calculations, we found AC losses in the order of 200 mW/m for the complete cable. This can be an issue for long superconducting cables but not for the demonstrator. One way to decrease the AC losses is to adjust the architecture of the wire in order to reduce the coupling losses.

### V.3.b-ii MgB<sub>2</sub> architectures

The same conclusion as III.3.e can be drawn from these results as the architecture of the MgB<sub>2</sub> wires is not well suited for low AC losses. From the previous results, the AC losses for pure AC regime excludes the use of this wire for large scale AC applications. But in the case of DC applications, the AC losses generated by the AC ripple are not too high. Nevertheless, the losses may be further reduced in order to have still a more competitive cable. By looking at Fig. V.8, it is clear that if a reduction of coupling losses can be obtained, the total losses of the wire will be also reduced. To go further, the architecture of the wire has been compared to other architectures made by changing the transverse resistivity and the twist pitch. Fig. V.10 displays the total AC losses generated for  $\delta_{AC}=1\%$  for five different architectures. Our calculations have been made with a wire with a twist pitch of 120 mm. In Fig. V.10, three twist-pitches have been considered : 300 mm and 120 mm and also a lower value of 5 mm. The calculations have been carried out with diverse matrix transverse resistivities 5 n $\Omega$ .m and 500 n $\Omega$ .m which are respectively the resistivity of nickel and monel.

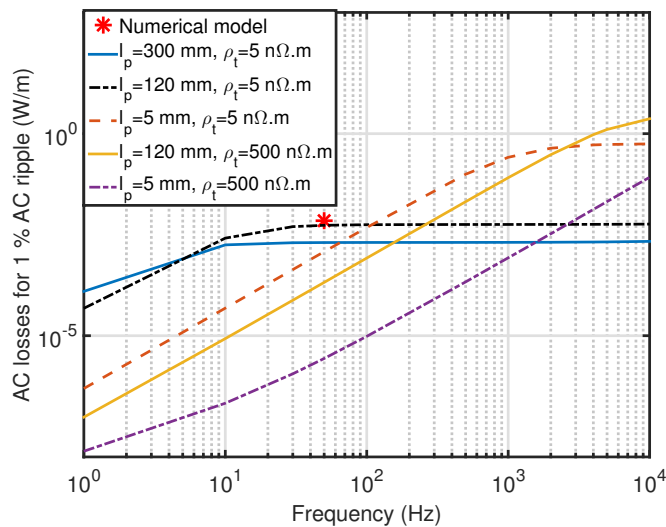


Fig. V.10 – Coupling losses comparison for diverse architectures of the MgB<sub>2</sub> wire to decrease the AC losses. The transverse resistivity was chosen as the nickel and monel elements. The hysteresis losses at 50 Hz are equals to  $8 \cdot 10^{-7}$  W/m.

In these calculations, the coupling losses are more than 80 % of the total AC losses. If we focus on the coupling losses, the analytical equation (I.20) for these losses can be rewritten at a fixed field ( $B=0.65$  T) as :

$$P_{tot} \approx P_{coup} \propto \frac{B_{max}^2}{2\mu_0} \left( \frac{\tau}{1-N} \right) \frac{\omega^2}{1+(\omega\tau)^2} \quad (V.2)$$

The losses are acting as a high pass filter with a cut frequency of  $f_c = 1/\tau \propto \rho_t/l_p^2$ . To reduce the losses, it is interesting to increase  $f_c$  by increasing the transverse resistivity and decreasing the twist pitch as it can be seen from Fig. V.10. If the fundamental frequency of the AC ripples is higher, above  $f_c$ , the coupling losses are mainly constant in the saturated regime with a gain of :

$$P_{coup}(f \gg f_c) \propto \frac{B_{max}^2}{(1-N)} \frac{1}{\tau} = B_{max}^2 \frac{\rho_t}{l_p^2} \quad (V.3)$$

This explains the fact that the coupling losses for a twist pitch of 300 mm are lower than in the case of a twist pitch of 120 mm. Two approaches can be formulated from this calculations. First, decreasing the twist pitch of the filaments by at least one order of magnitude and second, increasing of at least one orders of magnitude the resistivity of the matrix. Today, the amount of losses is 0.13 W/m which has to be divided by at least 10 to be considered for large scale applications. Dividing at least by two this amount is interesting for a large scale application, this would be done by only dividing the twist pitch by three or change the metal in the matrix, for example Stainless steel or Titanium.

### V.3.c Current inversion

With this new kind of power links in the grid, it is necessary to calculate the amount of energy dissipated when a inversion of power is made. The specification of the power link set by RTE is the ability of the cable to invert the transmitted power at a rate of 10 GW/s. We made a simulation with this rate and calculated the energy dissipated inside a wire, the result is plotted in Fig. V.11.

From this figure, the wire dissipates a maximum value of 178.8 mJ (on 20 mm), which is not a concern considering the measured Minimum Quench Energy<sup>2</sup> (MQE) of the wire [196]. This means that the cable should not quench during the inversion of current.

---

2. Deposited energy to start a quench

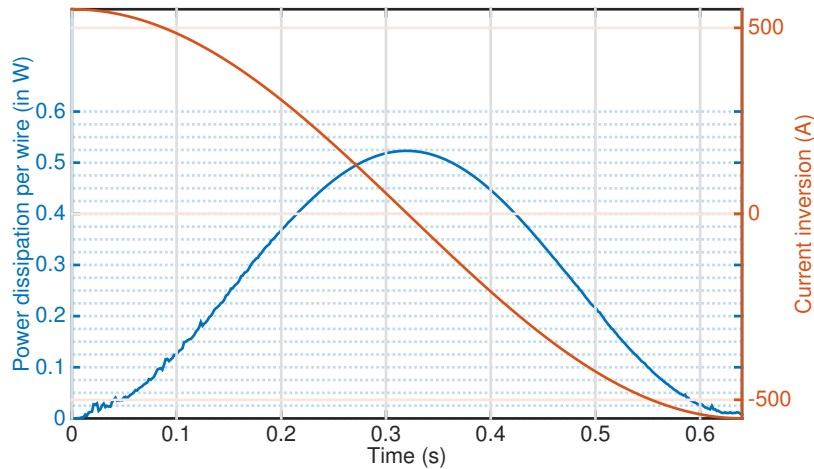


Fig. V.11 – Waveform of current for a current inversion and the amount of power dissipated in a wire.

## V.4 Quench modeling

In the specifications of the demonstrator lies the protection in the case of faults or defects. As the Minimum Quench Energy of the MgB<sub>2</sub> wire is several Joules [196], it is unlikely that the power cable could quench by accident. It is then interesting to study the behavior of the demonstrator i.e. the temperature and time required to cool down the cable only when a fault occurs.

### V.4.a Numerical model

This model has been developed in COMSOL, due to its capability of handling complex multi-physics problems. As the cooling will be located on the side of the wires (flow of helium gas), the model was made in 3-D. The twist pitch of the MgB<sub>2</sub> wires of the demonstrator is equal to 250 mm. To fill the hole inside its core and protect the cable, 19 copper wires (diameter of 1.33 mm) have been added. We measured the RRR of the copper wires at 145. The model uses bulk copper to reduce the number of elements, meaning that a hole inside the bulk (see Fig. V.12) is designed to take into account the spaces between the copper wires. To calculate the current in each MgB<sub>2</sub> wire and also inside the copper bulk, an electrical circuit is solved in parallel to the heat equation. The MgB<sub>2</sub> wires have been considered as homogeneous wires with equivalent properties as done in the past [197, 198, 199], so the equivalent heat capacity, thermal conductivities and electrical resistivity will be calculated according to the volume fraction  $f_i$  of the constituents in the wire and their properties. The heat equation can be written in all the domains as :

$$\gamma \cdot C_p(T) \frac{\partial T}{\partial t} = \nabla(\bar{\lambda}(T)\nabla T) + P_j + P_{conv} \quad (V.4)$$

In this equation  $\gamma$  and  $C_p$  are respectively the density (in kg/m<sup>3</sup>) and the heat capacity of the each domain (in J/(kg.K)) (more details in V.4.a-i).  $\bar{\lambda}$  is a matrix of thermal

conductivities detailed in V.4.a-i. The Joule losses  $P_j$  are calculated in each domain (MgB<sub>2</sub> wires and copper bulk) as :

$$P_j = \frac{1}{V_i} R_i(I, T) \cdot I_i^2 \quad (\text{V.5})$$

With  $V_i$  the volume of the domain and  $I_i$  the current inside the domain. The resistance  $R_i$  is calculate according to :

$$R_i(I, T) = \frac{1}{S_i} \int_{Cl} \rho(T, J) dl \quad (\text{V.6})$$

Where  $\rho$  is the equivalent electrical resistivity of the domain  $i$ ,  $S_i$  is the normal surface of the wire and  $Cl$  is the longitudinal path along the domain. As the model is homogeneous, all the properties are considered equivalent over the normal surface. The convection physics is taken into account with :

$$Q_{conv}(T) = \frac{1}{V_i} \cdot h \cdot (T - T_{op}) S_{out} \quad (\text{V.7})$$

Where  $T_{op}$  is the operating temperature (20 K),  $h^3$  and  $S_{out}$  is the convective heat coefficient (more details in V.4.a-ii).  $S_{out}$  is the external surface of the model where the helium gas cools down the cable, i.e. the complete surface of the MgB<sub>2</sub> wires but also the external surface of the copper bulk (no exchange in the copper hole). The circuit coupling and also the complete model are shown in Fig. V.12.

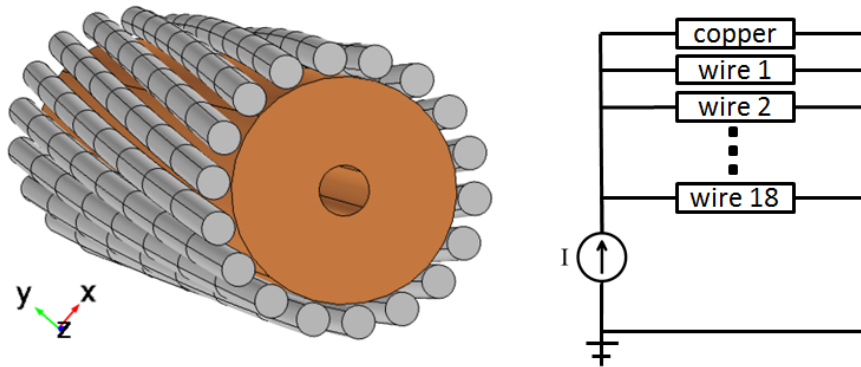


Fig. V.12 – Geometry of the model on the left and the circuit coupling on the right.

#### V.4.a-i MgB<sub>2</sub> conductor modeling

The MgB<sub>2</sub> wires are the same as the one used in III.3.d-ii with a diameter of 1.33 mm. This wire is composed of 15.5 % of MgB<sub>2</sub> compound. The critical current of the wire is equals to 850 A at 20 K, 0.7 T. The volume fractions of the constituent in the MgB<sub>2</sub> conductor can be found in Table. V.3.

3. In addition, the heat transfer coefficient is temperature dependent

Elements	volumetric fraction $f_i$
MgB <sub>2</sub>	15.5 %
Nickel	35 %
Monel	49.5 %

TABLE V.3 – Volumetric fraction  $f_i$  of each element inside the MgB<sub>2</sub> wire.

**Electrical resistivity** The equivalent resistivity of the wire  $\rho_{eq}$  will be calculated using the percolation law as :

$$\rho_{eq}(T, J) = \begin{cases} 0 & \text{if } |J| \leq J_{c0} \\ E_c \left( \frac{J}{J_{c0}(T)} - 1 \right)^{n_0} & \text{if } T < 39 \text{ K and } |J| \geq J_{c0} \\ \mathcal{F}_{NS}(T) & \text{if } T \geq 39 \text{ K} \end{cases}$$

Regarding the resistivity of the wire below 39 K, the critical current of the wire was measured in CERN at 850 A at 20 K at 0.7 T. The trend of critical current with temperature has been assumed as a linear decreases from 850 A to 0 from 20 K to  $T_c=39$  K, which underestimates the critical current near  $T_c$ . The relationship between  $J_c$  and  $J_{c0}$  has been assumed as  $J_{c0}=0.90J_c$  according to III.3.b-i. The  $n_0$  is kept constant and set at 10 which is a good value according to the measurement (see Fig. III.33). The resistivity in the normal state has been measured with respect to temperature between 39 K and 270 K and is plotted in Fig. V.13.

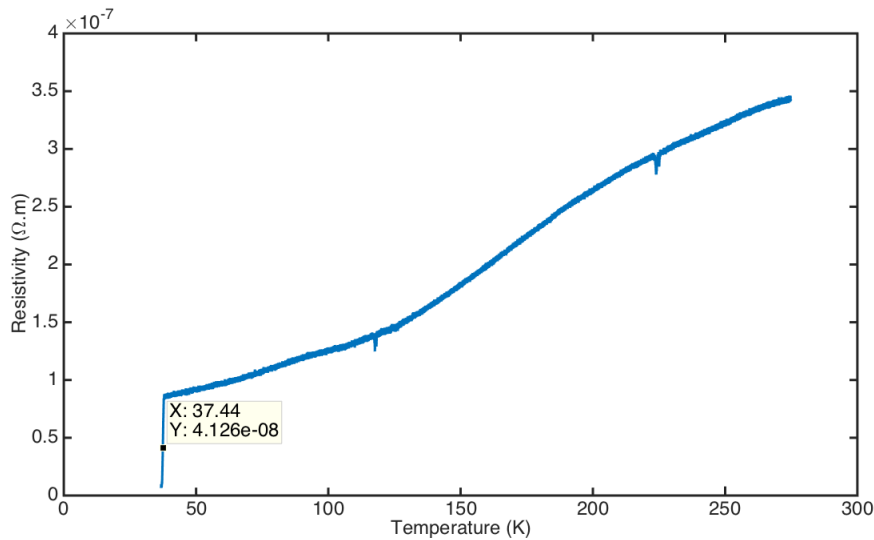


Fig. V.13 – Electrical resistivity versus temperature for the 1.33 mm MgB<sub>2</sub> wire. The function  $\mathcal{F}_{NS}(T)$  is defined with the measured electrical resistivity above 39 K.

**Thermal conductivities** The matrix of thermal conductivities is defined as a symmetrical matrix with thermal conductivities in the three directions with respect to the axis defined in Fig. V.12 :

$$\bar{\lambda}(T) = \begin{pmatrix} \lambda_{trans}(T) & 0 & 0 \\ 0 & \lambda_{trans}(T) & 0 \\ 0 & 0 & \lambda_{long}(T) \end{pmatrix}$$

In the matrix,  $\lambda_{long}$  and  $\lambda_{trans}$  are respectively the longitudinal and transverse equivalent thermal conductivities of the wire. Starting from the same method as previously for the equivalent electrical resistivity, the thermal conductivities along the x and y axis are calculated as radial conductivities defined as (with data from [200, 158]) :

$$\frac{1}{\lambda_{trans}} = \sum_i \frac{f_i}{\lambda_i(T)} \quad (V.8)$$

For the longitudinal axis, it can be expressed as :

$$\lambda_{long} = \sum_i f_i \cdot \lambda_i(T) \quad (V.9)$$

**Heat capacity and density** The heat capacity and the density of the equivalent wire can be calculated by using the volume fraction of all the constituents of the wire. The equivalent heat capacity of the wire is given by (with [201, 202]) :

$$C_{peq}(T) = \sum_i f_i C_{p_i}(T) \quad (V.10)$$

The density of the wire  $\gamma$  (in kg/m<sup>3</sup>) is calculated with  $\gamma_i$  the density of each constituent [203, 204] :

$$\gamma_{eq} = \sum_i f_i \gamma_i \quad (V.11)$$

#### V.4.a-ii Helium effect - external forced convection in tubes

To cool down the power cable, a circulation of helium gas at 20 K-20 bar is foreseen. During a fault current, the cable will be heated by current mainly going into the copper wires as the MgB<sub>2</sub> wires in normal state present a high resistivity. To take into account the effect of helium gas, a forced convective heat flux is added to the model by calculating a dedicated heat transfer coefficient. This coefficient is given by the experimental formula [205] :

$$h = 0.023 \cdot \frac{\lambda}{D} \left( \frac{D v_{GHe} \gamma}{\eta} \right)^{0.8} P_r^{0.23} \quad (V.12)$$

Where  $\lambda$  is the thermal conductivity of gaseous helium [206] and D is the diameter of the cryogenic envelop. In this equation, the Prandtl number is introduced as  $Pr = \eta C_p / \lambda$  where  $C_p$  is the heat capacity,  $\eta$  is the dynamic viscosity and  $\gamma$  the density of gaseous helium [207]. Finally  $v_{GHe}$  is the velocity of the gas given in meter per second. All the introduced parameters are dependent of the temperature, some values are given at 20 K, 90 K and 300 K with their units at 20 bars in Table. V.4.

It is also possible to plot the heat transfer coefficient h function of the temperature of the gas at a given velocity. In Fig. V.14, the coefficient is plotted in the range of velocity

Temperature	20 K	90 K	300 K
Density $\gamma$ (kg/m <sup>3</sup> )	47	10.3	3.2
$C_p$ (J.g <sup>-1</sup> .K <sup>-1</sup> )	6.1	5.2	5.19
Dynamic viscosity $\eta$ (Pa.s)	$4.31.10^{-6}$	$9.41.10^{-6}$	$2.10^{-5}$
Thermal conductivity $\lambda$ (W.m <sup>-1</sup> .K <sup>-1</sup> )	$3.2.10^{-2}$	$7.0.10^{-2}$	$15.1.10^{-1}$

TABLE V.4 – Gaseous helium properties at 20 bars.

of 0.1 m/s and 1 m/s which are the lower and upper limits of the gas velocity foreseen for the demonstrator (in agreement with [208]). The velocity of 0.3 m/s is added to the figure as it is one of the velocities considered for the operation of the demonstrator.

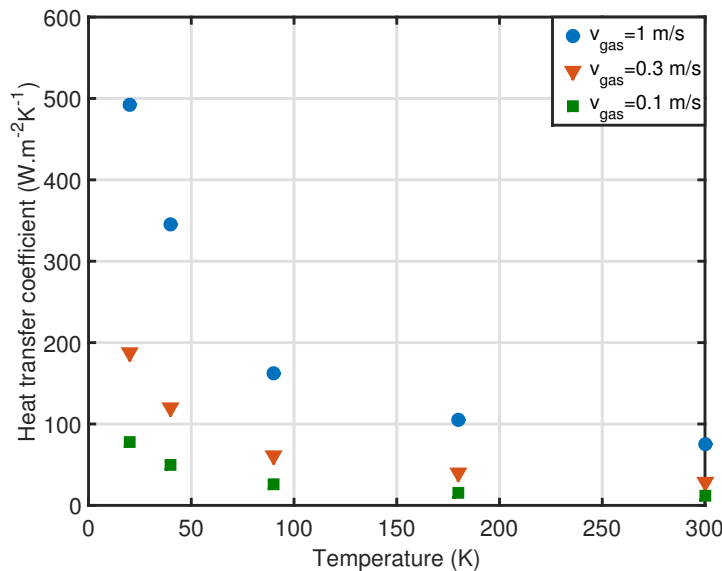


Fig. V.14 – Heat transfer coefficient versus temperature at different gas velocities.

As it was expected from (V.12), the coefficient  $h$  is increasing with an increase of the gas velocity. A high gas velocity leads to a higher heat transfer coefficient which means a more efficient cooling of the superconducting application. However, the dynamic losses of the turbine will also be increased, this is why we considered 1 m/s as the highest value.

#### V.4.b Simulations of faults

During a fault current, the current increases to high levels (three times the rated current) for a few hundreds of milliseconds and can damage the cable. Simulations have to be done to calculate the maximum temperature in the cable but also the time to cool-down the cable to bring it back to operating temperature ( $T_{op}=20$  K). Various parameters have been studied, for example the velocity of the gas or the duration of the fault. In the requirements, the cable should sustain a fault of 35 kA for 100 ms but it is still interesting to study all kinds of faults (variation of duration and peak value). The waveform of the fault used in the simulations (ideal form) is presented in Fig. V.15. In this figure, two quantities

are introduced  $t_{up}$  which refers to the raising time from operating current to the fault current and  $t_{fault}$  the duration of the fault. The fault current is written  $I_{fault}$ .

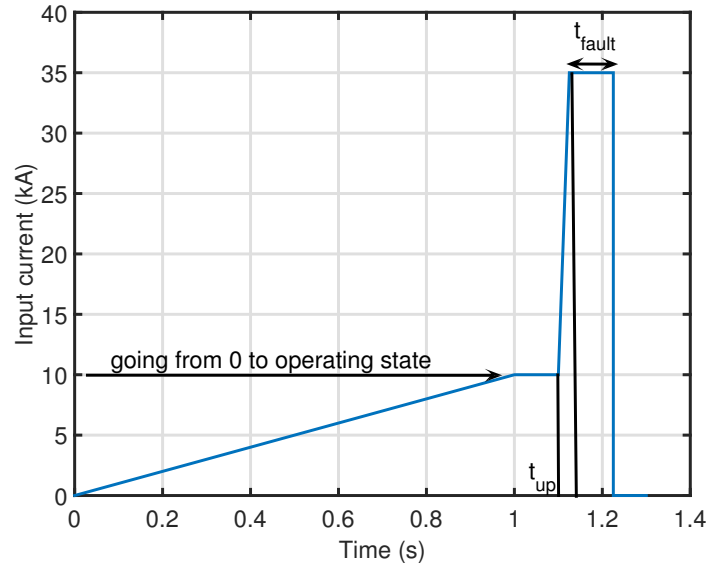


Fig. V.15 – Ideal fault current profile with  $t_{up}$  the raising time of the fault and  $t_{fault}$  the fault duration.  $I_{fault}$  is referring to the peak value of current during the fault.

**Effect of the GHe velocity against a fault current** At first, a 35 kA fault current with a duration of 100 ms was considered ( $t_{up}=2$  ms). Simulations have been made with various gas velocities. Low values of gas velocity will not offer a good cooling of the cable in the case of a hot spot and also may create a important temperature drop between the inlet and the outlet of the cable. The simulations have been performed with various velocities between 0.1 m/s and 100 m/s. The peak temperature of the copper and MgB<sub>2</sub> wires are displayed in Fig. V.16 with also the time required to cool down the cable after the fault.

From these simulations, it can be found that the temperatures do not exceed 90 K for the copper part and 45 K for the MgB<sub>2</sub> wires. With low gas velocities, the problem can be almost considered as quasi-adiabatic and no changes are noticed on the peak temperatures. Only the time required to cool down the cable is drastically increased, while with high gas velocities, the time required to cool down the cable is very small.

**Variations on fault values and durations.** As the gas velocity is selected to be comprised between 0.1 m/s and 1 m/s, the time to cool down the cable will be in the order of dozens of seconds according to previous paragraph. A parametric study has been made by considering different fault durations and peak values with the two velocity limits. First a gas velocity of 1 m/s is considered for the calculations and then a velocity of 0.1 m/s.

**Gas velocity set at 1 m/s** The maximum temperature in the copper part and the MgB<sub>2</sub> wires are displayed in Fig.V.17.

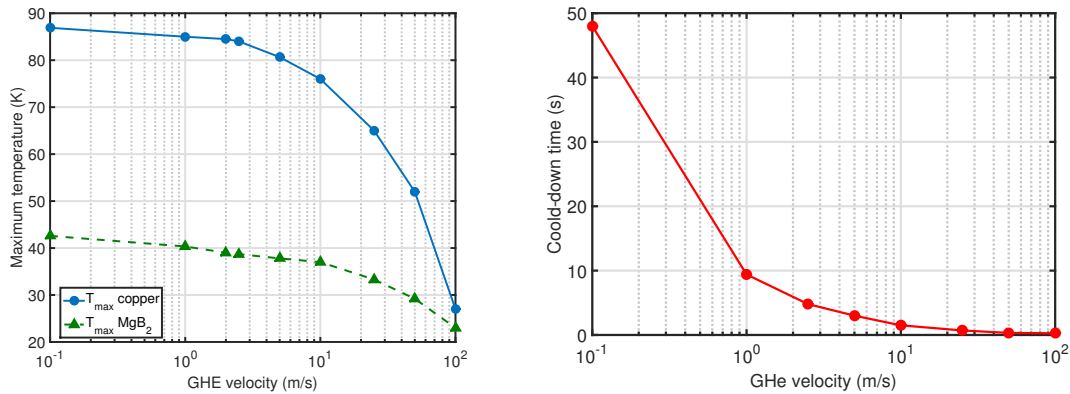


Fig. V.16 – Maximum temperature of the MgB<sub>2</sub> wires and copper bulk (on left) and cool-down time (on right) versus GHe velocity. It is also noticeable that if the model is adiabatic the temperatures found are the same at the one for a He velocity of 0.01 m/s.

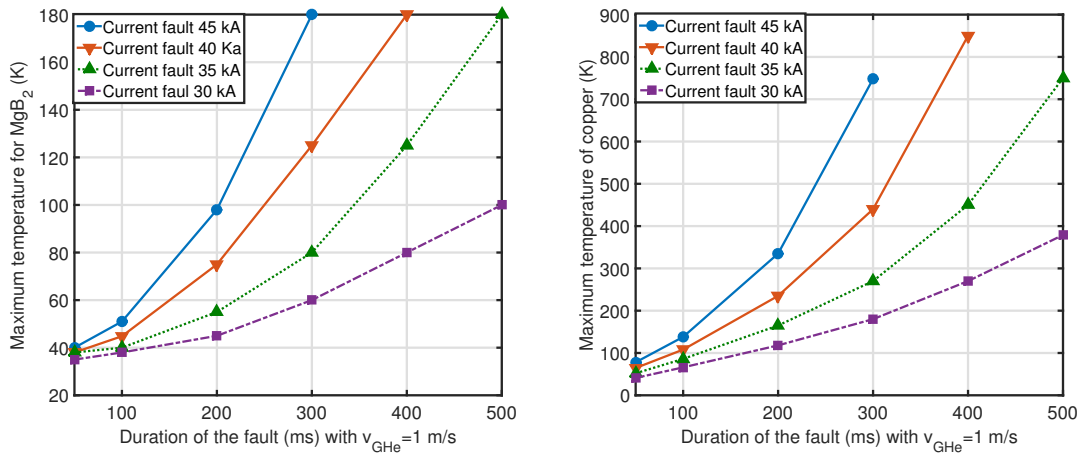


Fig. V.17 – Temperature in MgB<sub>2</sub> (left) and copper (right) for  $v_{GHe}=1$  m/s.

In these simulations, the temperature is increasing with the peak value of the fault and also the fault duration as expected. For example, if we consider a maximum temperature in the copper bulk of 400 K (limit of polymer materials in the cable), the cable is able to sustain a 220 ms fault current of 45 kA and a 500 ms fault current of 30 kA. For a fault in a real system, the typical time is comprised between 100 ms and 200 ms, which gives sufficient margin for the cable design before damaging the system. For a fault of 100 ms, the temperature in the MgB<sub>2</sub> wires and in the copper bulk does not change drastically with the fault current as the phenomenon is fast in time. The required time to cool-down the cable in each case has also been computed. In reality, 120 s is considered as a reasonable time for the cool-down.

A velocity of 1 m/s leads to a cool down time in the order of 10 s. In these calculations, the time to cool down is strongly dependent of the fault current when the fault is longer than 300 ms. For 100 ms, the time does not vary much with the fault current. If the demonstrator is working with a gas velocity of 1 m/s, the demonstrator is cooled down in 25 s in all the cases for a fault duration less than 100 ms. For example for a 500 ms fault

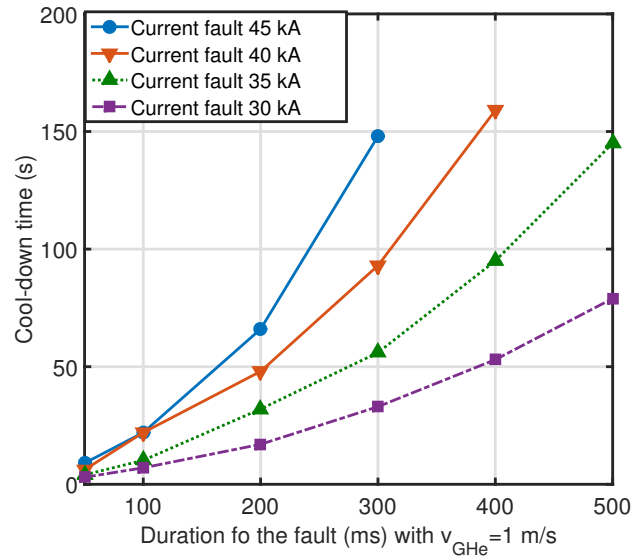


Fig. V.18 – Cool-down time required to recover to operating state versus the duration of the fault for a  $v_{GHe} = 1$  m/s.

with 30 kA, the time to cool down the cable is 75 s but the temperature in the copper core reaches 400 K, one can see that, in this case the temperature of the copper bulk is the limiting factor. However, if the copper section is smaller, the cable temperatures will be higher and the margins will be reduced (future work on the optimization can be carried out).

**Gas velocity set at 0.1 m/s** The maximum temperature in the copper part and the MgB<sub>2</sub> wires are displayed in Fig.V.19 with gas velocity of 0.1 m/s.

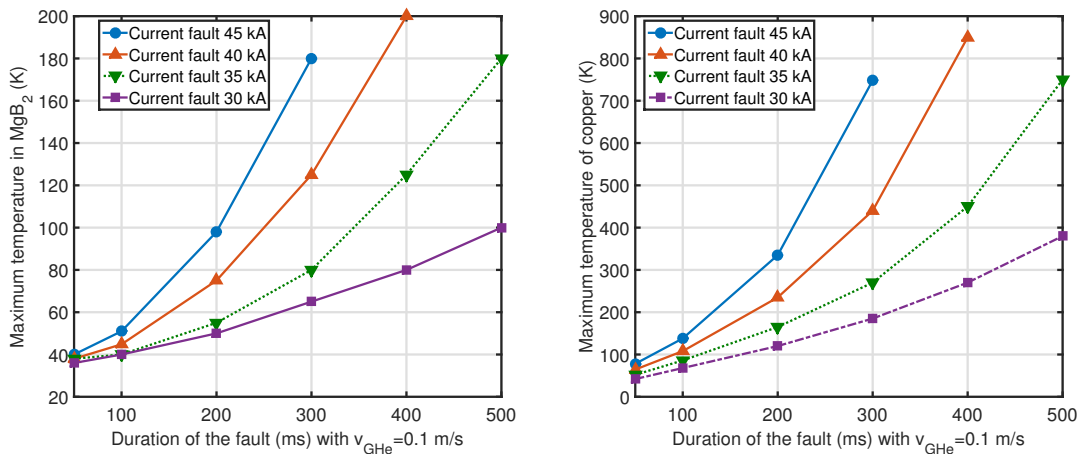


Fig. V.19 – Temperature in MgB<sub>2</sub> (left) and copper (right) versus the duration of the fault.

The same conclusion as before can be drawn concerning the increase of the temperature in the copper and in the MgB<sub>2</sub> versus the fault duration and the peak current. The

values are very close to the ones with  $v_{GHe}=1$  m/s according to Fig. V.16, where it has been observed a plateau of the peak temperature for gas velocities lower than 1 m/s. From the same figure, it is possible to see that the time required to cool-down the cable will be slightly higher. Fig. V.20 displays the cool-down time required for the demonstrator to go back at 20 K for all faults.

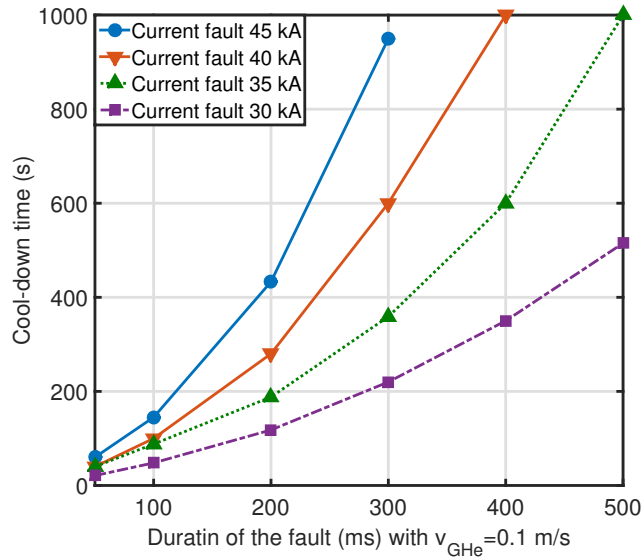


Fig. V.20 – Cool-down time required to recover to operating state versus the duration of the fault.

As it was expected, the time required for the cable to go back to the operating temperature (20 K) is in average, multiplied by a factor 4. This is explained by the heat transfer coefficient being dependent on the velocity ( $h \propto v_{GHe}^{0.8}$ ). A low heat transfer coefficient leads to a less efficient cooling. In these cases, three minutes are required to cool back down the cable to 20 K. The specified 120 s limit is overcome.

All the simulations have shown that the cable should not be damaged in the case of a 100 ms fault for a velocity of gas between 0.1 m/s and 1 m/s. The cool-down time required is found to be between 25 s and 180 s. In all these calculations, the thermal contact between the wires and the helium gas was supposed to be perfect. In reality, the cable will be wrapped with Kapton, creating a thermal contact resistance which is very difficult to assess. To have a reasonable idea of the time required to cool down, it is necessary to experimentally test the cool-down of the cable. In a case of very poor heat exchange, it is still possible to increase the gas velocity in order to reduce the cool-down time. Concerning the maximum temperature, as it was seen, the gas velocity does not impact the maximum temperature. Taking into account the thermal resistance should not have a dramatic impact on the maximum temperature. The heating is very fast and we are in a quasi-adiabatic condition.

## V.5 Conclusion

In this chapter, the numerical model developed previously has been used to perform calculations on a demonstrator cable conductor, expected to be tested in 2017. Our work reported in this thesis, is mainly numerical and dedicated to the sizing of the losses and to verify that the demonstrator will accept fault currents and current inversions.

First, the AC losses on the cable conductor have been calculated showing that the cable is capable of operating in DC with a 1 % of AC ripples without impacting the sizing of the cooling system (still lower than the losses of the cryogenic envelope). For the future and the integration of this kind of cables inside a grid, it is worth noting than the value of 1 % harmonic amplitude is a very high value compared to systems made today.

The current inversion at a rate of 10 GW/s was also investigated to verify if the cable is likely to quench during the transition. It has been numerically calculated that the cable is safe and stable during this inversion.

Added to these results, a thermal model has been developed to investigate the protection of the demonstrator and cable during a fault. In our demonstrator, no fault will be tested. For a use in a future grid, it is necessary to know if the cable might be damaged during a fault. It is also important to get an estimation of the time required to cool back down the cable and restart it. According to the model, for gas velocities comprised between 0.1 m/s and 1 m/s, the temperature reached by the cable is acceptable and the time required to cool-down the cable is less than 200 s. Unfortunately, the contact resistance between the wire and the helium flow is difficult to estimate and should be measured in further experiments.



---

## Final conclusion

Very high current cables are foreseen in the future, in relation with the strong increase of renewable energies. SC cables are a viable option but AC losses (created by AC current or ripples) must be accurately calculated.

The main aim of this thesis was to come up with a model for fast calculations of AC losses in high current superconducting cables. This was successfully reached with the use of a multi-scale model coupled with FEM or integral method. An international test benchmark, comparisons with analytical formulas in simple cases and several experimental data make possible to be confident in the work. The first step is the numerical calculation of AC losses of a single conductor with transport current and field. In this calculation, the most adapted method for example FEM method or integral method can be used. Modeling only one conductor allows to go into details, for example in the conductor characteristics, as it influences the AC losses. It also decreases the computation time in comparison of modeling a complete power cable.

For the manufacturing of high current cables, two conductors have been considered round wires made with REBCO tapes and  $MgB_2$  conductors. The first one uses its ability to work at 77 K for current cables up to 3 kA while the second one, working at 20 K is more suited for cable with higher rated currents. These two conductors have different forms and properties and we have selected the most efficient way to calculate rapidly the AC losses.

At first, a 2-D numerical model was made for the calculations of AC losses in REBCO tapes and round wires. This model was validated by experiments on REBCO tapes. The AC losses created by transport current and external magnetic field have been calculated for HTS tapes and round wires over a large range of operation. These calculations are important as analytical calculations do not exist for combined AC losses. Moreover, the possibility of using round wires as a good alternative compared to HTS tapes for compact high current cables has been investigated. For AC applications, these round wires are not suitable as they intend to generate high AC losses in the case of complete penetration of the superconducting layer by the external field, which is generally the case in operation.

Secondly, 3-D numerical models have been made for the calculations of AC losses in multi-filamentary geometries. An international benchmark with University of Tampere and

Polytechnique Montréal has been made on a three filament geometry to find the most efficient solving. This was the first step to compare the formulations but also the different softwares (commercial or home-made). We have made simulations with more and more complex material properties and for the first time, achieving to simulate numerically a model with superconducting material and an hysteresis matrix. After the development of this model, realistic models have been made up in order to calculate the AC losses in a real MgB<sub>2</sub> wire. After a series of characterization of the properties of the metals and a critical current measurements at different temperatures and magnetic fields, a model was set up integrating all the measured properties and solved.

After the calculations of the AC losses inside the two studied conductor and the knowledge of the dependency of these losses with respect to transport current and field, we developed a multi-scale model inside MATLAB for the calculations of the losses inside a superconducting cable. This method is fast and allows optimization of the design of high current cables. This model has been compared to some FEM simulation of the complete cable and the result show good correlation and validate the method.

As the power cables are likely to operate in DC, it was necessary to study the numerical modeling of the superconductor when this one is subjected to harmonics superposed to a DC current and external field. Some limitations of the power law model have been shown and we introduced the percolation law which seems more suitable in the case of AC+DC. It has a good correlation compared to analytical calculations. Finally, the impact of multi-frequency harmonics has been studied. The results validate the fact that instead of taking a complete FFT spectrum of the harmonics, only the shape signal with the sum of all the harmonics amplitude and the fundamental frequency can be taken into account, which simplifies considerably the solution.

As an application, the numerical model of the MgB<sub>2</sub> wire has been used to calculate the losses on a practical example : a 10 kA MgB<sub>2</sub> cable conductor for HVDC grid applications. The conception of the cable conductor and its cooling was validate. It was shown that a 1 % AC ripple superposed on a DC operating current dissipate few AC losses and can be considered for DC applications. Some calculations have also be made on the change of geometry of the MgB<sub>2</sub> wire, for example the change of twist pitch or the matrix resistivity to reduce even more the losses. A quench model was also used in this part to validate the fact that the cable sustains a possible fault current in the grid.

Considering the future of the thesis, three majors axis can be drawn :

1. The numerical model made with MgB<sub>2</sub> has been compared to analytical calculations. However, it is necessary to proceed with a series of extensive measurements with transport current and also external magnetic field to validate the model. This series of measurement allows also the possibility of extracting the transverse resistivity of the matrix as this quantity is difficult to measure.
2. The E-J models have been investigated but they show some limitations. We believe that the percolation model is more realist, for example in DC operation. However,

these two models do not transcript the actual behavior of the superconductor as they are macroscopic model of a transition. It is necessary to investigate on new model to be implemented inside numerical models. This can be done in various ways, new characterisation methods, or extensive search on the numerical models compared with experimental work.

3. New developments have to be made inside the software dedicated for superconducting modeling in order to improve the convergence et speed up the calculations. Some algorithms have been studied and show good promises. On a second time, some new formulations for example shell method can be interesting to implement to take into account the diffusion layer in the MgB<sub>2</sub> wire.

Finally, the code developed inside MATLAB is only developed for the produced wire in superconducting cables. The next step is to include the calculations of AC losses regarding the architecture of the wire to optimize the design of it. In a second time, the implementation of new calculations perspectives would be interesting for a pre-design step and the calculations of AC losses in SMES, FCL, high field magnets.



---

## References

- [1] K. Onnes, "In a superconductor : discovery."
- [2] H. A. Boorse, D. B. Cook, and M. W. Zemansky, "Superconductivity of Lead," *Physical Review Letters*, vol. 78, no. 635, 1950.
- [3] J. F. Cochran and D. Mapother, "Superconducting Transition in Aluminum," *Physical Review Letters*, vol. 111, no. 132, 1958.
- [4] J. Nagamatsu, N. Nakagawa, T. Muranaka, Y. Zenitani, and J. Akimitsu, "Superconductivity at 39 K in magnesium diboride," *Nature*, vol. 410, pp. 63–64, 2001.
- [5] Y. Kamihara, H. Hiramatsu, M. Hirano, R. Kawamura, H. Yanagi, T. Kamiya, and H. Hosono, "Iron-Based Layered Superconductor : LaOFeP," *Journal of the American Chemical Society*, vol. 128, pp. 10012–10013, aug 2006.
- [6] Y. Kamihara, T. Watanabe, M. Hirano, and H. Hosono, "Iron-Based Layered Superconductor La(O<sub>1-x</sub>F<sub>x</sub>)FeAs(x=0.05-0.12) with T<sub>c</sub> = 26 K," *Journal of the American Chemical Society*, vol. 130, pp. 3296–3297, mar 2008.
- [7] A. P. Drozdov, M. I. Erements, I. A. Troyan, V. Ksenofontov, and S. I. Shylin, "Conventional superconductivity at 203 K at high pressures," *Nature*, vol. 525, pp. 1–19, 2015.
- [8] CCAS, "CCAS."
- [9] W. Meissner and R. Ochsenfeld, "Ein neuer Effekt bei Eintritt der Supraleitfähigkeit," *Naturwissenschaften*, vol. 21, no. 44, pp. 787–788, 1933.
- [10] C. P. J. Poole, H. A. Farach, and R. J. Creswick, *Superconductivity*. Academic Press, 1995.
- [11] G. Fuchs, K.-H. Müller, A. Handstein, K. Nenkov, V. N. Narozhnyi, D. Eckert, and M. Wolf, "Upper critical field and irreversibility line in superconducting MgB<sub>2</sub>," *Solid State Communications*, vol. 118, no. 10, 2001.
- [12] I. J. Daniel and D. P. Hampshire, "Harmonic calculations and measurements of the irreversibility field using a vibrating sample magnetometer," *Physical Review B*, vol. 61, no. 10, pp. 6982–6993, 2000.
- [13] J. W. Anderson, J. A. Parrell, M. Polak, and D. C. Larbalestier, "Determination of irreversibility field variations in mono- and multifilamentary Bi , Pb . . . 2 Sr 2 Ca 2 Cu 3 O x tapes by transport current methods," *Applied Physics Letters*, vol. 71, no. December, pp. 3892–3894, 1997.

- [14] D. Larbalestier, A. Gurevich, D. M. Feldmann, and A. Polyanskii, "High-Tc superconducting materials for electric power applications.," *Nature*, vol. 414, no. 6861, pp. 368–377, 2001.
- [15] A. Stenvall, "Stability and Quench," 2008.
- [16] F. London, *Superfluids*. Wiley-Interscience, 1950.
- [17] V. Ginzburg and L. Landau, "On the theory of superconductivity," *Zh. Eksp. Teor. Fiz.*, vol. 20, pp. 1064–1082, 1950.
- [18] P. E. Goa, H. Hauglin, M. Baziljevich, E. Il, P. L. Gammel, and T. H. Johansen, "Real-time magneto-optical imaging of vortices in superconducting NbSe<sub>2</sub>," *Superconductor Science and Technology*, vol. 14, pp. 729–731, 2001.
- [19] S. R. Foltyn, L. Civale, J. L. MacManus-Driscoll, Q. X. Jia, B. Maiorov, H. Wang, and M. Maley, "Materials science challenges for high-temperature superconducting wire," *Nat Mater*, vol. 6, pp. 631–642, sep 2007.
- [20] B. Josephson, "Possible new effects in superconductive tunnelling," *Physics Letters*, vol. 1, pp. 251–253, jul 1962.
- [21] W. Anderson, "Theory of Flux Creep in Hard Superconductors," *Physical Review Letters*, vol. 9, no. 7, pp. 309–311, 1962.
- [22] J. H. Durrell, *Critical Current Anisotropy in High Temperature Superconductors*. PhD thesis, University of Cambridge, 2001.
- [23] Y. Kim, C. Hempstead, and A. Strnad, "Critical persistent currents in hard superconductors," *Physical Review B*, vol. 9, no. 7, pp. 306–309, 1962.
- [24] R. Griessen, "Flux Creep Phenomena," in *Concise Encyclopedia of Magnetic and Superconducting Materials*, Oxford, j.e. evett ed., 1992.
- [25] C. P. Bean, "Magnetization of High-Field Superconductors," in *Reviews of Modern Physics*, pp. 31–39, 1964.
- [26] D. Hampshire and D. Larbalestier, "The critical current of NbTi multifilamentary wire : a comparison between critical current densities using AC magnetization techniques ( JCM ) and DC transport measurement ( JCT ) throughout the superconducting phase," *IEEE Transactions on Magnetics*, vol. 25, no. 2, pp. 1956–1958, 1989.
- [27] T. Boutboul, S. Le Naour, D. Leroy, L. Oberli, and V. Previtalli, "Critical current density in superconducting Nb - Ti strands in the 100 mT to 11 T applied field range," *IEEE Transactions on Applied Superconductivity*, vol. 16, no. 2, pp. 1184–1187, 2006.
- [28] E. Zeldov, N. M. Amer, G. Koren, and A. Gupta, "Flux creep in Bi<sub>2</sub>Sr<sub>2</sub>CaCu<sub>2</sub>O<sub>8</sub> epitaxial films," *Applied Physics Letters*, vol. 56, no. 17, p. 1700, 1990.
- [29] W. Paul, D. Hu, and T. Baumann, "Voltage-current characteristic between 10-13 V/cm and 10-3 V/cm of BSCCO and time decay of the magnetization," *Physica C : Superconductivity*, vol. 185-189, pp. 2373–2374, 1991.
- [30] J. Rhyner, "Magnetic properties and AC-losses of superconductors with power law current-voltage characteristics," *Physica C : Superconductivity*, vol. 212, no. 3-4, pp. 292–300, 1993.
- [31] F. Fickett, "Standards for measurement of the critical fields of superconductors," *Journal of Research of the National Bureau of Standards*, vol. 90, no. 2, p. 95, 1985.

- [32] H. Boschman, H. H. J. Ten Kate, and L. J. M. Van de Klundert, "Critical current transition study on multifilamentary NbTi superconductors having a Cu, a CuNi or a mixed matrix," *IEEE Transactions on Magnetics*, vol. 24, no. 2, pp. 1141–1144, 1988.
- [33] M. Chudy, Z. Zhong, M. Eisterer, and T. Coombs, "n-Values of commercial YBCO tapes before and after irradiation by fast neutrons," *Superconductor Science and Technology*, vol. 28, no. 3, p. 035008, 2015.
- [34] M. Nilsson-Mellbin and K. Salama, "Effect of applied magnetic field on the IV characteristics of melt-textured YBa<sub>2</sub>Cu<sub>3</sub>O<sub>7</sub> superconductors containing grain boundaries," *Physica C : Superconductivity*, vol. 227, no. 1-2, pp. 40–48, 1994.
- [35] C. M. Friend, C. Wellstood, D. Vazquez, and E. Maher, "Variable-temperature critical current measurements on YBaCuO coated conductors," *Superconductor Science and Technology*, vol. 16, no. 1, pp. 65–70, 2003.
- [36] S. Weidong, S. J. Han, X. Shi, S. N. Ehrlich, J. Jaroszynski, A. Goyal, and Q. Li, "High current superconductivity in FeSe<sub>0.5</sub>Te<sub>0.5</sub> coated conductors at 30 tesla," *Nature Communications*, vol. 4, no. 1347, 2013.
- [37] T. J. Ypma, "Historical Development of the Newtown-Raphson Method," *SIAM Review*, vol. 37, no. 4, pp. 531–551, 1995.
- [38] B. Zeimetz, B. a. Glowacki, and J. E. Evetts, "Application of percolation theory to current transfer in granular superconductors," *European Physical Journal B*, vol. 29, no. April 2002, pp. 359–367, 2002.
- [39] H. Gonzalez-Jorge, J. Peleteiro, J. Troncoso, E. Carballo, G. Domarco, and H. Gonza, "Evidence of current stabilization after long-time decay in high- T C superconductors," *Cryogenics*, vol. 45, pp. 135–140, 2005.
- [40] K. Yamafuji and T. Kiss, "Current-voltage characteristics near the glass-liquid transition in high-T<sub>c</sub> superconductors," *Physica C : Superconductivity*, vol. 290, no. 1-2, pp. 9–22, 1997.
- [41] W. J. Carr, *AC loss and macroscopic theory of superconductors*. CRC Press, 2001.
- [42] M. Solovyov, *AC losses in Coated Conductors*. PhD thesis, Slovak Academy of Sciences, 2011.
- [43] R. Shaw and D. Mapother, "Irreversibility in the Superconducting Transition of Lead," *Physical Review Letters*, vol. 118, no. 6, 1960.
- [44] M. N. Wilson, "Advances in low loss NbTi Strand and Cable," 2008.
- [45] T. Klein, L. Lyard, J. Marcus, Z. Holanova, and C. Marcenat, "Magnetic field dependence of the coherence length and penetration depth of MgB<sub>2</sub> single crystals," *Physical Review B*, vol. 73, no. 18, pp. 1–6, 2006.
- [46] NDT Resource Center, "The Hysteresis Loop and Magnetic Properties."
- [47] S. Fetisov, A. Nosov, V. Zubko, N. Bykovky, S. Zanejin, V. Vysotcky, G. Svalov, S. Lee, V. Petrykin, and V. Kalitka, "First Model Power Cables Made of Russian 2G HTS Wires and their Test Results," *Superconductor Science and Technology*, vol. 507, no. 032063, pp. 3–7, 2014.

- [48] T. Yamaguchi, Y. Shingai, M. Konishi, K. Ohya, Y. Ashibe, and H. Yumura, "Large Current and Low AC Loss High Temperature Superconducting Power Cable Using REBCO Wires," *SEI Technical Review*, vol. 1, no. 78, pp. 79–85, 2014.
- [49] M. D. Sumption, R. Scanlan, and E. Collings, "AC loss properties of some Bi :2212/Ag Rutherford cables and a comparison with those of cables wound with NbTi and Nb3Sn," *Cryogenics*, vol. 38, no. 12, pp. 1225–1232, 1999.
- [50] P. Tixador, Y. Cointe, T. Trollier, E. Maher, and A. Usoskin, "Tests of a Bi/Y Transformer," *IEEE Transactions on Applied Superconductivity*, vol. 15, pp. 1847–1850, jun 2005.
- [51] V. Sokolovsky, V. Meerovich, S. Goren, and G. Jung, "AC Losses in BSCCO Cylinders Operating in Inductive Current Limiter," *IEEE Transactions on Applied Superconductivity*, vol. 9, no. 2, pp. 1361–1364, 1999.
- [52] C. A. Luongo, P. J. Masson, T. Nam, D. Mavris, H. D. Kim, G. V. Brown, M. Waters, and D. Hall, "Next Generation More-Electric Aircraft : A Potential Application for HTS Superconductors," *IEEE Transactions on Applied Superconductivity*, vol. 19, no. 3, pp. 1055–1068, 2009.
- [53] S. A. Sunshine, T. Siegrist, L. F. Schneemeyer, D. W. Murphy, R. J. Cava, B. Batlogg, R. B. van Dover, R. M. Fleming, S. H. Glarum, S. Nakahara, R. Farrow, J. J. Krajewski, S. M. Zahurak, J. V. Waszczak, J. H. Marshall, P. Marsh, L. W. Rupp, and W. F. Peck, "Structure and physical properties of single crystals of the 84-K superconductor Bi<sub>2.2</sub>Sr<sub>2</sub>Ca<sub>0.8</sub>Cu<sub>2</sub>O<sub>8+delta</sub>," *Physical Review B*, vol. 38, pp. 893–896, jul 1988.
- [54] T. S. K. Ercan, H. Ozkan, N. M. Gasanly, and I, "Critical currents in Bi-2223 tapes near T<sub>c</sub> under magnetic field and gamma-irradiation," *Superconductor Science and Technology*, vol. 13, no. 12, p. 1625, 2000.
- [55] B. Gao, C. B. Cai, Z. Y. Liu, J. L. Liu, L. L. Ying, S. X. Cao, J. C. Zhang, T. Thersleff, R. Hühne, and B. Holzapfel, "Single and binary rare earth REBa<sub>2</sub>Cu<sub>3</sub>O<sub>7-delta</sub> films prepared by chemical solution deposition," *Journal of Physics : Conference Series*, vol. 97, p. 012245, 2008.
- [56] Aalto University, "YBCO crystal."
- [57] Y. V. Cherpak, V. A. Komashko, S. A. Pozigun, A. V. Semenov, C. G. Tretiatchenko, E. A. Pashitskii, and V. M. Pan, "Critical Current Density of HTS Single Crystal YBCO Thin Films in Applied dc Field," *IEEE Transactions on Applied Superconductivity*, vol. 15, no. 2, pp. 2783–2786, 2005.
- [58] M. Lyatti, A. Savenko, and U. Poppe, "Ultra-thin YBa<sub>2</sub>Cu<sub>3</sub>O<sub>7-x</sub> films with high critical current density," *Superconductor Science and Technology*, vol. 29, no. 6, p. 65017, 2016.
- [59] A. Gurevich, "To Use or Not to Use Cool Superconductors?," *Nature materials*, vol. 10, pp. 255–259, 2011.
- [60] T. Masui, "Irreversibility field and coherence length of Ca-substituted YBCO single crystals," *Physica C*, vol. 431, pp. 335–339, 2005.
- [61] A. Goyal and M. P. Paranthaman, "The RABiTS Approach : Using Substrates for," *MRS Bulletin*, vol. 29, no. 08, pp. 552–561, 2004.

- [62] Y. Iijima, N. Kaneko, S. Hanyu, Y. Sutoh, K. Kakimoto, S. Ajimura, and T. Saitoh, "Development of IBAD/PLD process for long length Y-123 conductors in Fujikura," *Physica C : Superconductivity*, vol. 445-448, pp. 509–514, 2006.
- [63] SuperPower, "2G HTS wire."
- [64] D. K. Hilton, A. V. Gavrilin, and U. P. Trociewitz, "Practical fit functions for transport critical current versus field magnitude and angle data from ( RE ) BCO coated conductors at fixed low temperatures and in high magnetic fields," *Superconductor Science and Technology*, vol. 28, no. 7, p. 74002, 2015.
- [65] E. Comittee, "Eurotapes project."
- [66] N. Kosheleva, I. Shahrou, C. E. Bruzek, G. Vega, and G. Kolmogorov, "Development of a Simplified Numerical Model for the Design of 2G High-Temperature Superconductors," *IEEE Transactions on Applied Superconductivity*, vol. 26, no. 3, 2016.
- [67] C. E. Bruzek, A. Allais, S. Morice, C.-F. Theune, S. Petit, M. Mikolajczyk, N. Dechoux, C. Jimenez, E. Sarigiannidou, L. Porcar, J. Soubeyroux, P. Odier, and T. Waeckerle, "New HTS 2G Round Wires," *IEEE Transactions on Applied Superconductivity*, vol. 22, pp. 5800204–5800204, jun 2012.
- [68] Strauss and Marken, "S4E Paestum," 2014.
- [69] D. Larbalestier, J. Jiang, U. P. Trociewitz, F. Kametani, C. Scheuerlein, M. Dalban-Canassy, M. Matras, P. Chen, N. Craig, P. Lee, and E. Hellstrom, "Isotropic round-wire multifilament cuprate superconductor for generation of magnetic fields above 30 T," *Nature materials*, vol. 13, pp. 375–381, 2014.
- [70] K. Komori, K. Kawagishi, Y. Takano, S. Arisawa, H. Kumakura, and M. Fukutomi, "A New Approach for the Fabrication of MgB<sub>2</sub> Superconducting Tape with Large In-field Transport Critical Current Density," *Applied Physics Letters*, vol. 81, no. 6, pp. 1047–1049, 2002.
- [71] K. Müller, G. Fuchs, A. Handstein, K. Nenkov, V. N. Narozhnyi, D. Eckert, and F. Werkstofforschung, "The upper critical field in superconducting MgB<sub>2</sub>," *Journal of Alloys and Compounds*, vol. 322, no. 1-2, pp. 1–8, 2001.
- [72] READE, "Magnesium Diboride/ Magnesium Boride Powder (MgB<sub>2</sub>)."
- [73] J. Pelegrín, G. Romano, E. Martínez, L. a. Angurel, R. Navarro, C. Ferdeghini, S. Brisigotti, G. Grasso, and D. Nardelli, "Experimental and numerical analysis of quench propagation on MgB<sub>2</sub> tapes and pancake coils," *Superconductor Science and Technology*, vol. 26, no. 4, p. 045002, 2013.
- [74] C. Zhou, W. Offringa, a. Bergen, W. a. J. Wessel, H. J. G. Krooshoop, M. Dhallé, M. D. Sumption, E. W. Collings, M. Rindfleisch, M. Tomsic, H. H. J. ten Kate, and a. Nijhuis, "Intra-wire resistance and AC loss in multi-filamentary MgB<sub>2</sub> wires," *Superconductor Science and Technology*, vol. 26, no. 2, p. 025002, 2013.
- [75] Columbus, "Columbus Superconductors SPA."
- [76] A. Stenvall, A. Korpela, R. Mikkonen, and G. Grasso, "Quench analysis of MgB<sub>2</sub> coils with a ferromagnetic matrix," *Superconductor Science and Technology*, vol. 19, pp. 581–588, 2006.

- [77] P. Kováč, L. Kopera, T. Melišek, M. Rindfleisch, W. Haessler, and I. Hušek, “Behaviour of filamentary MgB<sub>2</sub> wires subjected to tensile stress at 4.2 K,” *Superconductor Science and Technology*, vol. 26, no. 10, p. 105028, 2013.
- [78] X. Li, L. Ye, and Z. Gao, “Close circuit test of MgB<sub>2</sub> coil with superconducting joints and a persistent current switch,” *Superconductor Science and Technology*, vol. 234, no. 02, p. 022020, 2010.
- [79] J. Ling, J. P. Voccio, S. Hahn, Y. Kim, J. Song, J. Bascuñán, and Y. Iwasa, “Construction and Persistent-Mode Operation of MgB<sub>2</sub> Coils in the Range 10-15 K for a 0.5-T/240-mm Cold Bore MRI Magnet,” *IEEE Transactions on Applied Superconductivity*, vol. 2014, no. October, pp. 2–6, 2014.
- [80] E. W. Collings, S. Kawabata, M. Bhatia, M. Tomsic, and M. D. Sumption, “Magnesium Diboride Superconducting Strand for Accelerator and Light Source Applications,” *IEEE Transactions on Applied Superconductivity*, vol. 16, no. 2, pp. 1445–1448, 2006.
- [81] R. Musenich, V. Calvelli, S. Farinon, R. Battiston, W. J. Burger, and P. Spillantini, “A Magnesium Diboride Superconducting Toroid for Astroparticle Shielding,” *IEEE Transactions on Applied Superconductivity*, vol. 24, no. 3, pp. 4–7, 2014.
- [82] N. Atomura, T. Takahashi, H. Amata, T. Iwasaki, K. Son, D. Miyagi, M. Tsuda, T. Hamajima, T. Shintomi, Y. Makida, T. Takao, K. Munakata, and M. Kajiwara, “Conceptual design of MgB<sub>2</sub> coil for the 100 MJ SMES of advanced superconducting power conditioning system,” *Physics Procedia*, vol. 27, pp. 400–403, 2012.
- [83] A. B. Abrahamsen, N. Magnusson, B. B. Jensen, D. Liu, and H. Polinder, “Design of an MgB<sub>2</sub> race track coil for a wind generator pole demonstration,” *Journal of Physics : Conference Series*, vol. 507, p. 032001, may 2014.
- [84] K. Kajikawa and T. Nakamura, “Proposal of a Fully Superconducting Motor for Liquid Hydrogen Pump With MgB<sub>2</sub> Wire,” *IEEE Transactions on Applied Superconductivity*, vol. 19, no. 3, pp. 1669–1673, 2009.
- [85] I. Marino, A. Pujana, G. Sarmiento, S. Sanz, J. M. Merino, M. Tropeano, J. Sun, and T. Canosa, “Lightweight MgB<sub>2</sub> superconducting 10 MW wind generator,” *Superconductor Science and Technology*, vol. 29, no. 2, p. 024005, 2016.
- [86] X. Obradors and T. Puig, “Coated conductors for power applications : materials challenges,” *Superconductor Science and Technology*, vol. 27, no. 27, p. 044003, 2014.
- [87] C. Senatore, M. Alessandrini, A. Lucarelli, R. Tediosi, D. Uglietti, and Y. Iwasa, “Progresses and challenges in the development of high-field solenoidal magnets based on RE123 coated conductors,” *Superconductor Science and Technology*, vol. 27, no. 10, p. 103001, 2014.
- [88] P. J. Masson, P. Tixador, J. C. Ordoñez, A. M. Morega, and C. A. Luongo, “Electro-Thermal Model for HTS Motor Design,” *IEEE Transactions on Applied Superconductivity*, vol. 17, no. 2, pp. 1529–1532, 2007.
- [89] S. Fukui, J. Ogawa, T. Sato, O. Tsukamoto, N. Kashima, and S. Nagaya, “Study of 10 MW-Class Wind Turbine Synchronous Generator With HTS Field Windings,” *Ieee Transactions on Applied Superconductivity*, vol. 21, no. 3, pp. 1151–1154, 2011.

- [90] NHMFL, “Engineering Critical Current Density vs. Applied Field,” 2014.
- [91] A. Morandi, “HTS dc transmission and distribution : concepts, applications and benefits,” *Superconductor Science and Technology*, vol. 28, no. 12, p. 123001, 2015.
- [92] A. Moyses Luiz, “Superconductivity Application in PowerSystem,” in *Applications of High-Tc Superconductivity*, InTech, Chapters, geun-joon ed., 2011.
- [93] J. F. Maguire, J. Yuan, W. Romanosky, F. Schmidt, R. Soika, S. Bratt, F. Durand, C. King, J. McNamara, and T. E. Welsh, “Progress and status of a 2G HTS power cable to be installed in the Long Island Power Authority (LIPA) grid,” *IEEE Transactions on Applied Superconductivity*, vol. 21, pp. 961–966, 2011.
- [94] M. Stemmler, F. Merschel, M. Noe, and A. Hobl, “Ampacity - Installation of Advanced Superconducting 10 kV System in City Center Replaces Conventional 110 kV Cables,” in *IEEE Transactions Conference on Applied Superconductivity and Electromagnetic Devices*, 2013.
- [95] Nexans, “AmpaCity power cable,” 2012.
- [96] T. Pultarova, “World’s longest superconductor cable works without a hitch,” 2014.
- [97] M. Takayasu, L. Chiesa, L. Bromberg, and J. V. Minervini, “HTS twisted stacked-tape cable conductor,” *Superconductor Science and Technology*, vol. 25, no. 014011, 2012.
- [98] D. C. van der Laan, “YBaCuO coated conductor cabling for low ac-loss and high-field magnet applications,” *Superconductor Science and Technology*, vol. 22, p. 065013, jun 2009.
- [99] M. Majoros, M. D. Sumption, E. W. Collings, and D. C. van der Laan, “Magnetization losses in superconducting YBCO conductor-on-round-core (CORC) cables,” *Superconductor Science and Technology*, vol. 27, p. 125008, dec 2014.
- [100] D. C. Van der Laan, X. F. Lu, and L. F. Goodrich, “Compact GdBa<sub>2</sub>Cu<sub>3</sub>O<sub>7-δ</sub> coated conductor cables for electric power transmission and magnet applications,” *Superconductor Science and Technology*, vol. 24, no. 042001, 2011.
- [101] A. Ballarino, “Development of superconducting links for the Large Hadron Collider machine,” *Superconductor Science and Technology*, vol. 27, p. 044024, apr 2014.
- [102] BEST-PATHS, “DEMO 5 Superconductor cables power up for DC grids,” 2015.
- [103] A. V. A. Gavrilin, J. Lu, H. Bai, D. K. Hilton, W. D. Markiewicz, and H. W. Weijers, “Observations From the Analyses of Magnetic Field and AC Loss Distributions in the NHMFL 32T All-Superconducting Magnet HTS Insert,” *IEEE Transactions on Applied Superconductivity*, vol. 23, no. 3, pp. 1–1, 2013.
- [104] K. Higashikawa, T. Kiss, M. Inoue, K. Imamura, T. Nakamura, S. Awaji, K. Watanabe, H. Fukushima, Y. Yamada, and Y. Shiohara, “Coupled analysis method for high-field magnet coil using coated conductor based on J-E characteristics as a function of temperature, magnetic field vector and mechanical strain,” *IEEE Transactions on Applied Superconductivity*, vol. 19, no. 3, pp. 1621–1625, 2009.
- [105] K. Koyanagi, M. Ono, S. Hanai, K. Watanabe, S. Awaji, T. Hamajima, T. Kiyoshi, and H. Kumakura, “Design of a 30 T Superconducting Magnet Using a Coated

- Conductor Insert,” *IEEE Transactions on Applied Superconductivity*, vol. 19, no. 3, pp. 1617–1620, 2009.
- [106] T. Schneider, M. Eisele, F. Hornung, M. Klaeser, P. M. Leys, and C. Ruf, “Future Upgrade of the Superconducting High Field Facility HOMER II to 25 T,” *IEEE Transactions on Applied Superconductivity*, vol. 25, no. 3, pp. 3–6, 2015.
- [107] M. Beckenbach, F. Hornung, M. Klaser, P. Leys, B. Lott, and T. Schneider, “Manufacture and test of a 5 T bi-2223 insert coil,” *Applied Superconductivity, IEEE Transactions on*, vol. 15, no. 2, pp. 1484–1487, 2005.
- [108] P. M. Leys, M. Klaeser, F. Schleissinger, and T. Schneider, “Angle-Dependent U(I) Measurements of HTS Coated Conductors,” *IEEE Transactions on Applied Superconductivity*, vol. 23, no. 3, pp. 4–7, 2013.
- [109] E. Pardo, M. Kapolka, P. Kovac, J. Souc, F. Grilli, and A. Piqué, “Three-Dimensional Modeling and Measurement of Coupling AC Loss in Soldered Tapes and Striated Coated Conductors,” *IEEE Transactions on Applied Superconductivity*, vol. 26, no. 3, 2016.
- [110] E. Pardo, P. Kovac, and J. Souc, “Power Loss in ReBCO Racetrack Coils Under AC Applied Magnetic Field and DC Current,” *IEEE Transactions on Applied Superconductivity*, vol. 23, no. 3, 2013.
- [111] K. Berger, J. Lévêque, D. Netter, B. Douine, and A. Rezzoug, “AC Transport Losses Calculation in a Bi-2223 Current Lead Using Thermal Coupling With an Analytical Formula,” *IEEE Transactions on Applied Superconductivity*, vol. 15, no. 2, pp. 1508–1511, 2005.
- [112] G. Mikitik, Y. Mawatari, A. T. Wan, and F. Sirois, “Analytical Methods and Formulas for Modeling High Temperature Superconductors,” *Journal of Latex Class Files*, vol. 23, no. 2, 2013.
- [113] F. Grilli, V. M. R. Zerme, E. Pardo, M. Vojen, and A. Kario, “Self-field Effects and AC Losses in Pancake Coils Assembled from Coated Conductor Roebel Cables,” *IEEE Transactions on Applied Superconductivity*, vol. 24, no. 3, pp. 1–5, 2014.
- [114] A. Kameni, D. Netter, F. Sirois, B. Douine, and J. Lévêque, “New hybrid FE-FV method for computing current distribution in 2-D superconductors : application to an HTS cylinder in transverse magnetic field,” *IEEE Transactions on Applied Superconductivity*, vol. 19, no. 3, pp. 2423–2427, 2009.
- [115] A. Kameni, S. Mezani, F. Sirois, D. Netter, J. Leveque, and B. Douine, “A 2-D robust FE-FV mixed method to handle strong nonlinearities in superconductors,” *IEEE Transactions on Magnetics*, vol. 46, no. 8, pp. 3445–3448, 2010.
- [116] W. T. Norris, “Calculation of hysteresis losses in hard superconductors carrying ac : isolated conductors and edges of thin sheets,” *Journal of Applied Physics*, vol. 3, no. 1930, pp. 489–507, 1969.
- [117] E. H. Brandt, “Superconductors of finite thickness in a perpendicular magnetic field : Strips and slabs.,” *Physical review. B, Condensed matter*, vol. 54, pp. 4246–4264, aug 1996.
- [118] B. Douine, *Étude des pertes dans les supraconducteurs*. PhD thesis, Université Henri Poincaré, Nancy-I, 2001.

- [119] Y. Mawatari, “Superconducting tubular wires in transverse magnetic fields,” *Physical Review B*, vol. 83, p. 134512, apr 2011.
- [120] G. Meunier, *The Finite Element Method for Electromagnetic Modeling*. Wiley-Interscience, ltd., iste ed., 2008.
- [121] O. C. Zienkiewicz, *The Finite Element Method : Its Basis and Fundamentals*. Butterworth, 7 ed., 2005.
- [122] P. Wriggers, *Nonlinear Finite Element Methods*. Springer, softcover ed., 2010.
- [123] E. Vinot, *Modélisation des supraconducteurs HTC Applications au calcul des pertes AC*. PhD thesis, Université de Grenoble, 2000.
- [124] F. Grilli, S. Stavrev, Y. L. Floch, M. Costa-bouzo, E. Vinot, I. Klutsch, G. Meunier, P. Tixador, and B. Dutoit, “Finite-Element Method Modeling of Superconductors : From 2-D to 3-D,” *IEEE Transactions on Applied Superconductivity*, vol. 15, no. 1, pp. 17–25, 2005.
- [125] Z. Hong, a. M. Campbell, and T. a. Coombs, “Numerical solution of critical state in superconductivity by finite element software,” *Superconductor Science and Technology*, vol. 19, pp. 1246–1252, dec 2006.
- [126] M. Ainslie, W. Yuan, Z. Hong, R. Pei, T. J. Flack, and T. A. Coombs, “Modeling and Electrical Measurement of Transport AC Loss in HTS-Based Superconducting Coils for Electric Machines,” *IEEE Transactions on Applied Superconductivity*, pp. 26–29, 2010.
- [127] V. M. R. Zermeno, F. Grilli, and F. Sirois, “A full 3D time-dependent electromagnetic model for Roebel cables,” *Superconductor Science and Technology*, vol. 26, p. 052001, may 2013.
- [128] A. Stenvall, V. Lahtinen, and M. Lyly, “An H -formulation-based three-dimensional hysteresis loss modelling tool in a simulation including time varying applied field and transport current : the fundamental problem and its solution,” *Superconductor Science and Technology*, vol. 27, p. 104004, oct 2014.
- [129] V. Lahtinen, A. Stenvall, F. Sirois, and M. Pellikka, “A Finite Element Simulation Tool for Predicting Hysteresis Losses in Superconductors Using an H-Oriented Formulation with Cohomology Basis Functions,” *Journal of Superconductivity and Novel Magnetism*, vol. 28, no. 8, pp. 2345–2354, 2015.
- [130] A. T. Phung, P. Labie, O. Chadebec, Y. L. Floch, and G. Meunier, “On the Use of Automatic Cuts Algorithm for T0-T-Phi Formulation in Nondestructive Testing by Eddy-Current,” *Intelligent Computer Techniques in Applied Electromagnetics*, Springer, vol. 119, pp. 55–62, 2008.
- [131] R. Brambilla, F. Grilli, D. N. Nguyen, L. Martini, and F. Sirois, “AC losses in thin superconductors : the integral equation method applied to stacks and windings,” *Superconductor Science and Technology*, vol. 22, p. 075018, jul 2009.
- [132] R. Brambilla, F. Grilli, L. Martini, and F. Sirois, “Integral equations for the current density in thin conductors and their solution by the finite-element method,” *Superconductor Science and Technology*, vol. 21, p. 105008, oct 2008.

- [133] J. Ogawa, S. Fukui, T. Oka, T. Sato, T. Ito, J. Sugisawa, and a. Tamura, “Experimental Evaluation of the Effect on AC Loss of a Polygonal Arrangement in YBCO Assembled Conductors,” *IEEE Transactions on Applied Superconductivity*, vol. 21, pp. 3285–3288, jun 2011.
- [134] K. Takeuchi, N. Amemiya, T. Nakamura, O. Maruyama, and T. Ohkuma, “Model for electromagnetic field analysis of superconducting power transmission cable comprising spiraled coated conductors,” *Superconductor Science and Technology*, vol. 24, p. 119501, nov 2011.
- [135] T.-t. Nguyen, G. Meunier, J.-m. Guichon, O. Chadebec, T.-s. Nguyen, and A. P. I. Equation, “An Integral Formulation for the Computation of 3-D Eddy Current Using Facet Elements,” *IEEE Transactions on Magnetics*, vol. 50, no. 2, pp. 2–5, 2014.
- [136] M. C. Ahn, J. Jang, S. Hahn, Y. G. Kim, and H. Lee, “Field mapping and automated shimming of an HTS magnet by ‘Internal’ active shim coils located in the bore of the magnet,” *IEEE Transactions on Applied Superconductivity*, vol. 25, no. 3, pp. 3–6, 2015.
- [137] P. Tixador, B. Bellin, M. Deleglise, J. C. Vallier, C. E. Bruzek, S. Pavard, and J. M. Saugrain, “Design of a 800 kJ HTS SMES,” *IEEE Transactions on Applied Superconductivity*, vol. 15, no. 2, pp. 1907–1910, 2005.
- [138] K. Ho-Le, “Finite element mesh generation methods : A review and classification,” *Computer-Aided Design*, vol. 20, no. 1, 1988.
- [139] M. Ainslie, *Transport AC loss in high temperature superconducting coils*. PhD thesis, University of Cambridge, 2012.
- [140] V. M. R. Zermeno, N. Mijatovic, C. Træholt, T. Zirngibl, E. Seiler, A. B. Abrahamsen, N. F. Pedersen, and M. P. Sørensen, “Towards Faster FEM Simulation of Thin Film Superconductors : A Multiscale Approach,” *IEEE Transactions on Applied Superconductivity*, vol. 21, no. 3, pp. 3273–3276, 2011.
- [141] V. M. R. Zermeno and F. Grilli, “3D modeling and simulation of 2G HTS stacks and coils,” *Superconductor Science and Technology*, vol. 044025, no. 27, p. 7, 2014.
- [142] F. Ossart and V. Ionita, “Convergence de la méthode du point fixe modifiée pour le calcul de champ magnétique avec hysteresis,” *The European Physical Journal Applied Physics*, vol. 69, pp. 63–69, 1999.
- [143] F. Sirois, F. Grilli, F. Sirois, and F. Grilli, “Potential and limits of numerical modeling for supporting the development of HTS devices,” *Superconductor Science and Technology*, vol. 28, no. 4, pp. 1–24, 2015.
- [144] SuperPower, “<http://www.superpower-inc.com/>.”
- [145] SuperOx, “SuperOx-Superconductivity.”
- [146] J. G. Hust, D. H. Weitzel, and R. L. Powell, “Thermal conductivity, electrical resistivity, and thermopower of aerospace alloys from 4 to 300 K,” *Journal of Research of the National Bureau of Standards*, vol. 75, no. 4, pp. 269–277, 1971.
- [147] D. R. Smith and F. R. Fickett, “Low-Temperature Properties of Silver,” *J. Res. Natl. Inst. Stand. Technol.*, vol. 100, no. 2, pp. 119–171, 1995.

- [148] H. Yamasaki, Y. Mawatari, Y. Nakagawa, and H. Yamada, "Nondestructive, inductive measurement of critical current densities of superconducting films in magnetic fields," *IEEE Transactions on Applied Superconductivity*, vol. 13, pp. 3718–3721, jun 2003.
- [149] B. Jönsson, K. Rao, S. Yun, and U. Karlsson, "Method to extract the critical current density and the flux-creep exponent in high-  $T_c$  thin films using ac susceptibility measurements," *Physical Review B*, vol. 58, no. 9, pp. 5862–5867, 1998.
- [150] P. Brownsey, D. Hazelton, M. Matsui, H. Sakamoto, A. Sundaram, J. Tanski, and J. Waterman, "Critical Current Measurements System for Short Sample REBCO Conductors at Varying Field ANgle and Temperature," 2014.
- [151] A. Xu, J. J. Jaroszynski, F. Kametani, Z. Chen, D. C. Larbalestier, Y. L. Viouchkov, Y. Chen, Y. Xie, and V. Selvamanickam, "Angular dependence of  $J_c$  for YBCO coated conductors at low temperature and very high magnetic fields," *Superconductor Science and Technology*, vol. 23, no. 1, p. 014003, 2010.
- [152] Haynes International, "Hastelloy C276."
- [153] T. Benkel, Y. Miyoshi, G. Escamez, D. Gonzales, X. Chaud, A. Badel, and P. Tixador, "REBCO Performance at High Field with Low Incident Angle and Preliminary Tests for a 10-T Inset," *IEEE Transactions on Applied Superconductivity*, vol. 26, no. 3, 2016.
- [154] P. Krüger, *Optimisation of hysteretic losses in high-temperature superconducting wires*. PhD thesis, Fakultät für Elektrotechnik und Informationstechnik des Karlsruher Institus für Technologie genehmigte, 2014.
- [155] F. Sirois and F. Grilli, "Numerical Considerations About Using Finite-Element Methods to Compute AC Losses in HTS," *IEEE Transactions on Applied Superconductivity*, vol. 18, no. 3, pp. 1733–1742, 2008.
- [156] Zienkiewicz, *The Finite Element Method in Engineering Science*. McGraw-Hill Publishing Company, 1971.
- [157] C. Geuzaine, P. Dular, and W. Legros, "A general environment for coupled finite element and boundary integral methods.," in *Proceedings of the 8th International IGTE Symposium on Numerical Field Calculation in Electrical Engineering*, pp. 106–111, 1998.
- [158] J. Jensen, W. Tuttle, R. Stewart, H. Brechna, and A. Prodell, "Electrical Resistivity of Some Metallic Elements and Commercial Alloys," tech. rep., Brookhaven National Laboratory, 1980.
- [159] G. Escamez, A. Badel, P. Tixador, B. Ramdane, G. Meunier, A. Allais, and C.-E. Bruzek, "Numerical Modelling of AC Hysteresis Losses in HTS Tubes," *IEEE Transactions on Applied Superconductivity*, vol. 25, no. 3, pp. 3–7, 2015.
- [160] CEDRAT, "FLUX software."
- [161] P. Tixador, G. David, T. Chevalier, G. Meunier, and K. Berger, "Thermal-electromagnetic modeling of superconductors," *Cryogenics*, vol. 47, no. 11-12, pp. 539–545, 2007.
- [162] V. Lahtinen, *Searching for Frontiers in Contemporary Eddy Current Model Based Hysteresis Loss Modelling of Superconductors*. PhD thesis, Tampere University of Technology, 2014.

- [163] F. Gomory, M. Vojenčiak, E. Pardo, and J. Souc, "Magnetic flux penetration and AC loss in a composite superconducting wire with ferromagnetic parts," *Superconductor Science and Technology*, vol. 22, no. 034017, 2009.
- [164] P. Hejda and T. Zelinka, "Generalized Preisach model of hysteresis — theory and experiment," *Czechoslovak Journal of Physics*, vol. 40, no. 1, pp. 57–68, 1990.
- [165] R. Chaplin, M. Coulson, R. Simpson, and R. Slater, "Representation of magnetic characteristic, including hysteresis, using Preisach's theory," *Electrical Engineers, Proceedings of the Institution of*, vol. 125, no. 6, p. 7972, 1978.
- [166] T. Yamaguchi, F. Ueda, and K. Takeda, "Automatic Measurement of Preisach Distributions in Soft Magnetic Materials," *IEEE Translation Journal on Magnetics in Japan*, vol. 2, no. 5, pp. 412–413, 1987.
- [167] S. J. Ye, A. Matsumoto, K. Togano, T. Ohmura, and H. Kumakura, "The critical current properties of 37-filament internal Mg diffusion-processed MgB<sub>2</sub> wires," *Superconductor Science and Technology*, vol. 26, no. 10, p. 105027, 2013.
- [168] Y. Miyoshi, A. Badel, X. Chaud, T. Benkel, B. Vincent, P. Tixador, J. Marpaud, F. Debray, T. Lécresse, M. Devaux, P. Fazilleau, and J.-m. Rey, "Performance Tests of Prototype High-Field HTS Coils in Grenoble," *IEEE Transactions on Applied Superconductivity*, vol. 25, no. 3, pp. 4600505–46010, 2015.
- [169] Y. Inoue, H. Kurahashi, Y. Fukumoto, and M. Shimada, "Critical Current Density and n-Value of NbTi Wires at Low Field," *IEEE Transactions on Applied Superconductivity*, vol. 5, no. 2, pp. 1201–1204, 1995.
- [170] J. Kováč, J. Šouc, P. Kováč, and I. Hušek, "AC losses of single-core MgB<sub>2</sub> wires with different metallic sheaths.," *Physica C : Superconductivity and its Applications*, 2015.
- [171] B. Legendre and M. Sghaier, "Curie temperature of nickel," *Journal of Thermal Analysis and Calorimetry*, vol. 105, no. 1, pp. 141–143, 2011.
- [172] R. L. Edwards, "The Magnetic Properties of Evaporated Nickel and Iron Films," *Physical Review*, vol. 29, pp. 321–331, feb 1927.
- [173] M. S. Boley, D. a. Franklin, and D. K. Rigsbee, "Heat treatment effects on sensitivity and hysteresis loops of magnetoelastic torque transducers," *Journal of Applied Physics*, vol. 87, no. 9, p. 7073, 2000.
- [174] R. Morita, S. Kobayashi, A. G. Odeshi, J. A. Szpunar, K. Miura, and Y. Kamada, "Effects of high-strain-rate deformation on magnetic hysteresis in high-tensile steels," *AIP Advances*, vol. 6, no. 5, p. 055903, 2016.
- [175] J. Dompierre, P. Labbe, M.-g. Vallet, and R. Camarero, "How to Suidvide Pyramids, Prisms and Hexahedra into Tetrahedra," tech. rep., Centre de recherche en calcul appliqué (CERCA), Montreal, Canada, 1999.
- [176] G. Li, Y. Yang, M. A. Susner, M. D. Sumption, and E. W. Collings, "Critical current densities and n -values of MgB<sub>2</sub> strands over a wide range of temperatures and fields," *Superconductor Science and Technology*, vol. 25, no. 02, p. 025001, 2012.
- [177] C. Y. Ho, M. W. Ackerman, K. Y. Wu, T. N. Havill, R. H. Bogaard, R. a. Matula, S. G. Oh, and H. M. James, "Electrical Resistivity of Ten Selected Binary Alloy Systems," 1983.

- [178] G. Escamez, F. Sirois, V. Lahtinen, A. Stenvall, A. Badel, P. Tixador, B. Ramdane, G. Meunier, R. Perrin-Bit, and C.-E. Bruzek, “3-D Numerical Modeling of AC losses in multi-filamentary MgB2 wires,” *IEEE Transactions on Applied Superconductivity*, vol. 26, no. 3, 2016.
- [179] M. N. Wilson, *Superconducting Magnets*. Oxford University Press, 1982.
- [180] V. Lahtinen and A. Stenvall, “The difficulty of modeling ripple field losses in superconductors using the eddy current model,” *IEEE Transactions on Applied Superconductivity*, vol. 23, no. 3, pp. 4900505–4900505, 2013.
- [181] F. Grilli and Z. Xu, “Modeling AC ripple currents in HTS coated conductors by integral equations,” *Cryogenics*, pp. 1–5, 2016.
- [182] E. San José Saras, “Impact Of Power Electronics On The Electrical Chain Of Renewable Energy Farm,” *Nexans Internal Report (confidential)*, 2012.
- [183] E-Highway, “e-Highway2050.”
- [184] BEST-PATHS, “BEST-PATHS project.”
- [185] J. Setreus and L. Bertling, “Introduction to HVDC Technology for Reliable Electrical Power Systems,” *Proceedings of the 10th International Conference on Probabilistic Methods Applied to Power Systems*, pp. 1–8, 2008.
- [186] M. Petit, S. Bacha, X. Guillaud, H. Morel, D. Planson, and B. Raison, “Les reseaux HVDC multi-terminaux : des defis multiples en genie électrique,” in *Symposium de Genie Electrique (SGE'14)*, pp. 8–10, 2014.
- [187] Management French Agency for Environment and Energy, “Photovoltaic Power Applications in France National Survey Report 2011,” tech. rep., Management French Agency for Environment and Energy, 2011.
- [188] Wind Europe, “Wind in power : 2013 European statistics.”
- [189] A. Marian, A. Ballarino, C. Catalan, N. Dittmar, G. Escamez, S. Giannelli, F. Grilli, S. Holé, C. Haberstroh, F. Lesur, C. Poumarède, M. Tropeano, G. Vega, and C.-e. Bruzek, “An MgB2 HVDC superconducting cable for power transmission with a reduced carbon footprint,” in *ED2E 2016*, pp. 1–7, 2016.
- [190] International Organization for Standardization (ISO) ISO 14044, “Environmental management - Life cycle assessment - Requirements and guidelines (2006),” tech. rep., IOS, 2006.
- [191] International Organization for Standardization (ISO) ISO 14040, “Environmental management - Life cycle assessment - Principles and framework,” tech. rep., IOS, 2006.
- [192] R. Jorge, “Life cycle assessment of electricity transmission and distribution - Part I : power lines and cables,” *The International Journal of Life Cycle Assessment*, vol. 17, pp. 9–15, 2012.
- [193] CIGRE, “DC side harmonics and filtering in HVDC transmission systems,” tech. rep., CIGRE, 1994.
- [194] CIGRE, “Cross-modulation of harmonics in HVDC schemes,” Tech. Rep. June, CIGRE, 1999.

- [195] CIGRE, “Murraylink, the longest underground HVDC cable in the world,” tech. rep., CIGRE, 2004.
- [196] S. Giannelli, G. Montenero, and A. Ballarino, “Quench Propagation in Helium-Gas-Cooled MgB<sub>2</sub> Cables,” *IEEE Transactions on Applied Superconductivity*, vol. 26, no. 3, pp. 3–7, 2016.
- [197] A. Stenvall, A. Korpela, R. Mikkonen, and G. Grasso, “Stability considerations of multifilamentary MgB<sub>2</sub> tape,” *Superconductor Science and Technology*, vol. 19, pp. 184–189, feb 2006.
- [198] P. J. Masson, V. R. Rouault, G. Hoffmann, and C. A. Luongo, “Development of quench propagation models for coated conductors,” *IEEE Transactions on Applied Superconductivity*, vol. 18, no. 2, pp. 1321–1324, 2008.
- [199] W. K. Chan and J. Schwartz, “A Hierarchical Three-Dimensional Multiscale Electro Magneto Thermal Model of Quenching in Coated-Conductor-Based Coils,” *IEEE Transactions on Applied Superconductivity*, vol. 22, no. 5, pp. 4706010–4706010, 2012.
- [200] W. R. G. Kemp, P. G. Klemens, and G. K. White, “Thermal and Electrical Conductivities of Iron, Nickel, Titanium and Zirconium at Low Temperatures,” *Australian Journal of Physics*, vol. 9, p. 180, 1956.
- [201] R. M. Swift and D. White, “Low Temperature Heat Capacities of Magnesium Diboride (MgB<sub>2</sub>) and Magnesium Tetraboride (MgB<sub>4</sub>),” *Journal of the American Chemical Society*, vol. 79, pp. 3641–3644, jul 1957.
- [202] V. G. Bessergenev, Y. A. Kovalevskaya, L. G. Lavrenova, and I. E. Paukov, “Low temperature heat capacity of the coordination compound : Nickel(II) nitrate with 4-amine-1,2,4-triazole attemperatures from 11 to 317 K,” *Journal of Thermal Analysis and Calorimetry*, vol. 75, no. 1, pp. 331–336, 2004.
- [203] A. Sagal, “Nickel Alloys.”
- [204] T. a. Prikhna, “Properties of MgB<sub>2</sub> bulk,” *cond-mat.supr-con*, 2009.
- [205] F. Incropera and D. DeWitt, *Fundamentals of Heat and Mass Transfer*. John Wiley & Sons, fifth ed. ed., 2002.
- [206] A. Lucianetti, D. Albach, and J.-C. Chanteloup, “Active-mirror-laser-amplifier thermal management with tunable helium pressure at cryogenic temperatures,” *Opt. Express*, vol. 19, no. 13, pp. 12766–12780, 2011.
- [207] A. Gupta, “Properties of Helium,” tech. rep., Brookhaven National Lab, 1980.
- [208] C. H. Kim, J.-g. Kim, and S. V. Pamidi, “Cryogenic Thermal Studies on Cryocooler-Based Helium Circulation System for Gas Cooled Superconducting Power Devices,” in *International Cryocooler Conference*, pp. 504–513, 2014.

---

## Résumé en français



---

# Introduction

L'objectif de ce travail est d'arriver à une méthode de calcul des pertes AC pour des câbles supraconducteurs rapide et efficace. Deux architectures sont proposées avec l'utilisation soit de fils  $\text{MgB}_2$  soit de rubans REBCO. La plage de fonctionnement envisagée est située entre 1.5 kA et 120 kA.

Ce travail a été réalisé pour la société Nexans dans le cadre d'une thèse CIFRE. Le laboratoire d'accueil est le G2ELab qui est notamment spécialisé dans la modélisation numérique ainsi que dans le domaine des applications supraconductrices. Pour les plates-formes de tests, les laboratoires de l'Institut Néel et du LNCMI ont été utilisés.

Le chapitre I présente brièvement la supraconductivité ainsi que les mécanismes de pertes lorsque ceux ci sont soumis à des contenus transitoires. Les conducteurs étudiés et plusieurs projets de câble supraconducteurs sont présentés. Le chapitre se termine sur la modélisation numérique des pertes AC dans les supraconducteurs.

Dans le chapitre II, les pertes sur les conducteurs REBCO sont présentées. Ce type de conducteur est commercialisé sous forme de rubans ce qui est donc très intéressant pour des bobinages. Toutefois, pour améliorer encore la compacité des applications comme les câbles, il est intéressant d'étudier d'autres types de géométrie. Il est présenté dans ce chapitre les pertes AC dans le cas d'un fil cylindrique REBCO créé à partir de rubans industriels.

Le chapitre III se focalise sur la modélisation 3-D des supraconducteurs et notamment les fils  $\text{MgB}_2$ . Un modèle étalon utilisé pour un benchmark international a été présenté suivi de caractérisations de fils  $\text{MgB}_2$ . Ces mesures ont permis d'établir un modèle numérique de fil  $\text{MgB}_2$  réaliste.

Après le calcul des pertes AC sur des conducteurs élémentaires dans les deux précédents chapitre, le chapitre IV présente la méthode proposée pour calculer les pertes dans un câble supraconducteur. Cette partie vise aussi à valider un certain nombre d'hypothèses concernant le calcul des pertes AC pour un câble complet.

Enfin, le chapitre V présente un exemple d'application : le démonstrateur supraconduc-

teur du projet *BEST-PATH*. En utilisant les différents résultats des précédents chapitres, il est possible d'estimer avec précision les pertes dans le démonstrateur et aussi les pertes pour une utilisation à grande échelle. Pour finir, la protection du câble est étudiée avec la création d'un modèle magnéto-thermique du démonstrateur.

## Chapitre I

# Introduction à la supraconductivité et à la modélisation numérique

## I.1 La supraconductivité

### I.1.a Généralité

La supraconductivité se définit comme une propriété de la matière à présenter une résistivité non mesurable (inférieure à  $10^{-12} \Omega.m$ ) sous certaines conditions bien spécifiques. Cette propriété se retrouve dans un bon nombre de matériaux : des métaux, des céramiques. Cette propriété est observée sous une température critique  $T_c$  et a été découverte en 1911 par Heike Kamerlingh Onnes. À partir de 1962, différents supraconducteurs à base de Niobium ont été commercialisés. En 1980, la supraconductivité a été découverte dans des céramiques avec des températures critiques supérieures à 77 K (température de l'azote liquide), on parle de HTc. En plus d'une température critique, la supraconductivité est une propriété qui n'existe que sous un champ critique  $B_c$  et un courant critique  $I_c$ . On parle de domaine supraconducteur (J,B,T) pour définir le volume dans lequel l'état supraconducteur existe (cf Fig. I.1).

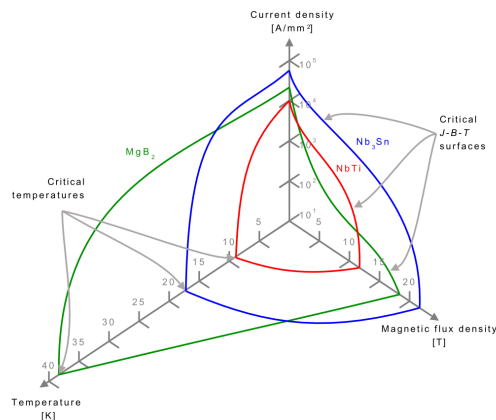


Fig. I.1 – Domaine supra pour différents supraconducteurs.

### I.1.b Représentation de la loi E-J des supraconducteurs

Lorsqu'un supraconducteur est dans son état supra (température et champ inférieurs aux valeurs critiques), il ne peut sortir de cet état que si le courant qui le traverse est supérieur au courant critique. Ce courant critique est généralement défini à un critère de tension mesuré sur le matériau. Si on mesure la tension en fonction du champ appliqué, on observe une tendance qui ressemble à la Fig. I.2. On observe sur cette figure trois

zones distinctes appelées états. L'état supraconducteur où la tension est quasi nulle. L'état normal où la résistivité est constante (matériaux non supra) et un état intermédiaire appelé état dissipatif.

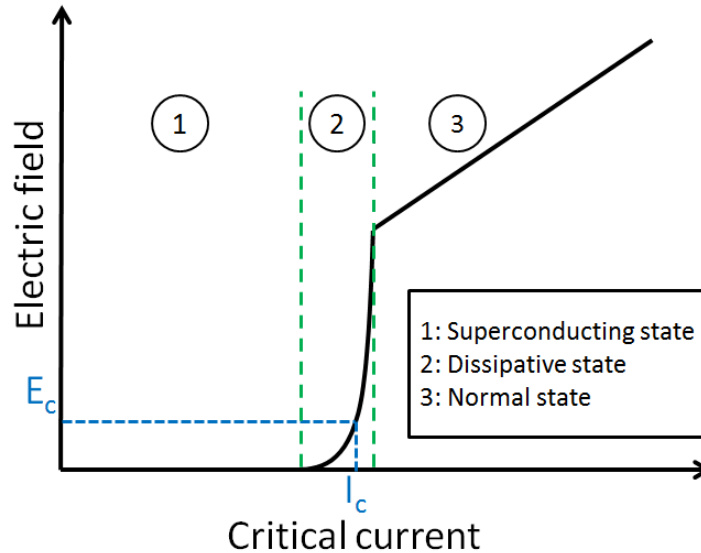


Fig. I.2 – État du supraconducteur (supra-dissipatif-normal) en fonction du courant de transport.

Comme nous le verrons plus loin, il est important d'être capable de modéliser avec précision le comportement E-J du supraconducteur car il impacte sur les calculs numériques. Plusieurs formes génériques visant à représenter cette courbe V-I ont été proposées : citons le modèle de Bean, la loi de puissance ou la loi de percolation.

### I.1.b-i Modèle de Bean

La modèle de l'état critique ou modèle de Bean a été proposé par Bean en 1964 comme une explication simple du comportement d'un supraconducteur lorsque celui-ci est soumis à un courant ou à un champ. Cette explication est macroscopique et propose de lier la densité de courant critique  $J_c$  présente dans le supraconducteur avec le champ électrique selon l'équation :

$$\forall |\vec{J}| < J_c, E = 0; \text{ for } |\vec{J}| \geq J_c, E \neq 0 \quad (\text{I.1})$$

Pour comprendre le comportement d'un supraconducteur lorsque celui-ci est soumis à un courant de transport ou un champ magnétique variable dans le temps, considérons un exemple simple à savoir un cylindre supra sous un champ magnétique extérieur représenté en Fig. I.3. Entre (I) et (II), le champ extérieur est progressivement augmenté jusqu'à la valeur de  $H_a$ , par conséquent, le supraconducteur écran le champ. Il est possible de voir avec l'équation (I.1) que seules trois densités de courant peuvent exister dans le supraconducteur  $\pm J_c$  ou 0. Le supraconducteur se remplit avec un courant qui circule dans le supraconducteur selon le plan de coup. À (II) si le courant reste constant, les densités de courant restent figées dans le supraconducteur. Lorsque le champ magnétique baisse de (II)

à (IV). Il se crée un courant circulant dans l'autre sens avec les mêmes densité de courants (valeurs quantifiées). On peut aussi définir dans cet exemple le champ de pénétration  $H_p$  tel que  $H_p = J_c a / 2$  avec  $a$  la demi-largeur du rectangle.

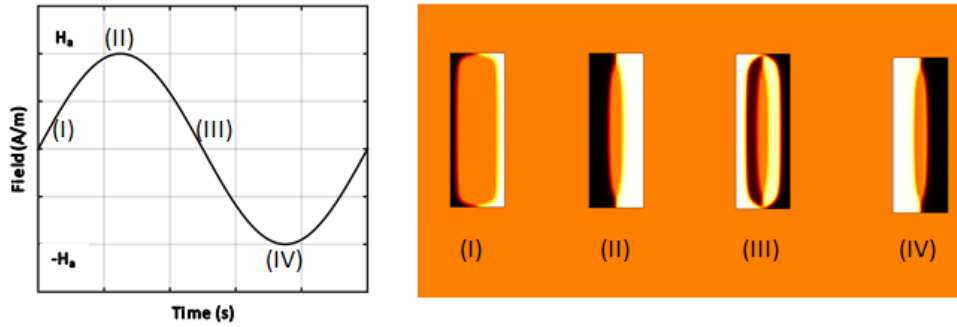


Fig. I.3 – Évolution de la densité de courant dans le supraconducteur lorsque celui-ci est soumis à un champ magnétique extérieur instationnaire.

Ce modèle a particulièrement été utilisé pour les premiers supraconducteurs ainsi que pour les calculs analytiques mais les supraconducteurs HTc ont généralement des transitions plus douces. Ce modèle n'est pas donc pas adapté et il a été proposé différentes lois tel que présentées ci-dessous.

### I.1.b-ii Loi en puissance de $n$

La forme des transitions dans les supraconducteurs HTc peut être approximée par un loi en puissance de  $n$ . La valeur de densité de courant critique  $J_c$  est ainsi définie à un critère de champ électrique  $E_c$ . Dans la pratique, on définit ce critère à  $E_c = 1 \mu\text{Vcm}^{-1}$ . On décrit la transition du supraconducteur par l'équation (I.2). Un exemple de caractérisation de courant critique est proposé pour un conducteur  $\text{MgB}_2$  à 20 K en Fig. I.4.

$$\text{Loi puissance : } \vec{E}(|\vec{J}|) = E_c \left( \frac{|\vec{J}|}{J_c(|\vec{B}|, T)} \right)^{n(|\vec{B}|, T)} \frac{\vec{J}}{|\vec{J}|} \quad (\text{I.2})$$

Cette loi en puissance est très utilisée dans la communauté car elle présente une bonne corrélation avec les mesures expérimentales. Toutefois, elle possède une résistivité non nulle pour toutes les valeurs de  $J$  ce qui est en contradiction avec l'état supraconducteurs. Cet erreur peut induire à des problèmes que nous verrons plus loin. Pour avoir un formule avec une résistivité nulle pour des valeurs de  $J \in \mathbb{R}^*$ , on peut proposer une autre loi appelée loi de percolation

### I.1.b-iii Loi de percolation

La théorie derrière la loi de percolation se base sur la physique statistique. La relation  $E$ - $J$  est défini selon l'équation (I.3) avec deux nouveaux paramètres :  $n_0$  et  $J_{c0}$ . Contrairement à la loi de puissance, la valeur de  $n_0$  est indépendante de la température et du champ. La

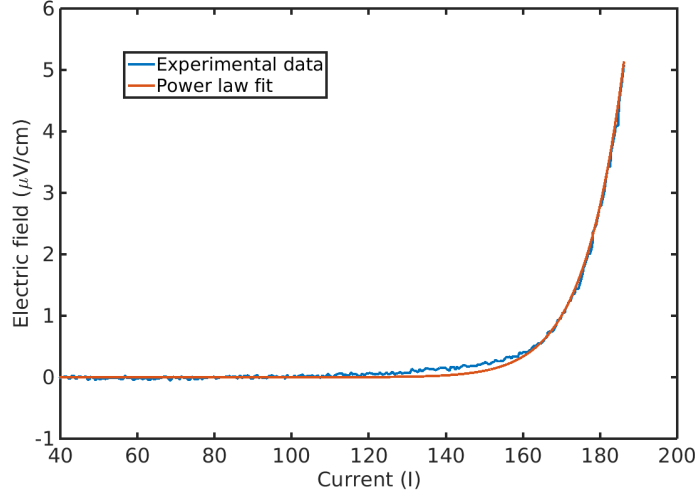


Fig. I.4 – Mesure V-I d'un supraconducteur MgB<sub>2</sub> at 20 K, 2.3 T, ainsi que la loi de puissance. Sur cet exemple, le courant critique et la valeur de n sont respectivement de 175 A et de 30.

valeur de  $J_{c0}$  qui est trouvée par fits récursifs correspond au seuil où l'absence de résistivité est observée.

$$\text{Loi percolation : } \vec{E}_{PM}(\vec{J}) = \begin{cases} 0, & \text{if } |\vec{J}| \leq J_{c0}, \\ E_c \left( \frac{|\vec{J}|}{J_{c0}} - 1 \right)^{n_0} \left( \frac{J_c}{J_{c0}} - 1 \right)^{-n_0} \frac{\vec{J}}{|\vec{J}|}, & \text{if } |\vec{J}| > J_{c0}, \end{cases} \quad (\text{I.3})$$

## I.2 Pertes AC

On parle de pertes AC, tout type de perte induite dans les matériaux conducteurs plongés dans un environnement (champ extérieur ou courant) variable dans le temps. La changement temporel de champ magnétique  $\vec{B}$  induit un champ électrique  $\vec{E}$  selon l'équation de Maxwell-Faraday :

$$\nabla \times \vec{E} = - \frac{\partial \vec{B}}{\partial t} \quad (\text{I.4})$$

Couplé à la présence de densité de courant, le champ électrique induit des pertes  $P_{AC}$  dans le volume  $V$ , qui pour un signal périodique de période  $f$  s'écrivent :

$$P_{AC} = f \int_{1/f} \iiint_V \vec{J} \vec{E} \, dV \, dt \quad (\text{en W}) \quad (\text{I.5})$$

Dans un supraconducteur les pertes AC existent sous différentes formes dues à la co-existence de matériaux supraconducteurs et de matrices métalliques. On retient deux catégories :

1. *Les pertes par hysteresis* qui ont lieu dans les matériaux supraconducteurs. Ces pertes sont créées par le changement local de polarité de la densité de courant (arrachage de vortex).
2. *Les pertes dans la matrice* qui sont principalement liées aux courants circulants dans la matrice.

### I.3 Matériaux supraconducteurs étudiés

Pour la création de dispositifs supraconducteurs de forte puissance, deux supraconducteurs sont aujourd'hui au coeur des développements, il s'agit des conducteurs REBCO et du  $MgB_2$ .

#### I.3.a Rubans REBCO et fils cylindriques

Les rubans REBCO sont des supraconducteurs à haute température critique (généralement  $T_c=92$  K) commercialisés sous forme de couche de quelque micromètre d'épaisseur sur une largeur comprise entre 4 mm et 12 mm. Ces matériaux sont particulièrement intéressants car ils sont capables de transporter de très forte densité de courant. Pour protéger cette couche supraconductrice, celle-ci est placée entre des couches métalliques (voir Fig. I.5), souvent du nickel, de l'argent ou du cuivre. Ces couches servent aussi à l'injection du courant.

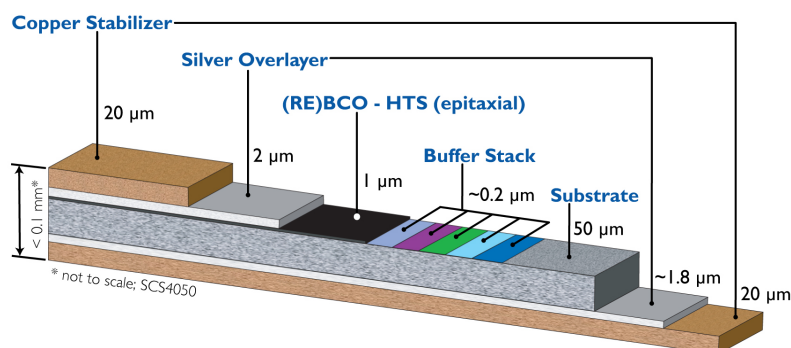


Fig. I.5 – Schéma générique d'un ruban Superpower.

A partir des rubans REBCO, Nexans a cherché à réaliser des fils cylindriques en adaptant la forme du conducteur. L'idée est dans un premier temps de déposer par électroérosion de sorte à placer la couche supraconductrice sur la fibre neutre du ruban. Ensuite le ruban est courbé par étape jusqu'à obtenir une forme cylindrique.

#### I.3.b Diborure de Magnésium $MgB_2$

Les propriétés supraconductrices du Diborure de Magnésium ont été découvertes en 2001 et le conducteur a été commercialisé à partir de 2002. La température critique du  $MgB_2$  est de 39 K pour un champ critique de 15 T. Compte tenu de la faible valeur de température critique il est possible d'utiliser de l'hélium liquide ou gazeux ou bien de

l'hydrogène liquide. Ce supraconducteur existe sous forme de poudre, il est donc possible de réaliser des structures multi-filamentaires. Ces conducteurs se présentent sous différentes tailles et formes (voir Fig. I.6). Aujourd'hui, la seule société qui commercialise le  $MgB_2$  est Colomus.

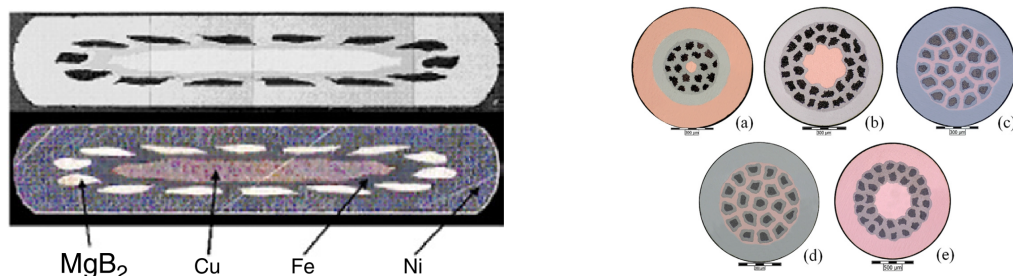


Fig. I.6 – Fils  $MgB_2$ .

Cette structure de fil est particulièrement intéressante pour la création de bobines supraconducteurs. Il est notamment envisagé pour la création de SMES ou pour des éoliennes.

## I.4 Câbles supraconducteurs

Les câbles supraconducteurs sont capables de transporter dix à vingt fois plus de courant que les câbles de cuivre sous la même tension. Ils permettent aussi la réduction de la taille des câbles. Nous présentons ici un exemple de câble déjà installé aux USA ainsi que les applications futures des câbles de puissance supra.

### I.4.a Le projet LIPA (2008)

Le câble LIPA (pour Long Island Power Authority) a été installé en 2008. Sa tension et son courant sont respectivement de 138 kV et de 2.4 kA. Le câble est de structure triphasée composé de rubans de BSSCO (autre supraconducteur HTc) de 600 m de long et refroidi à l'azote liquide à 73 K. Ce câble fournit de l'énergie à plus de 300 000 foyers autour de Long Island.

### I.4.b Les futures câbles supraconducteurs

Comparés à la précédente génération de câbles supraconducteurs réalisés avec des rubans HTc, la production de fils cylindriques permet de créer des câbles plus compacts. Il a aussi été montré qu'en utilisant ces fils, la densité de courant globale du câble est améliorée. Pour des câbles fort courant à partir de 10 kA, il est aussi possible d'utiliser le  $MgB_2$  à 20 K.



Fig. I.7 – Câble LIPA.

## I.5 Calculs des pertes par hystérésis dans les supraconducteurs

Le calcul des pertes par hystérésis est nécessaire pour dimensionner le système cryogénique. Il existe différentes méthodes pour les calculer : analytiquement ou numériquement. Les formules analytiques ont toutes comme hypothèse principale l'utilisation du modèle de Bean. De plus, les calculs ont été souvent réalisés sur des géométries simples. L'utilisation d'une méthode numérique permet d'avoir une plus grande flexibilité sur la loi E-J mais aussi sur les formes des conducteurs. Il est possible de prendre en compte des variations de performances (courant critique, valeurs de  $n$ ) en fonction de différents paramètres. Toutefois, ces calculs peuvent être longs lorsque le dispositif à simuler devient grand.

### I.5.a Modélisations Élément-finis

Concernant la modélisation numérique des supraconducteurs, nous avons utilisé la méthode des élément-finis car il s'agit de la technique de modélisation la plus répandue et la plus simple à mettre en place dans notre cas. En effet sous des logiciels commerciaux comme COMSOL ou FLUX il est possible de manière assez directe de résoudre des problèmes supraconducteurs. Plusieurs type de formulations existent pour résoudre ce problème : des formulations magnétiques ou électriques. Les formulations magnétiques calculent des variables d'état magnétique ( $H, J, B$ ) alors que des formulations électriques vont chercher à exprimer le champ électrique. Pour comprendre quel type de formulation est la plus adaptée à notre problème il est possible de représenter le résidu du problème. Compte tenu de la forme de la loi E-J du supraconducteur, le résidu aura une forme similaire en Fig. I.8.

D'après cette figure, il est clair qu'une formulation qui va exprimer le champ électrique en fonction de la densité de courant converge mieux qu'une formulation inverse, on sera donc plus tenté d'utiliser une formulation magnétique : une formulation en  $H$  ou  $T-\Phi$ .

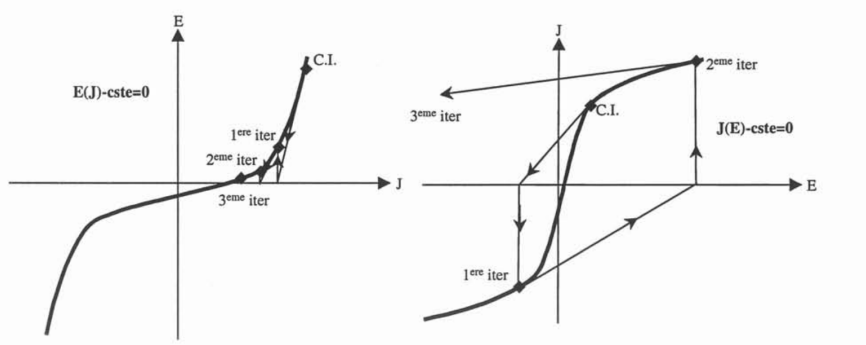


Fig. I.8 – Résidu du problème en considérant une formulation magnétique (à gauche) et électrique (à droite)

### I.5.a-i H-formulation

La formulation en H est celle qui a été le plus utilisée dans la communauté des modélisateurs supra car elle est facilement implémentable sous le logiciel COMSOL. Elle s'exprime sous la forme :

$$\nabla \times (\rho(|\vec{J}|) \nabla \times H) = -\mu \left( \frac{\partial \vec{H}}{\partial t} + \frac{\partial \vec{H}_0}{\partial t} \right) \quad (\text{I.6})$$

Le seul désavantage de cette formulation est que celle-ci ne conserve pas le courant dans le conducteur car une résistivité non infinie est définie dans l'air. Ceci peut induire des courants non physiques dans l'air. On privilégiera si possible des formulations plus difficiles à implementer comme la formulation T- $\Phi$  mais qui conserve fortement le courant.

### I.5.a-ii T- $\Phi$ formulation and associated formulations

La formulation T-  $\Phi$  a été développée initialement dans le logiciel FLUX. On définit le potentiel vecteur courant  $\vec{T}$ , un terme source  $\vec{T}_0$  et le potentiel scalaire magnétique  $\Phi$  dans l'air. Les équations à résoudre sont :

$$\begin{aligned} \nabla \times \rho \nabla \times \vec{T} + \frac{\partial}{\partial t} (\mu (\vec{T} - \nabla \Phi)) &= 0 \\ \nabla \cdot (\mu (\vec{T} - \nabla \Phi)) &= 0 \end{aligned} \quad (\text{I.7})$$

## I.6 Les difficultés liées la modélisation à grand échelle des supraconducteurs

Les modélisations numériques des applications supraconductrices ne sont pas évidente à réaliser et ceux pour un certain nombre de raisons :

1. D'abord les enroulements supraconducteurs sont constitués d'un grand nombre de rubans ou de fils. Modéliser chaque conducteur en détail peut rapidement être fastidieux et au delà de la capacité des ordinateurs. Pour pallier à ce problème, il est

possible d'utiliser des méthodes d'homogénéisation pour les rubans HTc mais aussi des formulations de type intégral qui permettent de diminuer le nombre de degrés de liberté du problème.

2. La non-linéarité inhérente de la loi E-J des supraconducteurs peut amener à des problèmes de convergence. Dans le cas de conducteurs multi-filamentaires, les matrices métalliques peuvent aussi être magnétiques et inclure une autre non-linéarité (perméabilité magnétique). Pour améliorer la convergence et accélérer la résolution du problème, on utilise généralement un algorithme de Newton-Raphson associé à des ajustements sur le coefficient de relaxation.



## Chapitre II

---

# Pertes AC dans les rubans supraconducteurs

Ce chapitre se focalise exclusivement sur le calcul des pertes AC dans les supraconducteurs HTc sous la forme de ruban ou de fils cylindriques. Compte tenu de la forme de ces conducteurs, seul une modélisation 2-D est possible ce qui simplifie en partie le problème. Dans un premier temps, le modèle est développé sur des rubans qui peuvent être mesurés expérimentalement. Ensuite, le modèle numérique est adapté aux fils cylindriques.

### II.1 Pertes AC dans les rubans supraconducteurs

Le ruban Superpower que nous avons modélisé est un ruban typique de YBCO de 4 mm de largeur analogue à celui présenté en Fig. I.5. Une couche d'argent de 2  $\mu\text{m}$  est placée au dessus de la couche supraconductrice. Le ruban a été caractérisé à 77 K à l'aide d'une mesure de courant critique avec  $E_c=1 \mu\text{V}\cdot\text{cm}^{-1}$ .

#### II.1.a Modélisation Éléments finis

La modélisation a été réalisée sous COMSOL avec un modèle 2-D et une formulation en H. Avec un modèle 2-D, le risque de courant non physique dans l'air est réduit car le courant est seulement défini selon une seule direction (perpendiculaire au plan). Il a été vérifié que les couches de substrats plus résistives que la couche de YBCO peuvent être négligées dans nos calculs. Le maillage a été réalisé avec l'aide de rectangles, particulièrement adaptés pour les calculs sur ce type de géométrie. Autour de la couche supra, on peut se permettre de mailler en triangle le domaine d'air délimité par des frontières sur lesquelles on applique des conditions de Dirichlet.

#### II.1.b Validation expérimentale

Nous avons comparé les résultats du modèle numérique et ceux obtenus par mesure expérimentale sur le ruban SuperPower. Les pertes AC ont été mesurées dans un bain d'azote liquide. La mesure a été réalisée électriquement. Les résultats sont présentés en Fig. II.1. On observe un excellent accord entre le modèle numérique et la manipulation expérimentale ce qui valide notre modèle.

### II.2 Pertes AC dans les fils cylindriques

Le modèle numérique a ensuite été adapté aux fils cylindriques. Toutefois, comme il n'a pas été possible de créer des fils cylindriques, seul des calculs numériques sont présentés. Le bon accord entre la manipulation expérimentale et les résultats numériques avec un ruban nous conforte concernant les calculs des pertes pour les fils.

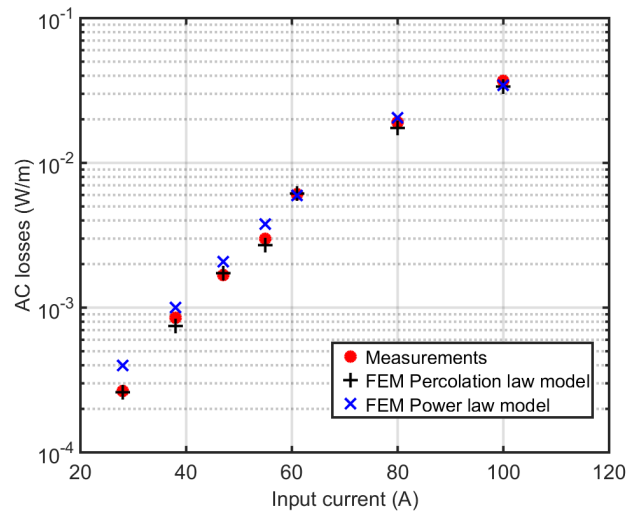


Fig. II.1 – Self field AC losses versus input current for the SuperPower tape.

### II.2.a Description du modèle

Le modèle a été adapté d'après les spécifications présentes dans le projet européen *EUROTAPES*. Le fil cylindrique possède un diamètre intérieur de 1.8 mm avec une couche supraconductrice de 2  $\mu\text{m}$  comme présenté en Fig. II.2.

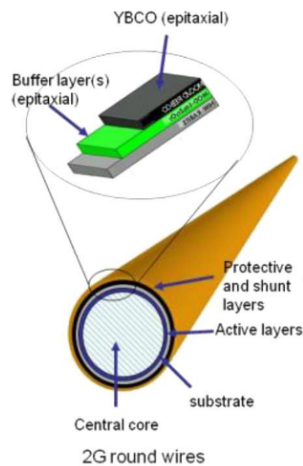


Fig. II.2 – Fil cylindrique du projet *EUROTAPES*.

Plusieurs calculs ont été réalisés d'abord pour trouver un maillage optimal qui permet de calculer les pertes AC de manière précise et rapide. Ensuite, les couches métalliques présentes autour de la couche ont été négligées après avoir vérifié que celles-ci n'influençaient pas sur le calcul des pertes AC.

### II.2.b Résultats pour le fil cylindrique

Tout d'abord les pertes AC créées par un courant de transport AC ont été calculées. En plus de ces pertes, les pertes pour un ruban sont présentées.

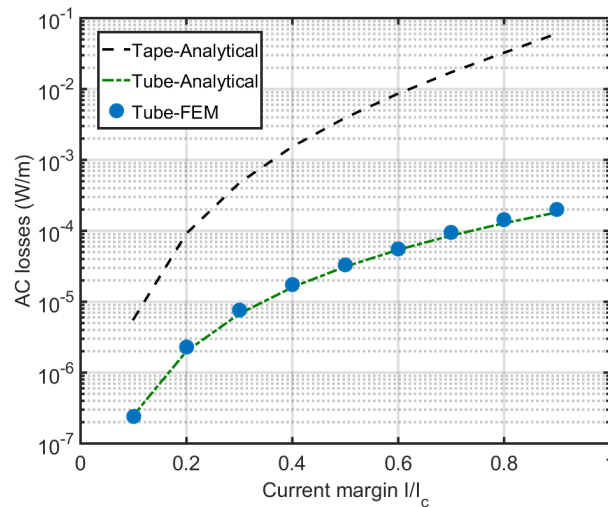


Fig. II.3 – Pertes AC en champ propre en fonction de la valeur max du courant AC pour un fil cylindrique et un ruban.

On observe un bon accord entre notre modèle numérique et les calculs analytiques ainsi qu’une baisse significative des pertes pour les fils comparés aux rubans. On peut ensuite réaliser une série de simulations en ajoutant un champ magnétique externe homogène et en phase avec le courant de transport. Ces simulations visent à recréer l’environnement d’un câble (présence d’autres conducteurs juxtaposés). Sur la Fig. II.4, on peut voir l’augmentation des pertes AC dues à la pénétration locale du courant dans le tube. A l’aide cet abaque il est possible maintenant de connaître l’ensemble des pertes pour tous les courants de transport et tous les champs ce qui n’est pas possible analytiquement.

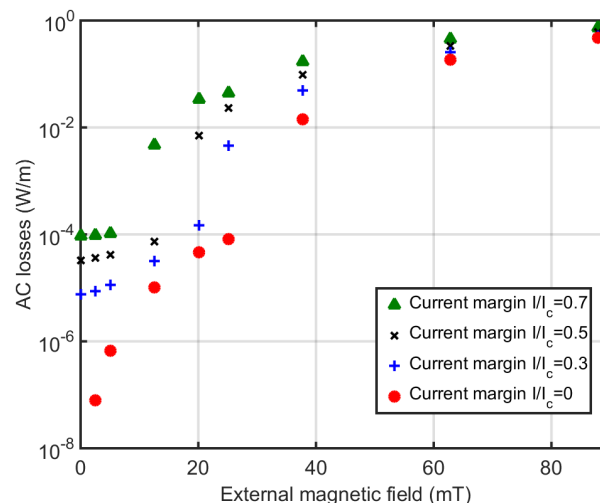


Fig. II.4 – Pertes AC créées par un courant de transport et une champ magnétique extérieur en phase.

Il est maintenant possible de réaliser des calculs rapides des pertes AC dans les câbles à base de fils cylindriques supraconducteurs. En effet en connaissant la valeur du champ

magnétique induite sur chaque fil ainsi que le courant de transport qui circule dans celui, on peut remonter à la valeur des pertes. Ces résultats ont été réalisés avec comme hypothèse une densité de courant constante, ce qui n'est pas le cas dans la réalité. Nous avons vérifié que une prise en compte de cette dépendance n'induit pas un grand écart dans les pertes AC calculées.

Nous terminons enfin avec des calculs rapides sur des câbles HTc fait de fils cylindriques. La conclusion globale est qu'il est nécessaire d'espacer de manière importante les fils cylindriques pour minimiser la valeur du champ magnétique externe induit sur chaque fil.

## II.3 Conclusion

Dans ce chapitre, il a été présenté un certain nombre de résultats sur les pertes AC dans les rubans supraconducteurs HTc et les fils cylindriques. Un modèle 2-D a été réalisé sous COMSOL et comparé à une mesure expérimentale. Les résultats ont permis de valider le modèle numérique. La géométrie a ensuite été adaptée pour la réalisation de calcul des pertes AC sur des fils ronds. Après avoir validé chaque hypothèse que nous avons faite pour la réalisation du modèle, les pertes AC avec un courant de transport et un champ magnétique extérieur ont été calculées. On déduit de ces calculs l'ensemble des pertes pour tous les courants et tous les champs externes ce qui peut permettre de calculer des calculs rapides sur des câbles compacts.

## Chapitre III

# Modélisation 3-D multi-filamentaires

Pour pouvoir modéliser correctement les pertes dans des supraconducteurs constitués de filaments torsadés, il est nécessaire de réaliser un modèle 3-D. Ceci est expliqué car, en présence d'un champ magnétique transverse, des courants dans la matrice vont circuler. Ce type de géométrie a été étudié analytiquement et expérimentalement mais peu de travaux numériques ont été réalisés. Ceci s'explique car les modèles numériques nécessitent rapidement d'importantes ressources matérielles.

Contrairement au chapitre précédent, où il a été possible de valider notre modèle numérique par des expériences, ici les modèles numériques ne sont pas toujours réels (modèles simplifiés). Il est donc intéressant de valider les résultats des pertes en comparant les résultats de différents logiciels. Une fois cette étape de validation effectuée, un modèle numérique complet du conducteur a été réalisé et simulé.

### III.1 Modèle étalon d'une géométrie trois filaments - Comparaison multi-logiciels

La géométrie étalon est composée de trois filaments torsadés dans une matrice cylindrique. Pour garder le modèle le plus simple possible, un pas complet de torsade a été fait. La géométrie est présentée en Fig. III.1.

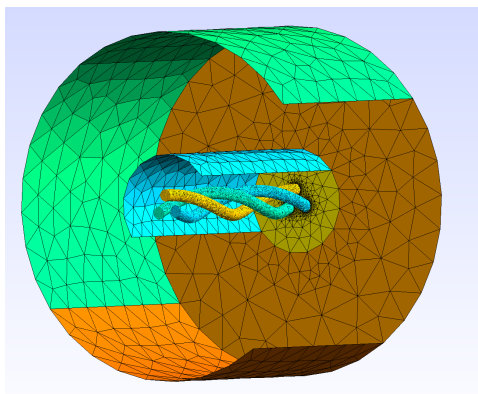


Fig. III.1 – Géométrie et maillage du modèle étalon.

Pour assurer une bonne visibilité sur nos résultats, deux coopérations internationales ont été réalisées. En plus d'utiliser COMSOL et FLUX, deux logiciels éléments-finis maison développés par l'École polytechnique de Montréal (Daryl-Maxwell) et l'Université de Tampere (LoSt) ont donné des résultats.

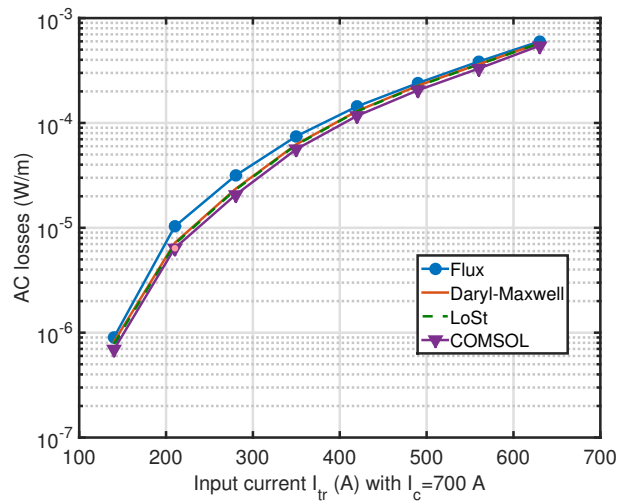


Fig. III.2 – Pertes AC en fonction de l'amplitude du courant de transport ( $I_c=700$  A) sans champ extérieur.

On observe un bon accord entre les logiciels ce qui nous a conforté dans le fait que les quantités calculées n'étaient pas fausses. De ces simulations, il a été possible de voir que des logiciels comme COMSOL ou FLUX ne sont pas adaptés pour ces simulations (simulations longues, difficultés d'ajouter un champ magnétique extérieur transverse, problèmes de convergence,...). Nos simulations ont ensuite été faites sous Daryl-Maxwell et COMSOL.

Après avoir ajouté un champ magnétique extérieur, il est possible de complexifier le modèle en ajoutant des propriétés à la matrice cylindrique (matrice résistive, magnétique, etc..). On peut par exemple voir le phénomène de couplage et de découplage des filaments supraconducteurs en faisant varier la fréquence du champ externe comme cela est montré en Fig. III.3.

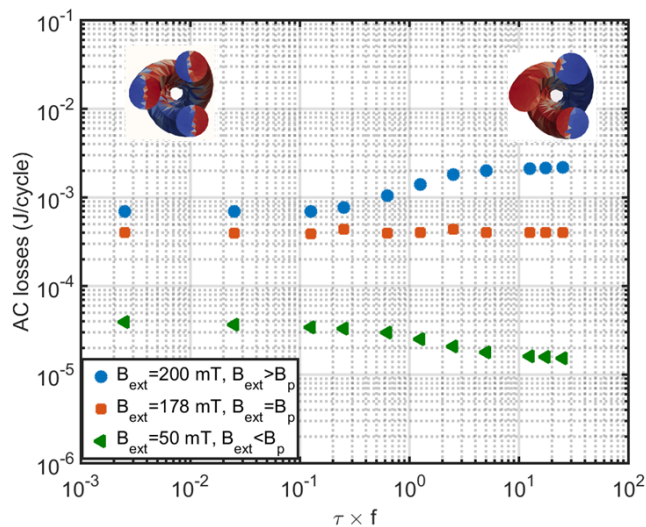


Fig. III.3 – Évolution des pertes en fonction de la fréquence du champ externe. On observe le phénomène de couplage et de découplage des filaments supra.

Plusieurs types de simulations ont été faites sur ces géométries, notamment en étudiant les propriétés de convergence de ce modèle en fonction des différentes lois de comportement E-J. Toutes ces simulations nous ont donné une certaine assurance sur la validité des résultats numériques. L'étape suivante a donc été de réaliser un modèle réaliste de conducteur  $\text{MgB}_2$ .

## III.2 Modélisations numériques d'un conducteur $\text{MgB}_2$

### III.2.a Caractérisation

Le conducteur  $\text{MgB}_2$  étudié est un conducteur multi-filamentaire composé de 36 filaments supraconducteurs dans une matrice de nickel pur. Les filaments sont répartis sur trois couches concentriques comprenant respectivement 6-12-18 filaments. La présence de nickel permet une bonne diffusivité thermique pour le refroidissement et sert de shunt dans le cas où le conducteur vient à transiter (états dissipatif ou normal). Une couche externe de monel est ajoutée pour des raisons mécaniques. Une image réalisée au Microscope Électronique à Balayage (MEB) est présentée en Fig. III.4.

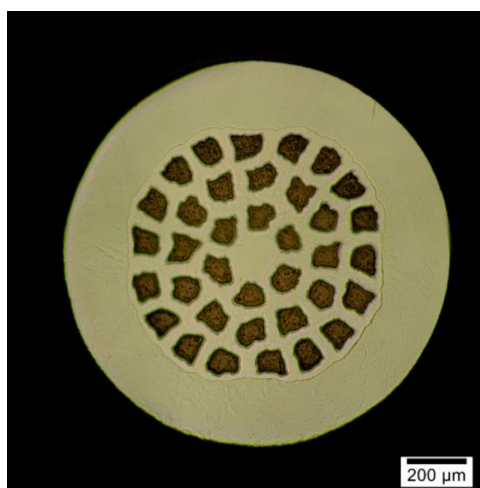


Fig. III.4 – Coupe du conducteur modélisé.

Pour pouvoir implémenter l'évolution du courant critique, une mesure expérimentale de courant critique sur un fil a été réalisée au LNCMI de Grenoble. La mesure a été faite sur un échantillon  $\text{MgB}_2$  de 1.13 mm de diamètre. Étant donné que l'augmentation du diamètre du fil s'accompagne d'une augmentation de  $\text{MgB}_2$  dans le fil, il est possible de considérer que l'augmentation des performances est linéaire avec le rayon du fil. Une régulation de température a permis de caractériser le conducteur entre 4.2 K et 20 K. Puisque les filaments supraconducteurs sont dans une matrice métallique, des longueurs de transfert importantes sont à prendre en compte. Elles permettent de faire passer l'intégralité du courant dans le supraconducteur. Le rayon de courbure du fil  $\text{MgB}_2$  est de l'ordre de 250 mm ce qui exclu la création de bobines compactes, il est donc nécessaire de mesurer les performances du fil sur un échantillon droit sur une canne de mesure pouvant accueillir ce type de long échantillon (environ 200 mm). Des radiateurs situés proches de l'échantillon permettent de vaporiser l'hélium liquide et ainsi de réaliser des mesures sous température

variable. La source de courant utilisée est une source 3 kA-5 V. L'évolution des courants critiques  $I_c$  en fonction de l'induction magnétique extérieure sous différentes températures est rapportée en Fig. III.5.

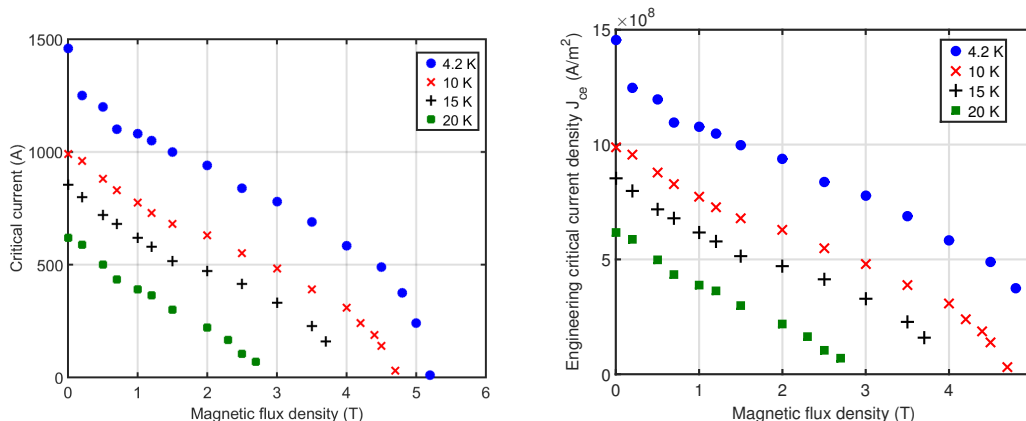


Fig. III.5 – Courant critique et densité de courant critique en fonction de la température et du champ pour un conducteur de 1.13 mm de diamètre ( $E_c=1 \mu V/cm$ ).

Une fois les performances d'un conducteur  $MgB_2$  étudiées, la résistivité et la perméabilité magnétique d'échantillons de nickel et de monel ont été étudiées. Les échantillons ont été préparés avec les mêmes traitements thermiques et mécaniques que le fil industriel. Les mesures ont été faites aux températures de fonctionnement du fil (4.2 K-25 K).

### III.2.b Calculs numériques du conducteur $MgB_2$

Concernant la géométrie et le maillage associé, ceux-ci ont été réalisés par une extrusion hélicoïdale d'une représentation de la face normale, dont les dimensions ont été déduites de Fig.III.4. Le maillage généré, composé de prismes, a ensuite été découpé en tétraèdres. Cette technique permet un maillage relativement fin dans les conducteurs supraconducteurs, là où se développent majoritairement les densités de courant. Sur cette géométrie, le nombre d'éléments du maillage est égal à 659 250 et le nombre de degrés de liberté est égal à 770 725. Le maillage est représenté en Fig. III.6. Nous avons utilisé le fait que la face du conducteur possède une symétrie de rotation de  $60^\circ$  pour pouvoir réduire le modèle selon l'axe du pas de torsade (seulement un sixième est nécessaire si on utilise des conditions de périodicité).

Un courant alternatif de 550 A a été injecté à l'intérieur du modèle auquel on a ajouté un champ magnétique extérieur transverse en phase (50 Hz). Les pertes AC calculées à l'aide du modèle sont présentées en Fig. III.7. Sur la figure, les pertes réduites sont tracées en fonction de la valeur de l'induction magnétique extérieure. Compte tenu que la résistivité des matériaux métalliques et de leurs perméabilités magnétiques qui varient peu avec la température entre 4,2 K et 30 K. Il est possible juste en utilisant le courant critique à la bonne température (à 0 T) d'estimer les pertes pour le dispositif complet à partir des pertes normalisées à 4,2 K  $(Q/\mu_0 I_c(0 T))^2$ . Les valeurs analytiques sont aussi tracées à titre de comparaison. Sur la figure, le *modèle complet* prend en compte toutes les dépendances (courant en fonction de B et  $\mu_R$ ) et le *modèle réduit* ne prend pas en compte

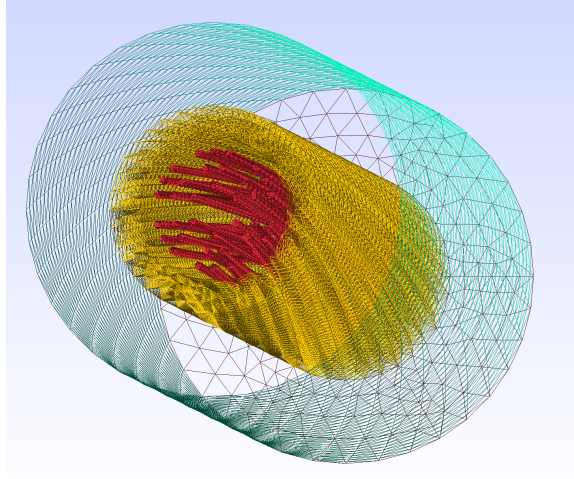


Fig. III.6 – Maillage du MgB<sub>2</sub>.

les perméabilités magnétiques des matériaux. Ceci a été fait pour observer l'influence des perméabilités magnétiques sur les pertes calculées.

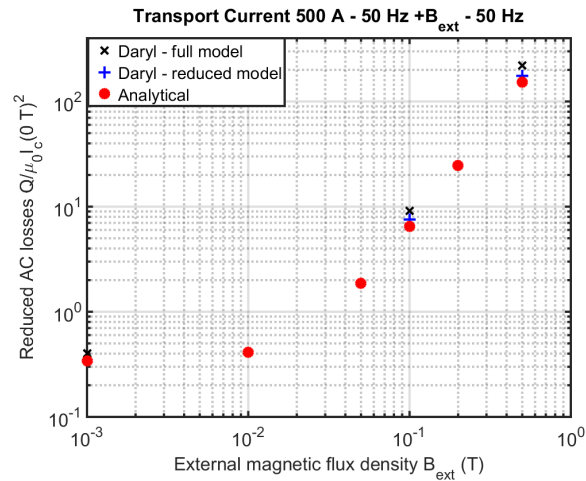


Fig. III.7 – Pertes AC réduites pour un courant de 550 A et une induction magnétique extérieure transverse.

Les 2 régimes à savoir le régime où les filaments supraconducteurs sont partiellement pénétrés et le régime où ils sont complètement pénétrés sont bien visibles avec deux pentes distinctes en fonction du champ magnétique. On observe de très fortes valeurs pour les pertes analytiques et calculées ce qui interdit l'utilisation de conducteur pour un usage pur AC. Ceci est lié aux pertes par couplage qui sont générées par la circulation de courant à l'intérieur de la matrice. La formule analytique de ces pertes est donnée par l'équation :

$$P = \frac{AB_{ext}^2}{2\mu_0} \left( \frac{\tau}{1-N} \right) \frac{\omega^2}{1+\omega^2\tau} \quad (\text{III.1})$$

Avec  $\tau = (1-N) \frac{\mu_0}{\rho_t} \left( \frac{l_p}{2\pi} \right)^2$ . Dans cette formule, N représente le coefficient de dé-

magnétisation, calculé analytiquement à 0.6,  $\rho_t$  la résistivité transverse de la matrice de nickel ( $\rho_t=4,5 \text{ n}\Omega.\text{m}$ ) et  $A$  la surface du conducteur. Le pas de torsade des filaments  $l_p$  est de 120 mm. Le champ magnétique extérieur de valeur pic  $B_{ext}$  et de pulsation  $\omega=2\pi f$  ( $f=50 \text{ Hz}$ ).

Dans le conducteur  $\text{MgB}_2$ , le pas de transposition est important ce qui augmente les pertes par couplage. Dans notre modèle numérique,  $\rho_t$  a été approximé comme la résistivité mesurée de l'échantillon de nickel ce qui n'est pas vrai car la composition de la couche de diffusion n'est pas connue. De cette figure, il est possible de voir qu'en prenant en compte l'ensemble des dépendances, on observe une différence de l'ordre de 30 % entre le *modèle complet* et l'analytique et autour de 10 % pour le *modèle réduit* et l'analytique. Entre le calcul analytique et le *modèle réduit* ceci est expliqué par la prise en compte du courant critique en fonction de l'induction magnétique et des courants dans le monel. Pour la différence entre l'analytique et le *modèle complet*, la prise en compte des perméabilités magnétiques concentre les lignes de champ sur les filaments ce qui augmente les pertes.

En conclusion, il est possible de voir que les pertes AC sont trop grandes pour une application industrielle en AC. Ceci vient notamment de l'architecture du fil  $\text{MgB}_2$  avec un pas de transposition important et une matrice à forte conductivité. L'ajout de barrières autour des filaments de  $\text{MgB}_2$  pourraient permettre une baisse substantielle des pertes.

### III.3 Conclusion

Dans ce chapitre, la modélisation 3-D de conducteurs supraconducteur a été étudiée. En partant d'un exemple simple, comprenant trois filaments, plusieurs simulations ont été réalisées en étudiant, les pertes sous courant de transport et champ magnétique extérieur. Les paramètres physique de la matrice ont été modifiés pour pouvoir estimer notre capacité à résoudre des problèmes complexes impliquant plusieurs centaines de milliers de degrés de liberté. Ces simulations ont fait l'objet d'une comparaison entre différents logiciels notamment à travers deux coopérations internationales.

Ensuite, le conducteur principalement utilisé par Nexans dans ces futures applications supraconductrices a été modélisé. La première étape a été de caractériser le fil ce qui a permis de déduire les quantités physiques tel que les performance du fil, la résistivité des constituants etc. Ensuite un modèle numérique conséquent à été développé et simulé.

## Chapitre IV

# Calcul des pertes pour un câble supraconducteur

Dans les deux précédents chapitres, des résultats sur les conducteurs REBCO et  $\text{MgB}_2$  ont été présentés. Compte tenu du temps de calcul, notamment sur les géométries 3-D (fil  $\text{MgB}_2$ ), il n'est pas possible de modéliser un câble complet en détail. Pour pouvoir estimer avec précision les pertes d'un câble complet, une méthode basée sur un principe multi-échelle a été développée. Les câbles envisagés pour installation sont pour des utilisations en courant continu. Ainsi, les contenus harmoniques vont induire des pertes AC dans le câble et il est nécessaire de savoir les calculer avec précision. Plusieurs développements concernant des modélisations de signaux transitoires superposés à des contenus continus sont aussi présentés.

### IV.1 Méthode multi-échelle pour le calcul des pertes AC dans un câble supraconducteur

Cette méthode se divise en deux parties, le calcul statique de la distribution de champ magnétique du câble suivi du calcul, conducteur par conducteur, des pertes en fonction du champ externe et du courant de transport. La méthode de calcul est très rapide et permet de possibilité d'optimisation du câble. Le code a été développé sous MATLAB. L'approche peut être synthétisée en Fig. IV.1.

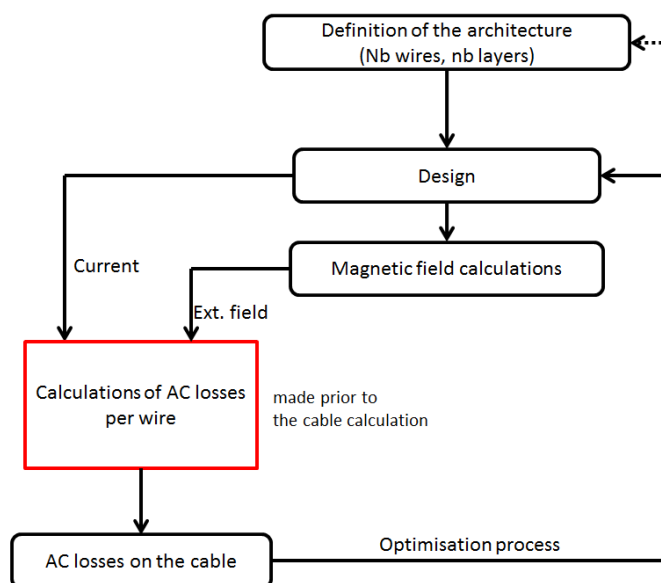


Fig. IV.1 – Principe du calcul des pertes pour un câble complet.

### IV.1.a Exemple

Un exemple de câble avec des fils cylindriques est donné ci dessous. Le câble est constitué de 18 fils cylindriques pour un total de 1.6 kA (chaque fil transporte 91 A). La distribution de champ magnétique du câble est donnée en Fig. IV.2.

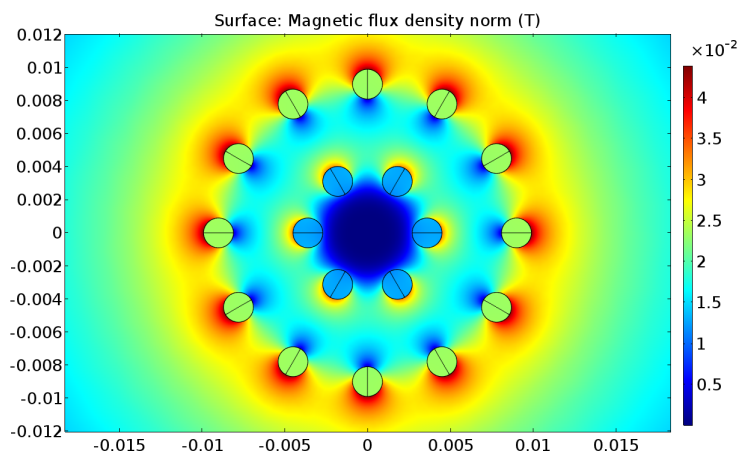


Fig. IV.2 – Distribution de champ magnétique pour un câble de 1.6 kA fait de fils cylindriques.

À partir du calcul magnéto-statique et de la connaissance des pertes en fonction du courant de transport et du champ, il est possible de calculer les pertes AC pour cette géométrie pour un fonctionnement pur AC. Les résultats sont donnés ci dessous :

Couche	Courant	Champ externe	Pertes AC par fil
Extérieur	91 A	24 mT	0.8 W/m
Intérieur	91 A	15 mT	5 mW/m
		Total	$\approx 10$ W/m

TABLE IV.1 – Pertes AC pour l'exemple pour une application pur AC.

Cette méthode a été validée à l'aide d'un modèle élément-finis. Les résultats sont cohérents avec une différence entre les deux méthodes constatée inférieure à 8 %.

## IV.2 Modélisations de signaux transitoires associés à un contenu continu

Expérimentalement, tant que le courant de transport est inférieur au courant critique, aucune différence sur les pertes AC n'est noté avec l'ajout d'un contenu continu superposé à un signal AC. Numériquement, les lois utilisées pour représenter le supraconducteur ne sont pas en accord avec cette constatation. Ceci est lié au fait qu'avec une loi en puissance (ou une loi de percolation), on induit un phénomène de pénétration lié une inhomogénéité de résistivité dans le conducteur. Ce phénomène est particulièrement visible pour une loi de puissance où le conducteur est toujours dissipatif.

## IV.2.a Limite du modèle en loi de puissance

Une simulation sur un supraconducteur avec une loi de puissance et un  $n$  de 30 est réalisée. On impose un courant constant dans le conducteur et on observe la distribution de densité dans le conducteur au cours du temps en Fig. IV.3.

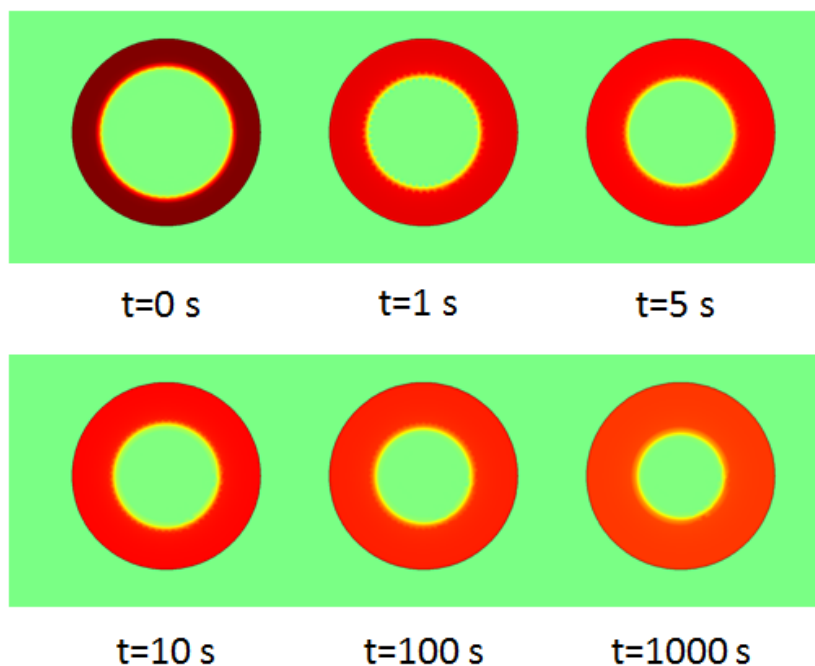


Fig. IV.3 – Distribution de densité de courant dans un supraconducteur au cours du temps avec une loi E-J en puissance.

Il est possible de voir que le conducteur se remplit complètement au cours du temps ce qui est en contradiction avec le modèle de Bean et l'état supraconducteur. En effet, lorsque le conducteur est complètement rempli, celui-ci devient dissipatif. Ce phénomène de pénétration est lié à la différence spatiale de résistivité dans le conducteur comme il est possible de le voir avec l'équation E-J :

$$\rho(J) = \frac{E_c}{J_c} \left(\frac{J}{J_c}\right)^{n-1} = \rho_0 \left(\frac{J}{J_c}\right)^{n-1} \quad (\text{IV.1})$$

Dans cette équation,  $\rho$  est égale à zéro seulement pour  $J=0$ . Lorsque le courant est maintenu constant à  $t=0$  s, la résistivité du conducteur est non uniforme. La zone qui transporte l'essentiel du courant à la valeur  $J=J_c$  possède une résistivité de  $\rho_0$  tandis que la zone centrale a une résistivité de 0. Pour uniformiser la résistivité du conducteur, le courant pénètre à l'intérieur de celui-ci. Cette constatation est en contradiction avec les mesures expérimentales et pose un problème plus fondamental à savoir que le conducteur est dissipatif. La vitesse du phénomène est fortement liée à la valeur de  $n$ .

Une alternative à cette loi de puissance est la loi de percolation (IV.2) car elle possède une résistivité nulle pour  $J \in [0, J_{c0}]$ .

$$\rho(|J|) = \frac{E_0}{|J|} \left( \frac{|J|}{J_{c0}} - 1 \right)^{n_0} \text{ if } |J| > J_{c0}, 0 \text{ else} \quad (\text{IV.2})$$

Avec deux paramètres déduits de fits expérimentaux :  $J_{c0}$  et  $n_0$ . On introduit  $E_0 = E_c(J_c/J_{c0} - 1)^{-n_0}$  comme champ critique réduit. Cette loi E-J a été utilisée dans ce manuscrit de thèse et il a été montré un très bon accord avec les mesures expérimentales. Le fait aussi que cette loi ne présente pas d'état dissipatif est plus proche de la réalité.

#### IV.2.b Pertes AC en présence d'un signal continu

La pénétration du courant induite par le contenu continu avec la loi de puissance va induire des pertes en plus des pertes AC liées aux contenus transitoires. Le phénomène de pénétration du courant est un phénomène qui tend à s'atténuer au cours du temps. L'erreur entre le modèle numérique et les résultats attendus diminue au cours du temps. Toutefois un modèle numérique, à traiter sur un temps long peut être rapidement chronophage et peu efficace. Pour comparer l'erreur faite avec ces deux lois, une simulation a été réalisée avec les deux lois de puissance. Un courant AC de 5 A (50 Hz) a été superposé à un courant  $I_{DC}$ . Les pertes sont calculées sur la première période du signal AC (après l'établissement du contenu DC) et à la 50ème période. Différents travaux ont montré que à partir de cette période, l'erreur est acceptable. Les résultats sont présentés en Fig. IV.4.

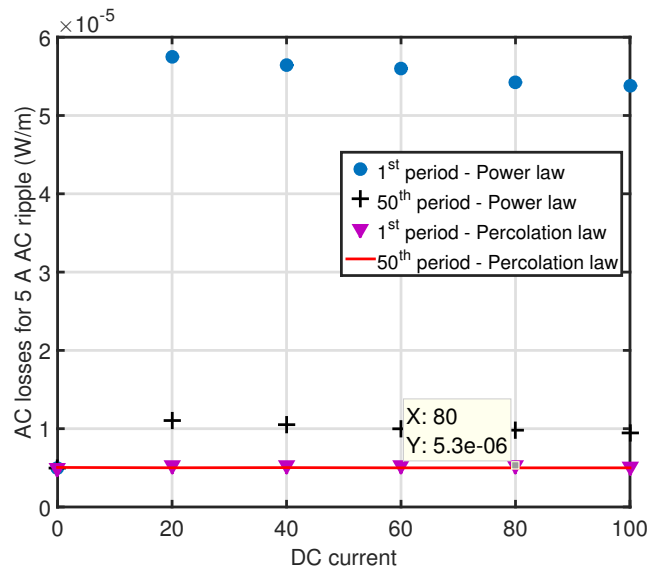


Fig. IV.4 – Pertes AC en présence d'un contenu continu avec les deux lois E-J.

On observe que les résultats avec la loi de puissance sont très largement supérieurs à ceux attendus. Ceci est lié à la pénétration du courant dans le conducteur. La loi de percolation elle donne des résultats cohérents avec ce qui est attendu (la valeur attendue est celle à  $I_{DC}=0$ ) très rapidement car même à la première période la différence est très faible. Il est donc fortement recommandé d'utiliser cette loi lorsque les simulations traitent de problèmes AC+DC.

## IV.3 Pertes AC créées par des harmoniques

Dans la section précédente, les calculs ont été réalisés sur des signaux AC+DC. Pour simplifier seulement un signal AC à 50 Hz a été considéré. Dans la réalité, des harmoniques liées aux convertisseurs de puissances vont être de différentes fréquences (de 50 Hz à 2 kHz) et de différentes amplitudes. Compte tenu du fait que la loi E-J est non linéaire, il n'est pas possible d'additionner les pertes fréquence par fréquence..

Les harmoniques sont fortement dépendantes du réseau et des convertisseurs, il est donc très difficile de calculer les pertes génériques. De plus si le spectre possède de nombreux harmoniques hautes fréquences, le calcul peut rapidement être très long (théorème de Shannon à respecter).

Dans cette partie, nous allons étudier les pertes AC en fonction de signaux multi-fréquence en le comparant à un signal témoin. Le signal témoin est défini comme une sinusoïde de fréquence égale au fondamental des harmoniques et d'amplitude égale à la somme des amplitudes des harmoniques. Ce signal témoin est généralement à 50 Hz ce qui va permettre de réduire le temps de calcul comparé aux signaux réels (plusieurs harmoniques). Toutefois les deux signaux sont différents, pour que ce signal témoin soit valable, il a été établi qu'il fallait respecter une différence inférieure à 10 % avec le signal réel.

### IV.3.a Principe de calcul. Simulations et résultats expérimentaux

Dans un premier temps, plusieurs signaux constitués de deux sinus ont été simulés mais aussi testés expérimentalement. Les signaux sont de la forme :

$$I(t, m, k, \alpha) = I_{ac}(\sin(2\pi \cdot 50 \cdot t) + m \sin(2\pi k \cdot t + \alpha)) \quad (IV.3)$$

Le courant est une addition de signaux sinusoïdaux avec un fondamental à 50 Hz d'amplitude  $I_{ac}$  et un second sinus d'amplitude  $m \cdot I_{ac}$  avec une fréquence  $k$  et un déphasage  $\alpha$ . Le signal témoin est donc défini comme un sinus à 50 Hz d'amplitude  $I_{peak} = (1+m) \cdot I_{ac}$ . Les pertes AC pour  $m=0.1$  et  $\alpha=0$  sont présentées en Fig. IV.5. Les points expérimentaux et les résultats numériques sont notés 'E' et 'C'. Il est à noter que le signal témoin est donné pour  $k=50$  Hz.

On observe dans ces cas de figure, que le critère de 10 % est bien valide.

### IV.3.b Exemple d'application

A l'aide du logiciel PSCAD®<sup>®</sup>, nous avons simulé une ferme de panneaux solaires en vue de calculer les harmoniques AC. Un filtre (passe bas avec fréquence de coupure de 1800 Hz) pour réduire ces harmoniques a aussi été ajouté. On note *OutInv* le signal en sorti de la ferme solaire et *InpTrans* le signal en entrée du transformateur (après le filtre) dont les contenus spectraux sont en Fig. IV.6.

Les amplitudes des signaux sont respectivement de 60 A et 82 A. Les pertes AC sont présentées en Table. IV.2.

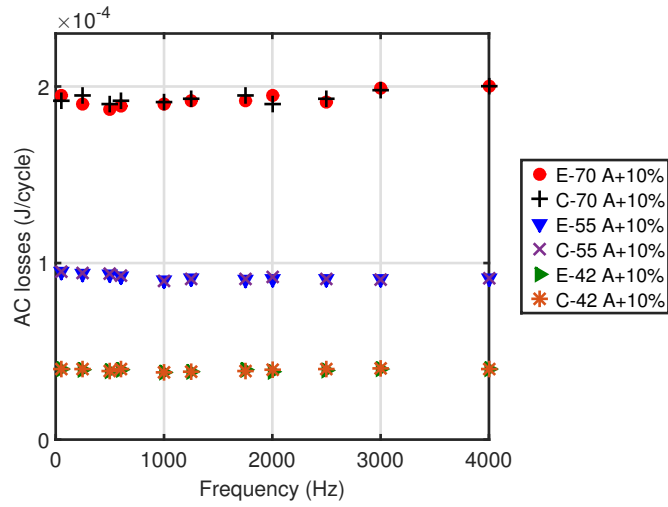


Fig. IV.5 – Pertes AC en fonction de  $k$  pour différents  $I_{ac}$  avec  $m=0.1$  et  $\alpha=0$ . 'E' sont les points expérimentaux et 'C' les valeurs numériques.

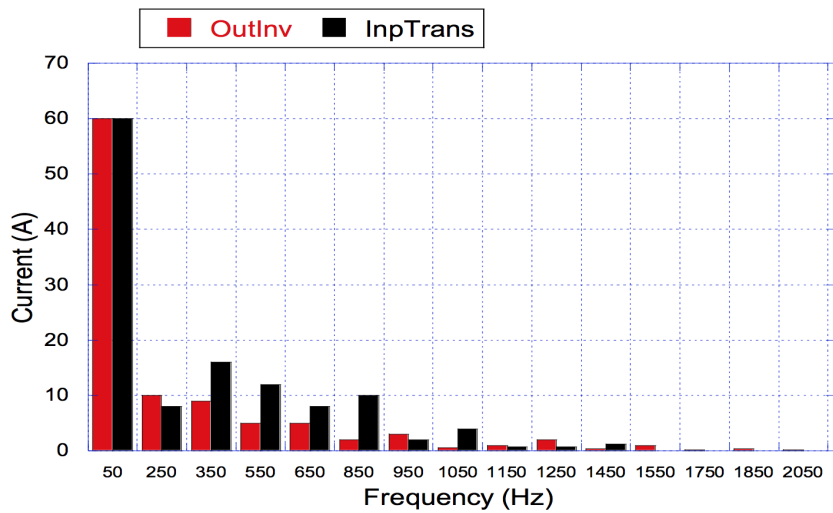


Fig. IV.6 – FFT des convertisseurs.

Forme du courant	Pertes AC (mJ/cycle)	Difference avec le signal témoin
60 A-50 Hz	0.106	
<i>OutInv</i> (COMSOL)	0.113	6.61 %
<i>OutInv</i> (Manip)	0.118	10.37 %
82 A-50 Hz	0.284	
<i>InpTrans</i> current (COMSOL)	0.306	7.74 %
<i>InpTrans</i> current (Manip)	0.314	10.5 %

TABLE IV.2 – Comparaison des pertes AC simulées avec le signal témoin et le courant réel (expérimentales et simulations numériques).

On peut conclure de ces résultats que le critère est validé même pour un signal composé de nombreux d'harmoniques. On considérera donc pour la suite un signal témoin comme celui présenté pour le calcul des pertes AC induites par des contenus harmoniques.

## **IV.4 Conclusion**

Dans cette section, il a été présenté une méthode de calcul des pertes AC pour un câble. En plus de définir une méthode rapide et permettant des optimisations, nous nous sommes intéressés aux différentes lois E-J dans le cas de calcul AC+DC et avec des harmoniques. Il en sort que la loi de percolation est mieux adaptée pour les calculs AC+DC et que le signal témoin est valide même pour des signaux avec beaucoup d'harmoniques.



## Chapitre V

---

# Exemple d'application. Le projet européen *BEST-PATH*

Ce dernier chapitre est légèrement différent des précédents. Il propose de synthétiser autour d'un exemple concret les méthodes, modèles et résultats obtenus dans les chapitre III et IV. Un démonstrateur HVDC de 10 kA est en cours de réalisation dans le projet européen *BEST-PATHS* et nos développements nous permettent de calculer les pertes AC du câble complet. Ajouté à cela, un modèle thermique a été développé pour étudier la protection du câble lors d'un court circuit sur le réseau.

### V.1 Le démonstrateur du projet *BEST-PATHS*

Le projet européen *BEST-PATHS* a pour objectif d'étudier de nouvelles architectures HVDC pour le réseau électrique de demain. Dans ce projet, un démonstrateur supraconducteur doit être réalisé. Les spécifications techniques sont listées en Table. V.1.

Caractéristiques	Détails
Structure	Monopole
Puissance	3.2 GW
Tension	320 kV
Courant	10 kA
Longueur	$\approx$ 20-30 m
Température de fonctionnement	20 K
Refroidissement	gas hélium pour les fils MgB <sub>2</sub>
Courant de court-circuit	35 kA en 100 ms
Changement de polarité	10 000 MW/s

TABLE V.1 – Spécification du démonstrateur.

La réalisation technique de ce démonstrateur est un défi car il convient d'allier la cryogénie à 20 K avec la haute tension à 320 kV. Pour ce faire un design unique a été proposé où l'hélium gazeux circule dans une boucle fermée. La boucle de retour sera connectée à la terre tandis que le démonstrateur situé plusieurs mètres au dessus du sol sera sous tension de fonctionnement. La Fig. V.1 présente un schéma du montage.

Une des architectures proposée pour le démonstrateur consiste à utiliser 18 fils MgB<sub>2</sub> de 1.33 mm de diamètre sur une seule couche. Le coeur du câble est rempli de cuivre. Chaque fil va porter un courant de 555 A pour un total de 10 kA. Dans un premier temps, il faut calculer le champ magnétique sur chaque fil. Ceci est fait à l'aide d'une étude magnéto-statique sous COMSOL. On trouve une valeur de 0.65 T sur chaque fil.

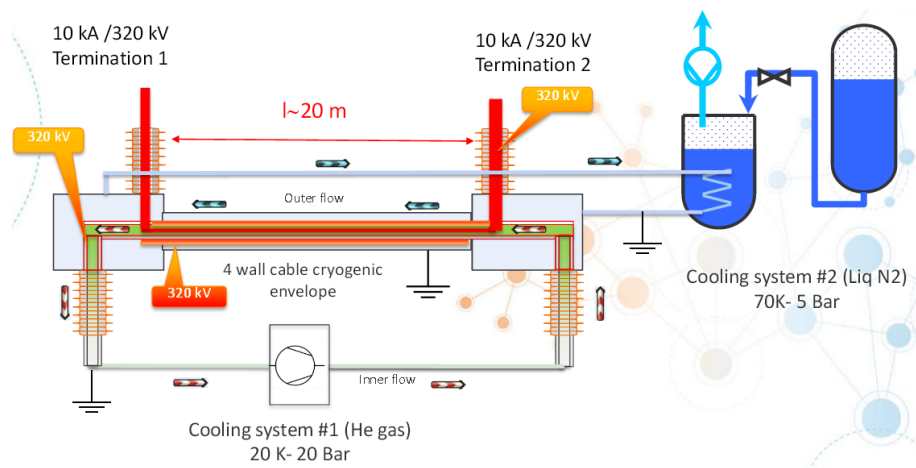


Fig. V.1 – DEMO 5 demonstrator working at 320 kV and 20 K. Four cryogenic envelopes are build for the cable and a liquid nitrogen shield is designed.

### V.1.a Calcul des pertes pour des harmonique de 1 % d'amplitude

Le câble va fonctionner en DC toutefois, les harmoniques AC présents sur le réseau vont induire des pertes dans les conducteurs. Bien que la valeur d'amplitude de ces harmoniques soit inconnue, nous avons choisi une valeur haute de manière à surévaluer légèrement les pertes calculées. Il apparait qu'une valeur de 1 % d'amplitude est intéressante à considérer. La Fig. V.2 présente les pertes AC en fonction de la fréquence du signal AC pour 1 % d'harmonique (en courant et en champ)

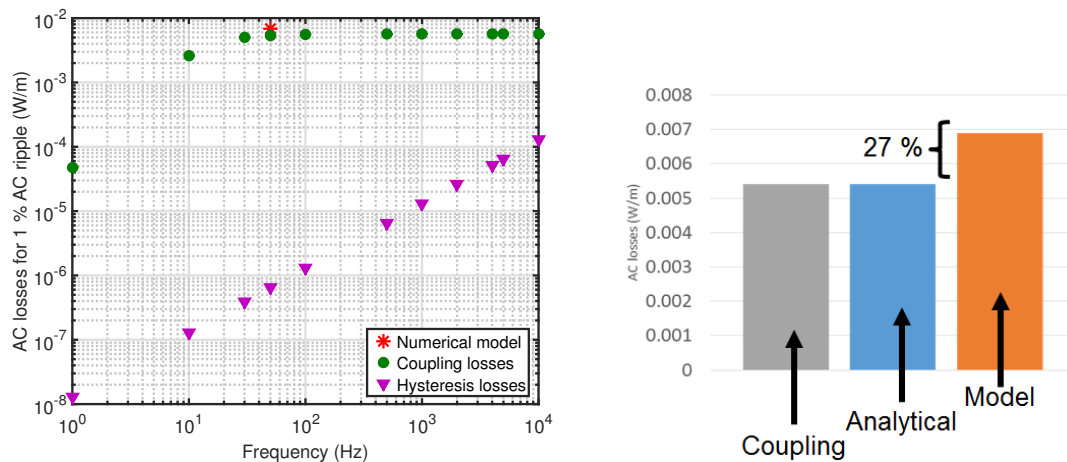


Fig. V.2 – Pertes AC calculées pour 1 % d'harmonique sur un fil. On observe que les pertes dans la matrice sont la principale cause de pertes dans le fil.

Les pertes générées par 1 % d'harmoniques restent importantes dans le dispositif il est donc intéressant d'étudier comment réduire les pertes dans la matrice, ceci peut être réalisé en modifiant le pas de torsade mais aussi en changeant la résistivité de la matrice. Différents approches ont été proposées comme de diviser le pas de torsade des filaments ou d'augmenter sensiblement la résistivité transverse de la matrice. Il est nécessaire de diviser au moins par 50 le pas de torsade des filaments pour réduire de 1000 les pertes mais ce

n'est pas possible industriellement à ce jour.

Toutefois, vu que les harmoniques sont de faibles amplitudes et que les pertes par couplage sont prépondérantes dans le fil, il peut être intéressant de détorsader les filaments dans les fils.

## V.2 Modélisation thermique

Après avoir dimensionné le système cryogénique du démonstrateur en calculant les pertes en fonctionnement, nous avons étudié la protection du câble pendant un court-circuit. Le démonstrateur qui sera installé à Nexans Hanovre ne sera pas sensible aux court-circuits. Toutefois si ces câbles sont installés dans le réseau électrique européen, il est important de savoir si le câble sera endommagé ou pas. Lors d'un court circuit, les fils supraconducteurs vont sortir de l'état supra et le courant va passer dans le cuivre ce qui va élever la température du câble. Le modèle magnéto-thermique a été réalisé sous COMSOL et présenté en Fig. V.3. Un couplage circuit est réalisé pour calculer les distributions de courant dans le démonstrateur.

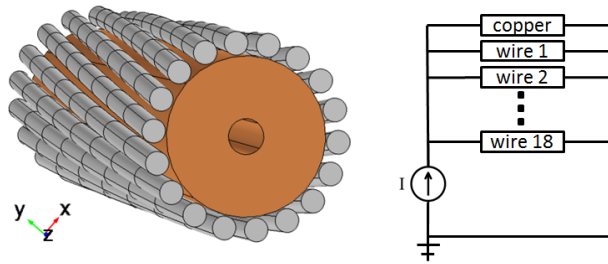


Fig. V.3 – Modèle 3-D du démonstrateur et couplage circuit.

Différents scénarios ont été simulés en faisant varier la vitesse de circulation du gaz, le temps de court circuit et son amplitude. Un exemple pour une vitesse de gaz de 0.1 m/s est présenté en Fig. V.4.

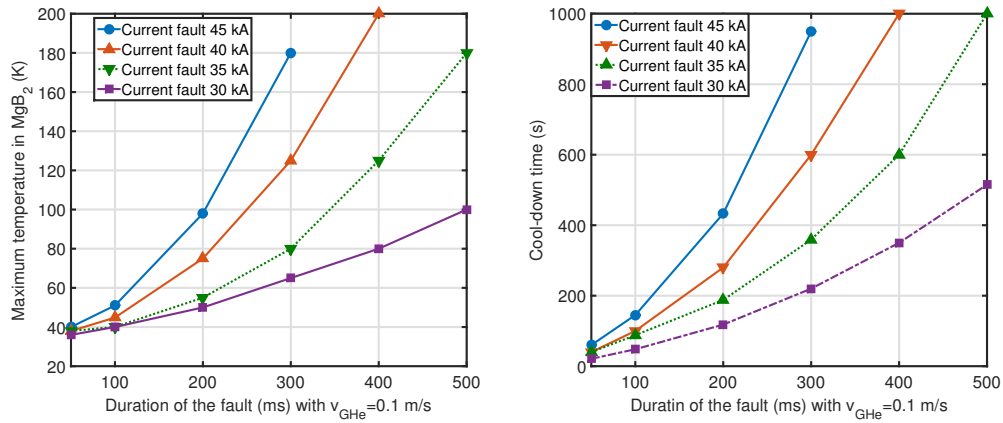


Fig. V.4 – Température maximale dans le câble et temps de refroidissement en fonction du temps de défaut pour plusieurs valeurs de court circuit.

De ces simulations, il est possible de voir que le câble ne dépasse pas 300 K pour des défauts inférieurs à 300 ms (temps de défaut typique de 100 ms). Le temps de refroidissement s'échelonne entre quelques secondes et plusieurs minutes. Ceci peut poser un problème dans le cas d'une installation à grande échelle.

---

## Conclusion

Ce travail de thèse a permis de calculer les pertes AC dans les câbles supraconducteurs en proposant une méthode de calcul multi-échelle. Après une étude approfondie des mécanismes de pertes dans deux conducteurs le  $\text{MgB}_2$  et le REBCO, les pertes AC ont été calculées sur la plage de fonctionnement en AC ou DC. De ces pertes il est possible de dimensionner rapidement le système cryogénique d'un câble supraconducteur et de réaliser des optimisations.

Ajouté à cela, plusieurs nouvelles approches notamment sur les lois de représentation des supraconducteurs et des critères de calculs des pertes sur un câble ont été proposées. Pour finir, un exemple d'utilisation est présenté avec le dimensionnement d'un démonstrateur supra dans le projet européen *BEST-PATH* celui-ci devrait être installé en 2018.



# PERTES AC DANS LES SUPRACONDUCTEURS : UNE APPROCHE MULTI-ÉCHELLE POUR LE DIMENSIONNEMENT DE CÂBLES FORT COURANT

**Résumé** Le travail de cette thèse porte sur l'étude des pertes AC dans les supraconducteurs pour des applications tels que les câbles ou les aimants. Les modélisations numériques rapportées sont de type éléments-finis ou méthode intégrale. Toutes ces méthodes visent à estimer avec précision les distributions de densité de courant et de champ magnétique en prenant en compte différents lois de comportement pour le supraconducteur. Deux conducteurs sont introduits dans ce mémoire. Tout d'abord, les supraconducteurs à haute température critiques sont étudiées avec l'introduction d'une nouvelle forme de conducteur HTc (fils cylindriques) qui sont envisagés pour des câbles fort courant de 3 kA. Dans un second temps, des simulations numériques 3-D sont réalisées sur un conducteur MgB<sub>2</sub>. Le chapitre suivant traite des contraintes de calculs des pertes dans le but de dimensionner l'ensemble des pertes d'un câble complet. Enfin, les modèles numériques développés précédemment sont utilisés sur un exemple concret : le démonstrateur 10 kA fait à l'aide du conducteur MgB<sub>2</sub> dans le projet européen *BEST-PATHS*.

**Mots clés** *Modélisation numérique, Éléments-finis, Méthodes intégrales, Pertes AC, Supraconductivité, Câbles de puissance supraconducteurs.*

---

## AC LOSSES IN SUPERCONDUCTORS : A MULTI-SCALE APPROACH FOR THE DESIGN OF HIGH CURRENT CABLES.

**Abstract** The work reported in this PhD deals with AC losses in superconducting material for large scale applications such as cables or magnets. Numerical models involving FEM or integral methods have been developed to solve the time transient electromagnetic distributions of field and current densities with the peculiarity of the superconducting constitutive E-J equation. Two main conductors have been investigated. First, REBCO superconductors for applications operating at 77 K are studied and a new architecture of conductor (round wires) for 3 kA cables. Secondly, for very high current cables, 3-D simulations on MgB<sub>2</sub> wires are built and solved using FEM modeling. The following chapter introduced new development used for the calculation of AC losses in DC cables with ripples. The thesis ends with the use of the developed numerical model on a practical example in the european *BEST-PATHS* project : a 10 kA MgB<sub>2</sub> demonstrator.

**Keywords** *Numerical modeling, FEM modeling, Integral methods, AC losses, Superconductivity, Superconducting power cables.*